https://theses.gla.ac.uk/

Theses Digitisation:

https://www.gla.ac.uk/myglasgow/research/enlighten/theses/digitisation/

This is a digitised version of the original print thesis.

Copyright and moral rights for this work are retained by the author

A copy can be downloaded for personal non-commercial research or study, without prior permission or charge

This work cannot be reproduced or quoted extensively from without first obtaining permission in writing from the author

The content must not be changed in any way or sold commercially in any format or medium without the formal permission of the author

When referring to this work, full bibliographic details including the author, title, awarding institution and date of the thesis must be given

Enlighten: Theses
https://theses.gla.ac.uk/
research-enlighten@glasgow.ac.uk

Fabrication and assessment of GaAs/AlGaAs multiple quantum well optical modulators

Submitted for the degree of
Doctor of Philosophy
to the
Faculty of Engineering,
University of Glasgow

by
Karen M^{c} ILvaney

January 1991

© Karen M^{c} ILvaney, 1990

ProQuest Number: 11007601

All rights reserved

INFORMATION TO ALL USERS
The quality of this reproduction is dependent upon the quality of the copy submitted.

In the unlikely event that the author did not send a complete manuscript
and there are missing pages, these will be noted. Also, if material had to be removed,
a note will indicate the deletion.

ProQuest 11007601

Published by ProQuest LLC (2018). Copyright of the Dissertation is held by the Author.

All rights reserved.
This work is protected against unauthorized copying under Title 17, United States Code
Microform Edition © ProQuest LLC.

ProQuest LLC.
789 East Eisenhower Parkway
P.O. Box 1346
Ann Arbor, MI 48106 – 1346

Acknowledgements

This work described in this thesis could not have been carried out without the use of the facilities and assistance of staff in this department headed by Prof. John Lamb. The support of Hughes Microelectronics and SERC are also acknowledged.

The bulk of the fabrication was carried out in the cleanroom area in the department which is supervised by Lois Hobbs whose technical and worldly knowledge aided this part of the work to its completion. Through the years I am also grateful to Tom Watson and Joan Carson for the help provided in this area. The dynamic duo of Dave Clifton and Jimmy Young cannot go unthanked for the patience and humor shown through the three years in dealing with the vacuum systems and the dry-etching equipment. The chromatography is carried out by Robert Harkins to whom I am very grateful especially for pointing out and correcting design errors. The technical assistance provided by the staff in the Ultra Small Structures Laboratory is also acknowledged as is John Cochrane, responsible for the photoluminescence results presented here. I am very grateful to Harry Anderson and his staff in the mechanical workshop for all the equipement provided and altered to suit requirements. The help and encouragement of George Boyle cannot go unnoticed, especially for the improvements to my golf handicap. I am also grateful to Gill Hunter for the careful reading of this manuscript.

The time during the PhD has been made more enjoyable by the friendship and support of many people in and out of the department. To mention a few my sister Anna Mc Ilvaney, Rebecca Cheung, Mary O'Neill, Patricia Connolly, and Lois Hobbs. Special thanks is due to Frances Laughton for all her help, particularly over the last few months.

For solving any problem I have presented to him whether it be concerned with equipement or politics, I am very grateful to Ray Hutchins. Solution to theoretical problems were found to expound from Dr. John Davies and Dr. Clivia Sotomayor Torres and many useful discussions with Bindi Bhumbra furthered my understanding of the theory. However with continual input from Prof. Richard De La Rue the actual show was run by my supervisor Dr. John Marsh. There is no doubt that his encouragement was the key factor in the completion of the work and the thesis.

Lastly I want to thank my family headed by my parents John and Winifred Mc Ilvaney for their incredible support and relentless encouragement and it is to them that I dedicate this thesis.

Contents

Page N°

Acknowledgements

List of figures

List of publications

Glossary

Abstract

Chapter One : Introduction 1

1.1 Optical communication systems 2

1.2 Modulation of light 4
1.2.1 Direct modulation of a light source
1.2.2 External modulation

1.3 Operating mechanisms of optical modulators 5
1.3.1 Acousto-optic modulators
1.3.2 Electro-optic modulators
1.3.3 Electroabsorption modulators

1.4 Electroabsorption 8
1.4.1 Electroabsorption modulators-Literature review
1.4.2 Transmission modulators-Waveguide structures
1.4.3 Reflection modulator devices
1.4.4 Transmission modulators-Perpendicular mode

1.5 Synopsis of thesis 13

References for Chapter 1 15

Chapter Two : Theory 19
Introduction
2.1 Semiconductors 20

2.2 Basic Semiconductor Theory : Energy Bands 20

2.3 Theoretical calculation of the energy bands 21
2.3.1 Free electron approximation
2.3.2 Tight binding model
2.3.3. Kronig-Penney model

2.4 Wavefunctions in quantum wells 25
2.4.1 Infinite potential well

2.4.2 Finite square well

2.5 Bandgap in semiconductors 29

2.6 Optical absorption 32
2.6.1 Electroabsorption in bulk semiconductors : The Franz-Keldysh effect
2.6.2 Quantum Confined Stark Effect (QCSE)
2.6.3. Theoretical modelling of the QCSE

2.7 *p-n* junction 39
2.7.1 *p-i-n* diode
2.7.2 I-V Characteristics

References for Chapter 2 42

Chapter Three Single Electroabsorption Modulator 47
Introduction
3.1 Design of modulator 48

3.2 Characterisation of CB 2 51
3.2.1 Photoluminescence
3.2.2 Current-voltage measurements

3.3 Fabrication of the electroabsorption modulator 56
3.3.1 Cleaning of the sample
3.3.2 Photolithography
3.3.2.1 Photoresist
3.3.2.2 Mask design
3.3.2.3 Exposure and developing
3.3.3 Evaporation of metal contacts
3.3.4 Lift-off
3.3.5 Chemical wet-etching
3.3.6 *n*-ohmic contact
3.3.7 Formation of mesa
3.3.8 Device mounting

3.4 Experimental set-up 63
3.4.1 Transmission measurements of CB 2
3.4.1.1 Light source
3.4.1.2 Chopper
3.4.1.3 End-fire rig
3.4.1.4 Detection of signal
3.4.1.5 Computer control of system
3.4.2 Experimental procedure

3.5 Transmission results of CB 2 66
3.5.1 Normalising curve

3.5.2 Zero bias spectrum of CB 2
3.5.3 The effect of an electric field on the transmission spectra
3.5.3.1 Low electric field effects< 1.0 x 10^4 V/cm
3.5.4 Electric fields below 2.8 x 10^4 V/cm
3.5.5 Electric fields between 2.8 x 10^4 V/cm and 5 x 10^4 V/cm
3.5.6 Electric fields between 50 kV/cm and 9.55 x 10^4 V/cm
3.5.7 Electric fields greater than 9.55 x 10^4 V/cm

3.6 Exciton broadening 79

3.7 Magnitude of exciton shift 81

3.8 Contrast ratio 85

3.9 Insertion loss 88

3.10 Speed of device 89

3.11 Calculation of the absorption coefficient 90

3.12 Discussion and conclusion 92

References for Chapter 3 94

Chapter Four : Spatial Light Modulator 97

Introduction

4.1 Spatial light modulator 98

4.2 Applications of spatial light modulators 98

4.3 Literature review: The spatial light modulator 99

4.4 Design and operation of the device 101

4.5 Fabrication of the spatial light modulator 103
4.5.1 Dry-etching of the SLM elements
4.5.2 Photosensitive polyimide
4.5.3 *p*-ohmic contact
4.5.4 Chemical wet-etching
4.5.5 *n*-ohmic contact
4.5.6 Alterations of the original design

4.6 Experimental set-up and procedure 114

4.7 Results and discussion 115

4.7.1 I-V Characteristics of the array elements
4.7.2 Zero Field Variation of the Absorption Spectra
4.7.2 Stark shift of the individual elements
4.7.4 Device operation : Optimised condition
4.7.5 Discussion

References for Chapter 4 **128**

Chapter Five : Coupled Quantum Well Modulators **131**
Introduction
5.1 Variations in the design of the absorption layer 132

5.2 Superlattice theory 132
5.2.1 Kronig-Penney Model

5.3 Literature review : Superlattice structures 134

5.4 Design of superlattice modulator layers- CB 102 135

5.5 Theoretical modelling of absorption spectra of superlattice structure 136

5.6 Superlattice CB 102-Experimental results 140

5.7 Comparison between theoretical and experimental results-CB 102 142

5.8 Theory of coupled quantum wells-Pairs of wells 146
5.8.1 Energy levels in pairs of coupled wells

5.9 Literature review : Coupled quantum wells 148

5.10 Pairs of quantum wells layer design-CB 184 149

5.11 Theoretical modelling of the absorption spectra of CB 184 149

5.12 Pairs of wells CB 184-Experimental results 151

5.13 Comparison between theoretical and experimental results-CB 184 155

5.14 Contrast ratio of CB 184 160

5.15 Discussion and conclusion 162

References for Chapter 5 **165**

Chapter Six Conclusions **168**
6.1 Conclusions 169

Appendix A Theoretical model to calculate the energy levels and the miniband widths of a superlattice 173

Appendix B Theoretical modelling of the absorption spectrum for a superlattice structure 175

List of figures

Chapter One

Figure 1.1 A schematic optical communications system

Figure 1.2 Acousto-optic modulation

Figure 1.3 A symmetric Mach-Zehnder electro-optic modulator

Figure 1.4 A directional coupler utilizing the electro-optic effect

Figure 1.5 Bulk GaAs waveguide modulator

Figure 1.6 Reflection modulator

Figure 1.7 LEAM and TEAM electroabsorption modulators

Figure 1.8 Perpendicular electroabsorption modulator

Chapter Two

Figure 2.2.1 Formation of the energy bands

Figure 2.3.1 E-k relation as derived using the free-electron model [Kittel 1976]

Figure 2.3.2 Periodic potential approximated by periodic square wells for the Kronig-Penney model

Figure 2.4.1 Finite quantum well

Figure 2.5.1 Energy band structure of GaAs

Figure 2.5.2 2D and 3D density of states functions

Figure 2.6.1 Effect of an electric field on the band edges of a semiconductor

Figure 2.6.2 The effect of an electric field on a quantum well system

Table 2.6.1 Calculated values of energy level shift (after Davies)

Chapter Three

Figure 3.1.1 Optical modulator structure layer CB 2

Figure 3.1.2 Multiple quantum well layers

Figure 3.2.1 Photoluminescence spectrum of CB 2 at 9.2 K

Table 3.2.1 Well width of the grown structure determined from Xton at 9.2 K

Table 3.2.2 Well width of the grown structure determined from Xton at 300 K

Figure 3.2.2 Room temperature photoluminescence of CB 2 (recorded at Sheffield)

Figure 3.2.3 Leakage current of CB 2 as a function of voltage

Figure 3.3.1 Sample exposed to U.V. light and the resist developed

Figure 3.3.2 Lift-off process

Figure 3.3.3 Top *p*-ohmic contact

Figure 3.3.4 Aligning of ohmic contacts

Figure 3.3.5 Multiple quantum well electroabsorption modulator

Figure 3.3.6 Mounting of the modulator

Figure 3.4.1 Experimental set-up

Figure 3.5.1	Normalizing curve
Figure 3.5.2	Transmission spectrum of CB 2 at zero applied bias
Figure 3.5.3	Transmission spectra of 0 V and -1 V
Figure 3.5.4	Transmission spectra from -2 V to -5 V
Figure 3.5.5	Transmission spectra from -6 V to -10 V
Figure 3.5.6	Selected transmission spectra from -11 V to -20 V
Figure 3.5.7	Selected transmission spectra from -20 V to -33 V
Table 3.6.1	Linewidths of various multiple quantum well structures at 300 K determined from absorption measurements at zero bias
Table 3.6.2	Broadening of the heavy hole exciton peak as a function of applied electric field to CB 2
Table 3.7.1	Exciton shift as a function of electric field for layer CB 2
Table 3.7.2	Magnitude of exciton shift of various well widths from literature
Figure 3.7.1	Comparison of the experimental shift of the exciton peak and the theoretical shift obtained using equation 2.50 for layer CB 2
Figure 3.7.2	Magnitude of the shift of the exciton peak for various well widths from the literature at an electric field of 5.5×10^4 V/cm
Table 3.8.1	Contrast ratios of the electroabsorption multiple quantum well modulator fabricated as outlined in Section 3.3
Figure 3.8.1	Variation of the contrast ratio with wavelength between an applied bias of -25 V and 0 V
Table 3.8.2	Contrast ratios for similar multiple quantum well modulators from the literature
Figure 3.9.1	Insertion loss of the modulator device fabricated from layer CB 2
Figure 3.11.1	Absorption coefficient as a function of wavelength for 0 and -25 V
Figure 3.11.2	The change in the absorption coefficient between 0 and -25 V applied bias to CB 2

Chapter Four

Figure 4.4.1	Electrical equivalent circuit of the diode array
Figure 4.4.2	Diode array with an applied voltage to Element 9
Figure 4.5.1.a	Fabrication of a spatial light modulator
Figure 4.5.1.b	Fabrication of a spatial light modulator
Figure 4.5.1.c	Fabrication of a spatial light modulator
Figure 4.5.2	Defining of the SLM elements by dry-etching
Figure 4.5.3	A layer of polyimide is spun onto the device
Figure 4.5.4	The polyimide is exposed and developed
Figure 4.5.5	Top *p*-ohmic contacts of the SLM
Figure 4.5.6	The substrate of the crystal is removed to reveal the modulator elements
Figure 4.5.7	The *n*-ohmic contacts are aligned perpendicularly to the *p*-ohmic contacts and the remaining

epitaxial layers removed from the top of the *p*-ohmic contacting pads (see also Photograph 4.7-4.9)

Figure 4.7.1 Variation of the exciton peak at zero applied field
Figure 4.7.2 Variation of the absorption edges of the SLM at zero applied electric field
Figure 4.7.3 a Transmission spectra of elements 1, 2, 3 and 4
Figure 4.7.3 b Transmission spectra of elements 5, 6, 7 and 8
Figure 4.7.3 c Transmission spectra of elements 9,10, 11 and 12
Figure 4.7.3 d Transmission spectra of elements 13, 14, 15 and 16
Figure 4.7.4 Optimised operating wavelength for a drive voltage of -25 V
Figure 4.7.5 Optimum wavelength of operation for a drive voltage of -20 V

Chapter Five

Figure 5.2.1 Formation of minibands due to the resonant tunnelling effect in the superlattice, and the effect of the electric field on the energy levels
Figure 5.2.2 Wavefunction in a superlattice conduction band, effect of electric field on the wavefunction
Figure 5.4.1 Superlattice layer CB 102
Figure 5.4.2 Overall design of modulator layers
Table 5.5.1 Parameters necessary for use in the Kronig-Penney model
Figure 5.5.2 cos (k) as a function of energy obtained from the Kronig-Penney model for a superlattice with 50 Å wells and 30 Å barriers
Table 5.5.3 Miniband edges and widths determined from Figure 5.5.2 for a superlattice with period 80 Å
Figure 5.5.4 Theoretically calculated absorption spectra of superlattice CB 102
Figure 5.6.1 Transmission spectra of CB 102 for applied voltages of 0 Volts and -1 Volt
Figure 5.6.2 Transmission spectra of CB 102 at applied voltages of 0 Volts,-10 Volts, -20 Volts and -30 Volts
Figure 5.7.1 Comparison between theoretical and experimental electroabsorption results for low applied electric fields
Figure 5.7.2 Comparison between theoretical and experimental electroabsorption results for high applied electric fields
Figure 5.8.1 The effect of an electric field on the energy levels in a pair of coupled quantum wells (after Chen 1987)

Figure 5.8.2 Coupling of the electronic wavefunction in a pair of coupled wells
Figure 5.10.1 Pairs of coupled wells layer CB 184
Table 5.11.1 Calculations of energy levels in the pairs of coupled wells (after Whiteaway)
Figure 5.11.2 Theoretical modelling of absorption spectra of layer CB 184
Figure 5.12.1 Transmission spectra of CB 184 obtained from photocurrent results for 0 V and -1 V
Figure 5.12.2 Transmission spectra of CB 184 at 0 V and -2 V
Figure 5.12.3 Transmission spectra of CB 184 at 0 V and -3 V
Figure 5.12.4 Transmission spectra of CB 184 for 0 V and -8 V
Figure 5.13.1 Theoretical absorption spectra of CB 184 corresponding to 0 V and -1 V
Figure 5.13.2 Theoretical transmission spectra of CB 184 corresponding to 0 V and -8 V
Figure 5.13.3 Theoretical absorption of of CB 184 at 24 000 V/cm
Figure 5.13.4 Experimental saturation of the 'blue shift' in CB 184
Figure 5.14.1 Contrast ratio between 0 V and -1 V spectra for CB 184
Figure 5.14.2 Contrast ratio between 0 V and -2 V spectra for CB 184
Figure 5.14.3 Contrast ratio between -1 V and -8 V spectra for CB 184

Chapter Six

Figure 6.1 Maximum change in the absorption coefficient obtained for CB 2
Figure 6.2 Maximum change in the absorption coefficient obtained for CB 102
Figure 6.3 Maximum change in the absorption coefficient obtained for CB 184

Appendix A

Figure A.1 Superlattice structure

List of photographs

Photograph 3.1 Wet-etching profile of the GaAs in the fast non-selective etch
Photograph 3.2 Effect of the selective etch which stops at the etch stop layer. The traces of the GaAs substrate will be removed by the etch
Photograph 3.3 Top contact viewed through the glass slide
Photograph 3.4 Bottom contact viewed from the top of the device
Photograph 3.5 View of the mesa process which isolates the device from the surrounding epitaxial layers
Photograph 4.1 The SLM elements are defined using dry-etching techniques
Photograph 4.2 Polyimide is spun onto the device
Photograph 4.3 The polyimide covers the elements and fills the area between each
Photograph 4.4 The polyimide is exposed to UV radiation and developed
Photograph 4.5 Photoresist is used to define the top *p*-ohmic contacts
Photograph 4.6 The top *p*-ohmic contacts are evaporated onto the device
Photograph 4.7 After the substrate is removed the bottom *n*-ohmic contacts are

evaporated

Photograph 4.8 Back view of the *n*-ohmic and *p*-ohmic contacts aligned to an element of the SLM

Photograph 4.9 Top view of elements in the device

Photograph 4.10 The remaining epitaxial layers are removed using dry-etching techniques to reveal the *p*-ohmic contacting pads

Photograph 5.1 The epitaxial layers of CB 184 after the removal of the substrate Area shown is at the edge of the crystal

Photograph 5.2 The epitaxial layers of CB 184 after the removal of the substrate Area shown is at the centre of the crystal

List of publications

K. Mc ILvaney, J.H. Marsh, J.S. Roberts and C.Button

'A low drive voltage GaAs/AlGaAs coupled quantum well modulator exhibiting blue and red absorption edge shifts'

Presented at the IEE

'Applications of quantum wells in optoelectronics'

13 June 1990

K. Mc ILvaney, J.H. Marsh, J.S. Roberts and C.Button

'Evaluation of MQW structures for use in spatial light modulators'

Gallium arsenide and related compounds 1990, Jersey, Channel Islands

Proceedings of the seventeenth international symposium on gallium arsenide and related compounds

September 1990

Page 621-626

K. Mc ILvaney, J.H. Marsh, J.S. Roberts and C.Button

'Matrix-addressed 4 x 4 spatial light modulator using the quantum confined stark effect in GaAs/AlGaAs quantum wells'

Electronic Letters

27th September 1990 Volume 26 No. 20

Page 1691-1693

K. Mc ILvaney, J.H. Marsh, J.S. Roberts and C.Button

'Two-dimensional 4 x 4 spatial light modulator fabricated in GaAs/AlGaAs multiple quantum wells'

Presented at the SIOE, Cardiff

March 1990

Glossary

F	Electric field (V/cm)
E_1	Energy of the lowest allowed energy level in the conduction band (meV)
H_1	Energy of the lowest allowed heavy hole energy level in the valence band (meV)
L_1	Energy of the lowest allowed light hole energy level in the valence band (meV)
ΔE_1	Miniband width associated with the lowest energy level in the condcution band (meV)
ΔH_1	Miniband width associated with the lowest heavy hole energy level in the valence band (meV)
ΔL_1	Miniband width associated with the lowest light hole energy level in the valence band (meV)
m_o	Electron rest mass (kg)
E_F	Fermi energy level (eV)
λ_c	Modulus of transfer integral between neighbouring wells = $\frac{\Delta E_1}{4}$ (meV)
λ_v	Modulus of transfer integral between neighbouring wells = $\frac{\Delta H_1}{4}$ (meV)
α_o	$= \frac{2\pi e^2 P^2 M}{n c m_o^2 \hbar^2 \omega} = 0.006$
M	in-plane reduced mass of the electron-hole pair
P	is the Kane matrix element
n	optical index
f	$= \frac{eFd}{(\lambda_c + \lambda_v)}$
Y	The unit step function
$J_m(x)$	Bessel fuction of order x and index m
h	Planks constant = 6.626×10^{-34} J-s

Abstract

This thesis outlines the design, fabrication and testing of electroabsorption modulators and modulator arrays in GaAs/AlGaAs multiple quantum well material.

Single electroabsorption modulators were designed to have a high contrast ratio and low insertion loss. For this purpose a 200 period structure, consisting of isolated wells 50 Å wide, was grown by MOVPE. The electric field was applied, and light was incident, perpendicular to the epitaxial layers of the device. On applying a reverse bias, a red shift of the absorption edge was observed. The performance of the modulator was as follows: for an applied voltage of 25 V and working at an optimised wavelength of 837 nm, the modulation depth was 8.95 dB accompanied by an insertion loss of 4.9 dB for a device with no anti-reflection coatings.

As a method of assessing the suitability MQW modulators for the routing of optical signals in a communications system, individual modulators were configured into a 4 x 4 array, thus forming a two dimensional spatial light modulator. One of the key requirements of such a device is to eliminate the need for many electrical connections which hinders the operation of large arrays. A row and column line addressing system was used which is capable of expansion to large arrays, but which reduces the maximum contrast ratio and alters the optimum wavelength of operation from that of single modulators. The modulation depth of the array was reduced to 6.1 dB at an optimised operating wavelength of 838.1 nm by a combination of the addressing system chosen and of nonuniformities in the epitaxial material.

Theoretical calculations have predicted that coupled well MQW structures have advantages over uncoupled MQW structures in terms of achieving a high contrast ratio without the need of a high drive voltage. Two devices containing coupled well structures were designed and fabricated. The first device contained a superlattice with 200 x 50 Å wells coupled through 30 Å barriers. Although changes in the absorption spectrum were seen for voltages as low as 2 V, the superlattice exhibited low modulation depths (8%). The second design used pairs of coupled wells isolated by thick barriers to enhance the electroabsorption effect. In contrast to structures containing isolated wells, under a reverse bias this structure exhibited an effective

blue shift in the absorption edge at low electric fields, > 9 x 10^3 Vcm^{-1}, and an effective red shift at fields > 3 x 10^4 Vcm^{-1}. This feature can be optimised to provide novel operation of modulator arrays and a modulation depth of ≈ 2 dB was predicted for a working voltage of 8 V. For single modulators, a maximum modulation depth of 3.8 dB was inferred from photocurrent data for an applied voltage switching between 1 V and 8 V and an operating wavelength of 818 nm.

Chapter One
Introduction

1.1 Optical communication systems

Conveying information by means of light is certainly not a new concept. Such transmission has taken place in many forms since the possibility to create fire, reflective surfaces and electric light has existed. The earliest demonstration of comparable technology to that presently employed for optical communications was perhaps the photophone, invented by Alexander Graham Bell in 1880. This device varied the intensity of sunlight in response to the amplitude of speech vibrations. A receiver could then be used to reconvert the sunlight variations into an electrical signal by means of a detector, and subsequently into sound. [Gagliardi 1976] This prototype system was capable of transmission over short distances (200 m) but, until the first demonstration of the laser in 1960 by Maiman at Hughes Aircraft, long haul communications were not feasible. [Tamir 1975] Alone, however, the laser could not solve the problems of strong absorption of light in the atmosphere. Therefore, despite the advantages over conventional electrical systems offered by this invention, it was not until the development of low-loss optical fibres, by Charlie Kao at S.T.L, that the potential of modern optical communication systems was realised.

There are many advantages of using the rapidly developing methods of optical communication systems over electrical wire systems. Conventional electrical systems are limited in their information bandwidth (which is utilised using multiplexing and coding techniques). For wire and coaxial lines the available frequency extends from d.c up to 10^8 to 10^9 Hz. By modulating light from sources such as lasers, the potential bandwidth available is several orders of magnitude higher than in electrical systems, thus much more information can be transmitted in a given time. The smaller, lighter and increasingly less expensive glass fibres are useful for applications where space is limited or, as in the case of underwater and aircraft cables, where size and weight are important. Optical fibres are immune to electrical noise and electromagnetic interference, with the advantage of no crosstalk problems since they do not generate their own electrical noise. At frequencies above several kHz, the losses of fibres are much less than those of metallic cables, needing fewer repeaters and therefore reducing costs. The realization of these benefits has led to the incorporation of optical systems in telecommunication networks for both long and short distance transmission.

Communication via optical methods has advanced greatly since Bell's fair weather invention. Improvements on existing systems are being continually made by reducing costs, and by increasing their capacity, speed and efficiency. Novel devices are being invented and, in a closely related field, the 'optical computer' is becoming a reality. Long term plans include the monolithic integration of compatible devices for use in optical computers and other systems requiring optical transmission.[Wheatley 1987, Miller 1984, Neff 1989] Of particular concern in this work are optical modulators, which will now be described in the context of an optical communications network.

Incorporated in an optical communications system, as shown in Figure 1.1, are a transmitter, a receiver and repeaters. The source of light for transmission in this case is a semiconductor laser. The laser consists of a p-n junction diode which, when forward biased, emits radiation at a wavelength principally determined by the bandgap of the semiconductor. This radiation can be detected by using a reverse biased *p-i-n* semiconductor diode. The electron and hole pairs, created by the photons, are separated and swept out of the depletion region in opposite directions, thus producing a current in the external circuit.[Sze 1985] For information to be placed upon the optical carrier some physical property of the beam must be modulated e.g. amplitude, phase or frequency. The signal is then carried by an optical fibre and, for long transmission distances, it is necessary to re-amplify the signal using repeaters. At the receiving end the signal is collected by a detector, demodulated and output in the form required, for example as a telephone signal, computer data or a television picture.

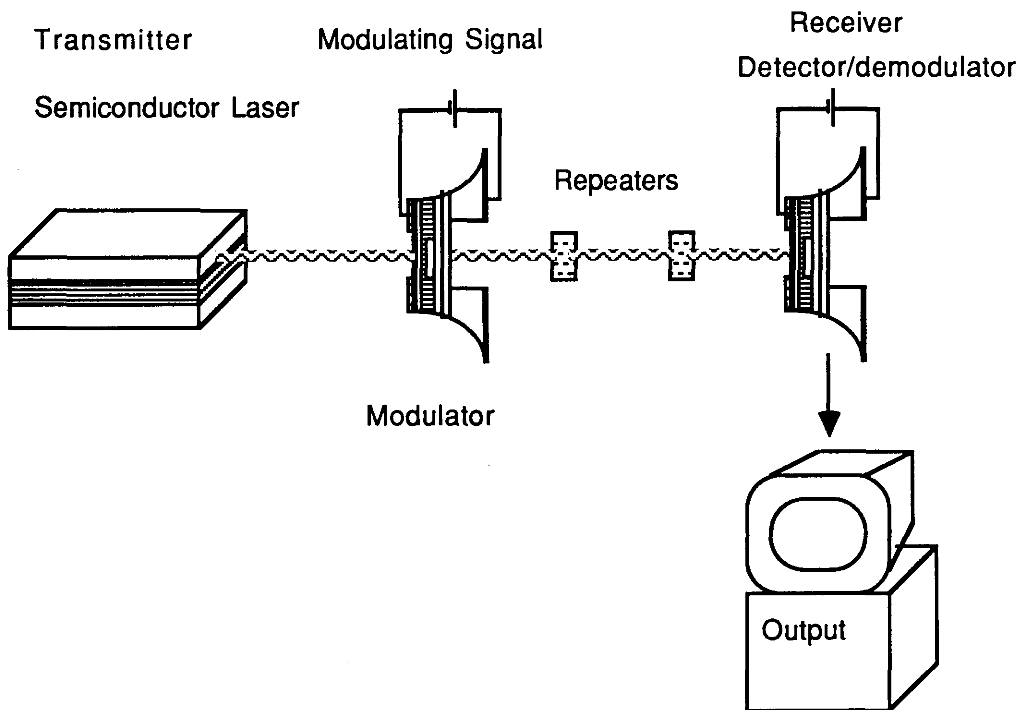

Figure 1.1 A schematic optical communications system

1.2 Modulation of light

In order to modulate light two approaches may be taken: direct modulation of the light source or, the topic of this thesis, use of an external modulator. Advantages exist in both methods but the development of external modulators has been necessary as the fundamental limitations of directly modulated injection lasers have been reached. [Wood 1989]

1.2.1 Direct modulation of a light source

The principal attraction of the direct modulation technique is its simplicity, leading to a reduction in the number of components and expense of a communications system. To perform the modulation, the laser is biased just above threshold and a signal is superimposed on the drive current; the output power of the laser is therefore an analog of the modulation waveform.

In conventional systems the output power is distributed over a number of longitudinal modes which may vary with time particularly if the system is

modulated.[Okano 1980] Fibre dispersion however dictates that for high bit rate, long-haul systems a single frequency laser, such as a distributed feedback (DFB) laser, is required. Even using DFB lasers frequency modulation or chirp can be caused by modulation induced variations in carrier density, giving rise to changes in the refractive index, changing the output optical frequency.[Linke 1984] In the time domain the overall turn-on and turn-off time are also influenced by the parasitics. Furthermore large signal responses which exhibit strong nonlinearities at high frequencies are inherent to the laser carrier and photon rate equations. Successful direct modulation has however been demonstrated at 1.7 Gbits/s [Hakki 1985] and bandwidths of 15-16 GHz at room temperature [Su 1985] with 22 GHz at cooled temperatures [Bower 1985] also being obtained. The largest bandwidth quoted in the literature is 30 GHz [Yariv 1987]

1.2.2 External modulation

The use of an external modulator allows more flexibility in the system. As yet modulators (of the type to be discussed) have not exhibited modulation speeds comparable with that of the fastest laser [Wood 1988] but possess other advantages and it is expected theoretically that they will have a very fast response.

The device area can be made small and, because of back biasing, the junction thickness can be large. Both of these contribute to a low capacitance, increasing the speed of modulation.[Wood 1985] Also in high speed applications the fact that modulators can operate at lower power dissipations may be an advantage. The flexibility, in design and choice of material, associated with external modulators means that they can be tailored to particular systems.[Wood 1989]

1.3 Operating mechanisms of optical modulators

A number of techniques which have been exploited in devices to modulate light are discussed below.

1.3.1 Acousto-optic modulators

For some applications in integrated optics, particularly at low modulation frequencies, the interaction of an optical beam with acoustic waves is exploited. Certain crystals exhibit changes in the refractive index due to the mechanical strain,

produced by the propagation of ultrasonic waves through them. This results in compressions and rarefactions which cause the refractive index to increase and decrease. Light incident onto the acousto-optic material is scattered off the alternating surfaces of high and low refractive index, each of which repeats at the acoustic wavelength, as in Figure 1.2. The optical frequency is shifted by an amount equal to the acoustic frequency. It is possible to obtained modulation depths as high as 95% using this method.[Bagshaw 1985]

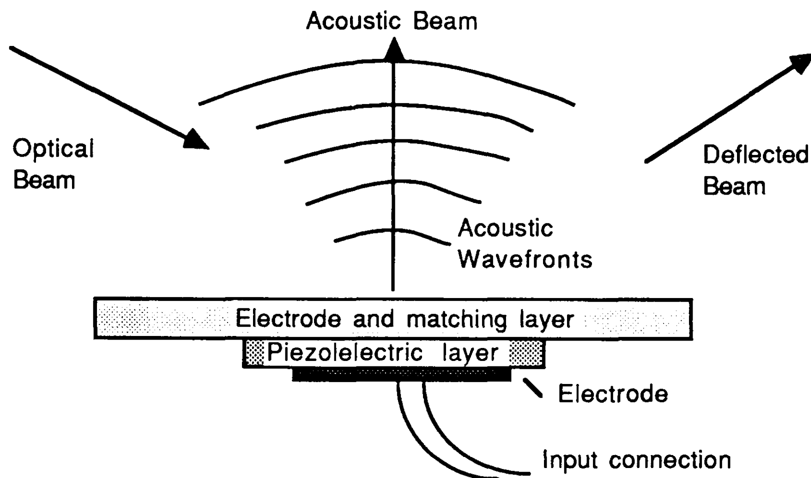

Figure 1.2 Acousto-optic modulation

A typical bulk acousto-optic modulator has a piezoelectric transducer bonded onto a block of acousto-optic material. The r.f. information is thus phase modulated onto the optical beam. Amplitude modulation is achieved by varying the r.f. power which changes the amount of the incident beam that is deflected.

1.3.2 Electro-optic modulators

The electro-optic effect can be broadly defined to include changes in refractive index, absorption and scattering caused by the application of an electric field to a material. The versatility of this effect deems that all forms of modulation (amplitude, phase, intensity and frequency) are possible, with broadband operation achievable at many optical wavelengths.[Tamir 1975]

The main electro-optic mechanism utilised in modulator devices is the Pockels effect, which is linear in applied electric fields. Consider a crystal which has the electric field and the direction of the propagating beam parallel to the optical axis. In the absence of the electric field any ray propagating in the direction parallel to the

optical axis is an ordinary ray. A second optical axis is induced by the electric field, in a plane perpendicular to the field, whose direction depends on the crystal structure. This anisotropy leads to rays polarised with their electric field vectors parallel to the induced optical axis experiencing a different refractive index known as the extraordinary refractive index. Therefore, in an electric field, the crystal acts on the light ray as a birefringent crystal whose optical axis lies in a plane perpendicular to the direction of propagation. The Pockels effect occurs for both parallel and perpendicular application of the electric field. It is possible to construct intensity, polarisation and frequency modulators utilising this effect.

A smaller, second order electro-optic effect, also exists. This effect, known as the Kerr effect, is quadratic in relation to the applied electric field but in general requires a greater drive voltage than the Pockels effect.

Electro-optic modulators utilising the Pockels effect have been demonstrated and are commercially available for many applications. In lithium niobate the processes of proton-exchange and titanium oxide in-diffusion are used to fabricate waveguides for use in Pockels effect intensity modulators. Travelling wave intensity modulators have been demonstrated [Izutsu 1988] which have an extinction ratio of 98% and a bandwidth of 18 GHz at a drive voltage of 8.8 V.

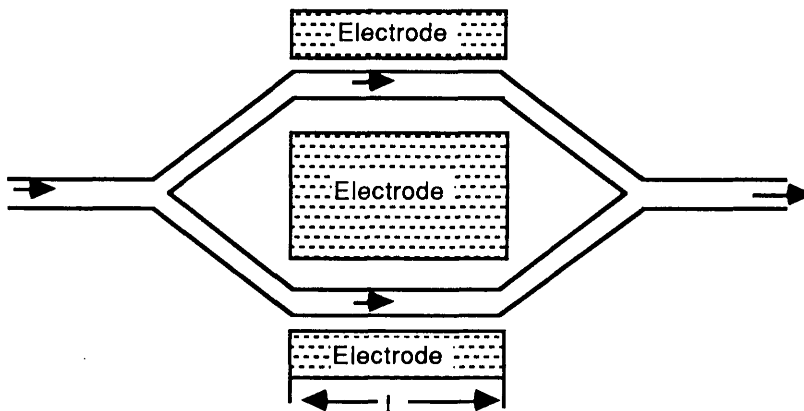

Figure 1.3 A symmetric Mach-Zehnder electro-optic modulator

The input light to the Mach-Zehnder electro-optic modulator is split into two portions using a Y-junction. Each arm of the symmetric Mach-Zehnder, shown in Figure 1.3, is phase modulated separately and the light is then allowed to combine

again either constructively or destructively in another Y-junction, thus a Mach-Zehnder interferometer is formed. Devices with drive voltages as low as 0.65 V [Duchet 1989] are now being demonstrated in a reflective Mach-Zehnder configuration, where the reflective structure is used to lower the drive voltage by increasing the interaction length.

Another method of modulating the light is to use a directional coupler (Figure 1.4) where the coupling of an optical beam between waveguides is varied by applying an electric field. In the absence of an electric field total transfer of energy from the launched guide into the unlaunched guide is obtained in a length called the coupling length. The application of a voltage reduces the portion of energy transferred between the two waveguides. Using this method of intensity modulation, modulation depths as high as 90% with a drive voltage of 17 V [Bozhevolnyi 1982] and also fast operation, 33 ps at a voltage of 8 V [Korotky 1983] have been demonstrated.

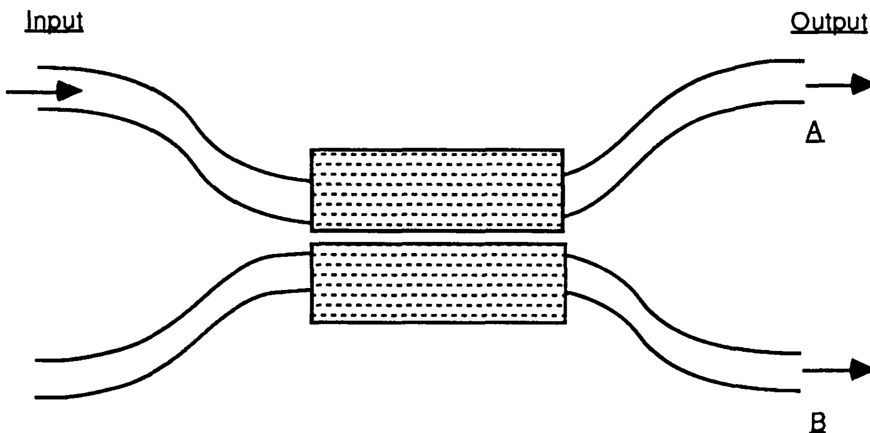

Figure 1.4 A directional coupler utilising the electro-optic effect

The potential of the electro-optic effect is also being realised in other material systems. A novel polymer modulator has been demonstrated [Diemeer 1989] achieving comparable figures of merit to lithium niobate. Thus high modulation depths, low drive voltages and fast operation are possible in organic materials using the linear electro-optic effect.

1.4 Electroabsorption

During the process of electroabsorption an electric field induces a change in the absorption spectrum of a material at energies near its bandgap.[Stillman 1976]

This occurs due to a shift of the band edges allowing transitions to take place at lower photon energies, which were forbidden in the absence of the electric field. Such dramatic alteration of the absorption leads to a very fast and simple method of modulating light. Interest in this effect is heightened by its added capability of providing a measure of the amount of light modulated. The incident photons generate electron-hole pairs which are swept out by the electric field producing a photocurrent. This enables the device not only to modulate light but also to detect it, therefore novel devices are possible [Miller 1988]. Electroabsorption is the result of two effects, the Franz-Keldysh effect in bulk semiconductors [Franz 1958 and Keldysh 1958] and the Quantum Confined Stark Effect in multiple quantum well systems.[Miller 1984]

The original effect in bulk material was independently proposed by Franz and Keldysh in 1958. Their theories, experimentally verified by J.R. Dixon and J.M. Ellis [1961], stated that when a semiconductor crystal is placed in a uniform electric field, absorption takes place at optical wavelengths where it would not normally occur. A detailed discussion of this effect is presented in Chapter 2.

In recent years emphasis has been placed on multiple quantum wells as a means of enhancing the electroabsorption effect [Miller 1985-1989]. In these structures, on the application of an electric field, there is a clear red shift of the absorption edge of the material. This mechanism forms the basis of the work presented in this thesis and is examined in detail in Chapter 2.

1.4.1 Electroabsorption modulators - Literature review

Modulators based on electroabsorption effects can be divided into three types. Firstly are devices configured into waveguide structures to provide strong light confinement, low insertion losses and high contrast ratios. Secondly are devices proposed relatively recently which are perpendicular reflection modulators which can also incorporate mirror stacks to form a Fabry Perot cavity providing high contrast ratios and low insertion losses, without penalties in the drive voltage.[Whitehead 1989] The insertion loss of the whole system is, however, increased by the necessary inclusion of a beam splitter to control the reflected beam of light. Finally the modulator design which is of interest to this thesis, operates in a

perpendicular mode where the light and electric field are perpendicular to the growth direction of the crystal. A literature review of devices operating in each of these modes will now be presented with emphasis on the material systems which will be examined in this work, i.e. gallium arsenide [GaAs hereafter] and aluminium gallium arsenide [AlGaAs].

1.4.2 Transmission modulators - Waveguide structures

A waveguide modulator is shown in Figure 1.5, where the light is incident parallel to the layers.[Weiner 1985] The layers are designed to provide strong light confinement and are configured in a *p-i-n* diode, to allow the application of moderately high electric fields (10^5 V/cm). Because the active region is thin only low reverse voltages are required. For a bulk GaAs waveguide modulator of length 390 μm the insertion loss was found to be less than 10% or 0.4 dB [Wight 1988] with an extinction ratio of 29 dB at an applied voltage of 38 V. On reducing the length of the devices a lower voltage of 8 V gave an extinction ratio of 20 dB and an insertion loss of 0.3 dB. In optimised devices it was predicted that an extinction ratio of 18.5 dB could be obtained for 62 μm long devices working at only 10 V. Attention was turned to multiple quantum well material to attempt to enhance the modulator characteristics.

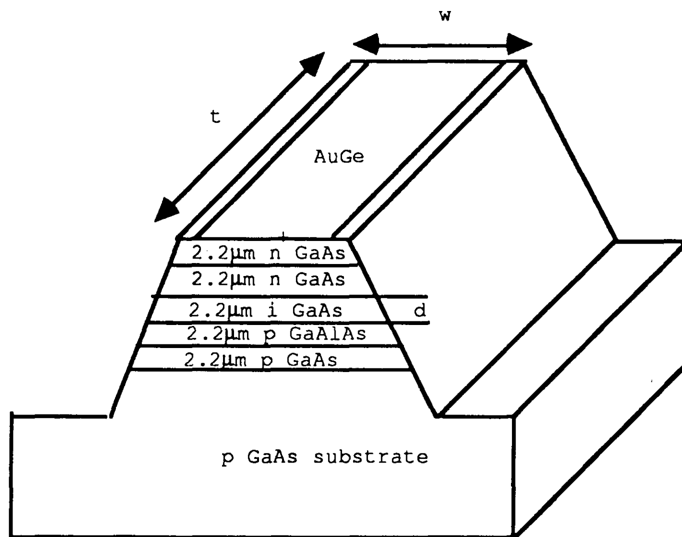

Figure 1.5 Bulk GaAs waveguide modulator

Quantum well systems exhibit clear confinement of excitons within potential wells

even at room temperature. This confinement leads to enhanced absorption effects and the excitonic absorption feature persists to relatively high electric fields. It should therefore be possible to fabricate devices capable of higher contrast ratios than those of the bulk devices. Hindering the progress of this relatively recent technology is the ability to control the thickness of the wells during growth and the quality of interfaces between the various layers. Advances in this field have enabled the fabrication of high quality devices capable of not only achieving high contrast ratios and low insertion losses but also fast modulation [Miller 1988].

A multiple quantum well waveguide modulator with a contrast ratio of 7:1 and a drive voltage of less than 1 V has been demonstrated in the GaAs/AlGaAs system [Weiner 1987]. A similar waveguide device has been demonstrated which has an on/off ratio of 10 dB and a speed of 97 ps. Although this device exhibited an insertion loss of 7 dB, neglecting coupling losses, it is expected that this could be reduced to a level as low as 0.1 dB by employing anti-reflection coatings [Wood 1988]. All of these devices work in transmission where the light is input to the waveguide, modulated in the active region and detected after leaving the device.

1.4.3 Reflection modulator devices

A novel method of improving the contrast ratio without penalties in the drive voltage is to operate a planar modulator in reflection mode. Light is incident perpendicularly onto the front face of the crystal. A reflective mirror, consisting of quarter wave stacks of alternating layers of AlAs and GaAlAs, is grown before the multiple quantum well layer. The incident light is reflected back through the active region experiencing twice the absorption. In this manner the advantage of twice the absorption is gained, possibly leading to a higher contrast ratio, without penalties in the drive voltage. Such devices (Figure 1.6) fabricated from GaAs/AlGaAs multiple quantum wells exhibited contrast ratios of 8:1 at an operating frequency of 5.5 GHz [Boyd 1989]. By varying the parameters involved, contrast ratios initially of 100:1 (insertion loss of 3.5 dB) and subsequently improved to 227:1 with the insertion loss of the device reduced to 2.6 dB, were achieved.[Whitehead 1989] With a drive voltage of 7 V, a contrast ratio of 7:1 was also obtained in this mode of operation.[Simes 1989]

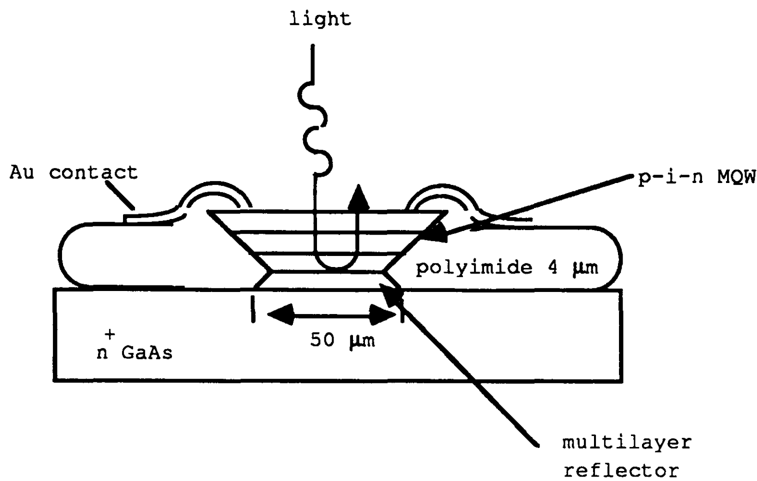

Figure 1.6 Reflection modulator

1.4.4 Transmission modulators-Perpendicular mode

In bulk GaAs, planar devices have been demonstrated [Wight 1985] with the electric field either parallel to the beam (LEAM) or perpendicular (TEAM), the light being incident perpendicular to the growth layers. (Figure 1.7 (a) and (b) respectively) A *p-i-n* structure is employed in the LEAM to allow the application of the electric field.

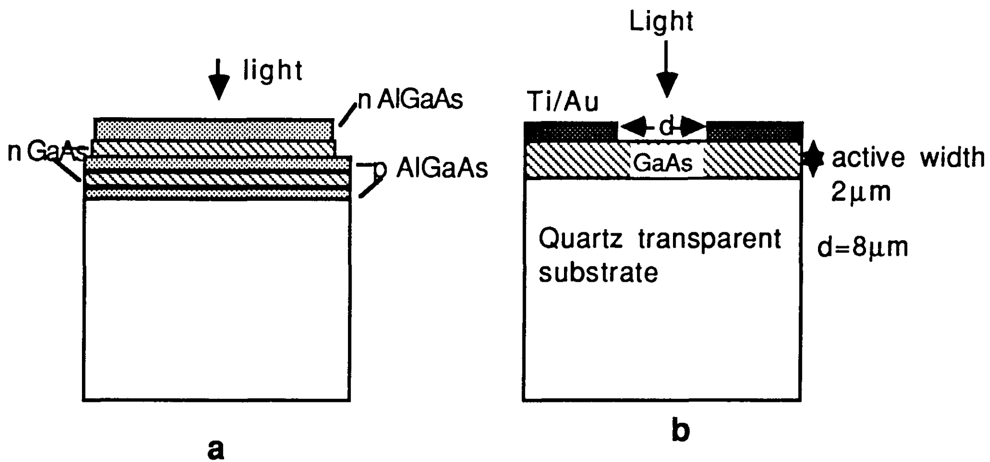

Figure 1.7 LEAM and TEAM electroabsorption modulators

In the transverse modulators, in which the electric field is applied between surface electrodes transverse to the optical path, a modulation depth as high as 50% was achieved for an applied voltage of 30 V. The depth achieved in the longitudinal

system, where the field is applied parallel to the optical path, was 25% at a drive voltage of 5 V. The expected bandwidth of such devices was 10 GHz.

Transmission modulators which operate in this mode have also been fabricated in MQW systems. These are particularly relevant to this thesis and an detailed analysis of these is presented in Chapter 3.

1.5 Synopsis of thesis

The aims of this thesis are to outline the steps taken in designing, fabricating and testing an electroabsorption modulator. The first step was to design and test a single electroabsorption modulator. The principle objectives were to achieve a high contrast ratio and low insertion loss for the device. For this purpose a 200 well structure was grown, from which the quality of the growth technique could also be assessed. The electric field and the transmitted light were both perpendicular to the epitaxial layers in this device as shown in Figure 1.8.

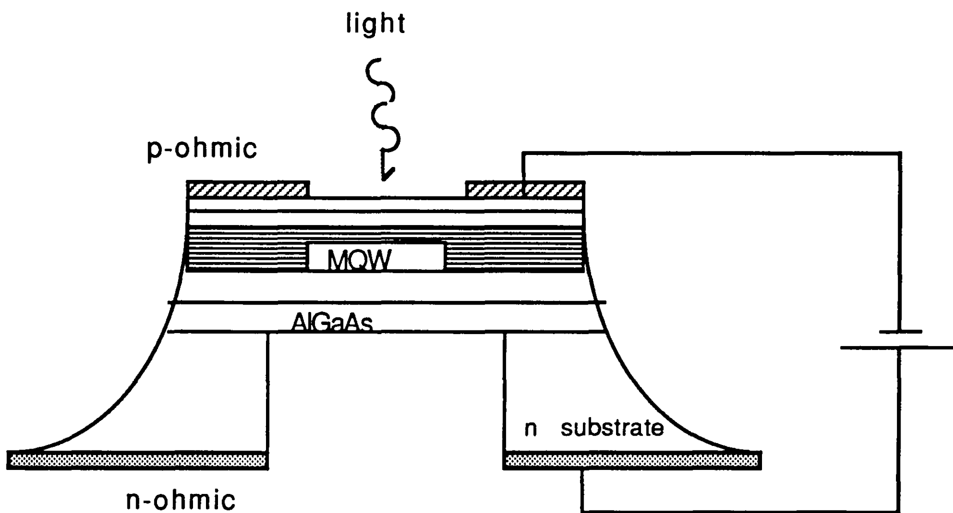

Figure 1.8 Perpendicular electroabsorption modulator

In the course of this work, as a method of assessing the suitability of the device for the routing of optical signals in a communications system, individual modulators were configured into a 4 x 4 array, to form a two dimensional spatial light modulator.[Feiteslon 1989] One of the key requirements of such a device is to eliminate the need for many electrical connections which hinders the operation of

large arrays and this problem and the complex fabrication is addressed in Chapter 4.

A problem associated with existing perpendicular modulators, operated in transmission mode, is the achievement of a high contrast ratio, without sacrifices in the overall insertion loss. As a means of improving the characteristics of planar MQW modulators, coupled well structures were studied. Two devices were designed and fabricated and the initial results for these are presented in Chapter 5.

The thesis is concluded in Chapter 6 with a discussion of the results. The three layer designs used for the single modulators are assessed. Future work in relation to this thesis, both in the layer designs and SLM area, is proposed.

Chapter One : References

J.M. BAGSHAW and T.F. WILLATS
'Some aspects of the performance of anisotropic Bragg cells'
IEE Colloquium on Microwave Acoustics and Acousto-optics
May 1985

D. BOTTELDOOREN, B. DECRAENE, R. BAETS and P. LAGASSE
'Theoretical optimisation of InGaAs multiple quantum well waveguide modulator for the 1.55μm wavelength region'
European Conference on Optical Communications IV MoA3-5
Page 42- 45
Gothenberg September 1989

N. BOTTKA and L.D. HUTCHESON
'Analytical aspects of electroabsorption modulators'
Journal of Applied Physics Volume 46 Number 6
Page 2645- 2650 6 June 1975

G.D. BOYD, D.A.B. MILLER ,D.S. CHEMLA, S.L. McCALL, A.C. GOSSARD and J.H. ENGLISH
'Multiple Quantum Well reflection modulator'
Applied Physics Letters Volume 50 Number 17
Page 1119-1121 27 April 1987

G.D. BOYD, J.E. BOWERS, C.E. SOCCOLICH, D.A.B. MILLER ,D.S. CHEMLA, L.M.F. CHIROVSKY, A.C. GOSSARD and J.H. ENGLISH
'5.5 GHz multiple quantum well reflection modulator'
Electronic Letters Volume 25 Number 9
Page 558- 559 27 April 1989

M.B.J. DIEMEER, F.M.M. SUYTEN, E.S. TROMMEL et al
'Polymeric channel waveguide modulators'
European Conference on Optical Communications IV ThB22-3
Page 425- 428 Gothenberg September 1989

C. DUCHET, P. FABRE, S. SAMSO, M. DI MAGGIO
'Electro-optic modulator with very low drive voltage and high thermal stability'
European Conference on Optical Communications IV ThB22-2
Page 421- 423 Gothenberg September 1989

J.C. DYMENT and F.P. KAPRON
'Extinction ratio limitations in AlGaAs electroabsorption light modulators'
Journal of Applied Physics Volume 47 Number 4
Page 1523- 1528 4 April 1976

W. FRANZ
Z. Naturforsch Number 13a Page 484
1958

R.M. GAGLIARDI (Ed)
Optical Communications
New York London 1976

D.R.P. GUY, D.D. BESGROVE, L.L. TAYLOR, N. APSLEY and S.J. BASS
'Experimental study of InGaAs-InP multiple quantum well electroabsorption modulators'
IEE Proceedings Volume 136 Part J Number 1
Page 46- 51 February 1989

D.R.P. GUY, D.D. BESGROVE, L.L. TAYLOR, N. APSLEY and S.J. BASS
'High contrast ratio electroabsorption GasInAs/InP quantum well modulator'
Electronic Letters Volume 24 Number 19
Page 1253- 1255 15 September 1988

D.R.P. GUY, N. APSLEY, L.L. TAYLOR and S.J. BASS
'Theory of an electro-optic modulator based on quantum wells in a semiconductor etalon'
Proceedings of SPIE- The International Society for Optical Engineering
Quantum Well and Superlattice Physics Volume 792
Page 189- 196 22-27 March 1987

D.R.P. GUY and N. APSLEY
'Optical devices using III-V Quantum Wells and multilayers'
Proceedings of SPIE- The International Society for Optical Engineering
Quantum Well and Superlattice Physics Volume 861
16-20 November 1987

D.R.P. GUY, D.D. BESGROVE, L.L. TAYLOR, N. APSLEY and S.J. BASS
'InGaAs-InP multiple quantum well electroabsorption modulators'
IEE ' Heterojunction and Quantum well devices' Colloquium
27 October 1988

L.V. KELDYSH
'Behaviour of non-metallic crystals in strong electric fields'
Soviet Physics Jetp Volume 6 Number 33
Page 763- 770
April 1958

W.KOWALSKY, U. PRANK, T. HACKBARTH and K.J. EBELING
'Combined planar AlGaAs schottky modulator and detector'
European Conference on Optical Communication ThB22-4
Page 429- 432 Gothenberg September 1989

P. LI KAM WA, J.H. MARSH, P.N. ROBSON, J.S. ROBERTS and N.J. MASON
'Non linear propagation in GaAs-AlGaAs multiple quantum well waveguides'
Proceedings of SPIE-International Society for Optical Engineering
Volume 578 1985

D.A.B. MILLER, D.S. CHEMLA, T.C. DAMEN, A.C. GOSSARD, W. WIEGMANN, T.H. WOOD and

C.A. BURRUS
'Novel hybrid optically bistable switch: The quantum well self- electro-optic effect device'
Applied Physics Letters Volume 45 Number 1
Page 13- 15 1 July 1984
J.A. NEFF
'Major initiatives for optical computing'
Optical Engineering Volume 26
Page 2-9
1989

J.S. ROBERTS, M.A. PATE, P. MISTRY, J.P.R. DAVID and R.B. FRANKS
'MOVPE grown multiple quantum well pin diodes for electro-optic modulators and photodiodes with enhanced electron ionisation coefficient'
Journal of Crystal Growth Volume 93
Page 877-884 1988

R.J. SIMES, R. H. YAN, D.G. LISHAN and L.A. COLDREN
'High-contrast low-voltage Fabry-Perot reflection modulator'
European Conference on Optical Communication ThB22-6
Page 437- 440 Gothenberg September 1989

G.E. STILLMAN, C.M. WOLFE, C.O. BOZLER and J.A. ROSSI
'Electroabsorption in GaAs and its application to waveguide detectors and modulators'
Applied Physics Letters Volume 28 Number 9
Page 544-546 1 May 1976

S.M. SZE
'Semiconductor Devices : Physics and technology'
Chapter 3
John Wiley and Sons 1985

T. TAMIR (Ed)
Integrated Optics
Springer Verlag 1975

A.P. THORN, P.C. KLIPSTEIN and R.W.GLEW
'Electro-optical modulation properties of GaAs doping superlattices'
IEE Proceedings Volume 136 Part J Number 1
Page 38- 45 February 1989

J.S. WEINER
'Physics and applications of quantum wells in waveguides'
Proceedings of SPIE-International Society for Optical Engineering
Volume 578 1985

J.S. WEINER, D.A.B. MILLER, D.S. CHEMLA, T.C. DAMEN, C.A. BURRUS, T.H. WOOD, A.C. GOSSARD and W. WIEGMANN
'Strong polarisation-sensitive electroabsorption in GaAs/AlGaAs quantum well waveguides'

Applied Physics Letters Volume 47 Number 11
Page 1148- 1150 1 December 1985

P. WHEATLEY, P.J. BRADLEY, M. WHITEHEAD, G. PARRY, J.E. MIDWINTER, P. MISTRY, M.A. PATE and J.S. ROBERTS
'Novel nonresonant optoelectronic logic device '
Electronic Letters Volume 23 Number 2
Page 92-93 16 January 1987
M. WHITEHEAD, G.PARRY and P. WHEATLEY
'An investigation of etalon effects in GaAs-AlGaAs multiple quantum well modulators'
IEE PROCEEDINGS Volume 136 Part J Number 1
Page 52- 58 February 1989

D.R. WIGHT, P.C. ALLEN, J.W.A. TRUSSLER, D.P. COOPER, D.J. ESDALE and P.E. OLIVER
'Ultra high speed micro-optical modulators in GaAs: The TEAM and the LEAM'
Institute of Physics Conference Ser. No. 79 Chapter 12
Page 667-672 1985

D.R. WIGHT, A.M. KEIR, G.J. PRYCE, J.C.H. BIRBECK, J.M. HEATON, R.J. NORCROSS and P.J. WRIGHT
'Limits of electroabsorption in high purity GaAs and the optimisation of waveguide devices'
IEE Proceedings Volume 135 Part J Number 1
Page 39- 44 February 1988

T.H. WOOD
'Direct measurement of the electric field dependent absorption coefficient in GaAs/AlGaAs multiple quantum wells'
Applied Physics Letters Volume 48 Number 21
Page 1413- 1415 26 May 1986

T.H. WOOD, C.A. BURRUS, D.A.B. MILLER, D.S. CHEMLA, T.C. DAMEN, A.C. GOSSARD and W.WIEGMANN
'High-speed optical modulation with GaAs/AlGaAs quantum wells in a p-i-n diode structure'
Applied Physics Letters Volume 44 Number 1
Page 16- 18 1 January 1984

T.H. WOOD, C.A. BURRUS, D.A.B. MILLER, D.S. CHEMLA, T.C. DAMEN, A.C. GOSSARD and W.WIEGMANN
'131ps optical modulation in semiconductor multiple quantum wells'
IEEE journal of Quantum Electronics Volume QE-21 Number 2
Page 117-119 February 1985

T.H. WOOD
'Multiple Quantum Well waveguide modulators'
Journal of Lightwave Technology Volume 6 Number 6
Page 743- 757 June 1988

CHAPTER TWO
THEORY

Introduction

In this chapter the physical properties of semiconductors and in particular those of multiple quantum wells are discussed.

The energy levels of the quantum wells are calculated for both finite and infinite potential wells and these solutions are modified to include the effects of an applied electric field. Using this model the effect of the electric field on the absorption spectrum of MQW structures is determined.

A full discussion of the electroabsorption effect in MQW's is presented here incorporating a review of theoretical models from the literature.

The latter part of this chapter is concerned with the physics associated with the *p-i-n* diode configuration used in the optical transmission modulators.

2.1 Semiconductors

For over a century studies into the properties of semiconductors have progressed, often in adverse conditions due to the poor material quality. Semiconductors were initially distinguished from metals on the basis of their negative temperature coefficient of resistance [Smith, R.A 1978] i.e. the resistance of a semiconductor falls with the increasing temperature while that of a metal rises. Subsequently other properties, which differentiate semiconductors from both insulators and conductors, emerged.

From an electronic viewpoint the difference in conductivities between three types of material is the most important: semiconductors have conductivities between those of conductors and insulators, the conductivities of semiconductors being generally sensitive to temperature, illumination, magnetic field, and minute concentrations of impurity atoms. The conductivity depends on two factors, the number of current carriers per unit volume and their motion under an applied electric field, i.e. the carrier mobility. The number of current carriers in a metal is essentially constant whilst in a pure semiconductor the number rises as the temperature is increased. The Hall effect was the first technique used to demonstrate this essential difference.

As further studies were made, more interesting properties and fundamental differences between individual semiconductor materials also emerged. Among the most popular materials investigated initially were silicon and its neighbouring periodic table member germanium. However recent interest in compound semiconductors, formed from elements from groups III and V (also latterly II and VI) of the periodic table, has led to the discovery of optical properties different to those of silicon. The flexibility of these compounds has provided new opportunities in the field of optoelectronics, their basic properties now being well understood as outlined in the next section. Of particular interest in this thesis is the III-V compound GaAs and the related alloy of (AlGa)As.

2.2 Basic semiconductor theory : Energy bands

The basic characteristics of semiconductors are outlined in many text books. [for example Smith 1978, Sze 1985, Nag 1980, and Seeger 1973] To understand the nature of these unique properties, it is necessary to investigate their

energy band structure.

In an isolated atom the electrons can only have discrete energy levels, described by the Bohr model of the hydrogen atom. When two atoms are brought close together the levels will split into two due to the interaction between the atoms and to the exclusion principle. Similarly if N such atoms are brought close together to form a crystal the level will split into N closely spaced levels, essentially forming a continuum. If the distance between the atoms is further reduced this band splits again into two bands, namely the conduction and valence bands, separated by a 'forbidden region' called the bandgap, as shown in Figure 2.2.1. [Sze 1985]

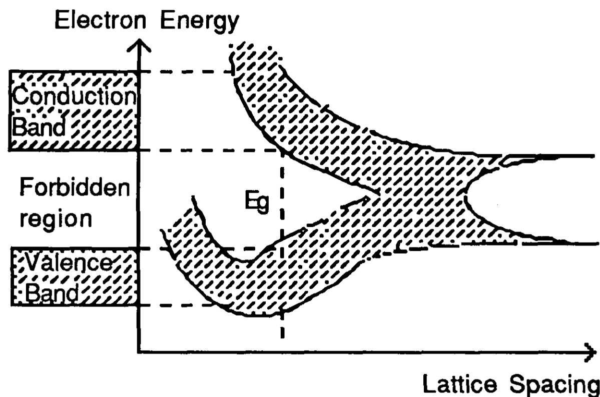

Figure 2.2.1 Formation of the energy bands

2.3 Theoretical calculation of the energy bands

To explain the nature of the energy band several theoretical models have been developed, of particular relevance are the free-electron, tight binding and the Kronig-Penney models.

2.3.1 Free electron approximation

The band structure or E-k relation for electrons in a solid is given by the solution of the time-independent Schrödinger equation :

$$\left(\frac{\hbar^2}{2m_o}\right)\nabla^2\Psi+[E-V(\mathbf{r})]\Psi=0 \qquad 2.1$$

$V(\mathbf{r})$	potential energy of an electron
E	kinetic energy [given by $\frac{\hbar k^2}{2m}$ (for a parabolic band)]
m_o	electron rest mass
Ψ	wavefunction
$\hbar$	Planck's constant divided by 2π

The general solution of this equation is the Bloch function

$$\Psi = u_k(r)\exp(i\mathbf{k}.\,\mathbf{r}) \qquad 2.2$$

$u_k(\mathbf{r}+\mathbf{d})=u_k(\mathbf{r})$ periodic function of $\mathbf{r}$

$\mathbf{d}$	primitive translation vector of the lattice
$\mathbf{k}$	labels state described by the wavefunction $k=\frac{2\pi}{a}$

In this model only states with an energy much larger than V(**r**) are considered. The E-k relation derived from it is shown in Figure 2.3.1.

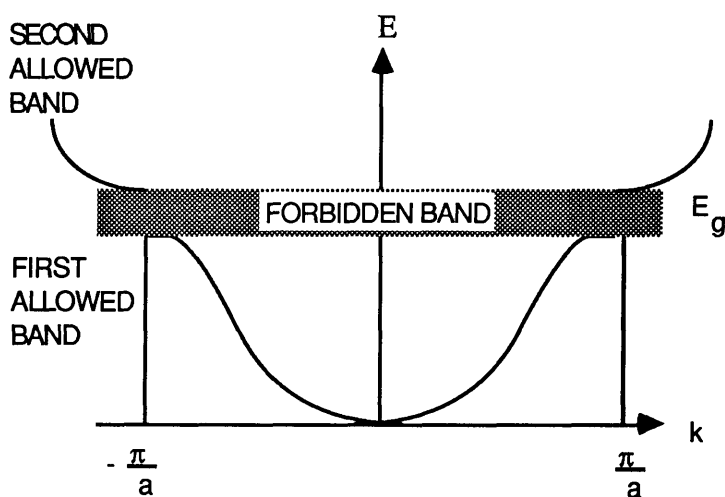

Figure 2.3.1 E-k relation as derived using the free-electron model [Kittel 1976]

The figure illustrates that the continuous energy levels of a free electron are grouped into bands in a solid. When the free electron model is valid, the widths of the forbidden bands are smaller than those of the allowed bands.

Near the band edges, i.e. when

$$\mathbf{k} = \frac{n\mathbf{k}_L}{2} \qquad 2.3$$

where $\mathbf{k}_L = \frac{2\pi}{a}$ and n is an integer

the E-k relation approximates to a parabolic relation. [Nag 1980] A more detailed discussion of this model can be obtained by referring to Kittel 1976, Chapter 7, and Nag 1980, Chapter 4.

2.3.2 Tight binding model

Another approach to study the nature of the energy band structure is to construct the crystal from single atoms which are infinitely far away from each other, and to see how the discrete atomic levels are changed during this process. When the atoms are far from each other the electrons are tightly bound to each atom, hence the name of the model.

The discrete atomic levels transform into bands due to the perturbation in the atomic potentials caused by the neighbouring atoms. If the spacing between the atoms is such that the perturbation in the potential is small, the electron wavefunction in the solid will have the basic character of the atomic wavefunction.

In the tight binding approximation, these conditions are assumed to hold and the electron wavefunction is taken to be

$$\Psi = \sum_n c_n u_o(\mathbf{r} - \mathbf{r}_n) \qquad 2.4$$

$u_o(\mathbf{r} - \mathbf{r}_n)$ represents the atomic wavefunction for an atom at $\mathbf{r}_n$

The results of the tight binding approximation apply only when m^*, the effective mass, is large. In compound semiconductors m^* is often small and the tight binding model is not valid.

2.3.3. Kronig-Penney model

This is perhaps the simplest model of the three models and is the one which will be used to calculate the properties of the energy bands for coupled well structures discussed in Chapter 5.

The periodic potential is approximated by periodic square wells. The Schrödinger equation for this potential distribution can be solved easily, and the results show that the discrete atomic energy levels broaden into bands in solids.

For the square well array in Figure 2.3.2 the wave equation is

$$\frac{\hbar^2}{2m}\frac{d^2\Psi}{dx^2} + U(x)\,\Psi = \varepsilon\Psi \qquad 2.5$$

$U(x)$	potential energy
ε	energy eigenvalue

To obtain a complete solution the wavefunction must be calculated within and outside the well.

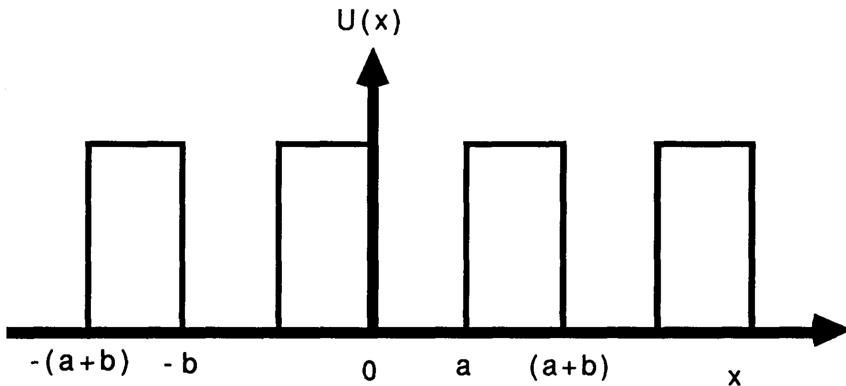

Figure 2.3.2 Periodic potential approximated by periodic square wells for the Kronig-Penney model

In the region $0 < x < a$ where U=0, the eigenvalue is a linear combination of plane waves travelling to the left and the right given by

$$\Psi = Ae^{iKx} + Be^{-iKx} \qquad 2.6$$

with energy

$$\varepsilon = \frac{\hbar^2 K^2}{2m} \qquad 2.7$$

In the region a < x < a+b (the barrier) the solution is of the form

$$\Psi = Ce^{Qx} + De^{-Qx} \qquad 2.8$$

with

$$U_o - \varepsilon = \frac{\hbar^2 Q^2}{2m} \qquad 2.9$$

The constants A,B,C,D are chosen so that Ψ and $\frac{d\Psi}{dx}$ are continuous at x=0. Continuity must also exist at x=a such that

$$Ae^{iKa} + Be^{-iKa} = Ce^{Qa} + De^{-Qa} \qquad 2.10$$

$$iKAe^{iKa} - iKBe^{-iKa} = QCe^{Qa} + QDe^{-Qa} \qquad 2.11$$

A final condition is that the values of Ψ and $\frac{d\Psi}{dx}$ at x=a be equal to those at x=-b, but advanced by the phase factor exp[ik(a+b)]. This is a consequence of the form of Bloch functions and the solution becomes :

$$A\exp\,[iKa - ik(a+b)] + B\exp\,[-iKa - ik(a+b)] \qquad 2.12$$

This can be solved using computational methods which are outlined in Appendix A.

2.4 Wavefunctions in quantum wells

2.4.1 Infinite potential well

By using two similar compound semiconductors in alternate layers, it is possible to engineer potential well systems which have special properties and can confine carriers into two dimensions.

The GaAs/AlGaAs quantum well system can be modelled as a 'square potential'. The potential V(r) in the Schrödinger equation is a function of z only, electrons and holes being free to move in the x and y directions. For this system it is necessary to solve the time-independent Schrödinger equation

$$\hat{H}\Psi(\mathbf{r}) = E\Psi(\mathbf{r}) \qquad 2.13$$

where

$$\hat{H} = -\frac{\hbar^2}{2m}\nabla^2 + V(z) \qquad 2.14$$

∇^2 represents $\left(\frac{\partial^2}{\partial x^2} + \frac{\partial^2}{\partial y^2} + \frac{\partial^2}{\partial z^2}\right)$

Since the electrons are free in the x and y directions, their wavefunctions are plane waves in x and y, therefore

$$\Psi(x, y, z) = e^{ik_x x} e^{ik_y y} u(z) \qquad 2.15$$

By substituting 2.14 and 2.15 into 2.13 then :

$$\left[\frac{\hbar^2}{2m}\left(k_x^2 + k_y^2\right) - \frac{\hbar^2}{2m}\frac{d^2}{dz^2} + V(z)\right]u(z) = E\,u(z) \qquad 2.16$$

is obtained and the plane waves cancel out. By then defining

$$\varepsilon = E - \frac{\hbar^2}{2m}\left(k_x^2 + k_y^2\right) \qquad 2.17$$

the result is the one-dimensional Schrödinger equation.

$$\left[-\frac{\hbar^2}{2m}\frac{d^2}{dz^2} + V(z)\right]u(z) = \varepsilon\,u(z) \qquad 2.18$$

This can be solved to give the eigen energies ε_n (equation 2.38), where n=1,2,3...., with corresponding wavefunctions $u_n(z)$. Then

$$E = \varepsilon_n + \frac{\hbar^2}{2m}\left(k_x^2 + k_y^2\right) \qquad 2.19$$

E depends on the three quantum numbers n, k_x and k_y, i.e. one per dimension.

2.4.2 Finite square well

Since no well is infinitely deep it is necessary to amend the previously derived solution to include the effects of finite well depth. In this case only the first few ε_n's are discrete, corresponding to bound states, and the higher ones form a continuum, corresponding to unbound states.

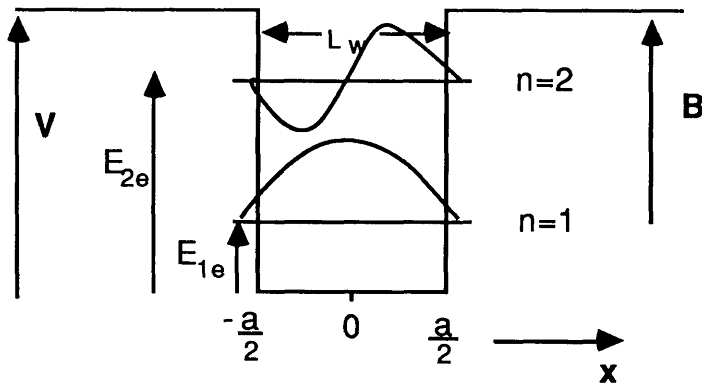

Figure 2.4.1 Finite quantum well

A well of finite depth V and width a is considered as shown in Figure 2.4.1. E is the energy of the state measured from the bottom of the well and B=V-E is called the binding energy and is the energy required to remove the electron from the well.

Inside the well, the solution of the Schrödinger equation gives

$$\Psi(x) = \alpha \begin{smallmatrix}\sin\\ \cos\end{smallmatrix} kx \qquad k = \sqrt{\frac{2mE}{\hbar^2}} \tag{2.20}$$

while outside it is

$$\Psi(x) = \beta e^{-\kappa x} \qquad \kappa = \sqrt{\frac{2m(V-E)}{\hbar^2}} \tag{2.21}$$

It is assumed that $0 < E < V$ and therefore the solution is a bound state.

Ψ and $\frac{d\Psi}{dx}$ need to be matched at $x = \frac{a}{2}$

$$\Psi \rightarrow \alpha \begin{smallmatrix}\sin\\ \cos\end{smallmatrix} k\frac{a}{2} = \beta e^{-\kappa\frac{a}{2}} \tag{2.22}$$

$$\frac{d\Psi}{dx} \rightarrow k\alpha \begin{smallmatrix}\cos\\ -\sin\end{smallmatrix} k\frac{a}{2} = -\kappa\beta e^{-\kappa\frac{a}{2}} \tag{2.23}$$

Dividing these two equations gives

$$k \begin{smallmatrix}\cot\\ \tan\end{smallmatrix}\left(\tfrac{1}{2}ka\right) = -\kappa \tag{2.24}$$

or

$$\begin{smallmatrix}-\cot\\ \tan\end{smallmatrix}\left(\tfrac{1}{2}ka\right) = -\frac{\kappa}{k} = \sqrt{\frac{\frac{2mV}{\hbar^2} - k^2}{k^2}} \tag{2.25}$$

This can only be solved numerically or graphically and is simplified by putting

$$\theta = \tfrac{1}{2}ka \qquad \textbf{2.26}$$

giving

$$\begin{matrix} -\cot \\ \tan \end{matrix}\,\theta = \sqrt{\frac{\dfrac{mVa^2}{2\hbar^2} - k^2}{k^2}} \qquad \textbf{2.27}$$

Both θ and $\frac{\kappa}{k}$ are positive.

The following deductions can be made from this model of the finite well.

1. There is always at least one solution, with $0 < \theta < \frac{\pi}{2}$ thus a one dimensional square well always has at least one bound state.
2. There are N solutions if

$$(N-1)\tfrac{\pi}{2} < \sqrt{\frac{mVa^2}{2\hbar^2}} < N\tfrac{\pi}{2} \qquad \textbf{2.28}$$

3. The energy of a particular level (n) rises as V increases. When V tends to ∞, θ_n tends to $(n+1)\frac{\pi}{2}$ and

$$\varepsilon_n = \frac{\hbar^2 k^2}{2m} = \frac{2\hbar^2}{ma^2}\theta^2 \longrightarrow \frac{\hbar^2\pi^2}{2ma^2}(n)^2 \qquad \textbf{2.29}$$

4. When V is very small, only θ_0 exists and it is small too. Only the $\tan\theta$ solution is relevant which corresponds to the cosine wavefunction. For small angles $\tan\theta \approx \theta$ therefore

$$\theta \approx \sqrt{\frac{mVa^2 - \theta^2}{\theta^2}} \qquad \textbf{2.30}$$

$$\theta^4 + \theta^2 - \frac{mVa^2}{2\hbar^2} = 0 \qquad \textbf{2.31}$$

Dropping θ^4 gives $\theta \approx \left(\frac{mVa^2}{2\hbar^2}\right)$ **2.32**

$$\varepsilon_1 = \frac{2\hbar^2}{ma^2}\cdot\frac{ma^2}{2\hbar^2}V = V \qquad \textbf{2.33}$$

Which implies $B_1 = V - \varepsilon_1$ i.e. no binding, so we need to keep the θ^4 term.

$$\theta^2 = \frac{1}{2}\left[\sqrt{1 + \frac{2mVa^2}{\hbar^2}} - 1\right] \tag{2.34}$$

$$\approx \frac{mV^2a^2}{2\hbar^2} - \left(\frac{mVa^2}{2\hbar^2}\right)^2 \tag{2.35}$$

$$B_1 = V - \varepsilon_1 \approx \frac{mV^2a^2}{2\hbar^2} \tag{2.36}$$

This shows the smallness of the binding energy in shallow potential wells. The wavefunction tunnels a long way into the confining region.

For the calculation of the energy levels of isolated finite wells a computer program was used. The program called XTON was written by Bindi Bhumbra, formerly of this Department, and is described in detail in his thesis [Bhumbra 1990].

2.5 Bandgap in semiconductors

In a semiconductor the bonds between neighbouring atoms are only moderately strong allowing thermal vibrations to break some of them, resulting in a free electron and hole. Due to the nature of the bandgap in a semiconductor it is possible for these free electrons to be excited to the conduction band, leaving a hole in the valence band. The width of this bandgap varies with the temperature and for GaAs can be calculated from the empirical relation [Sze 1985]

$$E_g = 1.52 - \frac{(5.4 \times 10^{-4})T^2}{(T + 204)} \tag{2.37}$$

GaAs is a direct semiconductor, because a transition from the valence band to the conduction band does not require a change in the crystal momentum as Figure 2.5.1 demonstrates. It is this property which for integrated optoelectronics gives GaAs certain advantages over other semiconductor materials such as silicon.

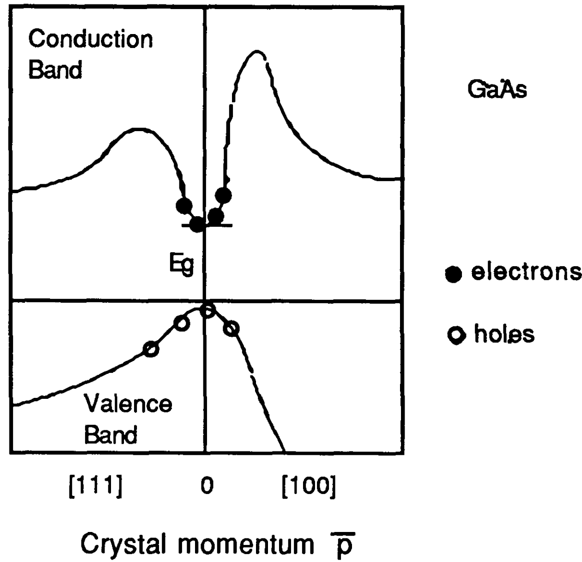

Figure 2.5.1 Energy band structure of GaAs

If an electron falls from the conduction band to the valence band the surplus energy can be emitted in the form of a photon leading to the material becoming a light source. To do this, the electron transition producing the photon must conserve not only energy but also momentum. In practice this means that indirect semiconductors are not expected to be good light emitters. GaAs on the other hand is not only an efficient light emitting diode but has also proved to be an important material for lasers. It also gives rise to a high absorption coefficient just above the bandgap unlike indirect materials such as silicon.

The main discussion of the GaAs/AlGaAs system will not be concerned with the emitting properties of these materials but rather with the absorption properties. To emphasize why alternate layers of these two materials are chosen rather than that of a thick layer of just one of the semiconductors it is necessary to look at the density of states for both 3D and 2D systems.

The density of states for a 2D system is shown in Figure 2.5.2. The density of states function is a series of steps which occur at the energies ε_n due to confinement in the well. This means that if V(z) were an infinitely high square well of width a, then

$$\varepsilon_n = \frac{\hbar^2}{2m}\left[\frac{\pi(n)}{a}\right]^2 \qquad \textbf{2.38}$$

The three dimensional density of states, also shown in Figure 2.5.2, is approached for large well widths. In this approximation the ε_n's are close together and the density of states merges into a parabola corresponding to a 3D system as the steps become close together. On the other hand, if the well width is small the energies ε_n are large.

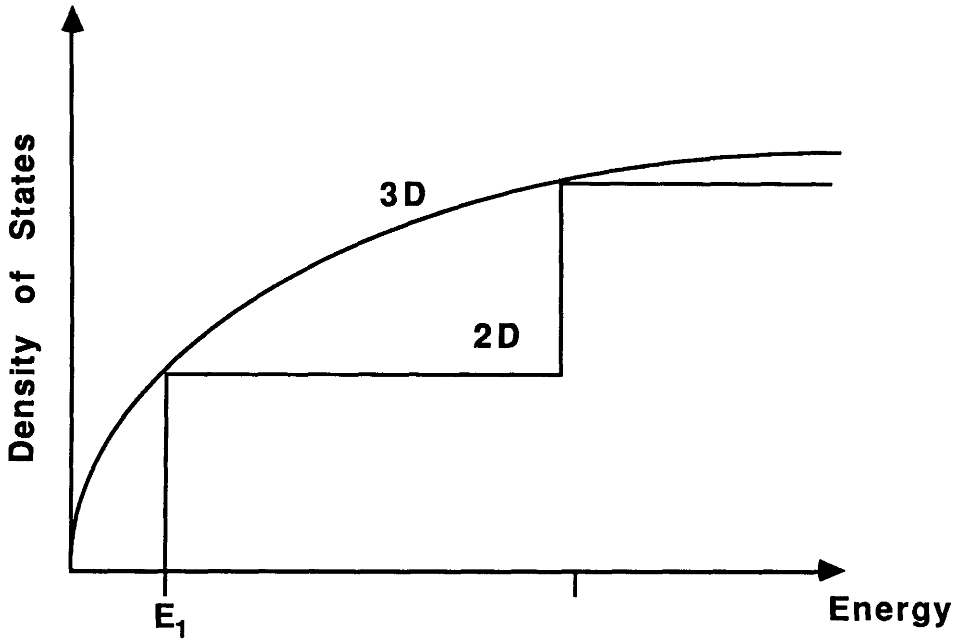

Figure 2.5.2 2D and 3D density of states functions

The above equations have been derived on the assumption that the mass of the electron is the same everywhere, but in reality it is slightly different in GaAs and AlGaAs. In such cases one should match

$$\frac{1}{m}\frac{d\Psi}{dx}$$

rather than the derivative itself, thus ensuring that the current is conserved.

The absorption spectrum follows the form of the density of states, and in quantum well systems the absorption spectrum is therefore a series of steps. This is an important property of the wells which can be utilised effectively in a modulator device. If a device is operated at an energy just below E_1, Figure 2.5.2, and a change the position of the energy levels shifts the absorption edge to this point, then there will be an accompanying large change in absorption. This change is much larger than that of the three dimensional system, and can be used to intensity modulate light incident on the material. It is proposed to move the energy levels by applying an

electric field to it. The effect of doing this is different for bulk and quantum well systems. The former is described by the Franz-Keldysh effect and the latter by the Quantum Confined Stark Effect both of which are outlined below.

Absorption can be dominated by the effects of excitons at room temperature. Excitons are essentially electrons and holes bound together by Coulomb attraction. Such a particle system can move through a crystal behaving as a single particle until acted upon by an external force e.g. an electric field.

2.6 Optical absorption

As light is incident on a semiconductor photons are absorbed leading to the creation of electron hole pairs if the photon energy is equal to or greater than the bandgap. If the photon energy is less than the bandgap energy then absorption can only take place if there are available energy states in the forbidden band gap, either arising from chemical impurities or physical defects. Another method of inducing states in the forbidden gap is to apply an electric field to the semiconductor.

2.6.1 Electroabsorption in bulk semiconductors:The Franz- Keldysh effect

The electroabsorption effect in bulk material is known as the Franz-Keldysh (F-K) effect. This effect is an electric field induced change of the complex dielectric constant of a direct bandgap semiconductor, occurring at optical energies close to the bandgap energy. The F-K effect has two parts- electroabsorption and electrorefraction- which are respectively changes of the absorption coefficient and refractive index due to an applied electric field. [Van Eck 1986]

Broadening of the absorption edge takes place on the application of an electric field perpendicular or parallel to the layers of a bulk semiconductor. This broadening is due to the reduction of the periodic potential symmetry of the lattice and produces an increase in the absorption coefficient at energies just below the bandgap and a reduction at energies just above the bandgap.

Consider, as in Figure 2.6.1, an electron excited into a virtual state by a quantum of insufficient energy, q, to take it into the conduction band. Since it does not have

enough energy to enter the conduction band it returns to the valence band. Under an applied electric field, Figure 2.6.1.b, it reaches the same level as before but it may now pass into the conduction band. This is often described as a tunnelling process but a more accurate description is that the effect of the field is to broaden the bands thus reducing the bandgap, and so less energy is required to excite the electron into the conduction band.

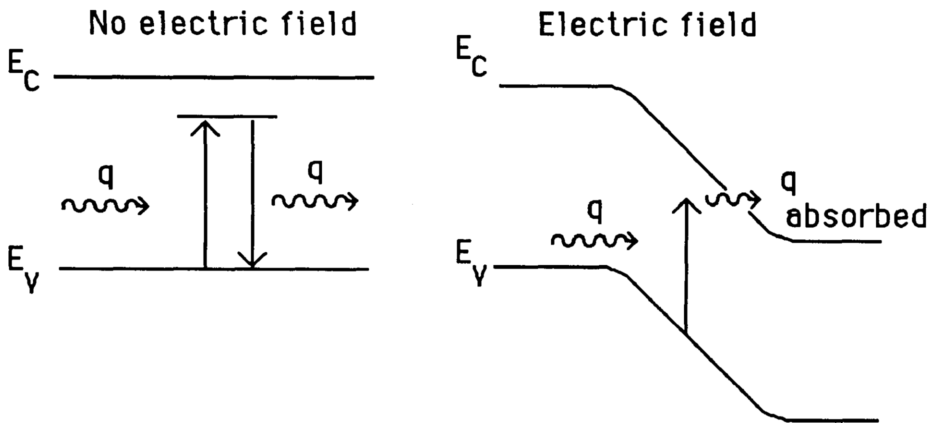

Figure 2.6.1 Effect of an electric field on the band edges of a semiconductor

This leads to an increase in the absorption at lower energies. Associated with this there is also a broadening of the exciton feature, due to field ionisation which results in reduced excitonic absorption.

2.6.2 Quantum Confined Stark Effect (QCSE)

Electroabsorption effects in quantum well systems are substantially different to those observed in bulk materials. Due to the confinement of electrons and holes in potential wells behaviour additional to that of the band edge tilting, is encountered. Thus, not only is there a change in the absorption above and below the bandgap, but also the exciton peaks remain well resolved up to high fields as opposed to the large amount of broadening encountered in the bulk Franz-Keldysh effect. The QCSE is of particular interest from a device point of view because it is possible to obtain a very large change in the absorption coefficient at room temperature.(typically $\sim$ 11000 cm^{-1} whereas in bulk the change is $\sim$ 280 cm^{-1})

The persistence of the exciton peak can be explained by considering that the field ionisation of the exciton is inhibited by the walls of the quantum well. The electrons

and holes are pulled to opposite walls of the quantum well by the field but they do not tunnel rapidly through the walls. The large shift in the peaks occurs because the particle is not destroyed by the field, and hence very large fields can be obtained.

The behaviour of quantum well systems is also different depending on whether the electric field is applied parallel of perpendicular to the layers, the behaviour with the field perpendicular being called the QCSE.[Miller 1984] Under the influence of an electric field applied parallel to the quantum well layers the effect is approximately the same as that of the bulk Franz-Keldysh effect since the electric field and the confinement of the electrons and holes do not occur in the same direction.

It is the behaviour of the quantum well system under the influence of the perpendicular electric field which is of interest to this work. Consider Figure 2.6.2 which shows the behaviour of a quantum well system under the application of an electric field.

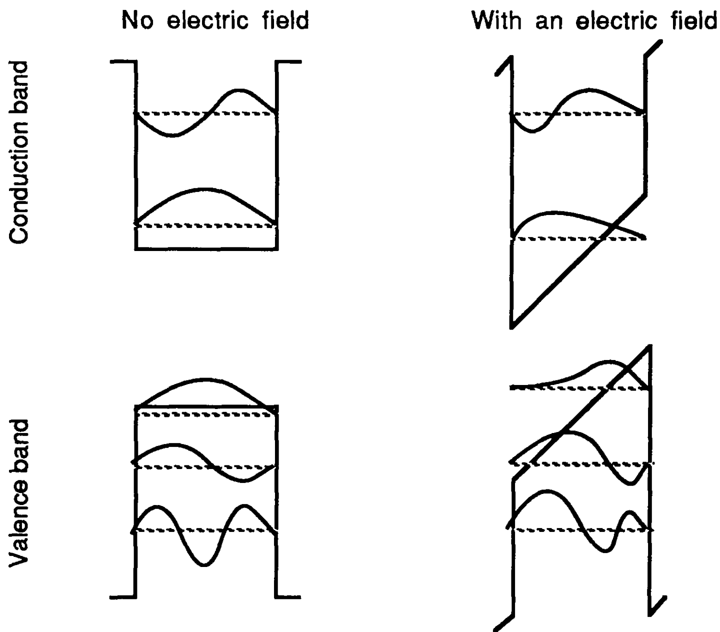

Figure 2.6.2 The effect of an electric field on a quantum well system

The energy of the lowest transition is reduced by the field, and the electron and hole in these states are pulled to opposite sides of the well. The energy shift is approximately quadratic at low fields but at higher fields there is a small deviation

from the quadratic behaviour because the kinetic energies of the electron and hole are increased as they are squeezed towards the walls of the wells.

As the electron and hole are pulled apart, the overlap integral between electron and hole wavefunctions decreases, reducing the step height for this transition. The shift of the heavy hole states is larger than that of the electrons because particles with larger mass are more easily perturbed because of their lower confinements energies [Chemla 1985]. It has been shown analytically [Miller 1984] that in the limit of the well thickness becoming infinite that this model becomes formally identical with the Franz-Keldysh effect, correctly predicting bulk behaviour neglecting exciton effects. For example wells of 300 Å and wider behave essentially as bulk material.

As discussed previously, the excitons in quantum well material behave differently depending on whether the electric field is applied perpendicularly or parallel to the wells. From experimental work [Miller 1986, Whitehead 1988] it is known that the excitons do not broaden strongly with a perpendicular field, and the peaks shift substantially, as opposed to the in-plane behaviour of the quantum well and bulk systems which show much broadening and little shift. The shift in the perpendicular case can be many times the binding energy of the exciton whereas it is almost negligible in the bulk case.

To understand fully the QCSE it is necessary to explain the persistence of the exciton peaks to high electric field. The reason for this is the prevention of field ionisation of the exciton by the walls of the well. As the field is applied the electron and hole are pulled to opposite sides of the well, but restrained from going any further. Thus while the exciton is not separated by the field, it is very strongly polarised with the electron and hole orbits being partly separated, with several complete classical orbits occurring before the exciton is destroyed. It is required that the tunneling time is significantly longer than the lifetime of the exciton from other causes, for quantum wells to exhibit the QCSE. It can also be deduced, therefore, that if the well is made much larger than the bulk exciton diameter then the exciton can be field ionised by pulling the electron and hole to opposite sides of the well, and so it is necessary to use thin wells.

On the application of an electric field the exciton becomes larger: this is because the Coulomb attraction is weaker when the electron and hole are pulled apart by the field. There is a significant decrease in the magnitude of the binding energy as the field is applied, resulting in an opposing shift to that of the single particle states. This absolute magnitude of the energy shift from the binding energy is not very significant compared with the shift of the single-particle states, but the increase in size can result in a significant change in the electron-hole overlap, reducing the absorption strength of the exciton line. [Schmitt-Rink 1989] To completely predict the behaviour of the absorption spectrum under an applied electric field it is necessary to include the shift resulting from the change in binding energies, however the simple model which is presented in the next section neglects this, only describing the dominant shift due to the shift in energy levels. It can therefore be described as the Quantum Confined Franz-Keldysh (QCFK) effect corresponding to the bulk counterpart.

Several theoretical models have been investigated to predict the behaviour of the both bulk and multiple quantum well systems under the application of an electric field. An excellent review of these is given by Schmitt-Rink [1989] where both the QCFK and QCSE are described.

2.6.3. Theoretical modelling of the QCSE

Figure 2.6.2 illustrates the effect of applying a uniform electric field to a quantum well. As shown the wavefunction is distorted with the average position of the electron shifted away from zero, where zero is the centre of the well, and therefore a dipole moment is generated. For a small electric field it is expected that the average displacement and the dipole moment are proportional to the electric field. This problem can be solved exactly in terms of Airy functions, but requires extensive computing. A more general technique is to assume that the potential is small and then use perturbation theory. The method outlined below was derived by Dr John Davies of this Department.

Consider an infinitely deep well of width a, with the origin at the centre of the well. The eigenfunctions and eigenvalues are

$$\varepsilon_n = \frac{\hbar^2 \pi^2}{2ma^2}(n)^2 \text{ where } n = 1, 2 \ldots \qquad 2.39$$

$$u_n = \left(\frac{2}{a}\right)^{\frac{1}{2}} \cos\left((n)\frac{\pi x}{a}\right) n \text{ odd}$$

$$= \left(\frac{2}{a}\right)^{\frac{1}{2}} \sin\left((n)\frac{\pi x}{a}\right) n \text{ even} \qquad 2.40$$

The eigenstates * $u_n(x)$ are even in x for n odd and consequently odd for n even.

By applying an electric field, a perturbation V(x) = eFx occurs, a function which is odd in x. By considering the matrix elements

$$V_{mn} = \int_{-\frac{a}{2}}^{\frac{a}{2}} dx \; u_m^*(x)\,[eFx]\,u_n(x) \qquad 2.41$$

then V_{mn} will vanish unless m is even and n odd, or m odd and n even. In particular $V_{nn}=0$

There are no first order change in the energies. To the second order

$$\Delta E_n = \sum_k \frac{|V_{kn}|^2}{\varepsilon_n - \varepsilon_k} \qquad 2.42$$

Consider the ground state n=1. The sum need only be over even k, therefore let k=2k hence

$$\Delta E_1 = -\sum_{k=1}^{\infty} \frac{|V_{2k,1}|^2}{\varepsilon_{2k} - \varepsilon_1} \qquad 2.43$$

A lower bound on the shift of the energy can be calculated by taking k=1 then

$$(-\Delta E_1) > \frac{|V_{21}|^2}{\varepsilon_2 - \varepsilon_1} \qquad 2.44$$

$$V_{21} = \frac{2}{a} \int_{-\frac{a}{2}}^{\frac{a}{2}} dx \; \sin\left(\frac{2\pi x}{a}\right) eFx \cos\left(\frac{\pi x}{a}\right) \qquad 2.45$$

$$= 2 . \frac{2}{a} . \frac{a}{\pi} . eF . \frac{a}{\pi} . \int_0^{\frac{\pi}{2}} dy \sin(2y) \cos(y) y \qquad 2.46$$

$$= \frac{16}{9\pi^2} eFa \qquad 2.47$$

$$\varepsilon_2 - \varepsilon_1 = \frac{3\hbar^2 \pi^2}{2ma^2}$$

$$\text{so} \; (-\Delta E1) > \frac{512}{243\pi^6} \frac{m(eF)^2 a^4}{\hbar^2} \qquad 2.48$$

which can be rewritten as

$$\left(-\Delta E_1\right) > \frac{256}{243\pi^4} \frac{(eFa)^2}{\frac{\hbar^2}{2m} \frac{\pi^2}{a^2}} \qquad 2.49$$

Thus a 'rule of thumb' to estimate the effect is

$$\left(-\Delta E_1\right) \approx \frac{1}{100} \frac{(\text{energy drop across well})^2}{(\text{energy of ground state})} \qquad 2.50$$

A minimum shift can now be calculated for different magnitudes of electric field and well widths as shown on Table 2.6.1. An upper bound can also be calculated, but this is unnecessary as the two boundaries are very close together. It is clear from the calculated results, Table 2.6.1, that wider wells provide much larger shifts of the energy levels for equivalent electric fields. The important aspect of the electroabsorption effect, from the point of view of this work however is the persistence of the exciton feature rather than the magnitude of the shift. It is this persistence that provides the maximum change in the absorption coefficient, therefore relatively narrow wells were used (50 Å).

Well width (Å) → Electric field (V/cm) ↓	50	62	80	100	150
2.5×10^4	0.224	0.53	1.47	3.59	18.25
5.0×10^4	0.897	2.12	5.88	14.3	72.7
7.5×10^4	2.1	4.77	13.2	32.3	164
1.0×10^5	3.59	8.5	23.5	57.4	290
1.25×10^5	5.61	13.2	36.7	89.7	454
1.5×10^5	8.08	19.1	52.9	129	654

Table 2.6.1 Calculated values of energy level shift (meV)(after Davies)

2.7 *p-n* junction

As will be outlined in Chapter 3 the application of the electric field to the modulator is performed by forming the layers into a *p-i-n* diode. The operation of this diode can be understood by considering the physics of a *p-n* junction.

A *p-n* junction consists of an abrupt transition from a donor-doped n-type region of a semiconductor, where the carriers are predominately electrons, to an acceptor-doped *p*-type region, where the carriers are holes. Such junctions rectify, that is they allow current to flow easily in one direction only.

There exists on either side of this junction a depletion region which is devoid of mobile carriers, but contains fixed dopant ions. On the *p*-side these ions are negatively charged acceptors and on the n-side they are positively charged donors. Under thermal equilibrium, with no external applied bias, these fixed charges generate a potential barrier which exactly opposes the diffusion current under the concentration gradient across the depletion region, so giving rise to a built-in potential.

2.7.1 *p-i-n* diode

p-i-n are often used in applications where a constant electric field is required. These diodes consist of an intrinsic high resistivity layer sandwiched between the *p* and *n* regions. The potential drop occurs mostly across this *i* region which can be tailored to ensure that most of the incident photons are absorbed within it. This configuration has the effect of increasing the junction width and hence decreasing the junction capacitance. The lower the capacitance of the junction then the greater the speed of operation of the device, as this is dependent on the RC time constant. The wider the depletion region the less chance of Zener breakdown of the diode. The Zener effect occurs due to quantum mechanical tunneling between the valence band and unoccupied conduction band states through an extremely thin depletion region.

2.7.2 I-V Characteristics

To assess the I-V characteristics of a *p-i-n* diode an external bias is applied to the diode. The undepleted semiconductor is of very low resistance in comparison to the depletion region and therefore nearly all the applied voltage appears across this depletion region.

Under forward bias the potential barrier is lowered thus increasing the number of majority carriers which can flood across the depletion region, hence large currents can flow. The magnitude of the current flow depends on the number of carriers having sufficient energy to surmount the barrier height. Since the carrier energy is distributed approximately according to Boltzmann statistics, the current should increase exponentially with increasing forward bias.

For the case of reverse applied voltage the potential barrier height is increased thus suppressing even further the diffusion of high energy majority carriers. The residual current in this instance consists of minority carriers drifting across the depletion region.

To determine the reverse breakdown voltage of the diodes, it was necessary to contact the material via metal contacts. The device was then analysed using a Hewlett-Packard spectrum semiconductor probe station. This process is outlined in Chapter 3.

Based on the theory presented here, a single electroabsorption modulator working on the principle of the QCSE was fabricated from a multiple quantum well GaAs/AlGaAs material system. Chapter 3 outlines this fabrication process and discusses the results obtained from the modulator.

Chapter Two : References

K. BAJEMA, R.MERLIN, F.Y. JUANG, S.C. HONG, J. SINGH, and P.K. BHATTACHARYA
'Electric field effects on interband transitions in quantum well structures'
Superlattices and Microstructures Volume 3 Number 6
Page 685- 687
1987

B. BHUMBRA Thesis 1990

A.M. BONCH-BRUEVICH and V.A. KHODOVOI
'Current methods for the study of the Stark /effect in atoms'
Usp. Fiz. Nauk 93 Page 71-110
September 1967

D.S. CHEMLA and D.A.B. MILLER
'Physics and applications of excitons confined in semiconductor quantum wells'
Heterojunctions
Editors G. Margaritondo and F.Capasso

D.S. CHEMLA, S.SCHMITT-RINK and D.A.B. MILLER
'Nonlinear optical properties of semiconductor quantum wells'
Internal report AT&T Bell Laboratories

Y. CHIBA and S. OHNISHI
'Quantum confined Stark effect on an exciton in a spherical quantum well of GaAs cluster embedded in AlGaAs '
Superlattices and Microstructures Volume 6 Number 1
Page 23- 26
1989

L.A. CURY and N. STUDART
'Stark states in semiconductor quantum wells and superlattices'
Superlattices and Microstructures Volume 3 Number 2
Page 175- 179
1987

J.D. DOW and D. REDFIELD
'Electroabsorption in semiconductors : The excitonic absorption edge'
Physical Review B Volume 1 Number 8
Page 3358- 3371
15 April 1970

N. K. DUTTA and N.A. OLSSON
'Electroabsorption in GaAs quantum well waveguides '
Electronic Letters Volume 23 Number 16
Page 853- 854
30 July 1987

S. HONG and J. SINGH
'Effect of the lifting of Kramer's degeneracy on excitonic linewidths in quantum well optical modulators'
Applied Physics Letters Volume 53 Number 9
Page 731- 733 29 August 1988

L.V. KELDYSH
'The effect of a strong electric field on the optical properties of insulating crystals'
Soviet Physics Jetp Volume 34 Number 7
Page 788 -790
November 1958

J. KHURGIN
'Novel configuration of self electro-optic effect device based on asymmetric quantum wells'
Applied Physics Letters Volume 53 Number 9
Page 779- 781
29 August 1988

A.KOST, E. GARMIRE, A. DANNER, and D. DAPKUS
'Large optical nonlinearities in GaAs-AlGaAs hetero n-i-p-i structure'
Applied Physics Letters Volume 52 Number 8
Page 637- 639

P. LI KAM WA, J.H. MARSH, P.N. ROBSON, J.S. ROBERTS and N.J. MASON
'Non linear propagation in GaAs-AlGaAs multiple quantum well waveguides'
Proceedings of SPIE-International Society for Optical Engineering
Volume 578
1985

J.H. MARSH
'Planar integration of linear and nonlinear III-V multiple quantum well optical components'
Cannes 1987

D.A.B MILLER, D.S. CHEMLA, T.C. DAMEN, A.C. GOSSARD, W. WIEGMANN, T.H. WOOD, and C.A.BURRUS
'Band -edge electroabsorption in quantum well structures: The Quantum confined Stark effect'
Physics Review Letters Volume 53 Number 22
Page 2173- 2176
26 November 1984

D.A.B. MILLER, D.S. CHEMLA,and S. SCHMITT-RINK
'Relation between electroabsorption in bulk semiconductors and in quantum wells: The quantum confined Franz Keldysh effect'
Physical Review A Volume 33 Number 10
Page 6976- 6982
15 May 1986

Kittel, C
Introduction to solid state physics
Wiley New York 1976

R.C. MILLER and D.A. KLEINMAN
'Excitons in GaAs quantum wells'
Journal of Luminescence Volume 30
Page 520- 540
1985

D.A.B MILLER, D.S. CHEMLA, T.C. DAMEN, A.C. GOSSARD, W. WIEGMANN, T.H. WOOD and C.A.BURRUS
'Electric field dependence of optical absorption near the band gap of quantum well structures'
Physical Review B Volume 32 Number 2
Page 1043- 1060
15 July 1985

I.A. MERKULOV and V.I. PEREL
'Effects of electron-hole interaction on electroabsorption in semiconductors'
Physics Letters Volume 45A Number 2
Page 83- 84
10 September 1973

D.A.B. MILLER, D.S CHEMLA, and S. SCHMITT-RINK
'Electric field dependence of optical properties of semiconductor quantum wells : Physics and Applications'
AT&T Bell Laboratories Internal Report

S. MONAGHAN, and S. BRAND
'Complex band structure calculations of the electric field dependence of the transmission of holes through a (100) GaAs-AlGaAs-GaAs barrier structure'
Superlattices and Microstructures Volume 3 Number 6
Page 697- 700
1987

D.J. NEWSON and A. KUROBE
'Effect of residual doping on optimum structure of multiple quantum well optical modulators'
Electronic Letters Volume 23 Number 9
Page 439- 440
23 April 1987

D.A. ROBERTS, J.P.R. DAVID, G. HILL, P.A. HOUSTON, M.A. PATE, J.S. ROBERTS, and P.N. ROBSON
'GaAs/AlGaAs multiple quantum well pin diodes grown by selective area epitaxy'
Electronic Letters Volume 24 Number 14
Page 896- 899
7 July 1988

M.E. PISTOL, S. NILSSON, P. SILVERBERG, L. SAMUELSON, M. RASK, and G. LANDGREN
'Optical properties of narrow high quality GaAs/AlGaAs quantum wells grown by MOVPE'
Superlattices and Microstructures Volume 2 Number 6
Page 501- 505

Smith, R.A
Semiconductors 2nd edit.
Cambridge Universal Press I979

Sze, S.M
Semiconductor Devices
Physics and devices technology
Wiley New York I985

1986

P.J STEVENS, M.WHITEHEAD, G. PARRY and K. WOODBRIDGE
'Computer modeling of the electric field dependent absorption spectrum of multiple quantum well material'
IEEE Journal of Quantum Electronics Volume QE-24 Number 10
Page 2807-2016
October 1988

G.E. STILLMAN, C.M. WOLFE, C.O. BOZLER, and J.A. ROSSI
'Electroabsorption in GaAs and its application to waveguide and modulators'
Applied Physics Letters Volume 28 Number 9
Page 544- 546
1 May 1976

K. TAI, J. HEGARTY, and W.T. TSANG
'Observation of optical Stark effect in InGaAs/InP multiple quantum well'
Applied Physics Letters Volume 51 Number 3
Page 152- 154
20 July 1987

K. THARMALINGHAM
'Optical absorption in the presence of a uniform field'
Physical Review Volume 130 Number 6 Page 2204- 2206
15 June 1963

T.E. VAN ECK, L.M. WALPITA, S.C. CAHNG, and H.H. WIEDER
'Franz-Keldysh electrorefraction and electroabsorption in bulk InP and GaAs'
Applied Physics Letters Volume 48 Number 7
Page 451- 453
17 February 1986

C. VAN HOOF, K. DENEFFE, J. DE BOECK, D.J. ARENT, and G. BORGHS
'Franz-Keldysh oscillations originating from a well-controlled electric field in the GaAs depletion region'
Applied Physics Letters Volume 54 Number 7
Page 608- 610
13 February 1989

L. VINA, M. POTEMSKI, J.C. MAAN, G.E.W. BAUER, E.E. MENDEZ, and W.I. WANG
'Stark and Zeeman effects in excitons in GaAs/AlGaAs quantum wells'
Superlattices and Microstructures Volume 5 Number 3
Page 371- 374
1989

K. WAKITA, Y. KAWAMURA, Y. YOSHIKUNI, and H. ASAHI
'Electroabsorption on room-temperature excitons in InGaAs/InAlGaAs multiple quantum well structures'

Electronic Letters Volume 21 Number 8
Page 338- 340
11 April 1985

J.S. WEINER
'Physics and applications of quantum wells in waveguides'
Proceedings of SPIE-International Society for Optical Engineering
Volume 578
1985

M. WHITEHEAD, G.PARRY, K. WOODBRIDGE, P.J. DOBSON and G. DUGGAN
'Experimental confirmation of a sum rule for room-temperature electroabsorption in GaAs/AlGaAs multiple quantum well structures'
Applied Physics Letters Volume 52 Number 5
Page 345- 347 1 February 1988

D.R. WIGHT, P.C. ALLEN, J.W.A. TRUSSLER, D.P. COOPER, D.J. ESDALE and P.E. OLIVER
'Ultra high speed micro-optical modulators in GaAs: The TEAM and the LEAM'
Institute of Physics Conference Ser. No. 79 Chapter 12
Page 667-672
1985

D.R. WIGHT, A.M. KEIR, G.J. PRYCE, J.C.H. BIRBECK, J.M. HEATON, R.J. NORCROSS, and P.J.WRIGHT
'Limits of electroabsorption in high purity GaAs and the optimisation of waveguide devices'
IEE Proceedings Volume 135 Part J Number 1
Page 39- 44
February 1988

M. WHITEHEAD, G.PARRY, J.S. ROBERTS, P. MISTRY, P. LI KAM WA, and J.P.R. DAVID
'Quantum confined Stark shifts in MOVPE grown GaAs-AlGaAs multiple quantum wells'
Electronic Letters Volume 23 Number 20
Page 1048- 1050
24 September 1987

T.H. WOOD, C.A. BURRUS, D.A.B. MILLER, D.S. CHEMLA, T.C. DAMEN, A.C. GOSSARD,and W. WIEGMANN
'131 ps optical modulation in semiconductor multiple quantum wells'
IEEE Journal of Quantum Electronics Volume QE-21 Number 2
Page 117- 119
February 1985

M. YAMANISHI and M. KUROSAKI
'Ultrafast optical nonlinearity by virtual charge polarisation in DC-biased quantum well structures'
IEEE Journal of Quantum Electronics Volume QE-24 Number 2
Page 325- 331

CHAPTER THREE
SINGLE ELECTROABSORPTION MODULATOR

Introduction

It was shown in Chapter 1 that electroabsorption modulators can be fabricated from different material systems and employ various modes of operation. The specific material system, GaAs/AlGaAs, and chosen mode of operation with the direction of propagation of light and electric field perpendicular to the growth direction, were discussed in Chapter 2. In this chapter the design, fabrication and performance of the modulator are presented. From the design of the epitaxial layers, the discussion moves on to the characterisation of the MOVPE grown crystal structure. This precedes an outline of the fabrication steps and the experimental set-up necessary to characterise the device. The latter sections of the chapter discuss the results and assess the merits of the modulator.

3.1 Design of modulator

The epitaxial layers of the modulator were designed to meet the objectives of a high contrast ratio and low insertion losses. The device was operated with the light propagation and applied electric field perpendicular to these layers. In order to achieve a high contrast ratio, it was essential to incorporate a large total thickness of GaAs in the intrinsic layer where the light was modulated. This allows a long interaction length between the light and the GaAs wells.

The first of the structures investigated contained isolated quantum wells as shown in Figure 3.1.1. This *p-i-n* structure was grown by metal-organic vapour-phase epitaxy at SERC Facility for III-V Semiconductors at the University of Sheffield, on a GaAs substrate.[J.S. Roberts 1988] The structure allowed the application of moderately high electric fields (1.3×10^5 V/cm) without the need for high current or voltage drives (<30 V). Under reverse bias conditions only a small leakage current flowed of the order of nanoamps.[Sze 1985] In this mode of operation the resistance (> 100 MΩ) was high and the capacitance low (<1 pF)which is essential for high speed operation. The speed of the device is dominated by the RC time constant as discussed in section 3.10. To ensure that the capacitance was low it was an advantage to have a wide intrinsic region, here the intrinsic region is 2.24 μm wide. One of the limitations on the width of the intrinsic region is that of the physical growth. It is easier to grow a good structure when fewer wells are required than to maintain the uniformity over a large number of wells. Therefore, the layer design in itself was of interest, from the viewpoint of studying the uniformity of a large number of wells grown by MOVPE. It was thought than any benefit gained from a thicker intrinsic region could be overshadowed by the effect of inhomogeneuos broadening due to the imperfect quality of the well interfaces and the well to well size fluctuations, inevitable over such a large number of wells. Additional problems arise due to the doping in the intrinsic region giving rise to a non-constant electric field.

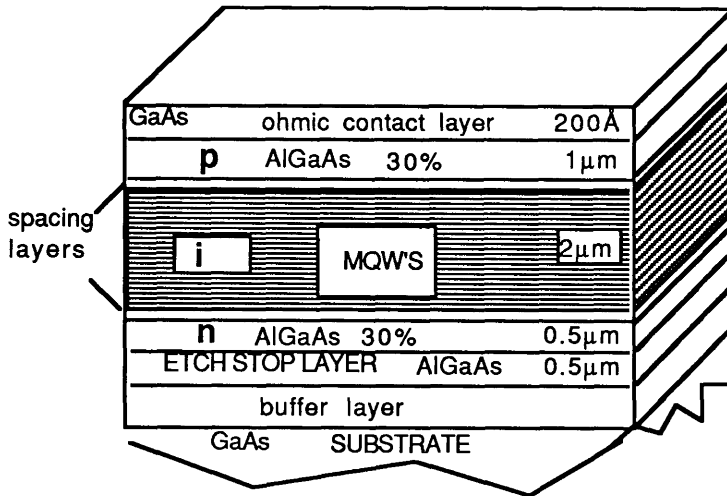

Figure 3.1.1 Optical modulator structure layer CB 2

On top of the device was a 200 Å thick GaAs capping layer. This was grown not only to protect the whole device but also to facilitate the formation of ohmic contacts to the AlGaAs. In its absence there would be a need to employ very high temperature alloying to form a low resistance contact with the AlGaAs layer. It was also advantageous to have this layer since GaAs oxidizes less quickly than AlGaAs.

The intrinsic region was clad by two contacting layers of *p*-type and *n*-type $Al_{0.3}Ga_{0.7}As$ to allow a voltage to be applied across the intrinsic region. These AlGaAs regions had a large enough bandgap to allow them to be optically transparent at the wavelengths at which light is strongly modulated. To isolate the intrinsic region from any dopant diffusion, two undoped buffer layers were inserted, each of which were 350 Å thick.

The multiple quantum well region (Figure 3.1.2) consisted of 200 alternate layers of 50 Å of $Al_{0.3}Ga_{0.7}As$, to form the barriers, and 50 Å of GaAs, to form the wells. The narrow well width allowed the excitonic features of the absorption spectra to be exploited. As explained in Chapter 2, on the application of an electric field to the quantum well structure the energy levels are changed, resulting in absorption at photon energies below the zero field bandgap. This is accompanied by the spatial separation of the electron and hole, changing the binding energy of the exciton and

reducing the oscillator strength. The former of these two effects is dominant in respect of the energy shift of the exciton peaks, but the latter has a dramatic effect on the change in absorption of the exciton peaks. For narrow wells the QCSE occurs less rapidly, requiring a high drive voltage for a useful shift, but the overlap of the exciton electronic wavefunctions is more easily maintained resulting in a higher absorption for the same shift as wider wells. If the well is too narrow however the electron and hole can spread into the barriers. The well width of 50 Å was optimised to provide a useful shift and also a high change in absorption between the on and off state of the device.

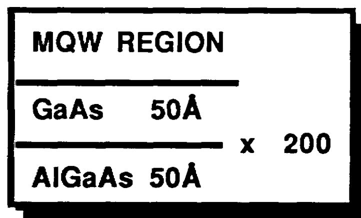

Figure 3.1.2 Multiple quantum well layers

Since the GaAs substrate upon which the structure was grown was highly absorbing and 400-500 μm thick, it was necessary to remove it to perform transmission measurements. This can be carried out by a number of methods, including mechanical polishing, dry-etching and chemical wet-etching.

Mechanical polishing was unsuitable for this purpose, due to the nonuniformity of the polished surface. The major drawback of this method was the inability to control the thickness of the remaining material and so stop the etching process before the MOVPE layers were damaged. It is often, however, used in conjunction with wet-etching as it is faster than the wet-etching process. The use of dry-etching techniques was also impractical for this purpose. Although dry-etching can be controlled to very accurate depths, the rate of etching is very slow, 0.1 μm-1 μm/minute, and so to etch a structure 400μm-500μm thick would take many hours.

The best solution to this problem, and the technique used here, is chemical wet-etching. It was necessary to use a selective etch which would etch the GaAs substrate

but not the epitaxial layers. Thus an etch stop layer was included to protect the epitaxial layers. As both the wells and the substrate are made of GaAs, it was necessary to find an etch which is sensitive to the aluminium content in the structure. Two types of etchants were used, one which would etch the GaAs quickly and another slower, more selective etch. As an insurance against removing the epitaxial layers, the etch stop layer was graded from 50% to 30% AlGaAs. The second of the chemical etches would only attack the etch stop layer very slowly, while more quickly removing the remaining GaAs.

3.2 Characterisation of material

3.2.1 Photoluminescence

The first method of optically characterising the device material was to measure the wavelength and intensity of radiation produced when excited by photons of an energy greater than the bandgap, i.e. photoluminescence. The emitted radiation from the crystal was at a lower photon energy than the excitation energy, i.e. the emitted radiation has a longer wavelength than the excitation radiation. From the resulting photoluminescence spectrum, the width of the exciton peak, the position of the heavy hole and light hole exciton and the percentage of aluminium in the contacting layers were determined. The well width can be calculated from the position of the exciton peak.

The sample, CB 2, was excited with an incident power of 14.4 mW from a He-Ne laser with a spot size of 0.5 mm. The spectrum was obtained using a 1 metre spectrometer with input and output slitwidths of 0.05 mm coupled to a germanium detector monitored using a lock-in amplifier. The spectrum shown in Figure 3.2.1 was recorded at a temperature of 9.2 K and the experiment was carried out by John Cochrane in this Department.

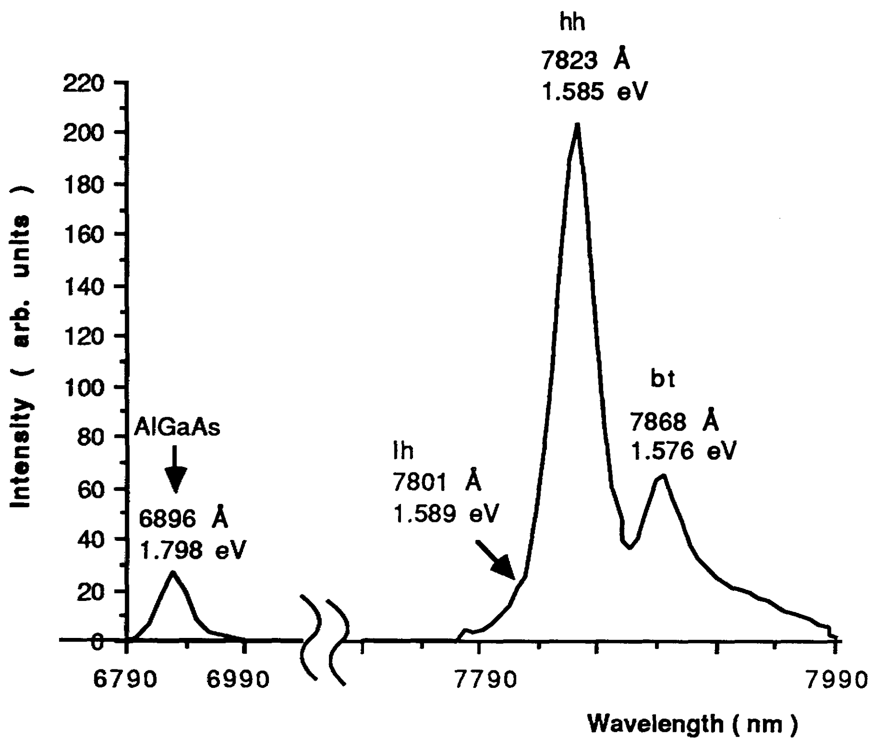

Figure 3.2.1. Photoluminescence spectrum of CB 2

Although a detailed analysis of the photoluminescence spectra is outwith the scope of this thesis, it was possible to estimate the well width and the linewidth of the heavy hole exciton from the spectra. The important peaks are labelled in the diagram. The highest intensity peak occurring at 7830.5 Å (1.583 eV). The inflection on the high energy side of the peak, at 7801 Å (1.589 eV), is attributed to the light hole exciton (lh). On the lower energy side of the spectrum the peak at 7868 Å (1.576 eV) was probably due to bound transitions (bt) [Chen 1987] which will be thermalised as the temperature is increased. The aluminium concentration determined from the peak at 6896 Å (1.798 eV) was 26 %.

Well Width	Aluminium Concentration	Exciton Binding Energy		Exciton Transitions			
		Heavy hole	Light Hole	Heavy		Light	
Å	%	meV	meV	eV	nm	eV	nm
62	26	11.1	12.5	1.592	779.1	1.605	772.7

Temperature 9.2 K

Table 3.2.1 Well width of the grown structure determined using the program Xton from PL data obtained at 9.2 K

The room temperature photoluminescence spectrum is also shown in Figure 3.2.2. From this spectrum (measured at Sheffield) the aluminium concentration in the barriers was also determined as 26% and the well width in the intrinsic region was found to be 62 Å compared to the design thickness of 50 Å.

Using the program Xton described in Chapter 2 it was possible to compare the well width from both of the photoluminescence spectra to that determined at Sheffield. From Table 3.2.1 it clear that the calculated heavy hole exciton transition, 7791 Å, for a well of width 62 Å is very close to that actually obtained from the photoluminescence spectrum, 7823 Å. For the light hole exciton transition the experimental value at 300 K was 823 nm which was very close to that obtained theoretically of 824 nm.

Well Width Å	Aluminium Concentration %	Exciton Binding Energy Heavy hole meV	Light Hole meV	Exciton Transitions Heavy eV	nm	Light eV	nm
62	26	11.0	12.4	1.493	831.1	1.505	824.0

Temperature 300 K

Table 3.2.2 Well width of the grown structure determined from Xton at 300 K

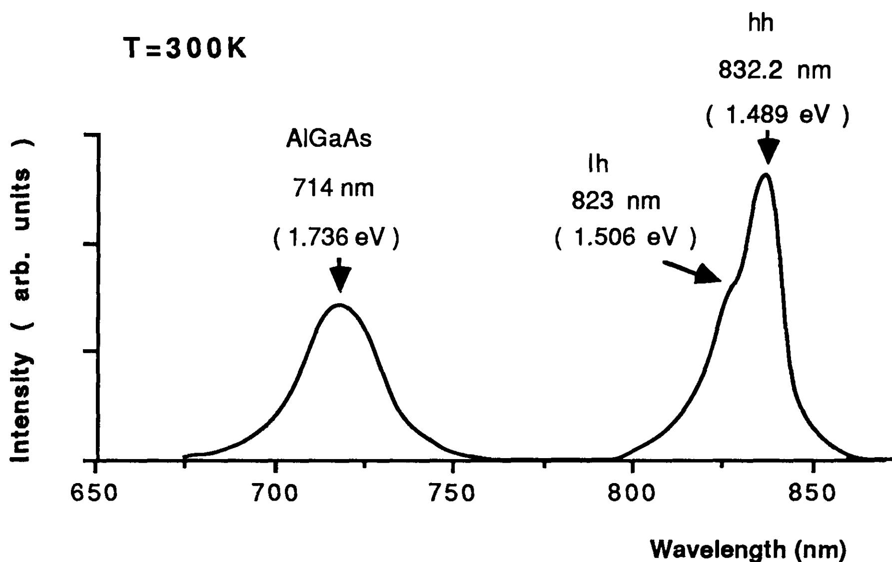

Figure 3.2.2 Room temperature photoluminescence of CB 2 as performed at Sheffield

The well width determined from the photoluminescence spectrum at 300 K was again used in the program Xton along with an aluminium concentration of 26% and the results are shown on Table 3.2.2. This time both the heavy hole and light hole exciton transition are much closer to the values obtained experimentally with only 1 nm difference between these theoretical results and those obtained from the spectrum. Thus, in future calculations it is assumed that the layer CB 2 has a well width of 62 Å.

The next parameter to be analysed was the exciton linewidth. This can be an important factor in the operation of an electroabsorption modulator, particularly in this case where a relatively narrow well width has been used which reduces the energy shift obtainable for a particular applied electric field. The broader the linewidth, the less possible it is to obtain a high contrast ratio. Furthermore the width of the exciton in photoluminescence spectra at low temperature is an indication of the quality of the material.

The linewidth of the excitonic transition can be attributed to two main mechanisms: homogeneous and inhomogeneuos broadening. The sources of inhomogeneuos broadening include the effects of impurities, quantum well interface roughness, alloy clustering in ternary structures and well to well fluctuations in the multiple quantum well region. Impurity broadening is due to the interaction of impurity donors or acceptors with excitons and is proportional to the number of scattering centres in the crystal. For high purity material, with $n < 10^{15}$ cm^{-3}, the effect of impurity broadening is negligible.

Homogeneous broadening is due to the interaction of excitons with phonons, i.e. the dissociation of the excitons by phonons. This effect makes the dominant contribution to the linewidth and both optical and acoustic phonons are involved in the process at room temperature. The phonon contribution to the linewidth is proportional to the number of phonons present.

The full width at half maximum (FWHM) of the heavy hole exciton peak, at 9.2 K, was 4.8 meV (2.4 nm). From the room temperature PL results, the FWHM was 8.9 meV, therefore there is considerable broadening of the exciton

feature due to the increase in temperature. Further broadening will also take place on application of the drive voltage and the effect of this and a comparison between the linewidth of this device and other similar devices from the literature are discussed in Section 3.6.

3.2.2 Current-voltage measurements

The total electrostatic potential between the *p*-side and the *n*-side neutral regions at thermal equilibrium is called the built-in potential V_{bi} given by :

$$V_{bi} = \frac{kT}{q} \frac{\ln N_A N_B}{n_i^2} \qquad 3.1$$

N_A is the acceptor impurity density (cm^{-3})
N_B is the donor impurity density (cm^{-3})
n_i is the intrinsic density (cm^{-3})

The region where the free carrier density is zero is called the depletion region. Under forward bias the total electrostatic potential across the junction decreases by V_F the applied forward voltage. Therefore V_{bi} is replaced by V_{bi}-V_F and the depletion width is reduced. A large current will flow for forward bias > V_{bi}. A reverse bias, by contrast, increases the total electrostatic potential across the junction by V_R, the applied reverse voltage. Under reverse bias conditions there is therefore an increase of the depletion width.

I-V analysis of the device was performed using a Hewlett-Packard 4515A Semiconductor Parameter Analyser. It is possible to determine the reverse breakdown of the device using this equipment and also the reverse leakage current below breakdown. The latter is an indication of the quality of the diode, the lower the leakage current the better the uniformity of the electric field across the depletion region.

The leakage current of one device, fabricated as outlined in Section 3.3 from layer CB 2, is shown in Figure 3.2.2. The leakage current was small, ~ 10 nA (1μA/cm^2) for the voltages (< -30 V) of interest. The diode began to break down below a voltage of -30 V but as will be seen later in this chapter, this modulator was only

required to operate at voltages above -30 V.

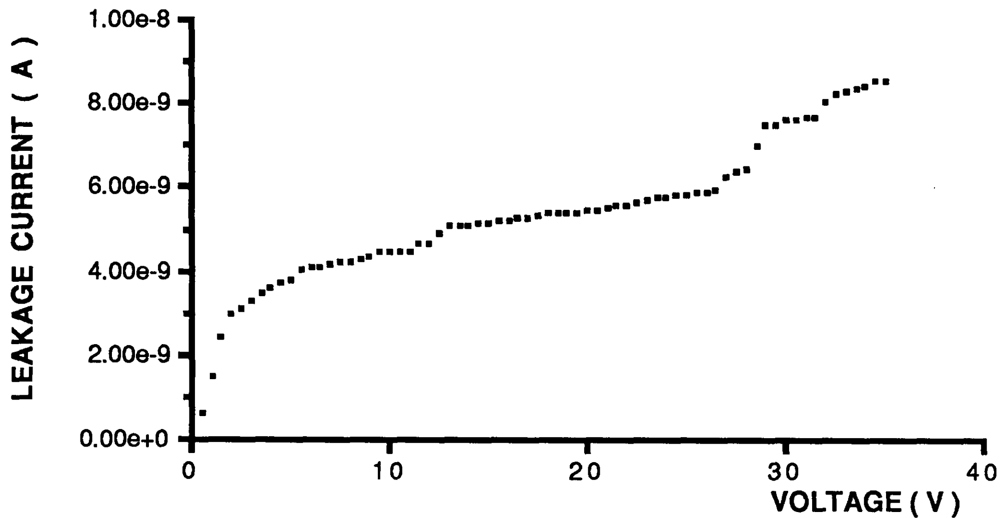

Figure 3.2.2 Leakage current of CB 2 as a function of voltage

3.3 Fabrication of electroabsorption modulator

In order to use layer CB 2 as a transmission electroabsorption modulator it was necessary to remove the substrate and form ohmic contacts with the *n* and *p* layers, as described below.

3.3.1 Cleaning of sample

It was necessary that the crystal surface was clean to ensure that good ohmic contacts were formed on the device. The sample was therefore degreased with a solution of soap and water followed by rinsing in acetone, methanol and finally de-ionised water. If the surface was very dirty it was often necessary to use trichloroethelyne before a final rinse with acetone and methanol. The cleaning processes were improved if carried out in an ultrasonic bath.

3.3.2 Photolithography

The top *p*-type ohmic contact was defined using conventional photolithography.(Figure 3.3.1)

3.3.2.1 Photoresist

A layer of photoresist, which is sensitive to ultra-violet radiation, was spun onto

the sample at 8000 rpm. A positive photoresist (Shipley AZ 1450J) was used and soft baked in an oven for 30 minutes at a temperature of 90°C.

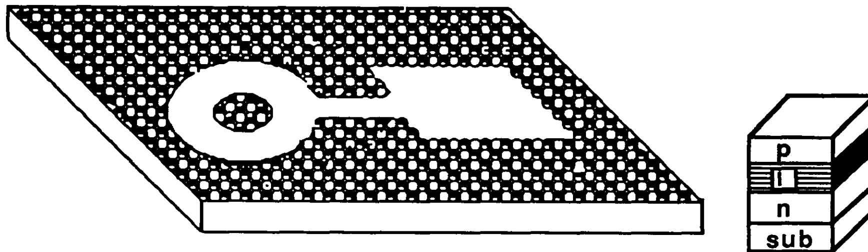

Figure 3.3.1 Sample exposed to UV light and the resist developed

The baking process was interrupted after 15 minutes to immerse the resist in a solution of chlorobenzene for a period of 10 minutes. This hardens the resist and causes an overhang profile at the edges of the exposed area [Mimura 1986] which allowed a subsequent lift-off process to take place more easily.

3.3.2.2 Mask design

The dark field mask consists of an annular ring, outer circle 400 μm in diameter and inner circle 100 μm in diameter, connected to a square pad, 400 μm x 400 μm. The areas of the ring and the square ohmic pad are transparent to UV radiation, with the inner circle and the rest of the mask opaque.

3.3.2.3 Exposure and developing

The resist coated sample was mounted in the mask aligner and exposed to UV radiation for 6 seconds. This sample was then placed in a solution of Shipley developer, diluted 1:1 with de-ionised water, for 55 s or until the exposed area of resist was fully developed. The sample was then rinsed in de-ionised water to halt the developing process. The device was now ready to have the top *p*-ohmic contact evaporated.

3.3.3 Evaporation of Metal Contacts

An ohmic contact is defined as a metal-semiconductor contact that has negligible contact resistance compared to the bulk series resistance of the semiconductor. A

satisfactory ohmic contact can pass the required current with a voltage drop that is small in comparison to the drop across the active region of the device.

For a *p-i-n* structure it is necessary to evaporate both *n*-ohmic and *p*-ohmic contacts. Based on work to optimize the performance of contacts previously carried out in this Department, the metal layers and thicknesses chosen for the *p*-ohmic were

gold-300 Å
zinc-300 Å
gold-300 Å

The sample was placed in an evaporator filled with a liquid nitrogen cooled trap and the pressure was reduced to 10^{-6} mTorr. The sample surface was cleaned in a RF plasma for a period of 15 minutes, in order to remove any native oxide layer, before evaporation. The *p*-ohmic metals were then evaporated onto the sample, the thickness of the metal layers being observed using an Intellimetrics thickness monitor. It was found that the exact thickness of the metal layers was not crucial to the performance of the device, but these were generally kept close to the recipe given above.

3.3.4 Lift-off

The sample was removed from the evaporator and placed in a bath of acetone which dissolved the remaining photoresist and so 'lifted-off' the metal from the non-exposed areas. (Figure 3.3.2) The *p*-ohmic contact is shown in Photograph 3.3.

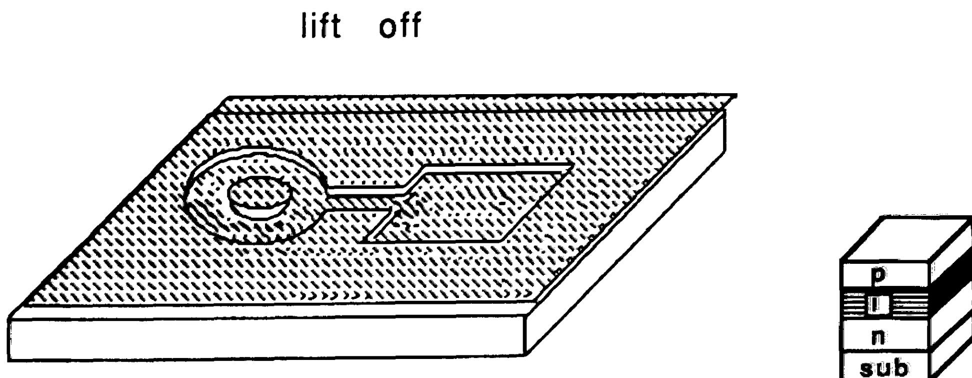

Figure 3.3.2 Lift-off process

The remaining metal formed the *p*-ohmic contact. To make the contact ohmic it was annealed in a furnace, in an atmosphere of argon, at a temperature of 350°C for one minute. Figure 3.3.3 shows the top *p*-ohmic contact. The sample was then attached, *p*-side down, onto a transparent slide, in preparation for the removal of the GaAs substrate. A Logitech epoxy resin with a refractive index of 1.54 (to match that of glass) was used for this purpose and was cured at a temperature of 65°C for one hour. This epoxy resin is capable not only of withstanding the chemicals in the various etching solutions, but also the high alloying temperatures used in the formation of the ohmic contacts.

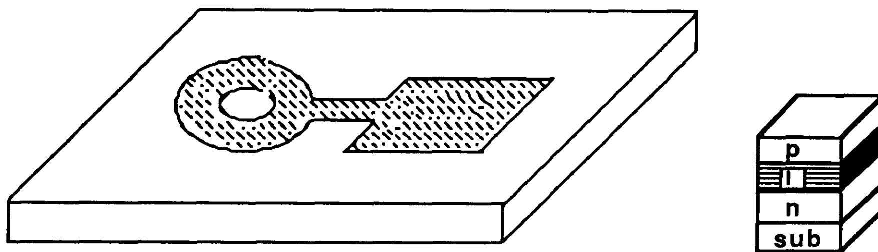

Figure 3.3.3 The top *p*-ohmic contact

3.3.5 Chemical Wet-Etching

During the first attempts to fabricate the modulator devices, an effort was made to leave the substrate on the layer for support and merely etch a window through it to form the aperture of the device. This process was difficult, as many of the masks used to protect the substrate were inadequate and easily removed by the chemical etchants. After this method proved fruitless it was decided that the entire substrate would be removed and a glass slide employed to support the remaining thin layers.

The opaque GaAs substrate was removed by a process of wet chemical etching. This was chosen rather than dry-etching techniques due to the thickness of the substrate. The processing time involved using dry-etching techniques makes them unsuitable for this purpose. To remove the thick GaAs substrate (400 μm) it was necessary to use two different etchants. The first of these was a fast non-selective etch, that is it would dissolve both GaAs and AlGaAs. This was replaced, on nearing the epitaxial layers, by a slower more selective etch, which does not significantly etch

AlGaAs.[GEC Wet etching report]

The fast etch was a solution of

1	8	1
H_2O	H_2O_2	H_2SO_4
de-ionised water	hydrogen peroxide (30 %)	sulphuric acid (98 %)

The sample was placed in the etching solution on a hot-plate at a temperature of 30°C to give a controllable and uniform etch rate. A magnetic stirrer was used to keep the solution flowing over the sample during the process. This not only makes the etch rate more uniform but helps to keep the surface etching even by preventing dissolved metal or dirt from clogging on top.

Over a period of 20 minutes the etch rate can vary from 25 μm to 17 μm per minute. These rates differ with time as the etching solution quickly degrades. Any fluctuation in temperature of the hot-plate or the room can also have an effect on the rate of etching. These problems can be alleviated by changing the solution frequently or by adjusting the length of the process times accordingly. As shown in Photograph 3.1 this etch is anisotropic and thus the different crystal orientations etch at different rates.

The sample thickness of the device was monitored by examining it under an optical microscope. By focussing on the bottom of the sample and then the top, and referring to the distance travelled by the focus control, the thickness of the remaining material was established. It was necessary to remove the sample frequently from the chemical etch and rinse it in de-ionised water to perform this analysis.

As the desired depth was approached (typically after 400μm) the solution was changed to a selective etch to prevent any removal of the remaining layers on the sample. This was:

20	1
H_2O_2	NH_4OH
hydrogen peroxide (30%)	ammonia solution (30%)

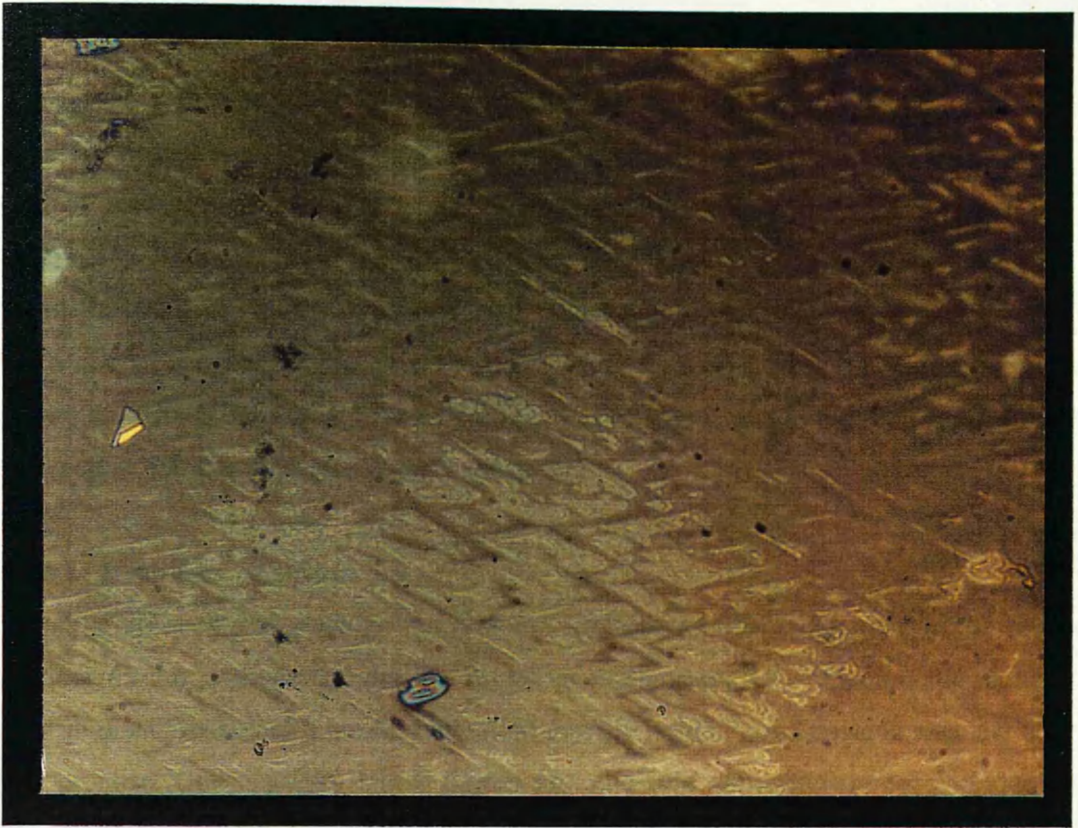

Photograph 3.1 Wet-etching profile of the GaAs in the fast non-selective etch

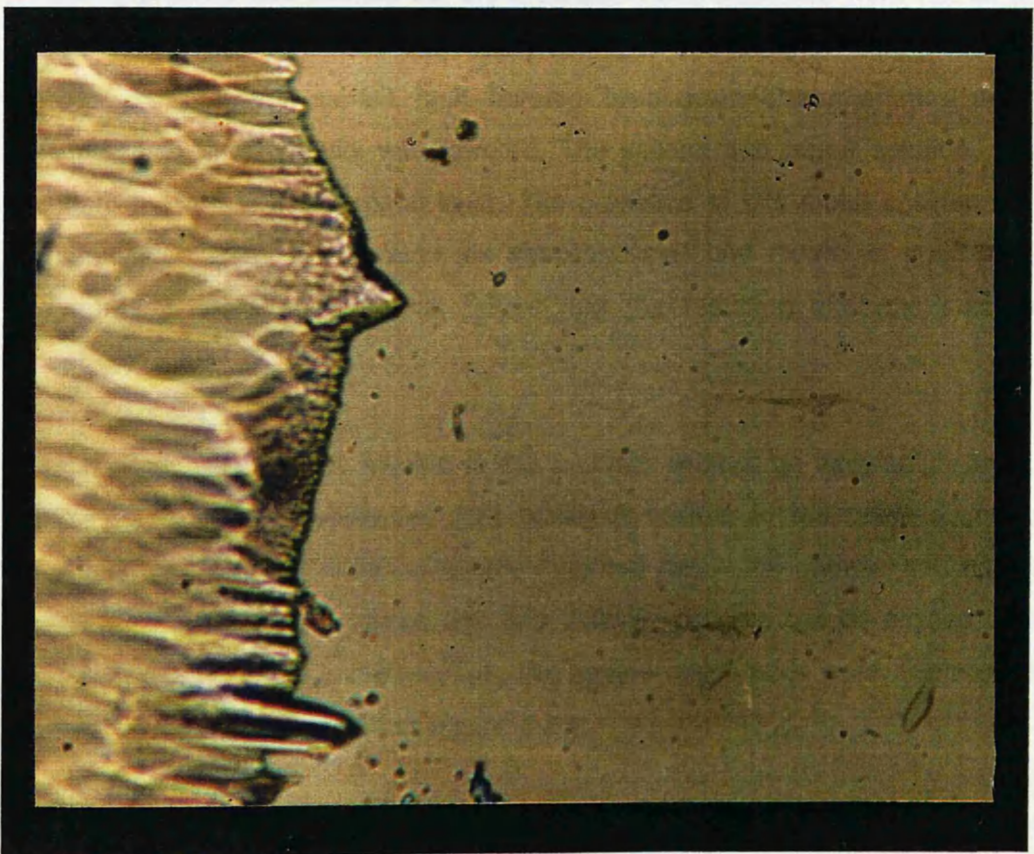

Photograph 3.2 Effect of the selective etch which stops at the etch stop layer. The traces of the GaAs substrate will be removed by the etch

This ratio is the optimum for fast etching of the GaAs (~1μm/ minute) and very slow etching of the AlGaAs layer (~0.1μm/minute). The best temperature for this part of the process was 0°C which allowed a constant and slow etch rate to be maintained. This was slow enough to observe the change in appearance of the crystal when the AlGaAs layer was encountered. This etch stops successfully at a layer of AlGaAs with a concentration of aluminium graded from 50% to 30%. Photograph 3.2 shows the difference between the etchant on GaAs/AlGaAs, and to the right hand side of the picture the flat etch stop layer is observed.

3.3.6 *n*-ohmic contact

Having removed the substrate the *n*-ohmic contact was now evaporated in the same manner as the *p*-ohmic contact, as shown in Photograph 3.4. Although this contact was annealed as before it became apparent that the yield of good devices was low after this process. Devices were tested before and after the annealing process to identify the problem. It was eventually discovered that the annealing process itself was causing the short circuits. Two solutions to this problem were found : firstly the annealing process was omitted but the breakdown characteristics were not as sharp as previously and the contacts were easily damaged during the bonding process. The devices did however exhibit high reverse breakdown characteristics and the percentage of short circuits was lowered. The second and better solution, was to eliminate the nickel in the metal layer. The presence of this metal accelerates the germanium diffusion rate through the semiconductor and results in short circuits. The contacts were annealed as before and the resulting characteristics were acceptable.

The *n*-ohmic contact was aligned to the *p*-ohmic contact by imaging through the sample using infra-red radiation. This facility is built-in to the mask aligner and consists of an infra-red radiation source mounted below the sample and a vidicon camera above the sample. Hence with little difficulty patterns can be aligned to each other with a precision of a few microns. The square ohmic pads were displaced 180° from each other as illustrated in Figure 3.3.4.

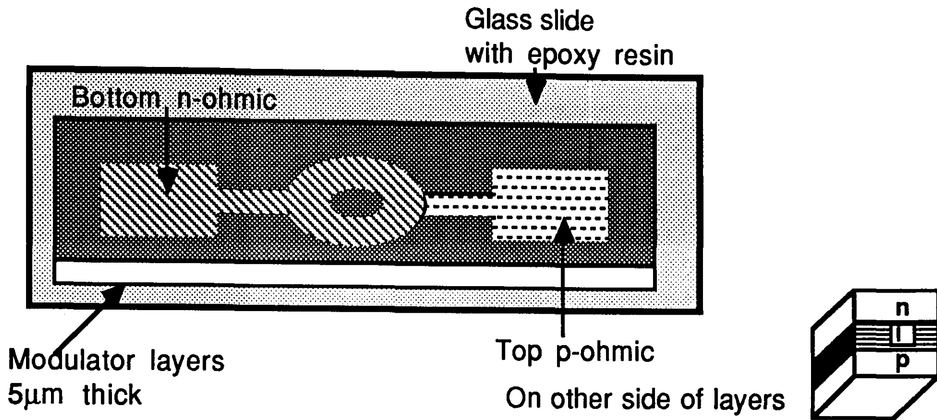

Figure 3.3.4 Aligning of ohmic contacts

3.3.7 Formation of mesa

The final processing step was to remove the epitaxial layers from the top of the *p*-ohmic pad. During this process the device was mesa-ed by protecting an enlarged area around the n-ohmic contact using resist, and then etching the remaining material using the fast non-selective etch, as shown in Figure 3.3.5. This isolated the modulator structure from the rest of the crystal, and allowed the top of the *p*-ohmic pad to be accessed, as shown in Photograph 3.5.

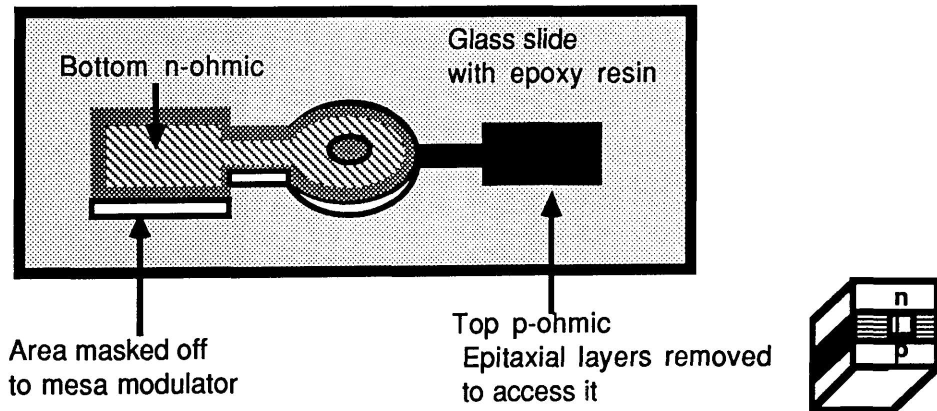

Figure 3.3.5 Multiple quantum well electroabsorption modulator

3.3.8 Device mounting

The device was mounted using epoxy resin on a copper vero board, with an aperture. Electrical contact was made using two metal probes soldered onto the copper board and placed by hand on the device contact pads, as shown in Figure 3.3.6. This

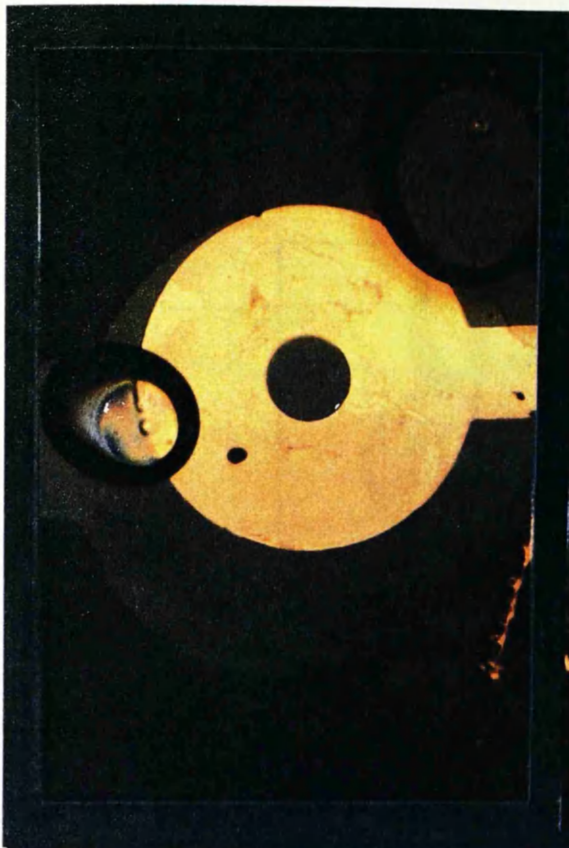

Photograph 3.3
Top contact viewed through the glass slide

Photograph 3.4
Bottom contact viewed from the top of the device

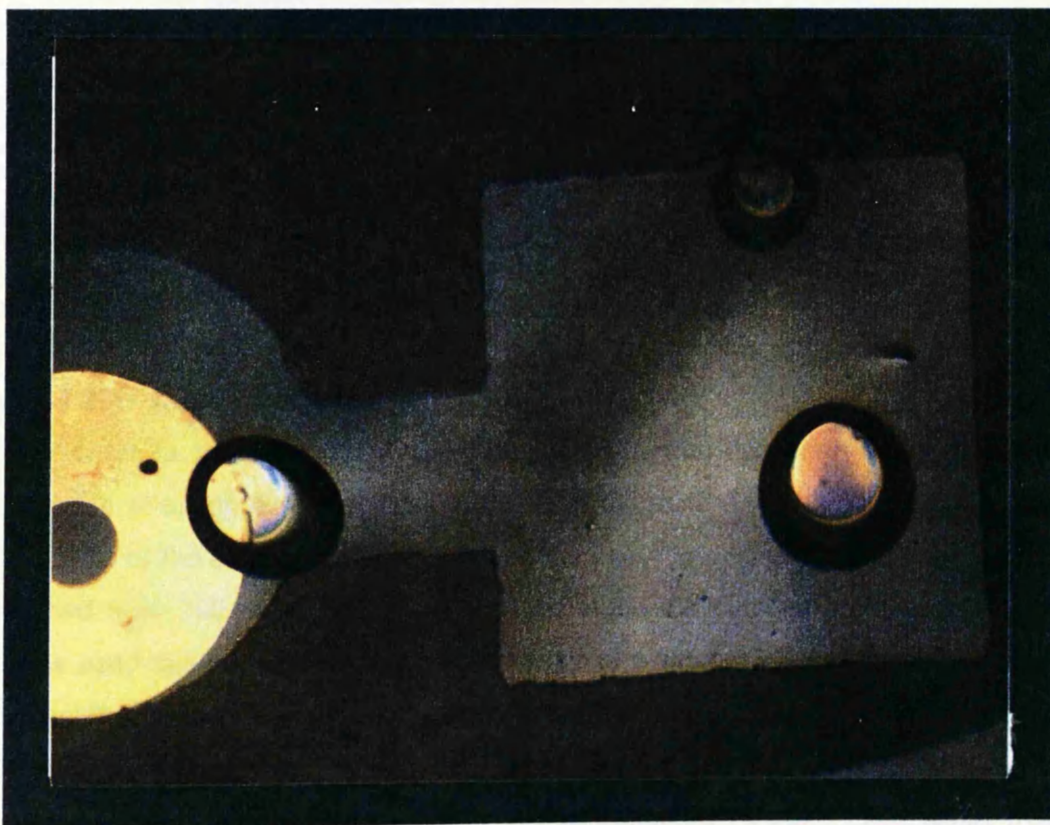

Photograph 3.5 View of the mesa process which isolates the device from the surrounding epitaxial layers

arrangement was more successful than the wire bonding machine which either destroyed the contacts or would not fuse the wire to the thin metal layers.

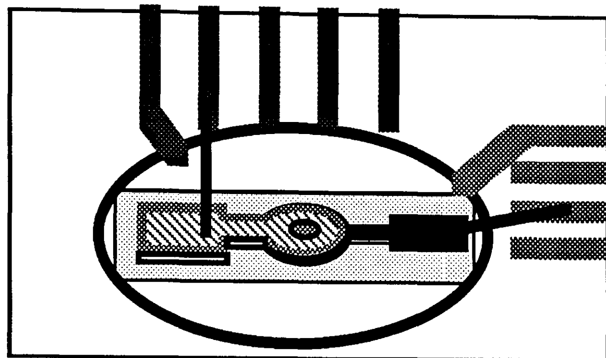

Figure 3.3.6 Mounting of the modulator

3.4 Experimental set-up

There are two means of assessing the absorption spectrum of the modulator structures : the first is to measure the photocurrent response of the sample. This is the simpler of the two as it does not require the removal of the opaque substrate of the crystal and will be described in Chapter 5. The other, more time consuming method employed here, is to fabricate modulators as described in Section 3.3 and measure their transmission spectra.

3.4.1 Transmission measurements of CB 2

The apparatus to measure the transmission of the modulator as a function of reverse bias voltage is shown in Figure 3.4.1.

3.4.1.1 Light source

In order to transmit light through the layers it was necessary to use a source capable of tuning over a suitable wavelength range. The region of interest here, for analysis of the band edge absorption and the heavy and light hole exciton transitions, varied from 790 nm to 850 nm. At first an argon ion pumped a Styryl-9 dye laser was used but this was abandoned in favour of a more stable and reliable system, consisting of a white light source and a monochromator.

The system consisted of an Ealing 100 W Tungsten Halogen flash lamp, with a stabilized power supply 4 - 12 V, capable of supplying sufficiently high optical

powers to examine the structure (> 800 nW after monochromator). The light was dispersed through a double 0.25 m Spex spectrometer with 600 lines/mm gratings. The monochromator was operated in second order to obtain higher output powers. A high frequency cut-off filter (Schott RG 715 glass), permitting only the transmission of light above 700 nm, was inserted after the monochromator, to eliminate the undesirable higher energy components of the signal.

3.4.1.2 Chopper

A chopper was used with a lock-in amplifier in order to eliminate the effects of background light and other stray signals. The light was chopped at suitable frequency to minimise mains interference - not for example at an integral multiple of 50 Hz - and this reference frequency was used as as the input to the lock-in amplifier. By this means only signals at the chopper frequency were amplified. A lens was placed after the chopper to couple the light into an end-fire rig.

3.4.1.3 End-fire rig

The end-fire rig system consisted of two microscope objectives, pointing towards each other, mounted on x, y and z translation stages. This flexible arrangement allowed accurate alignment of the light beam through the modulator. The device was placed between the objectives on a stage capable of movement in the x, y and z directions plus angular rotation allowing the beam of light to be incident at exactly 90° to the modulator surface. X20 microscope objectives were used.

3.4.1.4 Detection of signal

The signal was detected using a germanium photodiode placed at the output of the end-fire rig. This was connected to an Oretec Brookdeal 9503-SC precision lock-in amplifier. For ease of alignment the detector was also mounted on an x,y,z translation system. The whole system was mounted on an optical bench for stability. All the transmission experiments were carried out at room temperature (300 K).

Figure 3.4.1 Experimental Set-up

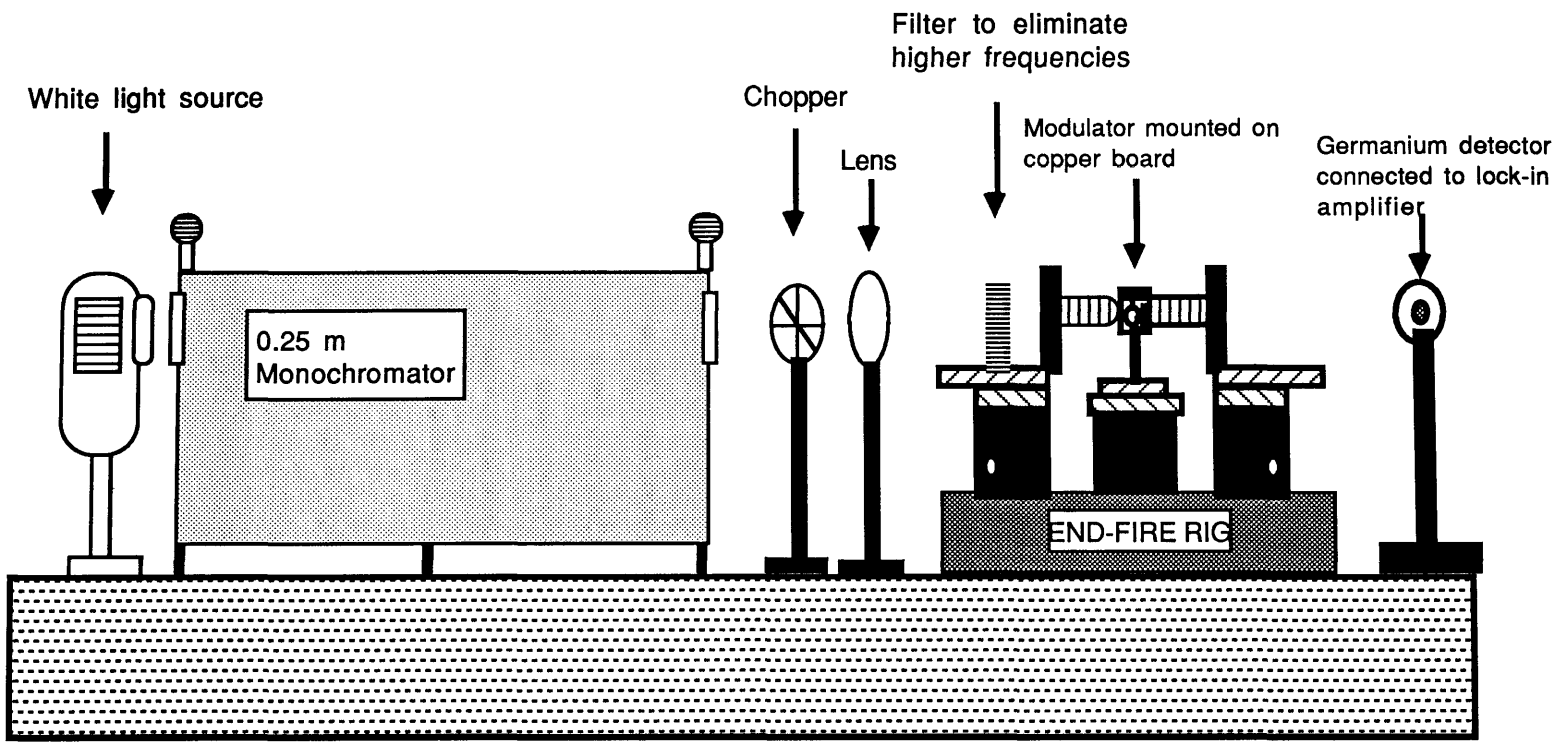

3.4.1.5 Computer Control of System

An IBM XT 286 computer was used to simplify data acquisition. Firstly the monochromator was interfaced to the computer using one of the printer ports. Software was written to set the wavelength range of the monochromator, the wavelength step size and the time delay between successive measurements. The lock-in amplifier was interfaced to the computer via an analogue to digital converter. This allowed the detected signal to be collected in digital form by the computer.

3.4.2 Experimental Procedure

To align the whole system initially the modulator was replaced by a piece of epoxy covered glass. The beam was then aligned by removing the filter and using visible light. To optimize the signal, the focus and relative positions of the lamp, microscope objectives, lens and detector were all adjusted. The slit widths of the monochromator were made as small as possible to improve the wavelength resolution : in the case of the transmission spectra in Section 3.5 these were 0.1mm. The detected signal was of the order of 100 μV. To align the modulator a pellicle beam splitter was placed before the input objective and a portion of the light was focussed onto an infra-red camera. In this way the aperture of the device could be located, and the same step was taken at the output to ensure that the light was transmitted through the structure. To minimise noise, the voltage was applied to the device using a battery and a potentiometer with the voltage being monitored using a digital voltmeter.

The experiments were carried out by firstly recording the system response by replacing the sample with a glass slide This spectrum was used to determine the response of the whole system as a function of wavelength, and was subsequently used to normalise the modulator spectra.

3.5 Transmission results of CB 2

The transmission spectra, recorded as outlined Section 3.4.2, are presented in this section. By comparing these spectra, obtained at the various applied reverse voltages, it is possible to quantify the QCSE shift.

3.5.1 Normalising curve

The system response is shown in Figure 3.5.1. As previously described this was used to eliminate the effects of the variation in the system response with wavelength. Included in this spectrum are absorption and reflection effects due to the glass slide, microscope objectives, low pass filter, the lens and the epoxy.

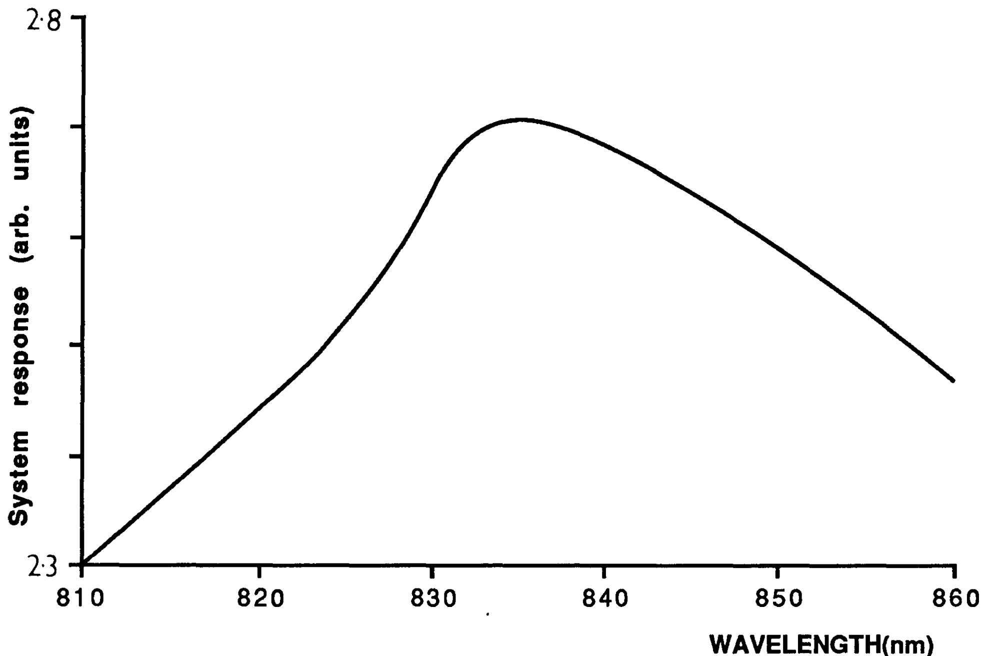

Figure 3.5.1 Normalising curve

3.5.2 Zero bias spectrum of CB 2

Figure 3.5.2 shows the absorption spectrum of CB 2 with no applied field. The results for the shift of the heavy hole exciton peak and the broadening resulting from the application of the electric field, presented in this section, are determined relative to this zero applied bias condition and are not corrected for the zero bias built-in field.

The positions of the the heavy and light hole excitons are shown in Figure 3.5.2. The heavy hole peak occurs at a wavelength of 831 nm (1.492 eV) and since this exciton is closest to the absorption edge and therefore has the most influence on the contrast ratio, it is this peak which is of most interest. The light hole exciton is also resolvable at zero bias and occurs at a wavelength of 823 nm (1.5066 eV). The position of the two exciton transition peaks can be compared to those found using the

program Xton described in Chapter 2.

To do this it is necessary to correct the experimental data for the built-in field at zero bias. Assuming a built-in voltage of 1.4 V then the electric field in the intrinsic region, width 2.24 μm, will be approximately 6.25 x 10^4 V/cm. From equation 2.49 this results in a shift of 4 x 10^{-5} eV for the e_1-hh_1 transition, which will not significantly affect its position in the experimental spectrum. From Xton, assuming a well width of 62 Å and 26 % aluminium content as obtained from the PL spectra, the e_1-hh_1 transition occurs at 831.1 nm. There is therefore excellent agreement between the experimental and theoretical results.

Figure 5.3.2 shows Fabry-Perot resonances at higher wavelengths. Resonances of this type have recently been utilised by Whitehead [1989] in the novel etalon devices discussed in Chapter 1. The position of the resonances near the heavy hole exciton in this device is detrimental to the device performance.

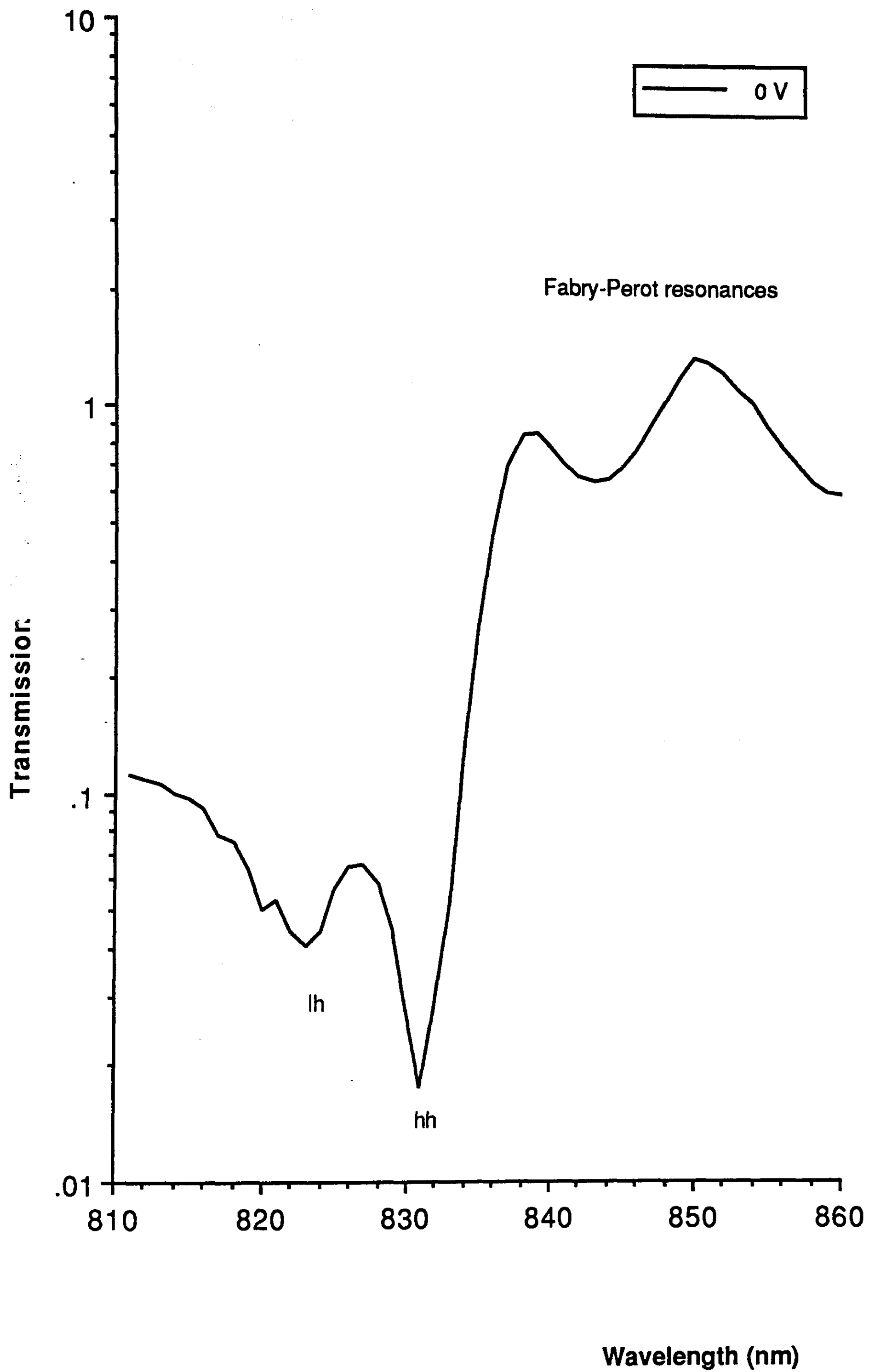

Figure 3.5.2 Transmission spectrum of CB 2 at zero applied electric field

3.5.3 The effect of an electric field on the transmission spectra

The transmission spectra for applied voltages between 0 V and -33 V are presented in this section as a function of wavelength. These are subsequently used to calculate the magnitude of the Stark shift and the exciton broadening.

3.5.3.1 Low electric field effects < 1.0×10^4 V/cm

Figure 3.5.3 presents a comparison between the zero bias transmission spectrum and that of an applied voltage of -1 V. It is assumed that electric field is constant in the depletion region.[Miller 1988] The electric field in the depletion region is 6.25×10^3 V/cm, as previously calculated, for zero applied voltage, and at -1 V the corresponding electric field in the diode is 1.0×10^4 V/cm. It can be seen that there is little or no broadening of the heavy hole exciton as a result of this low field but the light hole is beginning to broaden.

The small shift in the exciton energies is expected due to the narrowness of the wells used for this design. One of the main aims when designing the modulator was to obtain a high contrast ratio and to achieve this narrow wells were chosen. The adverse effect of using narrow wells is the 'slowness' in the shift of the exciton. From equation 2.49

$$\text{shift in energy levels} \propto a^4$$

thus the larger the well width the larger the shift.

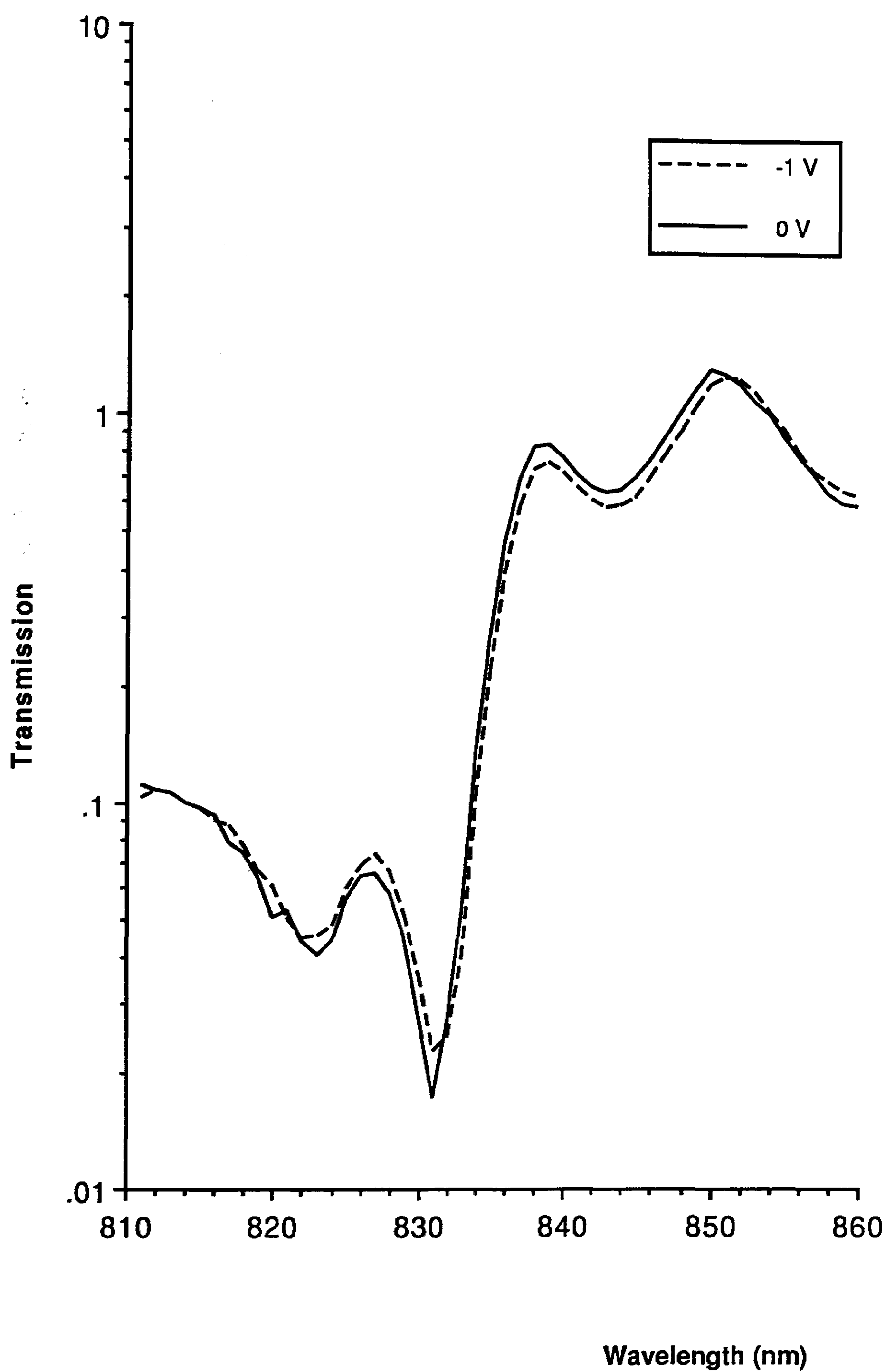

Figure 3.5.3 Transmission spectra of CB 2 at 0 V and -1 V

3.5.4 Electric fields below 2.8 x 10^4 V/cm

Figure 3.5.4 shows transmission spectra for applied voltages of 2, 3, 4 and 5 V together with the zero bias spectrum.

At these fields (maximum field 2.8 x 10^4 V/cm) there is still no real shift of the absorption edge, although a slight shift in the position of the heavy hole exciton peak is visible (10 Å at 5 V). The heavy hole exciton peak is beginning to broaden and lose oscillator strength due to the reduction in overlap of the electron and hole wavefunctions (Section 2.5).

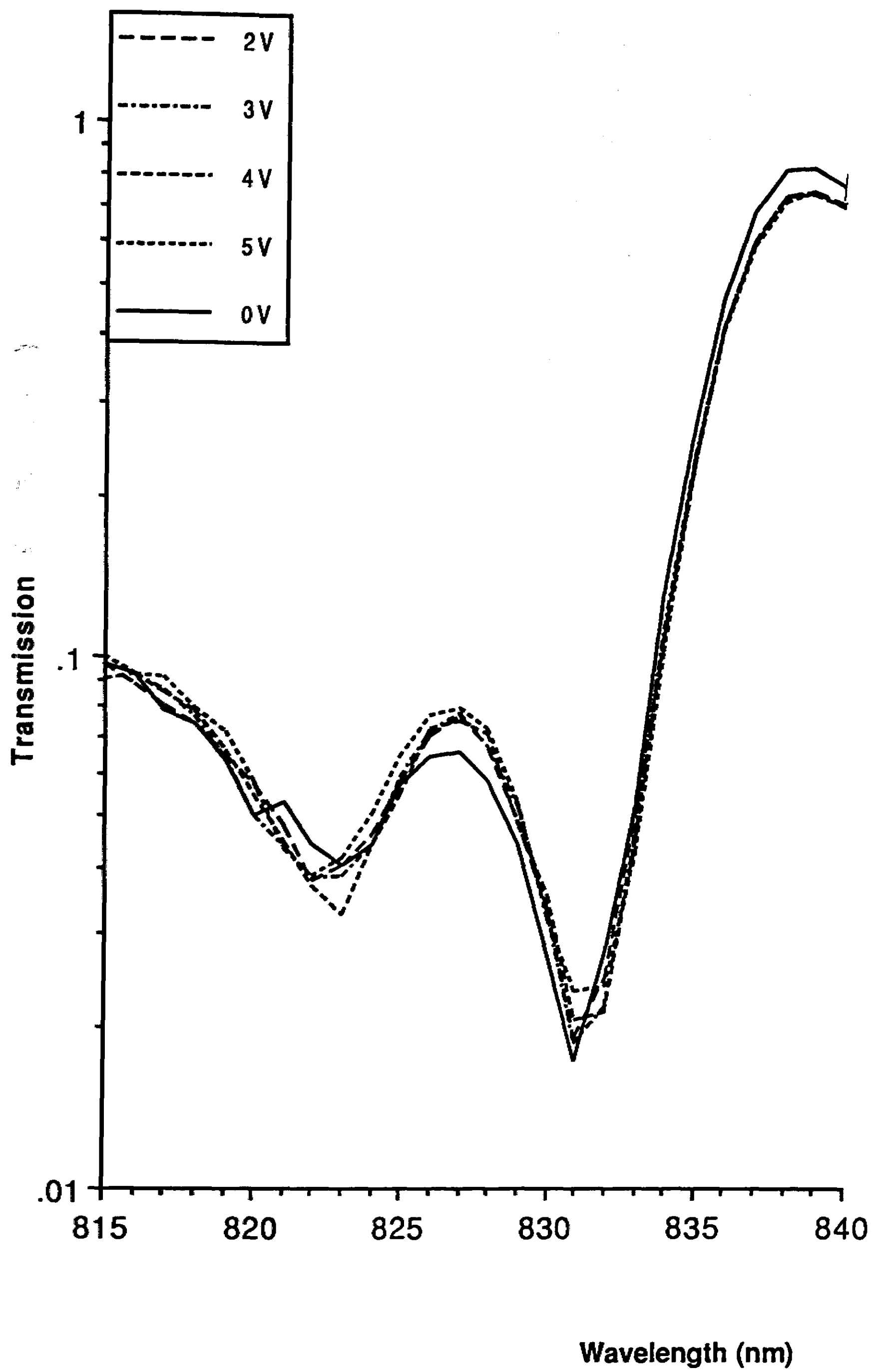

Figure 3.5.4 Transmission spectra for applied voltages between -2 V and -5 V

3.5.5 Electric fields between 2.8 x 10^4 V/cm and 5 x 10^4 V/cm

Between applied voltages of -5 V and -10 V a shift in the exciton peak and hence the absorption edge becomes apparent. At the lower applied voltages in this range the magnitude of the shift is fairly small rising nonlinearly with increasing field. At an applied bias of -10 V the shift is 2.02 meV. Both the heavy hole and light hole exciton peaks are broader in this range than they were for the zero bias condition. The broadening of the heavy hole exciton peak is discussed later in this chapter. As the electric field is increased the suppression of the absorption for both exciton transitions continues, as shown in Figure 3.5.5.

3.5.6 Electric fields between 50 kV/cm and 9.55 x 10^4 V/cm

The fields between 50 kV/cm and 9.55 x 10^4 V/cm correspond to the applied voltages of -10 V to -20 V: selected spectra are shown in Figure 3.5.6. The trend of the shift of the absorption edge to longer wavelengths and peak absorption reducing with increasing field continues. The broadening of the exciton peak is prominent in these higher field spectra with the peak persisting to the highest of these voltages(-19 V). The behaviour of the light hole peak is as predicted: it also broadens, shifts, though less dramatically, and experiences a reduction in absorption.

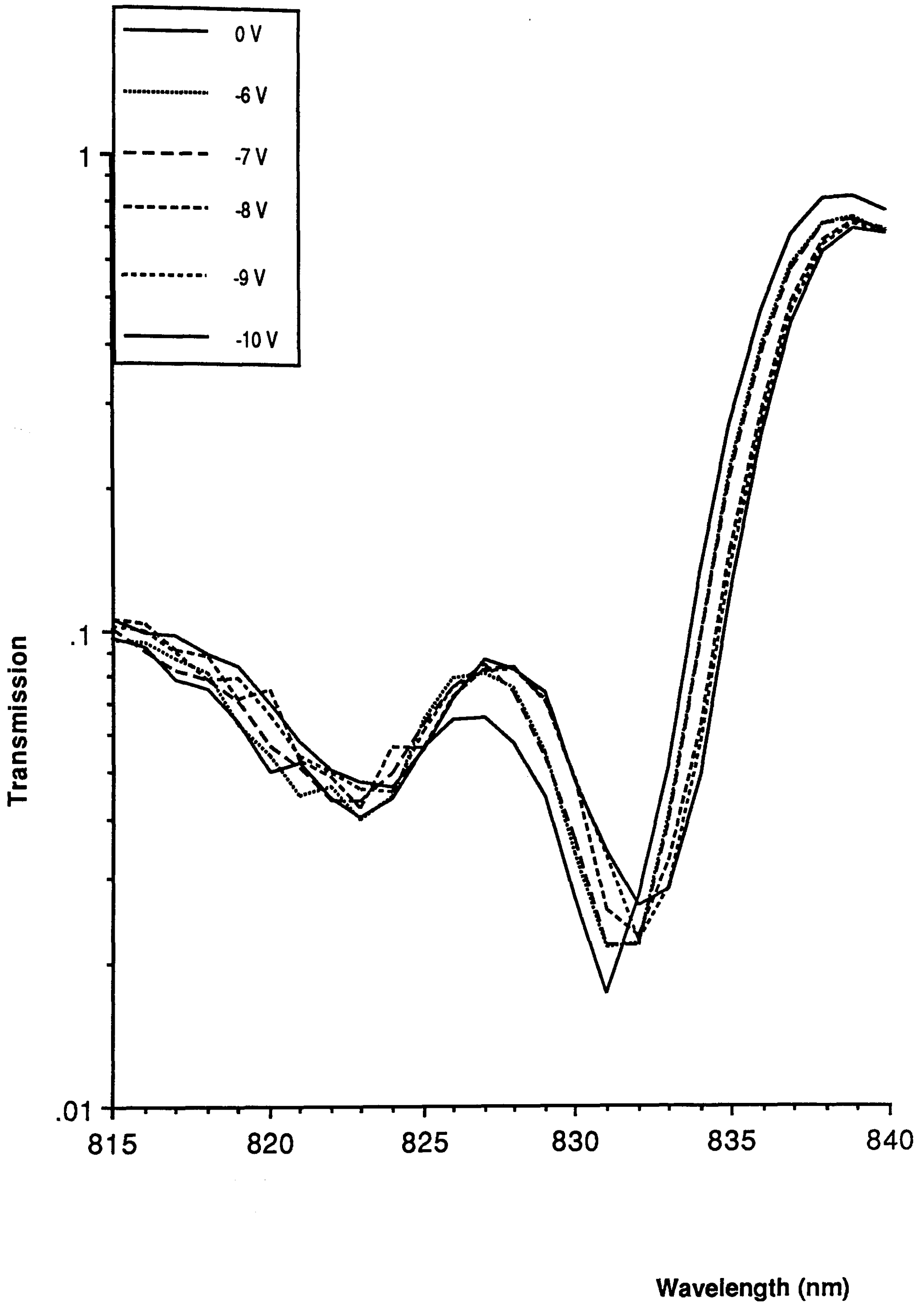

Figure 3.5.5 Transmission spectra of CB 2 for -6,-7,-8,-9 and -10 V

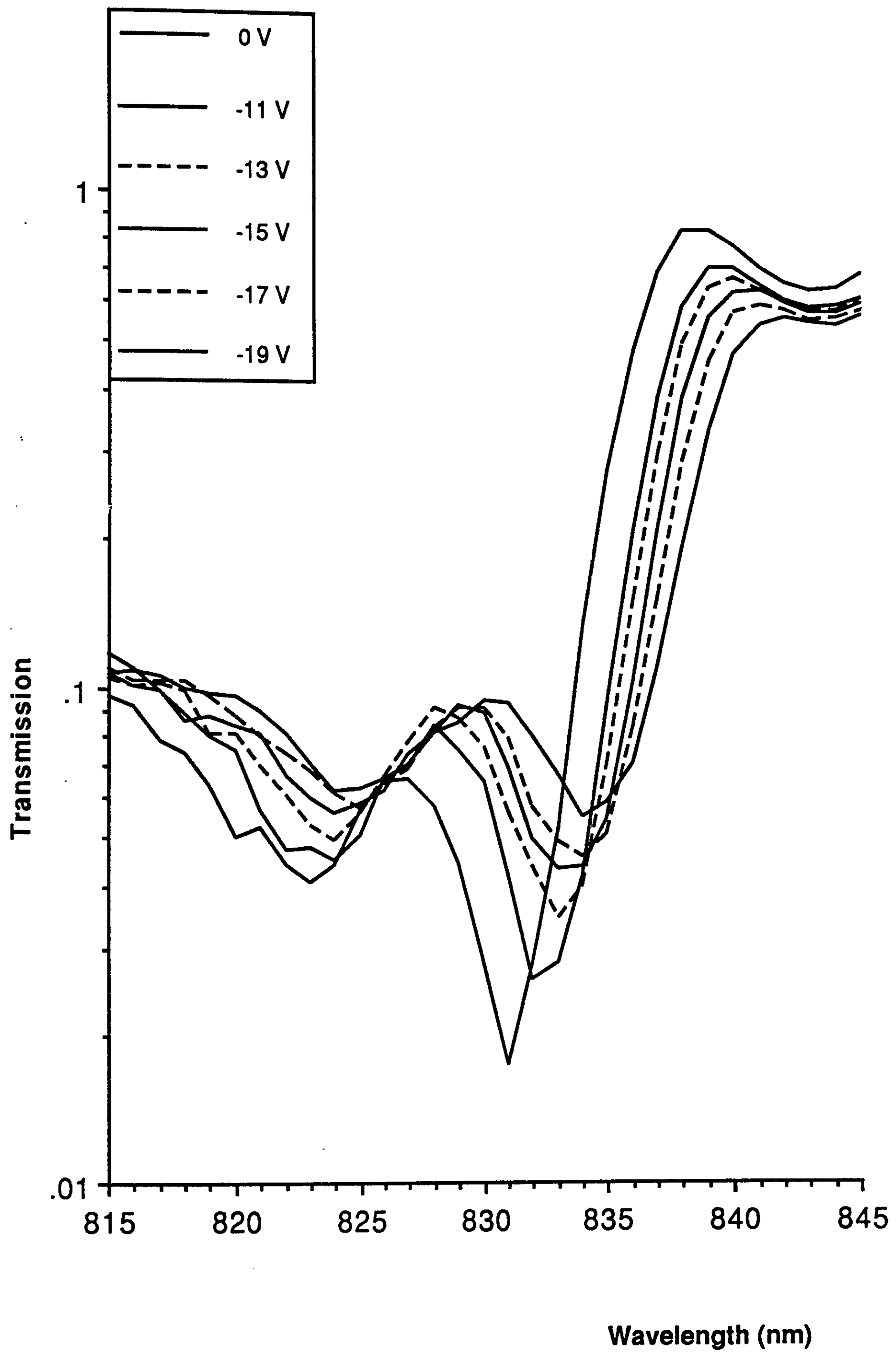

Figure 3.5.6 Transmission spectra of CB 2 for -11,-13,-15,-17 and -19 V

3.5.7 Electric fields greater than 9.55×10^4 V/cm

Figure 3.5.7 shows results for electric fields above 9.55×10^4 V/cm. As before the absorption edge and heavy hole exciton peak continue to shift towards the red end of the wavelength spectrum. The width of the heavy hole exciton peak expands with the applied electric field and there is the associated change in the absorption of this peak.

The light hole exciton peak has almost disappeared at these higher voltages. The maximum applied voltage was -33 V above which it was difficult to resolve the heavy hole exciton peak. The suppression of the heavy hole exciton peak continued as did the Stark shift. Even at -33 V the heavy hole exciton peak is almost unresolvable and the maximum contrast ratio was obtained at a reverse voltage of -25 V.

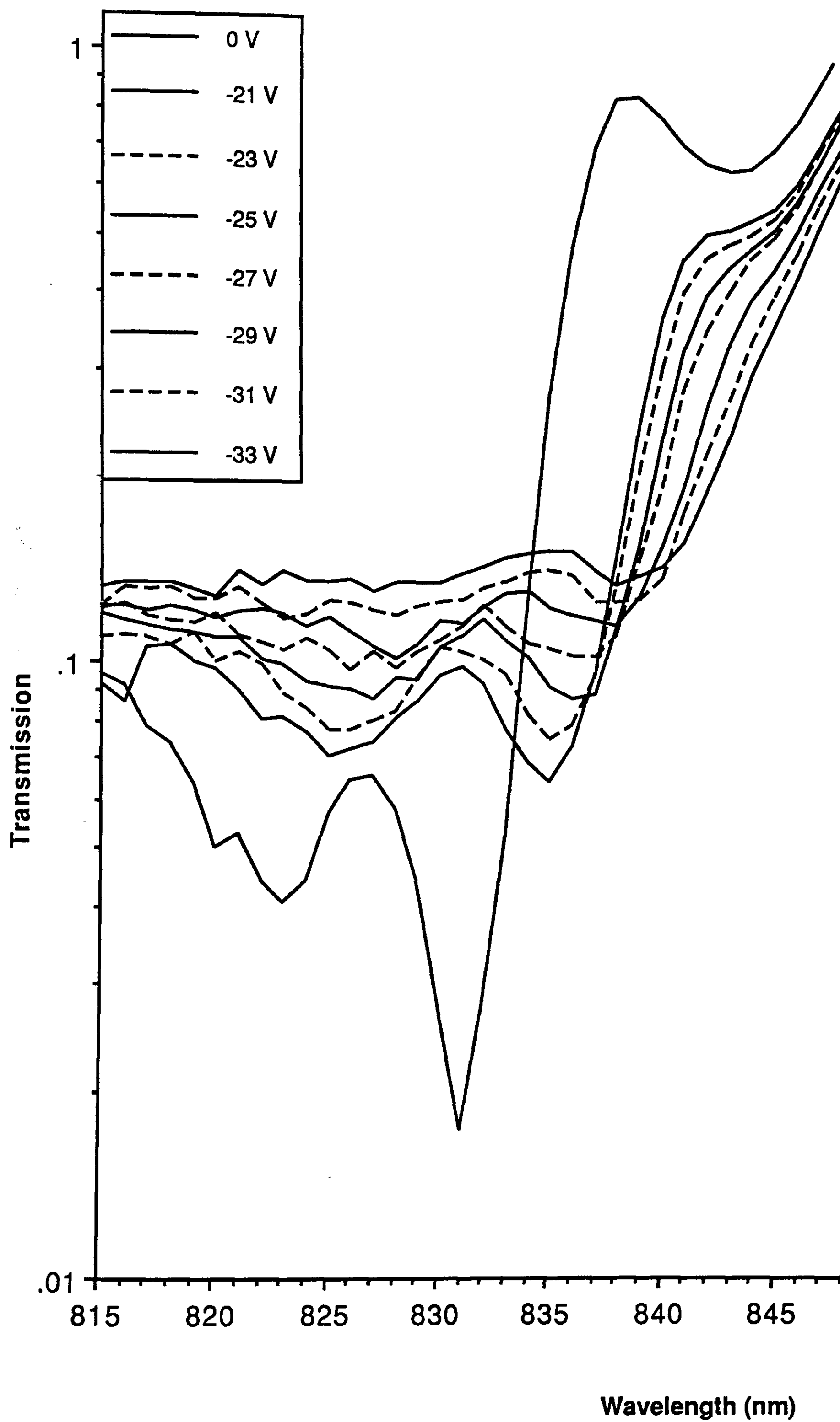

Figure 3.5.7 Transmission spectra of CB 2 at -21,-23,-25,-27,-29,-31 and -33 V

3.6 Exciton broadening

Broadening of the heavy hole exciton peak can dominate the performance of the modulator : a narrow exciton linewidth, which does not broaden significantly with electric field can lead to a high contrast ratio for relatively low electric fields. The width of this peak at low temperature is an indication of the quality of the material and accuracy of the growing process. The effect of increasing the temperature on the exciton peak width can be determined by examining the room temperature PL. Finally the effect of the electric field on the linewidth of the peak can also be assessed from the transmission results for various values of electric field.

As discussed before in Section 3.2, the width of the exciton peak is partly determined by the quality of the material. In this particular case there is a detrimental effect from the large number (200) of wells in the intrinsic region. At 9.2 K the FWHM of the heavy hole exciton peak was found to be 4.8 meV which at room temperature rose to 8.9 meV. Thus this rise in temperature has a large effect on the linewidth of the exciton. A slight variation in the temperature would however not have any significant effect on the FWHM of this peak. The room temperature widths of various modulator layers are presented in Table 3.6.1. From this table it can be seen that the linewidth of the heavy hole exciton peak of CB 2 is reasonable considering the number of wells included in the structure. Better results are obtained by Hsu [1988] using a different growth technique, but it is impossible to deduce what causes the difference in the linewidths. The only valid conclusion which can be drawn from this comparison is that the layer does not appear to exhibit any extreme detrimental effects due either to the number of wells or to the narrow well width.

Reference	Growth Technique	Well Width (Å)	Number of Wells	FWHM (meV)
Hsu 1988	MBE	94	200	5.2
Whitehead 1987	MOVPE	105	60	7.8
Wood 1984	MBE	95	50	7.5
CB 2 1990	**MOVPE**	**62**	**200**	**8.9**

Table 3.6.1 Linewidths of various multiple quantum well structures at 300 K determined from absorption measurements at zero bias

At zero applied bias the heavy hole FWHM can be obtained by extrapolating the curve as shown in Figure 3.5.2. By applying this method to all the recorded spectra the broadening of exciton peaks due to the electric field can be determined. Data are tabulated in Table 3.6.2. Clearly at higher electric fields and at that of optimum operation (11.8×10^4 V/cm) the field has a large effect on the width of the exciton peak, which is increased by more than a factor of two compared to the zero applied field condition.

Number of Wells	Well Width (Å)	Applied Voltage (V)	Electric Field (V/cm)	Heavy Hole Width (meV)	(nm)
200	62	5	2.85×10^4	8.96	5
		10	5.08×10^4	10.7	6
		15	7.32×10^4	11.6	6.5
		20	9.55×10^4	13.9	7.83
		25	**11.8×10^4**	**18.3**	**10.2**
		30	14.0×10^4	20.5	11.6

Table 3.6.2 Broadening of the heavy hole exciton peak as a function of applied electric field to CB 2

3.7 Magnitude of the shift

Table 3.7.1 summarises the experimentally and theoretically obtained shift of the heavy hole exciton peak for layer CB 2. The experimental shift was recorded relative to the zero applied bias condition since data for the condition of zero electric field were not recorded. When calculating the theoretical shift using equation 2.49 this fact has been taken into consideration and the shift has been calculated relative to an applied bias of 6.25×10^3 V/cm corresponding to a built-in voltage of 1.4 V of the diode. This results in an adjustment of 0.03 meV to the theoretical results. There is close agreement between the experimental and theoretical shifts, shown in Figure 3.7.1, particularly at the lower electric field end of the spectra where the two curves are in excellent agreement. Thus the validity of the simple theoretical model has been confirmed.

Table 3.7.2 summarises experimental shifts obtained from the literature for a few transmission electroabsorption modulators with various well widths. An electric field of 5.5×10^4 V/cm was chosen to compare these results with those obtained for CB 2 as shown in Figure 3.7.2. As expected the shift at a particular electric field is

larger for wider wells, see equation 2.49, with a slight discontinuity found between the 95 Å wells, [Miller 1985] and the 94 Å wells [Hsu 1988]. The curves of both the 47 Å and 147 Å wells were interpolated to find the shift at this particular field. The magnitude of the shift for the 62 Å wells shows reasonable agreement with these results.

In conclusion, the experimental shift of the heavy hole exciton peak for structure CB 2 is close to theoretical predictions. In addition the behaviour is consistent with other experimental results in the literature.

Number of Wells	Well Width (Å)	Applied Voltage (V)	Electric Field (V/cm)	Magnitude of Shift (meV) Experimental	Theoretical
200	62	5	2.85×10^4	0.56	0.65
		10	5.08×10^4	2.02	2.15
		15	7.32×10^4	4.50	4.51
		20	9.55×10^4	6.95	7.70
		25	11.8×10^4	9.75	11.78

Table 3.7.1· Exciton shift as a function of electric field for layer CB 2

Reference	Number of Wells	Well Width (Å)	Applied Voltage (V)	Electric Field(V/cm)	Magnitude of Shift(meV)
Whitehead 1988	75	47	12	1.5×10^5	9.87
			16	2.0×10^5	16.45
			20	2.5×10^5	23.55
	60	87	4	4.53×10^4	4.42
			8	9.00×10^4	13.5
			12	1.35×10^5	28.4
	45	147	2	2.14×10^4	6.59
			4	4.30×10^4	8.88
Miller 1985	50	95	4	4.12×10^4	4.7
			6	6.18×10^4	8.9
Hsu 1988	200	94	5	1.33×10^4	1.51
			10	2.66×10^4	3.2
			15	4.00×10^4	5.3
			20	5.32×10^4	7.69

Table 3.7.2 Magnitude of exciton shift of various well widths from literature

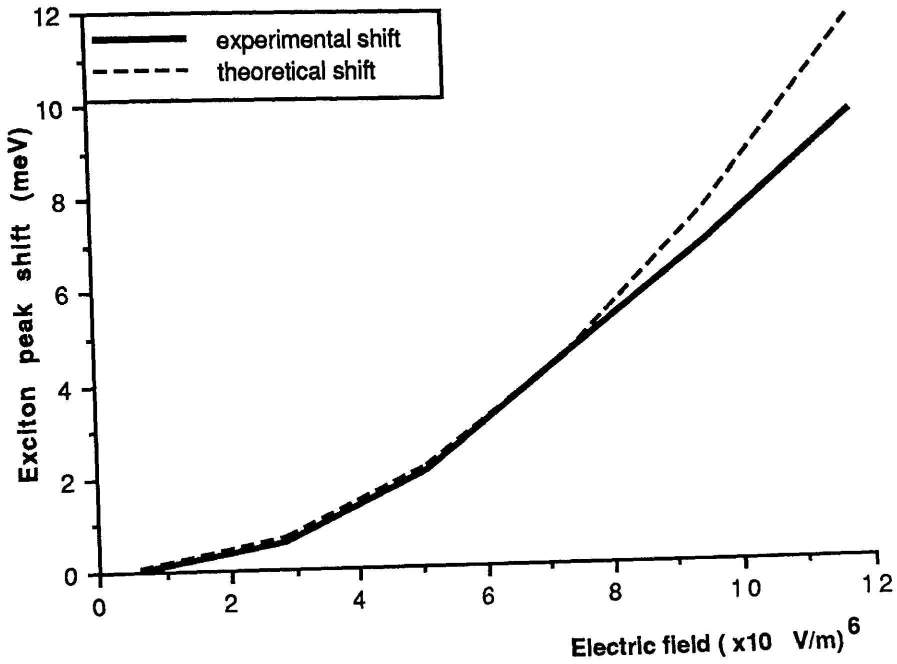

Figure 3.7.1 Comparison of the experimental shift of the exciton peak and the theoretical shift obtained using equation 2.49 for layer CB 2

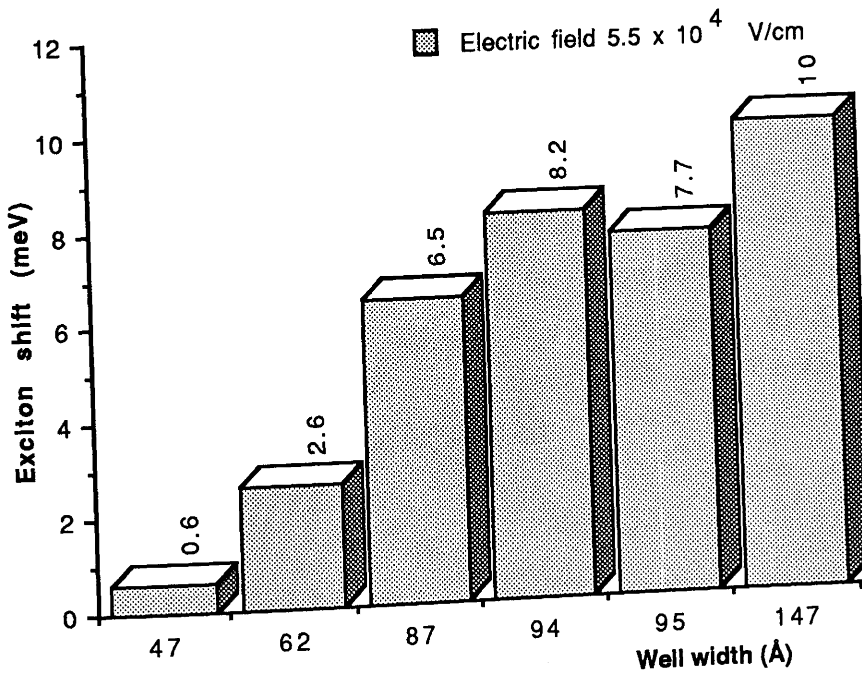

Figure 3.7.2 Magnitude of the shift of the exciton peak for various well widths from the literature at an electric field of 5.5×10^4 V/cm

3.8 Contrast ratio results for CB 2

The optical contrast ratio is simply the ratio of the transmitted intensity at zero bias to the intensity of the signal under reverse bias conditions. This can be expressed as either a simple ratio or quoted in dB:

$$\text{CONTRAST RATIO} = 10 \text{ LOG} [\text{ TRANSMISSION RATIO }] \text{ dB} \qquad 3.2$$

One of the main aims here was to improve upon the contrast ratio previously achieved with electroabsorption modulators operated in this mode, and Table 3.8.2 summarises a selection of contrast ratios from the literature. In order to do this the interaction length of the light in the modulating region was designed to be high. This was achieved by using 200 wells. The unfortunate consequence of this, since

$$F = \frac{V}{d} \qquad 3.3$$

is that if the interaction length (d) is increased to obtain the necessary electric field (F) for a sufficient Stark shift, then the applied voltage (V) must also be increased. A double penalty is incurred in this case since narrow wells have been used which require a higher electric field than wider wells to obtain a similar shift. The use of narrower wells should however maintain a large enough overlap between the electron and hole wavefunctions at higher fields to provide a device with a good optical contrast.

Table 3.8.1 summarises the maximum optical contrast ratio for various values of electric field and the wavelength at which they were obtained, for layer CB 2. The maximum contrast ratio (8.95 dB) was at a wavelength of 837.5 nm for a drive voltage of -25 V (11.8×10^4 V/cm). The contrast ratio as a function of wavelength at this electric field is shown on Figure 3.8.1.

Number of Wells	Well Width (Å)	Wavelength (Å)	Applied Voltage (V)	Electric Field (V/cm)	Contrast Ratio(dB)
200	62	8340	5	2.85×10^4	1.14
		8344	10	5.08×10^4	4.06
		8356	15	7.32×10^4	6.9
		8367	20	9.55×10^4	8.26
		8375	**25**	$\mathbf{11.8 \times 10^4}$	**8.95**
		8383	30	14.0×10^4	8.42

Table 3.8.1 Contrast ratios of the electroabsorption multiple quantum well modulator fabricated as outlined in Section 3.3

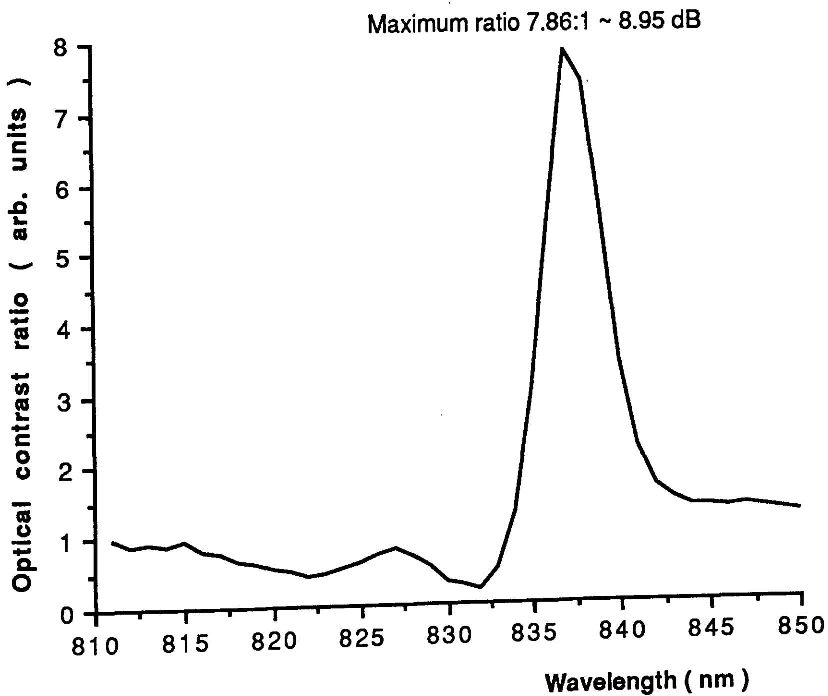

Figure 3.8.1 Variation of the contrast ratio with wavelength between an applied bias of -25 V and 0 V

The maximum contrast ratio, operating wavelength and drive voltages for a few modulators of similar design but with varying wavelengths obtained in recent years are given in Table 3.8.2. According to this table the best ratio obtained with this type of device in GaAs/AlGaAs was 10 dB at an electric field of 5.32 x 10^4 V/cm. [Hsu 1988] This device also employed the technique of increasing the interaction length of the light in the modulating region by using 200 wells. In this case a much higher absorption was obtained as the wells were 94 Å wide. Similarly a lower electric field was required, due to the width of the wells, but since the intrinsic region was so wide this required an applied voltage of -20 V. The other results quoted in this table do not achieve the same optical contrast as much smaller total thickness of absorbing material were used in the intrinsic region.

Reference	Number of Wells	Well Width (Å)	Applied Voltage (V)	Electric Field(V/cm)	Contrast Ratio(dB)	Wavelength (Å)
Whitehead	75	47	16	2.0×10^5	**1.76**	8167
1988			20	2.5×10^5	**2.8**	8289
	60	87	8	9.00×10^4	**2.0**	8565
			12	1.35×10^5	**3.4**	8473
	45	147	4	4.30×10^4	**0.78**	8711
			8	8.60×10^4	**2.50**	8618
Miller	50	95	4	4.12×10^4	**3.0**	8548
1985			6	6.18×10^4	**4**	8578
Hsu	200	94	15	4.00×10^4	**7.16**	8510
1988			**20**	$\mathbf{5.32 \times 10^4}$	**10**	**8510**

Table 3.8.2 Contrast ratios for similar multiple quantum well modulators from the literature

3.9 Insertion loss of CB 2

The insertion loss of a modulator device is a measure of the amount of light which is lost and consists of absorption and reflection losses : in systems applications it is vital to have low insertion losses. The insertion loss is defined as

$$\text{INSERTION LOSS} = 10\ \text{LOG}\ [\ 100\ /\ \text{HIGHER TRANSMISSION}\ ] \qquad 3.4$$

where the transmission is a percentage of the total amount of light incident on the device. The insertion losses were measured here for the device alone. The losses associated with the system were eliminated by recording the optical power spectrum of the system using a glass slide instead of a modulator device, as outlined in Section 3.4. The power recorded at the output detector with the glass slide in the set-up was then taken as the input power to the device. A similar recording with the modulator in place was taken at the output detector to determine the insertion loss of the device.

Figure 3.9.1 shows the insertion loss of the modulator as a function of wavelength. At the position of maximum optical contrast, 837.5 nm the insertion loss was found to be 4.9 dB. It is difficult to compare this figure with those quoted in the literature since often the measurements can include the total system losses, or are adjusted to account for the reflection losses associated with the interfaces of the device. One of the approaches to reducing the insertion losses is to use anti-reflection coatings on the device . This was not attempted as part of this work but could be included in future work arising from this project. Approximately 3 dB of the insertion loss can be ascribed to Fresnel reflection losses, so the use of A.R. coating would reduce the insertion loss to 1.9 dB.

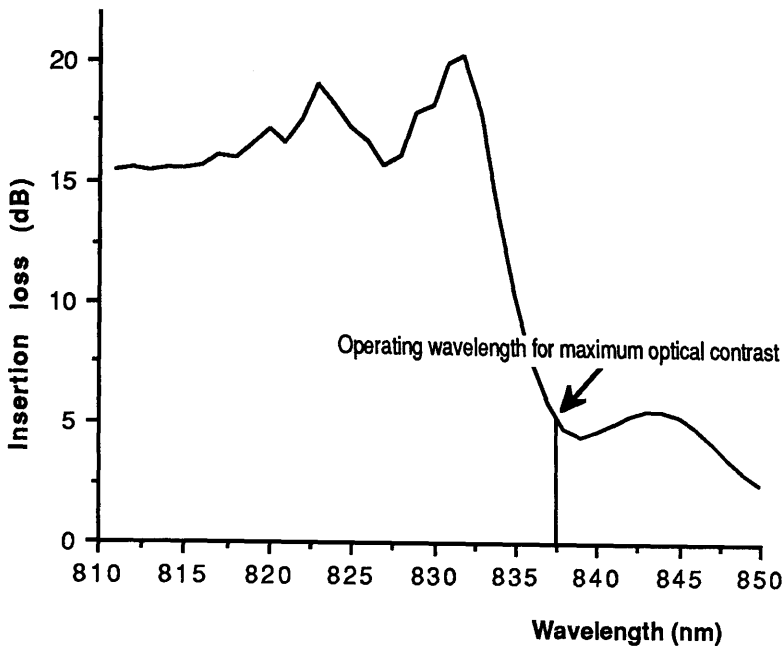

Figure 3.9.1 Insertion loss of the modulator device fabricated from layer CB 2

3.10 Speed of the device

The speed of electroabsorption modulators can be measured in many ways. Wood et al (1985) assessed the speed by measuring the modulator impulse response. The device was driven by 122 ps electrical pulses between 0.5 V and -8.5 V. At the optical output of the device a fast Si *p-i-n* photodiode detected the response of the modulator. By a process of deconvolution the actual speed of this device was found to be 131 ps.

The limit of the speed of QCSE devices has not yet been reached and is thought to be dominated by the RC time constant [Wood 1988] which is the time it takes to charge the capacitor of the diode. Thus these devices can have improved speeds of operation if the capacitance is kept low by fabricating small area devices with wider intrinsic regions, see equation 3.5.

The speed of the electroabsorption modulator fabricated as part of this work can be calculated theoretically by considering the capacitance of the device.

$$C = \frac{\varepsilon_r \varepsilon_o A}{d} \qquad 3.5$$

ε_r permitivity of GaAs

ε_o permitivity in a vacuum

A area of device

d width of intrinsic region

The calculated capacitance of the device alone was found to be 0.45 pF which corresponds to an RC time constant of 22 ps, when a 50Ω resistor is used. This equation does not take into consideration the capacitance associated with the electrical contacts to the device. It is therefore expected that it would operate slower than this estimation but by reducing the size of the device still faster operation could be achieved.

3.11 Calculation of the absorption coefficient

It is possible to obtain a value for the absorption coefficient by using the transmission data in Section 3.5. This can be calculated using the equation

$$\frac{I_t}{I_o} = \frac{(1-R)^2}{e^{\alpha d} - R^2 e^{-\alpha d}} \qquad 3.6$$

I_t is the transmitted light intensity through the sample

I_o is the incident light intensity

R is the reflection coefficient estimated to be 0.3

α is the absorption coefficient

d is the thickness of the absorbing region

A computer program was written to solve this equation to obtain alpha, by finding the roots of the resulting quadratic equation. Using this program the absorption coefficient as a function of wavelength for each of the applied voltages was obtained. Figure 3.11.1 presents the absorption coefficient for both the zero bias condition and the operating voltage -25 V.

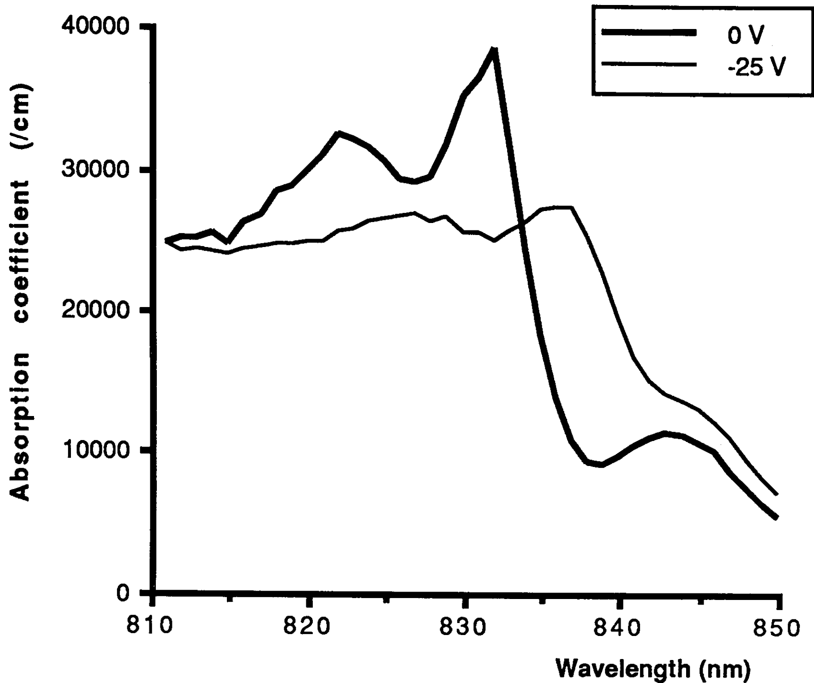

Figure 3.11.1 Absorption coefficient as a function of wavelength for 0 and -25 V

At the exciton peak at a wavelength of 832 nm the change in the absorption coefficient, $\Delta\alpha$, between the two spectra is 13611 cm^{-1}. The operating wavelength is chosen to be 837 nm where the maximum change in absorption is found to be 16579 cm^{-1}(see Figure 3.11.2). This value is much greater than found with devices employing bulk GaAs (280 cm^{-1}). For other GaAs/ AlGaAs modulators values of $\Delta\alpha$ of 15000 cm^{-1} have been observed. [Wood 1985] From Wood [1988] the contrast ratio for this type of device is defined as

$$R = \exp(\Delta\alpha L) \qquad 3.7$$

Therefore with the interaction length L in this case equal to 1.42 μm the contrast ratio, at 837 nm, is 7.8:1, as previously determined from the transmission results.

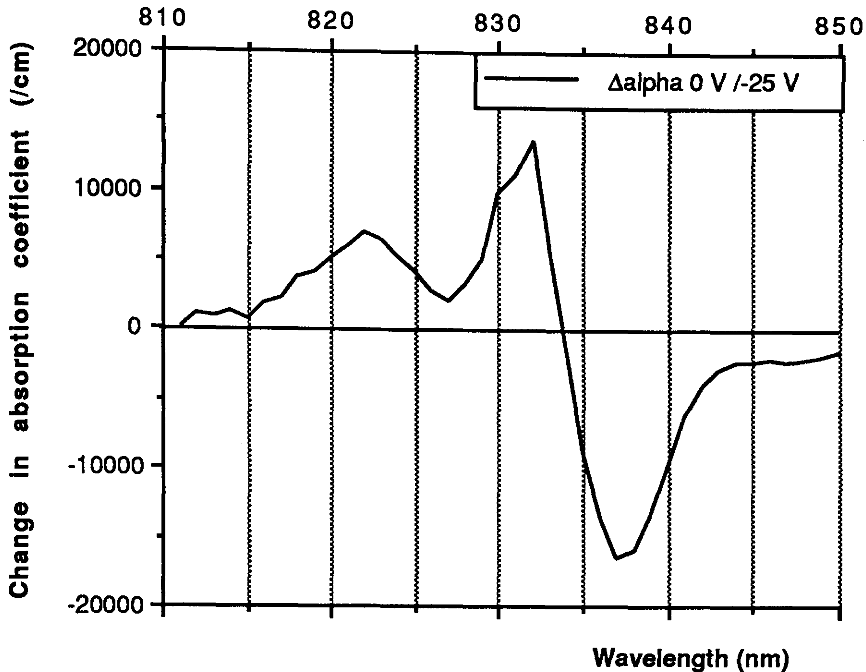

Figure 3.11.2 The change in the absorption coefficient between 0 and -25 V applied bias to CB 2

3.12 Discussion and conclusion

The fabrication of a single electroabsorption modulator was successfully completed using the GaAs/AlGaAs quantum well system. The intrinsic region of this device was configured from 200 x 62 Å wells and 50 Å barriers, giving a total thickness of 2.24 μm to provide high contrast ratios. The linewidth of the the heavy hole exciton peak was not significantly distorted by the large number of quantum wells, this being 8.9 meV at room temperature.

After the evaporation and testing of ohmic contacts the yield of devices with a larger reverse breakdown than -30 V was high, in the region of 85%, with the mesa-ing process to isolate the device after the evaporation of the metals being the most vital step in achieving a high yield of devices. The fabrication of these transmission modulators required that the substrate be removed. This process was carried out by using a combination of wet etchants and in the design of the layers AlGaAs graded from 30% to 50% aluminium was used to protect the other epitaxial layers from these etchants. The final device was mounted on a transparent glass substrate for support.

An automated computer system was set-up and used to assess the transmission characteristics of the modulator. This consisted of a white light source coupled through a monochromator and into the device. Data were collected using a germanium detector, the signal was amplified in a lock-in amplifier and subsequently analysed using the computer, where it was also necessary to normalise the data to eliminate the system response.

From these results at zero bias the heavy hole exciton peak was found to be at 832 nm which was consistent with theoretically calculated results. There was no significant Stark shift on the application of an electric field until the field induced in the device was greater than 5×10^4 V/cm. At fields higher than this the shift was quadratic with field as expected. The theoretically calculated shift and that experimentally observed were in good agreement at lower electric fields but above an electric field of 8×10^4 V/cm the experimentally observed shift was slightly less than that calculated using equation 2.49.

The insertion loss of the device was 4.9 dB at the wavelength of operation. This could be reduced to around 1.9 dB if the device was anti-reflection coated. Theoretically it is thought that the device is capable of operating at a speed of 22 ps a value which could be improved upon by fabricating devices with a smaller electrically active area.

A main aim of the design was to achieve high optical contrast. The maximum contrast ratio obtained was 8.95 dB for a drive voltage of -25 V. The use of narrow wells, which resulted in the exciton persisting even at high electric fields, and the large amount of absorbing material in the intrinsic region both contributed to this relatively high value for this type of modulator. The maximum change in the absorption coefficient was found to be 16579 cm^{-1} at a wavelength of 837 nm for a drive voltage of -25 V.

One problem with this device is the high drive voltage required to obtain the best performance. For incorporation in systems presently in use it is better to have devices which are compatible with TTL drive voltages for example. One solution to this is to change the layer design. This approach is taken in Chapter 5 where coupled well structures are investigated. Before investigating other designs of modulators isolated well devices of the type discussed in this Chapter were configured into a 4 x 4 array to form a spatial light modulator, as now discussed in Chapter 4.

Chapter Three : References

N. BOTTKA and L.D. HUTCHESON
'Analytical aspects of electroabsorption modulators'
Journal of Applied Physics Volume 46 Number 6
Page 2645- 2650
6 June 1975

J.C. DYMENT and F.P. KAPRON
'Extinction ratio limitations in AlGaAs electroabsorption light modulators'
Journal of Applied Physics Volume 47 Number 4
Page 1523- 1528
4 April 1976

D.S. CHEMLA and D.A.B. MILLER
'Physics and applications of excitons confined in semiconductor quantum wells'
Heterojunctions
Editors G. Margaritondo and F.Capasso

D.R.P. GUY and N. APSLEY
'Optical devices using III-V Quantum Wells and multilayers'
Proceedings of SPIE- The International Society for Optical Engineering
Quantum Well and Superlattice Physics Volume 861
16-20 November 1987

S. HONG and J. SINGH
'Effect of the lifting of Kramer's degeneracy on excitonic linewidths in quantum well optical modulators'
Applied Physics Letters Volume 53 Number 9
Page 731- 733
29 August 1988

D. MARCUSE
'Optimal electrode design for integrated optics modulators'
IEEE Journal of Quantum Electronics Volume QE-18 Number 3
Page 393- 398
3 March 1982

D.A.B MILLER, D.S. CHEMLA, T.C. DAMEN, A.C. GOSSARD, W. WIEGMANN, T.H. WOOD and C.A.BURRUS
'Electric field dependence of optical absorption near the band gap of quantum well structures'

Physical Review B Volume 32 Number 2
Page 1043- 1060
15 July 1985

J.S. ROBERTS, M.A. PATE, P. MISTRY, J.P.R. DAVID and R.B. FRANKS
'MOVPE grown multiple quantum well pin diodes for electro-optic modulators and photodiodes with enhanced electron ionisation coefficient'
Journal of Crystal Growth Volume 93 Page 877-884
1988

P.J STEVENS, M.WHITEHEAD, G. PARRY and K. WOODBRIDGE
' Computer modeling of the electric field dependent absorption spectrum of multiple quantum well material'
IEEE Journal of Quantum Electronics Volume QE-24 Number 10
Page 2807-2016
October 1988

G.E. STILLMAN, C.M. WOLFE, C.O. BOZLER and J.A. ROSSI
'Electroabsorption in GaAs and its application to waveguide detectors and modulators'
Applied Physics LettersVolume 28 Number 9
Page 544-546
1 May 1976

M. WHITEHEAD, G.PARRY, K. WOODBRIDGE, P.J. DOBSON and G. DUGGAN
'Experimental confirmation of a sum rule for room-temperature electroabsorption in GaAs/AlGaAs multiple quantum well structures'
Applied Physics LettersVolume 52 Number 5
Page 345- 347
1 February 1988

D.R. WIGHT, P.C. ALLEN, J.W.A. TRUSSLER, D.P. COOPER, D.J. ESDALE and P.E. OLIVER
'Ultra high speed micro-optical modulators in GaAs: The TEAM and the LEAM'
Institute of Physics Conference Ser. No. 79 Chapter 12
Page 667-672
1985

D.R. WIGHT, A.M. KEIR, G.J. PRYCE, J.C.H. BIRBECK, J.M. HEATON, R.J. NORCROSS and P.J. WRIGHT
'Limits of electroabsorption in high purity GaAs and the optimisation of waveguide devices'
IEE Proceedings Volume 135 Part J Number 1
Page 39- 44

February 1988

T.H. WOOD
'Direct measurement of the electric field dependent absorption coefficient in GaAs/AlGaAs multiple quantum wells'
Applied Physics Letters Volume 48 Number 21
Page 1413- 1415
26 May 1986

T.H. WOOD, C.A. BURRUS, D.A.B. MILLER, D.S. CHEMLA, T.C. DAMEN, A.C. GOSSARD and W.WIEGMANN
'High-speed optical modulation with GaAs/AlGaAs quantum wells in a p-i-n diode structure'
Applied Physics Letters Volume 44 Number 1
Page 16- 18
1 January 1984

T.H. WOOD
'Multiple Quantum Well waveguide modulators'
Journal of Lightwave Technology Volume 6 Number 6
Page 743- 757
June 1988

CHAPTER FOUR
SPATIAL LIGHT MODULATOR

Introduction

One of the devices lacking in the field of optoelectronics and hindering the progress towards the optical computer is the Spatial Light Modulator [Feitelson 1988] This is a device that is capable of modulating the cross section of a beam.

In an attempt to obtain fast SLM's which can be both electrically and optically addressed, the QCSE is exploited. Having successfully fabricated single electroabsorption modulators in the multiple quantum well layer CB 2, an array of such devices was fabricated.

As will be outlined in this chapter, this required changes to the fabrication process used for the single modulators. The fabrication and results obtained for the SLM are presented and discussed later in this chapter but the initial discussion is concerned with the device applications.

4.1 Spatial light modulator

A spatial light modulator (SLM) is a device that in some way modulates a cross section of a beam of light. A very simple example of this is a photographic transparency. [Feitelson] After passing through a transparency, different areas in the beam's cross section have different intensities, thus the beam has been modulated. Various applications are possible using this device.

4.2 Applications of spatial light modulators

To date the main use of SLM's has been for the displaying of large television images and thus the refresh rate required is slow, typically 30 Hz. Applications in optical computing require much faster devices and the SLM is required in a number of crucial roles. For example, the conversion of an incoherent image into a coherent one requires the use of an input transducer where the intensity of the input image is analysed and used as an SLM, which modulates a coherent beam of light. They can also be used as spatial filters, which eliminate the transmission of higher order diffraction radiation within an optical system, or for two dimensional Fourier Transform optical processing, i.e. for image processing or contrast enhancement. Other potential applications include spectrum analysers for pattern recognition and analog signal processing. The most immediate application of the device designed and tested here is for the routing of optical signals in a communications system. The array of elements, each element equivalent to one of the single devices already assessed, can be coupled to a bundle of fibres for this purpose. Modifying the design of the device allows the possibility of the other applications which have been discussed.

Systems which utilize optical fibres and semiconductor lasers, require SLM's and lasers which work at the same wavelength. Semiconductor devices have the advantages of potential for integration and inherent speed. In particular integration of QCSE modulators into an SLM array is feasible. Before the design of the array of modulators is discussed, a literature review of recent SLM's is presented. These devices are fabricated within a number of different material systems depending on the application and type of modulation which is required.

4.3 Literature review : The spatial light modulator

Presently, SLM's for use in coherent optical signal processing and large screen projection displays are available from manufacturers such as Marconi. These use a silicon vidicon microdiode array as a photoconducting layer, and a dielectric mirror provides optical isolation between the photoconductor layer and a liquid crystal layer. The read beam passes through the liquid crystal and is reflected by the dielectric mirror. This can then be spatially modulated by a write beam incident on the photoconductor. This type of device is capable of operating with a rise time of 25 ms and a fall time of 35 ms.

SLM's based on a liquid crystal television have also been under investigation for use in optical data processing. [Mok 1986]. These can be both electrically and optically addressed but, because of thickness variations over the aperture of the screen of the devices, their usefulness for coherent optical processing is limited. One device is a 5.4 cm x 4.4 cm screen consisting of a two dimensional mosaic of individually addressable liquid crystal cells containing 90° nematic liquid crystals sandwiched between two glass plates. The plates have horizontal and vertical transparent electrodes on the inner surfaces. Two linearly polarised sheets are glued to the outer surfaces of the glass plates with the polarisation axes parallel. When there is no electric field the plane of polarisation for linearly polarised light is rotated through 90° by the twisted liquid crystal molecules and no light is transmitted through the second polariser. In the presence of an electric field the twist and tilt of the liquid crystal is altered resulting in the transmission of a controllable and variable fraction of the light. The major drawback of this device was phase non-uniformity due to the poor quality of the polariser sheets and work is progressing to eliminate this problem.

In GaAs based systems the most popular approach has been the development of arrays of charge coupled devices. Early versions of this device were developed in bulk GaAs [Kingston 1982 and 1984]. Charge coupled devices are essentially analog shift registers. The basic device consists of a closely spaced array of electrodes on a continuous insulator layer that covers the semiconductor substrate. The electrodes are all maintained at the same potential except one which is placed at a higher potential. Hence material beneath this electrode is depleted more than beneath

the other electrodes and a potential well for minority carriers is formed there. These carriers can be clocked around the array by varying the potential of neighbouring electrodes. Since GaAs has a high electron mobility the transit times can be made relatively small in CCD's at low E-fields, hence obtaining high speed operation with minimum power dissipation.

The function of the CCD in an SLM is to control the electric field in the CCD channel, thus modifying the optical absorption. The basis of operation is the Franz-Keldysh effect, outlined in Chapter 2, where transmission at lower photon energies than the bandgap both through and along the structure of the CCD is controlled by the signal charge in the wells, through the change in the electric field with charge. The modulation depth obtained for light propagation perpendicular to the MQW structure is only 10 - 20 %. This has been improved to a depth approaching 100 % by using an optical waveguide beneath the gate electrodes for one-dimensional operation. Kingston [1984] predicts that high speed operation (as fast as 1 GHz) and excellent optical uniformity because of the single crystal structure used are possible. To improve upon the contrast ratio for two dimensional operation attention turned to MQW systems.

A CCD device in GaAs / AlGaAs multiple quantum wells has been developed by Nichols [1988]. Here the CCD structure was used to modulate the electric field across the MQW. The basis of operation is the QCSE which is fundamentally fast, as outlined in Chapter 2. The CCD's are capable of high speed clocking, ~GHz, with low power consumption and the charge patterns can be established by clocking charge into the device from an electrical input, or they can be generated directly in each CCD well by optical means. The latter method is particularly fast because all of the CCD wells can be illuminated simultaneously. A contrast ratio of 1.45 : 1 was obtained at 847 nm for an input pulse of 10 V.

The lattice-matched InP/GaInAs material system has also been utilised to fabricate a two-dimensional spatial light modulator [Rejman-Greene 1988]. Each element in a 3 x 3 array was electrically accessed by individually wire bonding to them by means of a thermocompression technique. Modulation depths were not quoted but the variation of the absorption edge at zero bias was given as 4 nm over the whole MBE

grown array.

A more efficient method of electrically accessing an SLM may be to address each pixel individually. The method proposed to do that is to use a two dimensional array of electrodes and thus specify the pixel required to be "on". This may cause some problems as other elements in close proximity would also be affected by the electric field induced in a particular element. However as demonstrated by [Wood 1987] when a 2 x 2 array of such elements were tested the electric field in the nearest neighbours of those accessed was found to be 200 times less than that in the active element. Bonds were forged to individual elements in order to achieve electrical access making the device unfeasible for large arrays. A contrast ratio of 1.45 : 1 for a drive voltage of 6 V was obtained and the speed of operation was estimated to be 130 ps.

4.4 Design and operation of the device

The fabrication of a Spatial Light Modulator was based on the single electroabsorption modulator in Chapter 3. Layer CB 2 was fully characterised establishing its suitability for use in the SLM. Thus with the material system, GaAs/AlGaAs, and mode of operation, the QCSE, of the device selected, the design of the array was undertaken.

The main objective of an SLM is to be able to modulate a cross section of an optical beam, that is affect various parts of the beam differently. In order to do this an array of electroabsorption modulators can be used, where each element can be individually accessed, both electrically and optically. This requires the elements to be electrically isolated from each other which can be achieved by ion implantation or, as in this case, dry-etching. It is undesirable and extremely difficult with present bonding techniques, particularly for larger arrays, to electrically contact each element in the array individually, therefore the use of a line addressing system was employed.

A 4 x 4 array of electroabsorption modulators was fabricated as outlined in Section 4.5. The elements were isolated from each other by a dry-etching process and held in place by a layer of polyimide. The polyimide performs two functions: first to planarise the device for the evaporation of the top ohmic contacts and

secondly to electrically isolate the *p* and *n* ohmic contacts from each other.

Two line addressing contacts were used for the top and bottom of the device. These were oriented 90° to each other forming a grid, thus individual elements could be biased as required. The electrical circuit of the SLM is shown in Figure 4.4.1. The diodes are reverse biased for operation, and from this circuit it is possible to determine the effect of a voltage applied to one element on the other elements in the array.

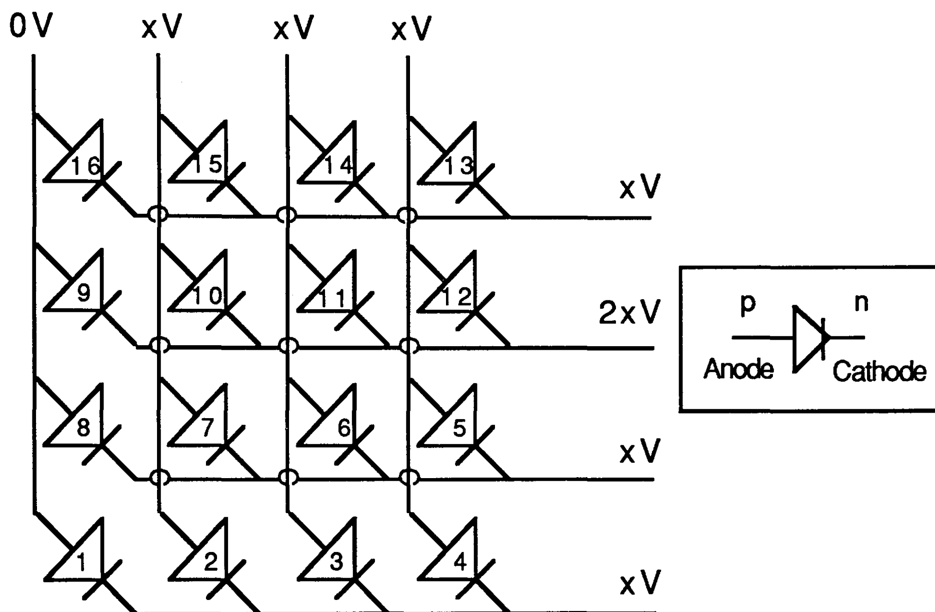

Figure 4.4.1 Electrical equivalent circuit of the diode array

Consider Figure 4.4.1 where in order to apply a reverse bias to the diodes it is necessary to maintain the required *p* line contact at a lower potential than the *n* line contact. Thus to select element 9 the first top left contact is biased at 0 V. Each of the other *p* lines are then biased with *x*V. Similarly the *n* line contact of element 9 is biased with 2*x*V, while the other *n* line contacts are biased with *x*V. Therefore while a bias of 2*x*V is applied to element 9 all the other elements are only biased with either 0V or *x*V. This gives a minimum ratio of 2:1 between selected and non-selected elements which, for the operating voltage of these devices, provides an adequate optical contrast ratio, as shown later in this chapter.

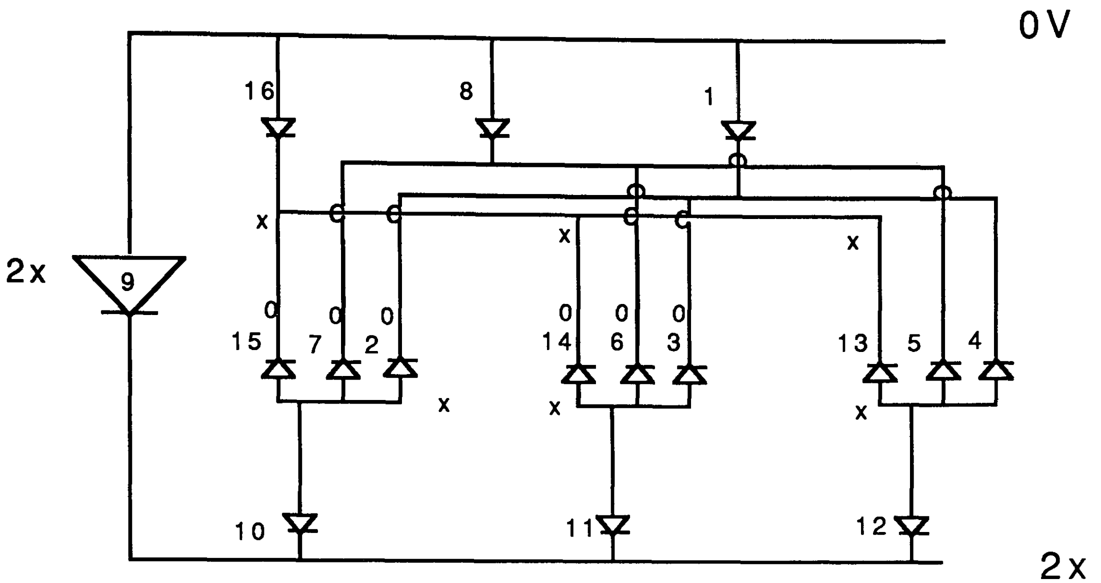

Figure 4.4.2 Diode array with an applied voltage to element 9

4.5 Fabrication of the spatial light modulator

The fabrication of the spatial light modulator required many changes to the process steps followed for that of the single modulator because the design required that each element be electrically isolated from the others. It was essential to fabricate the device such that a short circuit could not occur between the top and bottom ohmic contacts. A summary of the fabrication steps can be seen in Figure 4.5.1, but a detailed description of each step is presented below.

4.5.1 Dry-etching of the SLM elements

The first part of the process, as before, was to ensure the sample was clean using acetone, methanol and trichloroethelyne. The modulator elements were initially defined using photolithography, and pillars were formed using dry-etching. This allowed polyimide to be put down and cured and avoided taking the structure to high temperatures later in the process. The resulting pillars are shown in Photograph 4.1.

For the process of defining the elements wet-etching techniques are unsuitable, due to limitations including selective etching of the crystal planes and undercutting. For smaller elements than those defined here undercutting could lead to the complete

removal of the top layers. Also if shallow etch depths are needed then it is difficult to control wet-etching accurately. The dry-etching method used reactive-ion etching in an atmosphere of $SiCl_4$.

RIE uses the kinetic energy of an inert gas ion to physically remove material. [GaAs school 1987] A beam of ions is generated in a gun assembly consisting of a suitable electrode and source of inert gas. The sample is placed on an electrode which obtains a dc bias from the R.F. power used, and this bias results in directionality of the etching of the sample. By varying the gas pressure and the RF power the etch rate and direction can be controlled. A complete description of the dry-etching system and technique employed is given by Thoms [1986].

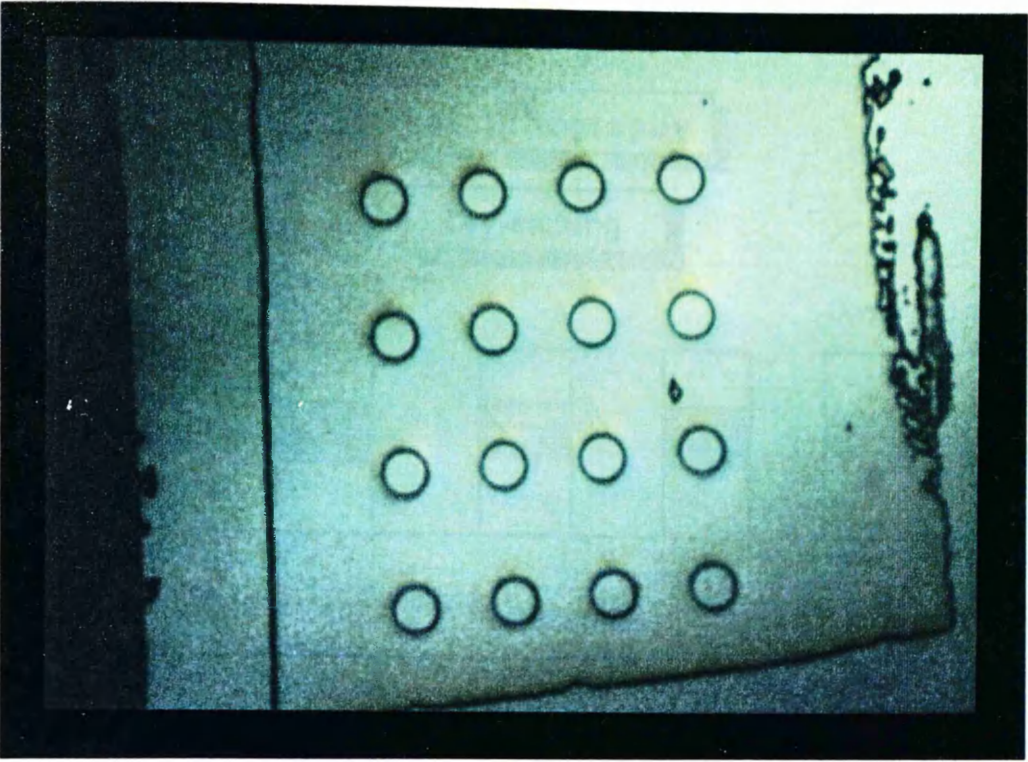

Photograph 4.1 The SLM elements are defined using dry-etching techniques

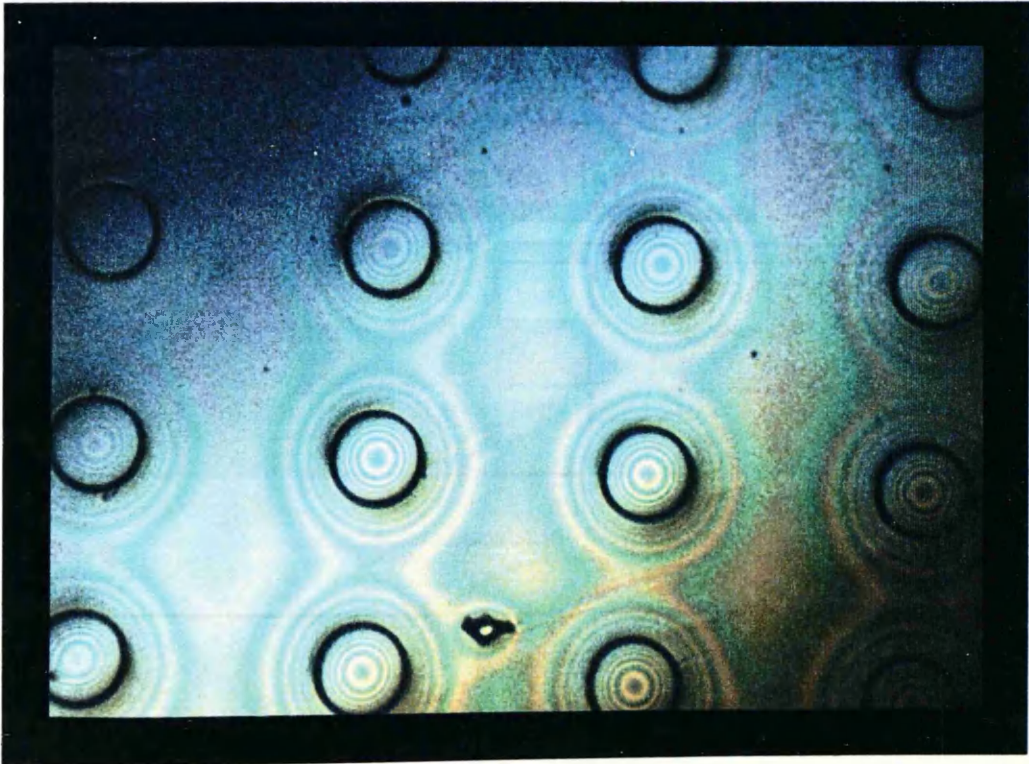

Photograph 4.2 Polyimide is spun onto the device

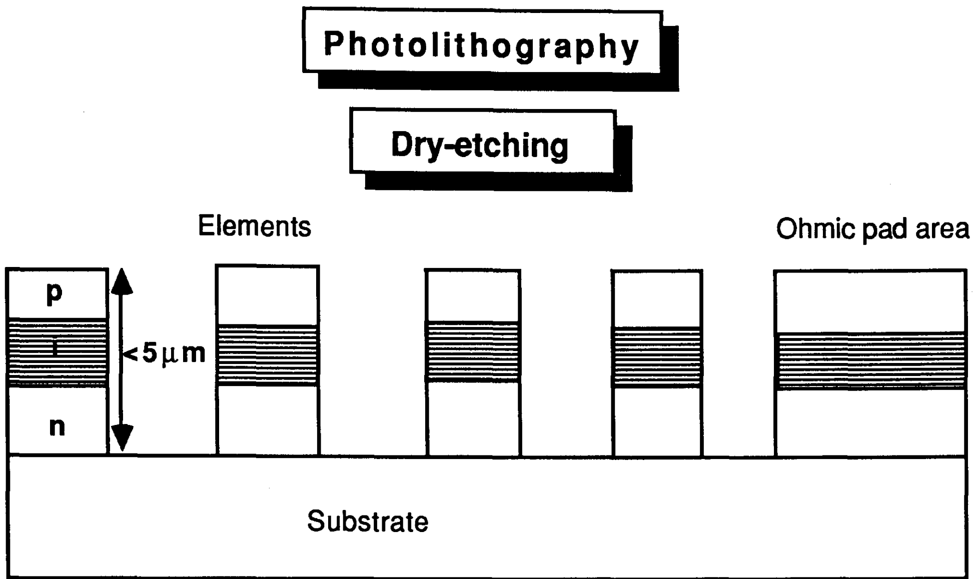

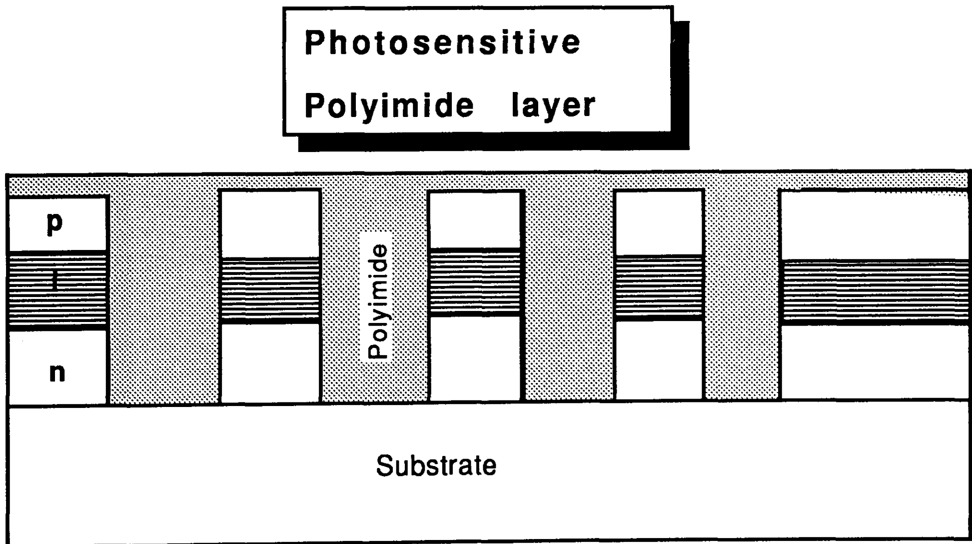

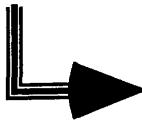

Figure 4.5.1.a Fabrication of a spatial light modulator

Developing

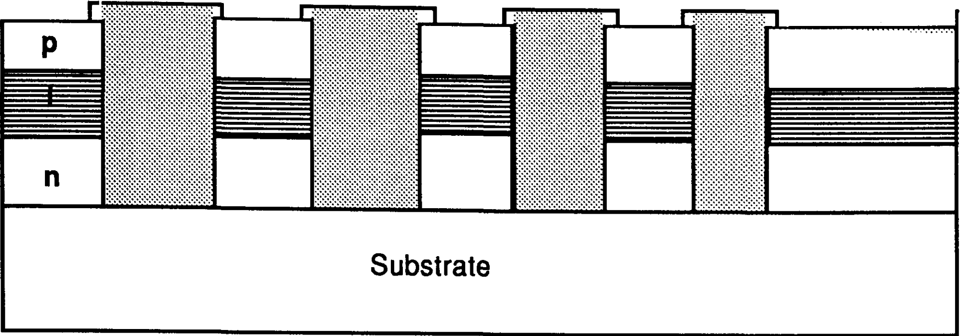

Evaporation of *p*-ohmic contacts

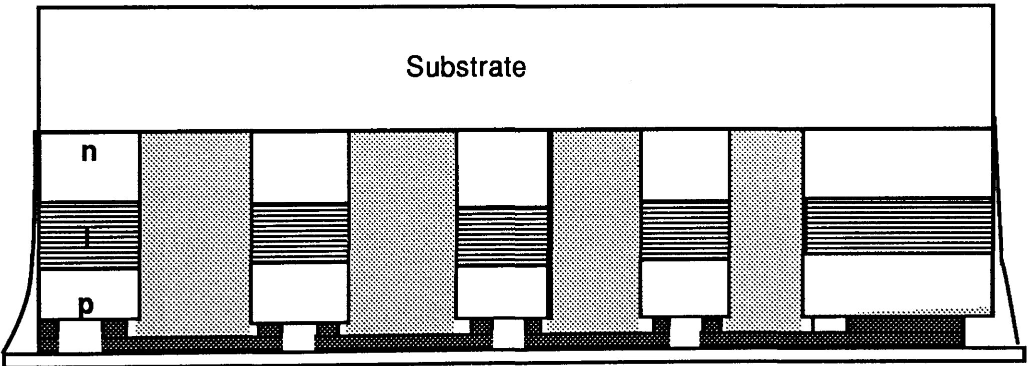

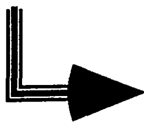

Figure 4.5.1.b Fabrication of a spatial light modulator

Wet-etching : removal of GaAs substrate

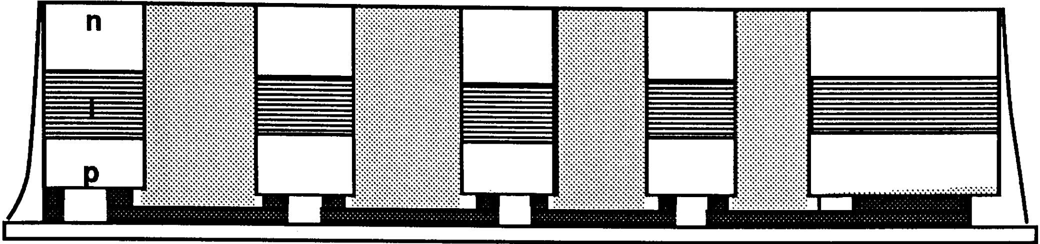

Transparent substrate for support

Evaporation of *n*-ohmic contacts

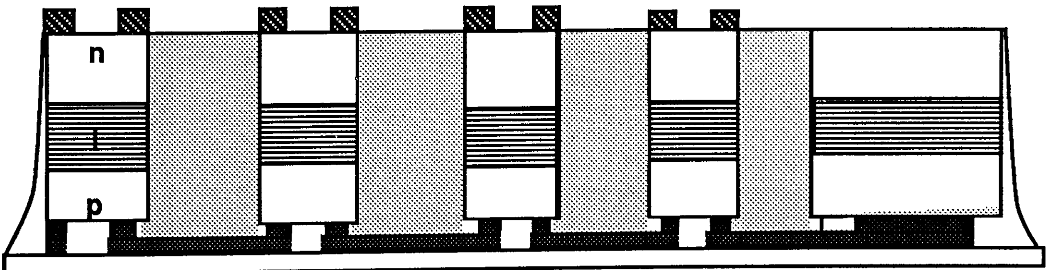

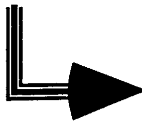

Figure 4.5.1.c Fabrication of a spatial light modulator

Dry-etching for access to *p*-ohmic contact pads

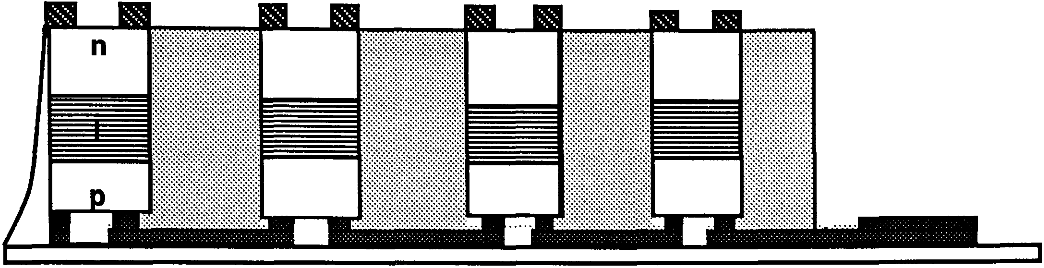

Figure 4.5.1.d Fabrication of a spatial light modulator

The use of dry-etching allows good control of the etch depth allowing the *n*-ohmic contact to be exposed in the etched areas.

Each element was 100 μm in diameter, as shown in Figure 4.5.2. There was also an area of the crystal which was not removed by etching, as shown, where the *p*-ohmic contacting pads were to be placed. If these are evaporated onto this region rather than the polyimide area it is easier to access them at the end of the fabrication process. After dry-etching, the device was cleaned with acetone to remove the resist. A polyimide layer was now spun onto the device, as shown in Photograph 4.2 and 4.3.

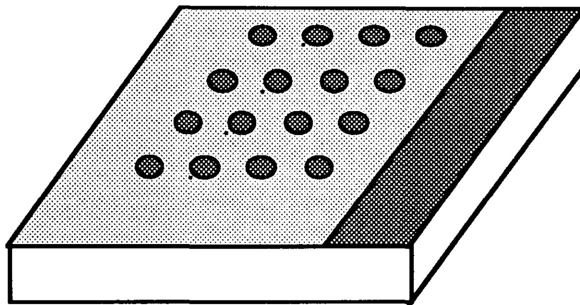

Figure 4.5.2 Defining of the SLM elements by dry-etching

4.5.2 Photosensitive polyimide

The use of the polyimide strengthens the device in many ways. Originally it was used to isolate the elements from each other by planarising the device and allowing contacts to be evaporated onto it, while the material between each individual element could then be removed to electrically isolate the elements. This it does successfully but in the process provides a strong skin which holds the elements in the array when the substrate is removed. It also allows the *n*-ohmic contact to be isolated from the top *p*-ohmic as it fills in the area between them, see Photograph 4.3.

A number of polyimides were tested for this purpose, with the undesirable remnants being removed by plasma ashing. This technique was unreliable as a skin of polyimide was always left on top of the sample after the ashing step, preventing a

good contact to the device. If this was successfully removed then, after the curing process, the polyimide would shrink and leave the device susceptible to short circuits down the side walls of the elements. A few types of liquid glass were also unsuccessfully employed because a technique to remove the undesired areas of the glass could not be found. These problems were overcome by using a photosensitive polyimide.

The polyimide employed was the Hitachi photosensitive polyimide pl-2035, together with Hitachi pl 2035 developer. The polyimide was used as a normal negative photoresist. The polyimide adheres well to the etched surface and, even though it does shrink slightly on curing, still coats the side walls well enough to avoid any problems. A double precaution was taken by designing masks which enabled a 'lip' to be left over the top of the etched pillar to compensated for the shrinking process.(Photograph 4.4)

The polyimide was applied by spinning at a speed of 4000 revolutions per minute providing a layer of 4.2 μm. This thickness filled the etched region of the device, as shown in Figure 4.5.3.

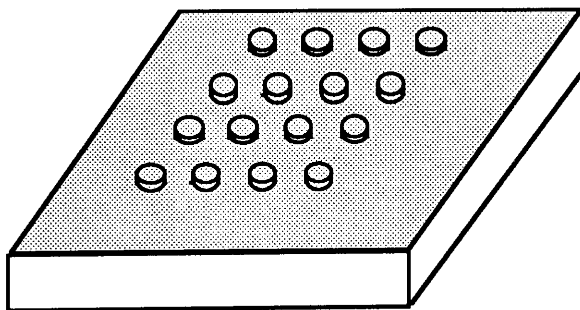

Figure 4.5.3 A layer of polyimide is spun onto the device

After a short bake, 90 seconds, in an oven at a temperature of 90°C, the semi-cured polyimide was exposed to ultra violet light via a photolithography mask for 4 seconds. The next step was to develop the sample in developer for 30 seconds and spin it off, followed by a further 40 seconds developing and a final 6 seconds rinse in ethanol. These times are not crucial since the polyimide is a negative resist and

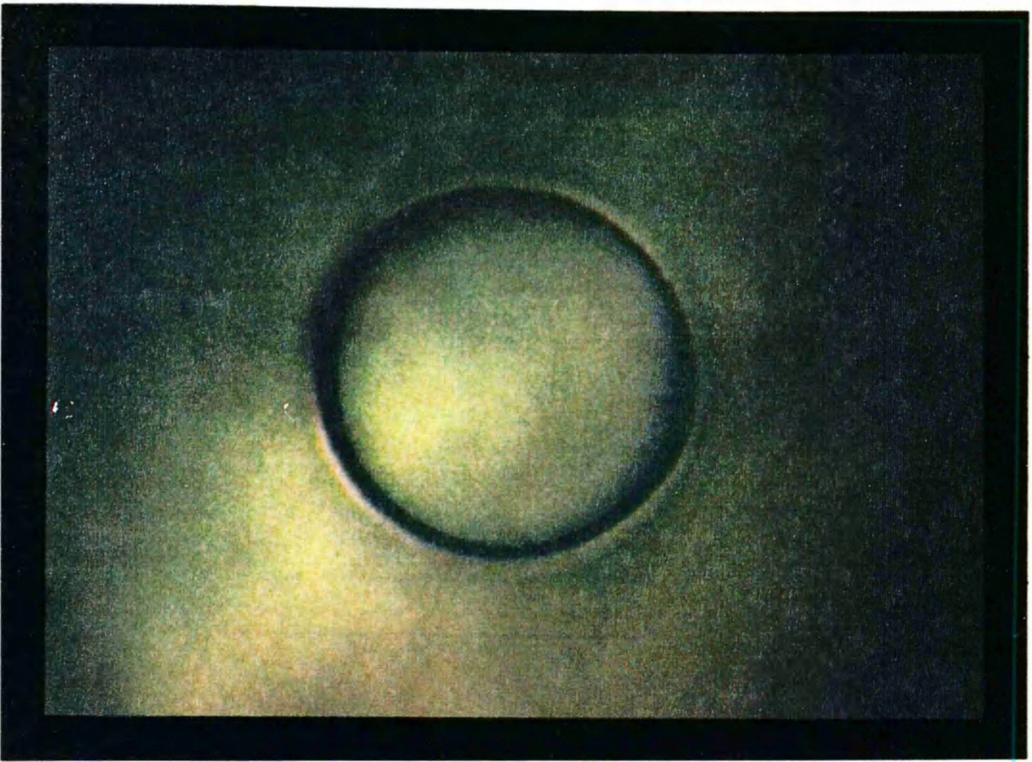

Photograph 4.3 The polyimide covers the elements and fills the area between each

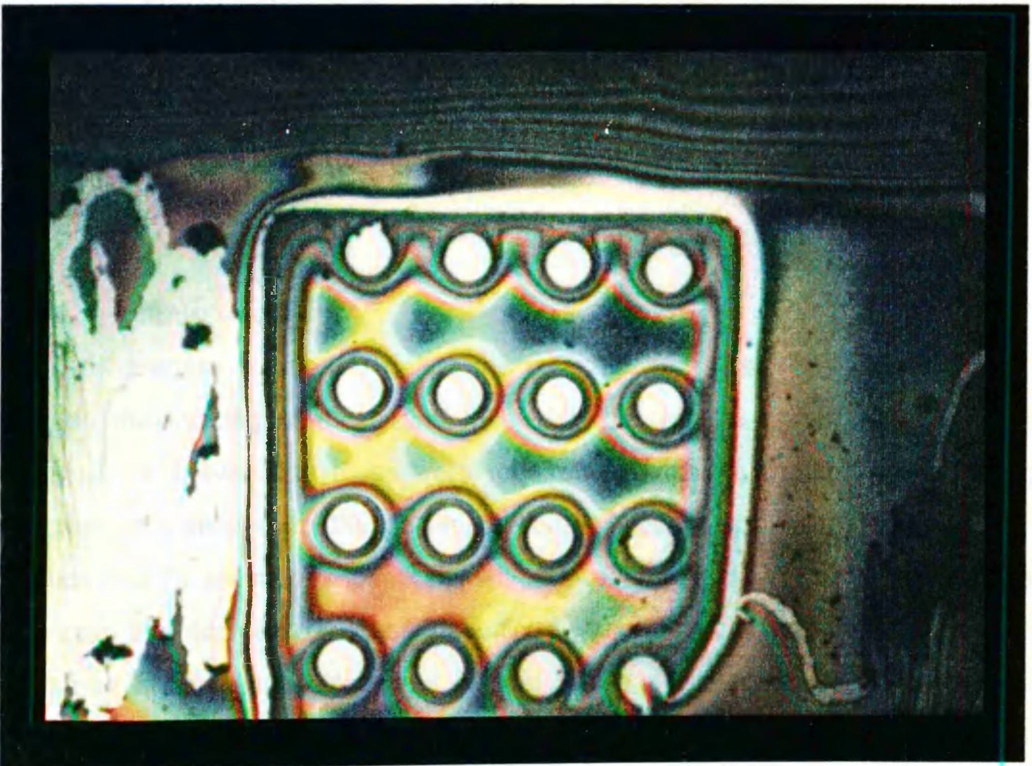

Photograph 4.4 The polyimide is exposed to UV radiation and developed

negative resists are not sensitive to over developing. As shown in Figure 4.5.4 the areas left without polyimide were the top of the elements and the side area where the *p*-ohmic contacting pads were subsequently evaporated.

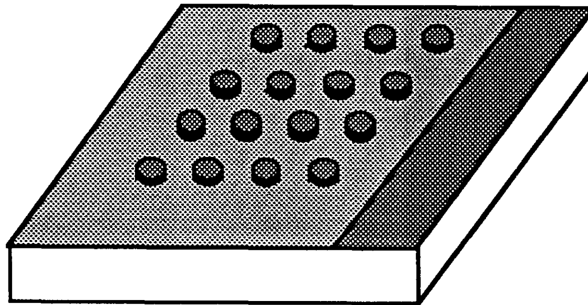

Figure 4.5.4 The polyimide is exposed and developed

A four stage curing process took place in a programmable oven. The first temperature was 100°C for a period of 30 minutes followed by successive increases in temperature to 200°C (1hr), 250°C (0.5hr) and, finally, 350°C (0.5hr). Exact times did not appear to be critical but the device had to be taken to a final temperature of 350°C to cure the polyimide fully. The sample was then cooled over a period of 30 minutes in preparation for the photolithography to define the *p*-ohmic contact lines.

4.5.3 *p*-ohmic contacts

A lift off process is used to define the *p*-ohmic contacts. The only differences between the forming of these and those for the single element was that longer exposure and developing times were required to account for the reduced sample reflectivity resulting from the polyimide layer. These times were found to be 10 seconds and 75 seconds respectively, with the resulting pattern shown in Photograph 4.5. Again the chlorobenzene soak technique was utilised to help the lift-off process. The same metals and thicknesses utilised previously (Section 3.3), were used to form the *p*-ohmics. The resulting line addressing contacts are shown in Figure 4.5.5.

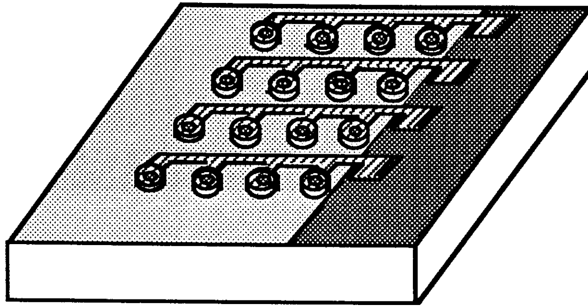

Figure 4.5.5 Top *p*-ohmic contacts of the SLM (see also Photograph 4.6)

4.5.4 Chemical wet-etching

After mounting the device on a glass slide with index matching epoxy, the substrate was completely removed using the selective wet-etch technique described in Section 3.3.5.

This time it was much easier to determine that the etch had reached the epitaxial layers as the pillars had been etched completely through the epitaxial layers. Therefore, on reaching the back etch stop layer the elements became visible, as shown in Figure 4.5.6. The polyimide is inert and was not affected by the etch.

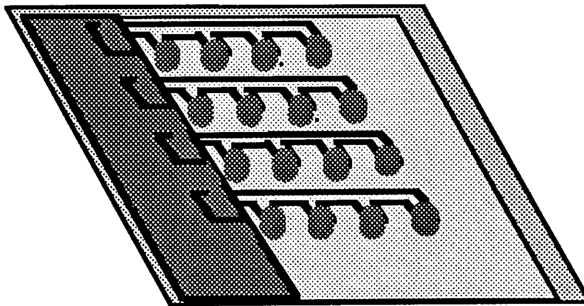

Figure 4.5.6 The substrate of the crystal is removed to reveal the modulator elements

4.5.5 *n*-ohmic contacts

The sample was then cleaned as before and prepared for the evaporation of the *n*-

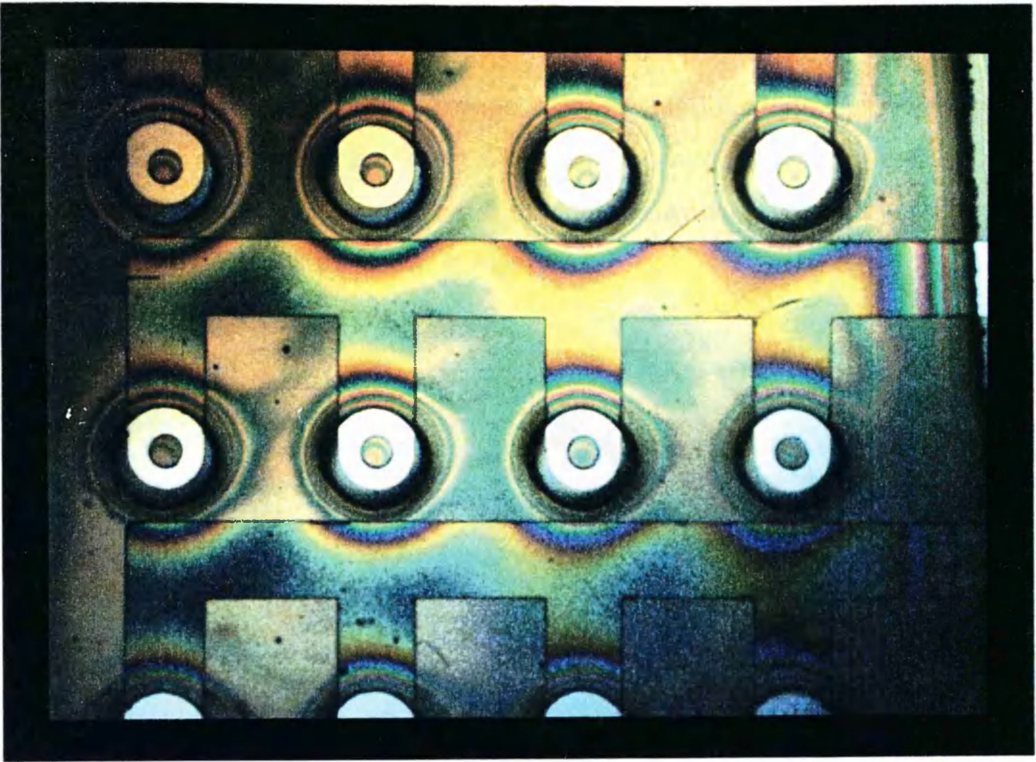

Photograph 4.5 Photoresist is used to define the top *p*-ohmic contacts

Photograph 4.6 The top *p*-ohmic contacts are evaporated onto the device

ohmic contacts. In the following processes it was required that very little acetone was used as it attacks the polyimide. The *n*-ohmic contacts were defined 90° to the top *p*-ohmic contacts forming the electrical network which allowed individual elements to be selected, as shown in Figure 4.5.7.

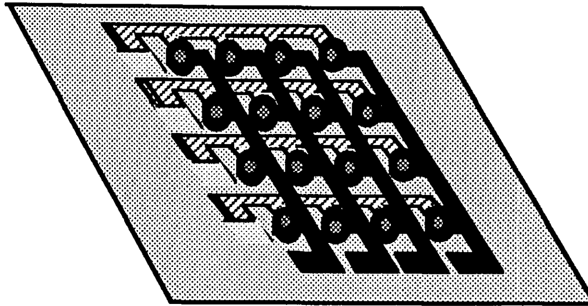

Figure 4.5.7 The *n*-ohmic contacts are aligned perpendicularly to the *p*-ohmic contacts and the remaining epitaxial layers removed from the top of the *p*-ohmic contacting pads (see also Photograph 4.7-4.9)

Again it was necessary to adjust the photolithography parameters to account for the reduction of light involved in the exposure technique from back scattering. This was due to the absence of a reflecting substrate and also to the polyimide layer which is strongly absorbing at UV wavelengths. One method of compensating for this was to place a highly reflecting slide under the sample, such as a glass slide covered in aluminium. This increased the back scattering and reduced the exposure time. This was desirable as it minimised the vibrational effects otherwise associated with long exposure time, and so allowed better definition of the pattern. Again the ability of the mask aligner to transmit infra-red light through the device allowed the contacts to be very accurately aligned to each other, although due to reflections from the slide visibility was poor. A chlorobenzene soak was also employed to aid the process of lift-off after the contacts were evaporated.

The *n*-ohmic was evaporated as outlined in Section 3.3.6 and after the lift-off process the contact was annealed for 60 seconds at 350 ^{o}C.

The last stage in the process was to remove the remaining epitaxial layers from the

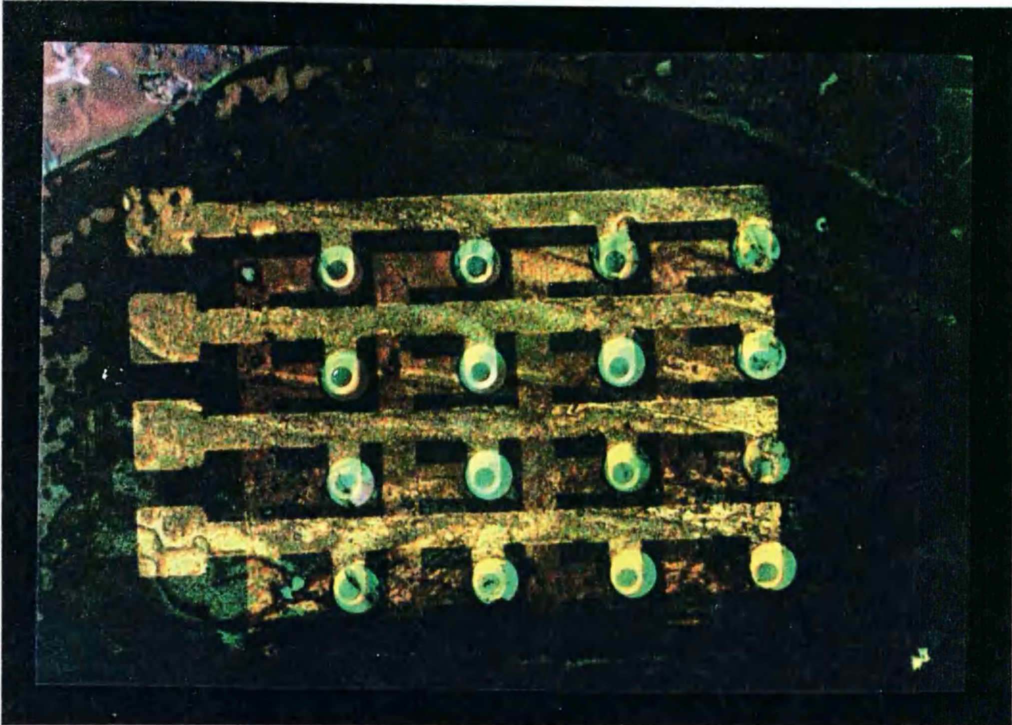

Photograph 4.7 After the substrate is removed the bottom *n* - ohmic contacts are evaporated

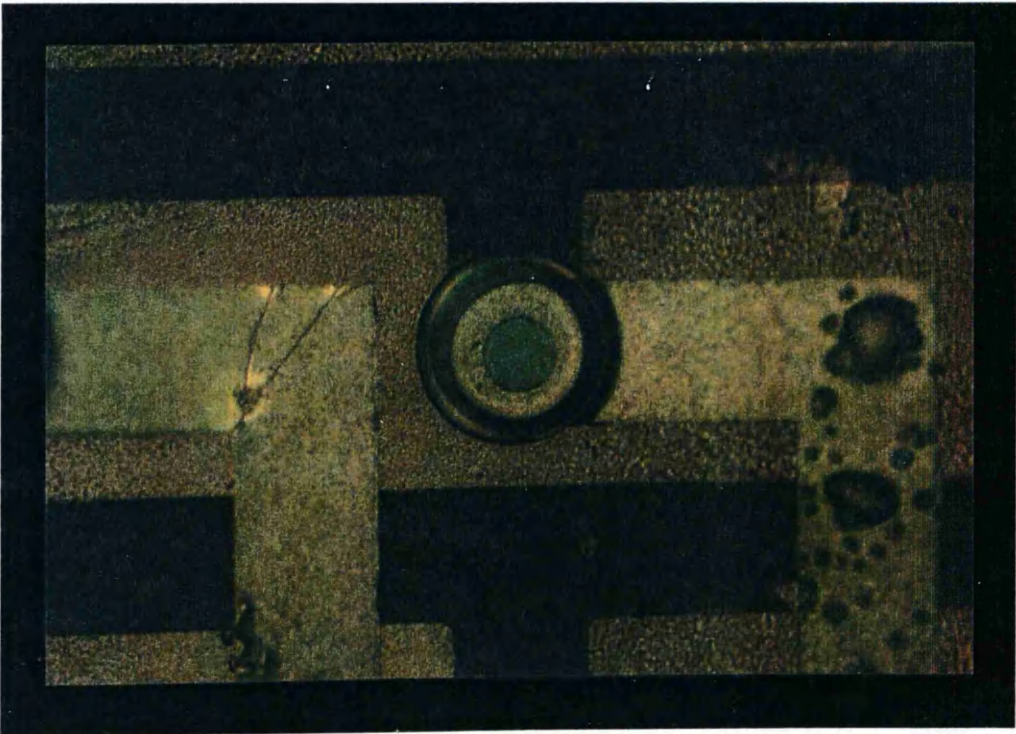

Photograph 4.8 Back view of the *n* -ohmic and *p* -ohmic contacts aligned to an element of the SLM

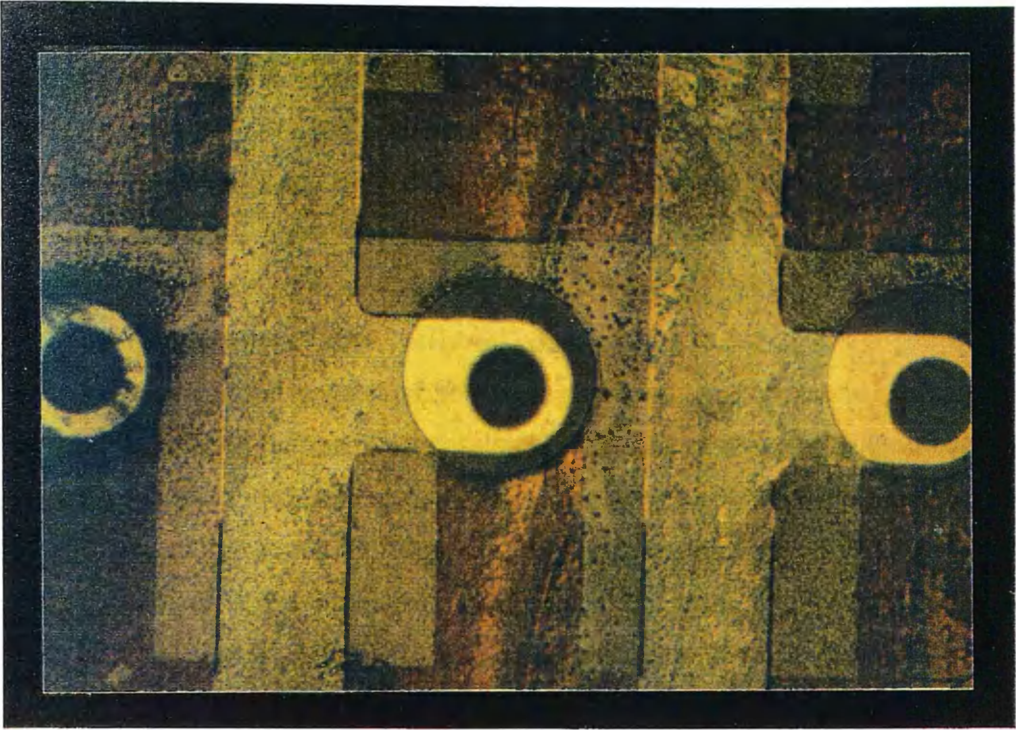

Photograph 4.9 Top view of elements in the device

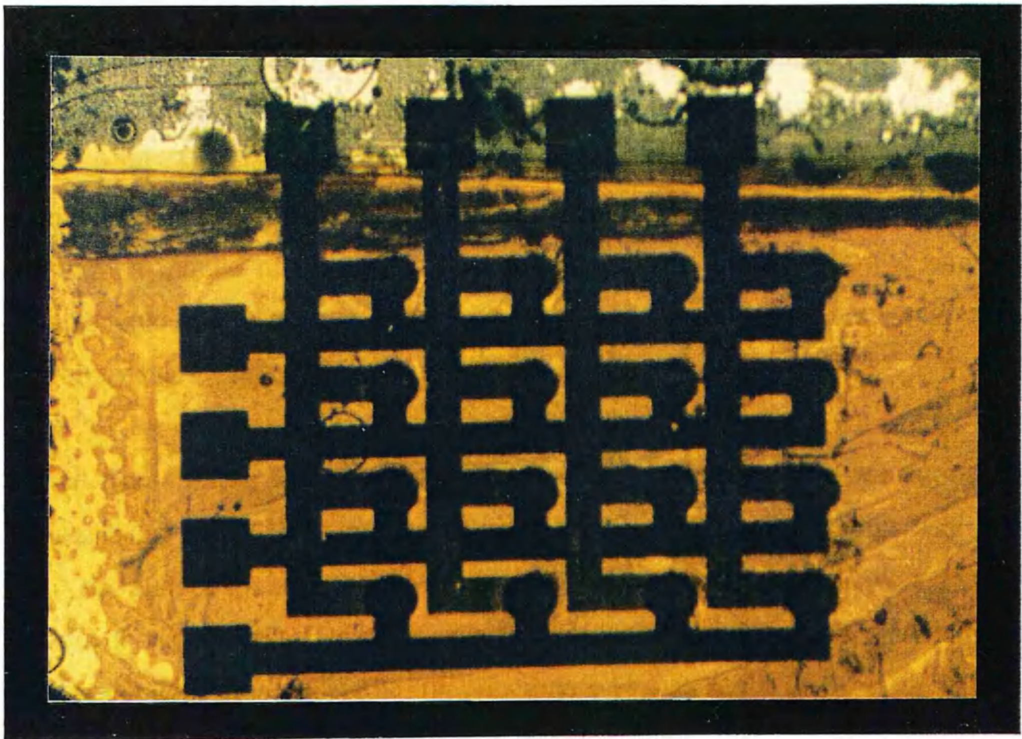

Photograph 4.10 The remaining epitaxial layers are removed using dry-etching techniques to reveal the p -ohmic contacting pads

top of the *p*-ohmic contacting pads. Having failed to do this successfully with a wet-etch without the use of elaborate masking techniques to protect the modulator elements, dry-etching with $SiCl_4$ was used. The completed device is shown in Photograph 4.10.

4.5.6 Alteration of the original design

An additional step incorporated at the beginning of the process would also allow this device to be used for image processing. This would involve the evaporation of gold or a similar opaque material onto the glass slide, which could then be removed from the apertures of the elements. This would be carried out after the sample had been firmly attached to the slide and, again, use of the mask aligner infra-red capabilities would simplify this process. In this configuration, with an expanded beam incident onto the device, light would be transmitted only through the element apertures. This would also eliminate the problem of light leaking round the elements which was encountered during the testing of the device actually fabricated.

4.6 Experimental set-up and procedure

The apparatus used to test the spatial light modulator was described in Section 3.4. The SLM elements are much smaller than the single electroabsorption modulator and the microscope objectives necessary to focus the light through the single elements were x 50. The aim of this experiment was to demonstrate that such a modulator could be suitable for use in a communication system where it would be accessed through a bundle of fibres. Thus it was only tested using a narrow beam of light coupled into one element at a time and not an expanded beam which would be required for applications such as image processing.

Each element was electrically accessed and optically tested to demonstrate that they all exhibited the QCSE. Light was coupled into the individual elements using the 'end-fire' rig and collected by the output objective. A horizontal slit was incorporated before the input objective to narrow the vertical beam from the monochromator. A reverse voltage was applied to the appropriate line contacts.

For each element the spectra at zero applied voltage and -30 V were recorded, with selected elements being tested to monitor the magnitude of the Stark shift between

these extremes.

4.7 Results and discussion

Firstly measurements were made of the position of the absorption edge and exciton positions in each of the elements at zero field. Clearly a narrow spread in the relative positions is desired. The second measurements verified that each of the elements exhibited the Stark shift already demonstrated by layer CB 2 in the single electroabsorption modulator. Before the transmission experiments were undertaken it was necessary to ensure that each element was capable of achieving a reverse breakdown of at least -30 V and therefore the I-V characteristics of all the elements were recorded.

4.7.1 I-V Characteristics of the array elements

The I-V characteristics were measured using the Hewlett Packard Semiconductor Parameter Analyser as before. The measures taken to ensure electrical isolation between the *p* and *n* ohmic contacting lines proved successful, with all the elements achieving a reverse breakdown of at least -35 V.

4.7.2 Zero Field Variation of the Absorption Spectra

As described in Section 4.6, the results for this particular experiment were obtained by focussing the output of the monochromator through each element at zero applied field. Figure 4.4.1 indicates the numbering system used for the elements in the array, where it is assumed that the device is being viewed from the *n*-contacting side. This numbering system is adhered to in all the experiments. The absorption spectrum was recorded for each element and normalised for the system variation with wavelength. Two particular features in the spectra were examined to determine the suitability of the crystal layer for this device. The first of these was the heavy hole exciton peak and the second the position of the absorption edge at high transmission.

Figure 4.7.1 presents the zero field variation of the heavy hole exciton peak. For a direct comparison to be drawn between the elements the transmission has been normalised at the higher and lower wavelength ends of the spectrum. This scaling eliminates the effect of background light and the light leaking round the elements

which could not be physically eradicated during the experiment.

The absorption spectra of the elements are bound by the two extreme spectra. The heavy hole peak which occurs at the lower end of the wavelength scale, at 824 nm is that of element 10. The top end of the scale is bound by the spectrum of element 2 and the peak occurs at 826 nm. The position of the exciton peaks is obtained by locating the point of maximum absorption. From Figure 4.7.1, in the case of the lower bounding spectrum, the exciton peak is not very well resolved. This is not a characteristic of the material but rather an experimental problem. It was in this case difficult to prevent some light leakage round the element, despite using slits to aperture the beam. The problem with this method was the resultant loss of optical power. The best solution available was to prevent light leakage using slits in front of the device and to increase the optical power by opening the slits in the monochromator. By doing this the resolution was degraded for some of the spectra as shown in Figure 4.7.1. Obviously the best solution to this problem would have been to use a tunable laser system but a suitable system was not available.

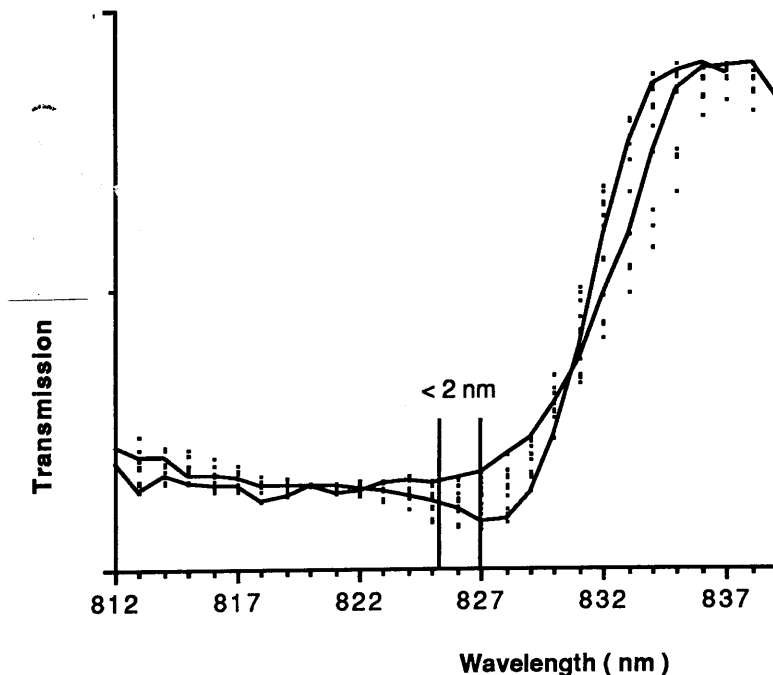

Figure 4.7.1 Variation of the exciton peak at zero applied field

The results presented in Figure 4.7.1 show that the spread in the exciton peak is 2 nm, at zero applied electric field over all the elements. The significance of this spread is discussed later in this chapter when the optimum operating wavelength of the device is determined. The width of this spread is higher than expected, and this can be explained by the fact that material from the edge of the crystal wafer was used for this device. Obviously the most desirable area to chose for the device would have been the centre of the crystal, however this was used for the single modulator structures described in Chapter 3. The spread at zero bias is 2 nm less than that quoted by [Rejman-Greene 1988] of 4 nm for a similar device fabricated in InP/InAlAs and is therefore encouraging.

Comparing the zero field results from the spatial light modulator to those obtained for the single modulator outlined in Chapter 3, the effects of using different parts of the crystal for the separate devices is accentuated. The largest difference between one of the elements of the spatial light modulator (occurring at 824 nm) and the single modulator heavy hole exciton peak, shown in Figure 3.5.2 at 831 nm, is 7 nm. This is rather large but the outer area of a wafer, which was used for this device, often exhibits large variations in uniformity. A less significant but possible contribution to this spread is that the larger width, 0.5 mm (0.1 mm for previous experiments), of the monochromator slits implies that the exciton feature is not so clearly resolved in the SLM case. This leads to an apparent reduction in the sharpness of the exciton feature which CB 2 demonstrated in Chapter 3. The exact position of the heavy hole exciton peak is masked by these problems which contributes partly to the large variation observed.

The important feature in the SLM is the position of the exciton peaks relative to each other over the array area rather than to devices from other parts of the crystal. Thus the results presented for this experiment, despite the pitfalls outlined, are encouraging. The spread in the absorption spectra over the area of the array will be shown to be tolerable when calculations of the crosstalk are made and the optimum operating wavelength is determined.

Another feature of the absorption spectra shown in Figure 4.7.2 is the loss of the

sharpness of the absorption edge, possibly for the same reasons as the loss of resolution of the exciton feature. The higher transmitting regions of the device are emphasised in this graph. The spread in the absorption edge in the high transmission region is larger than the spread in exciton peaks.

This variation of the absorption edge in different elements is ~4 nm . The fact that the spread in the higher transmitting region of the spatial light modulator is much larger than that at the exciton peak supports the theory the extra light which is not going through the epitaxial layers is responsible for the loss in the sharpness of the edge.

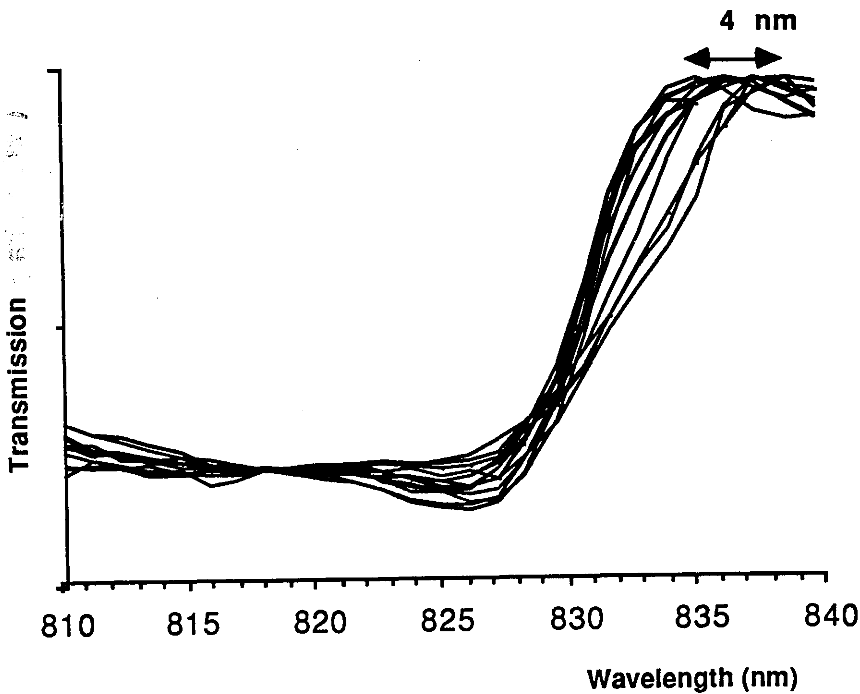

Figure 4.7.2 Variation of the absorption edges of the SLM at zero applied electric field

4.7.2 Stark shift of the individual elements

The second experiment verified the modulating capabilities of each element by use of the line addressing design. The absorption spectrum of each element was measured at zero applied volts and also at -30 V. These results are presented from Figure 4.7.3 a to d for the sixteen elements. These graphs clearly show the Stark Shift of each element. The magnitude of the shift varies from element to element and is difficult to quantify due to the quality of the spectra. This variation is thought not to be a consequence of the addressing system used but rather the inability to accurately determine the shift from the recorded data. For these spectra the magnitude of the Stark shift appears to be in the region of 9 meV ± 1.5 meV compared with the more clearly defined shift of the single modulator of 13.8 meV.

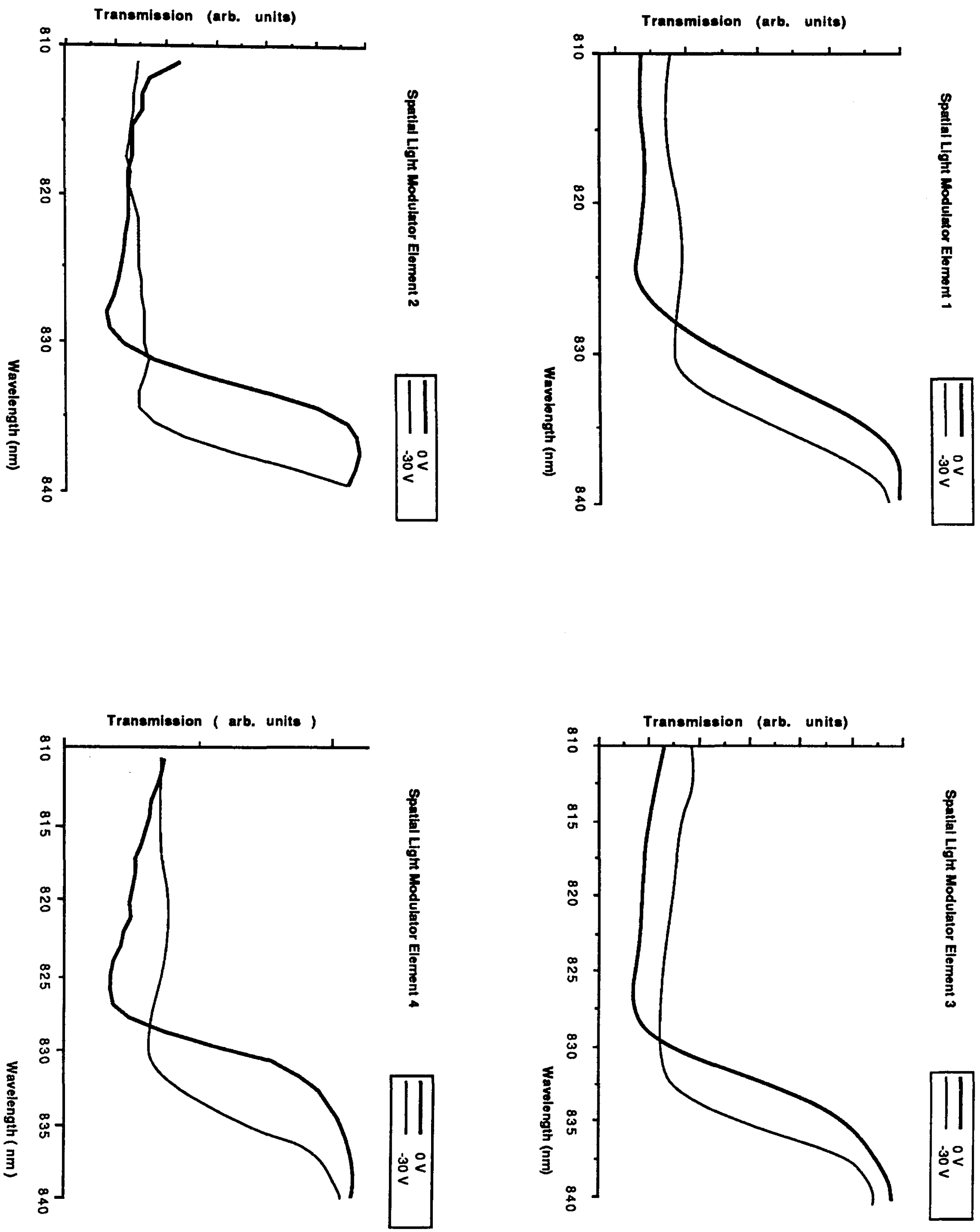

Figure 4.7.3 a Transmission spectra of elements 1, 2, 3 and 4

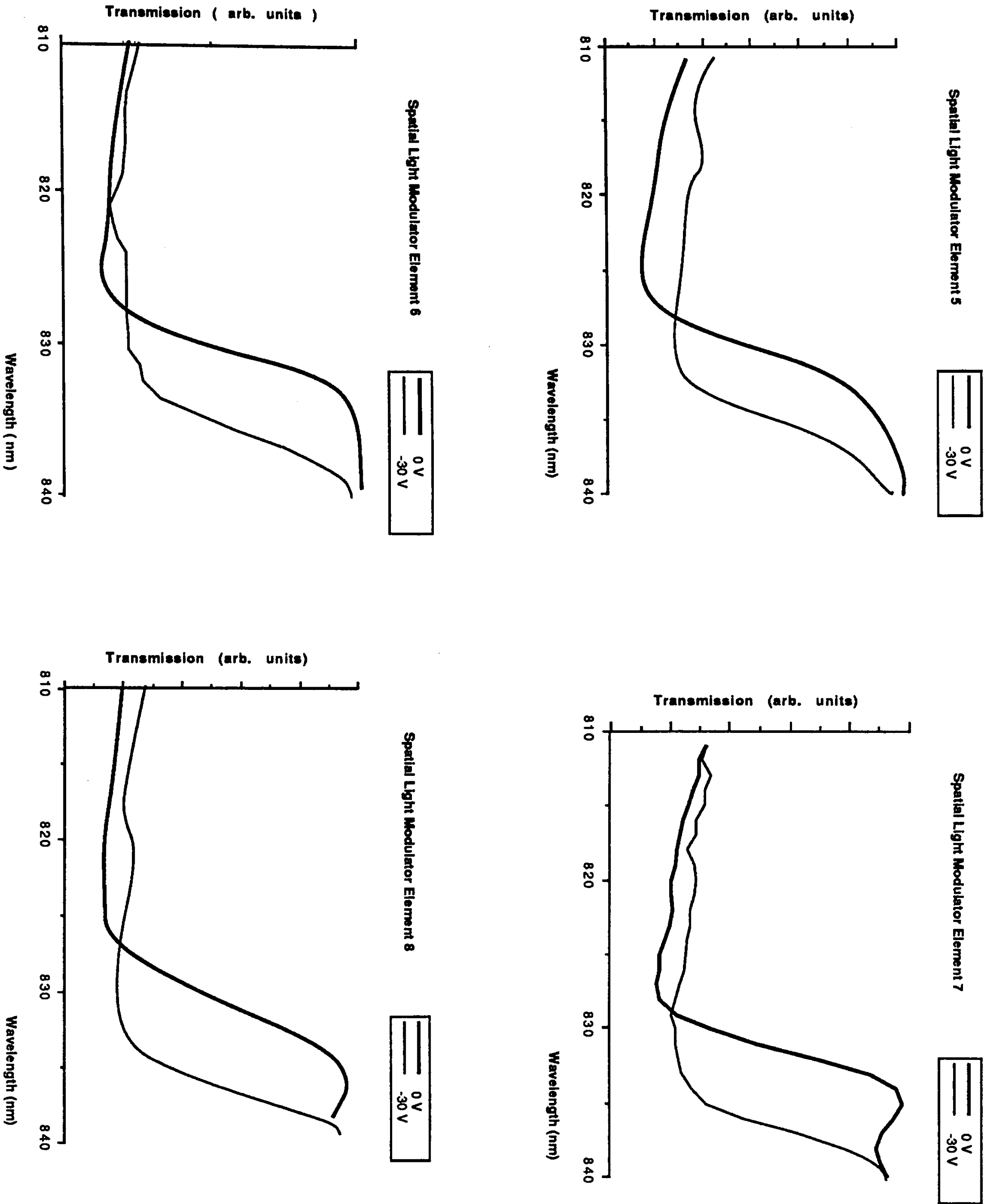

Figure 4.7.3 b Transmission spectra of elements 5, 6, 7 and 8

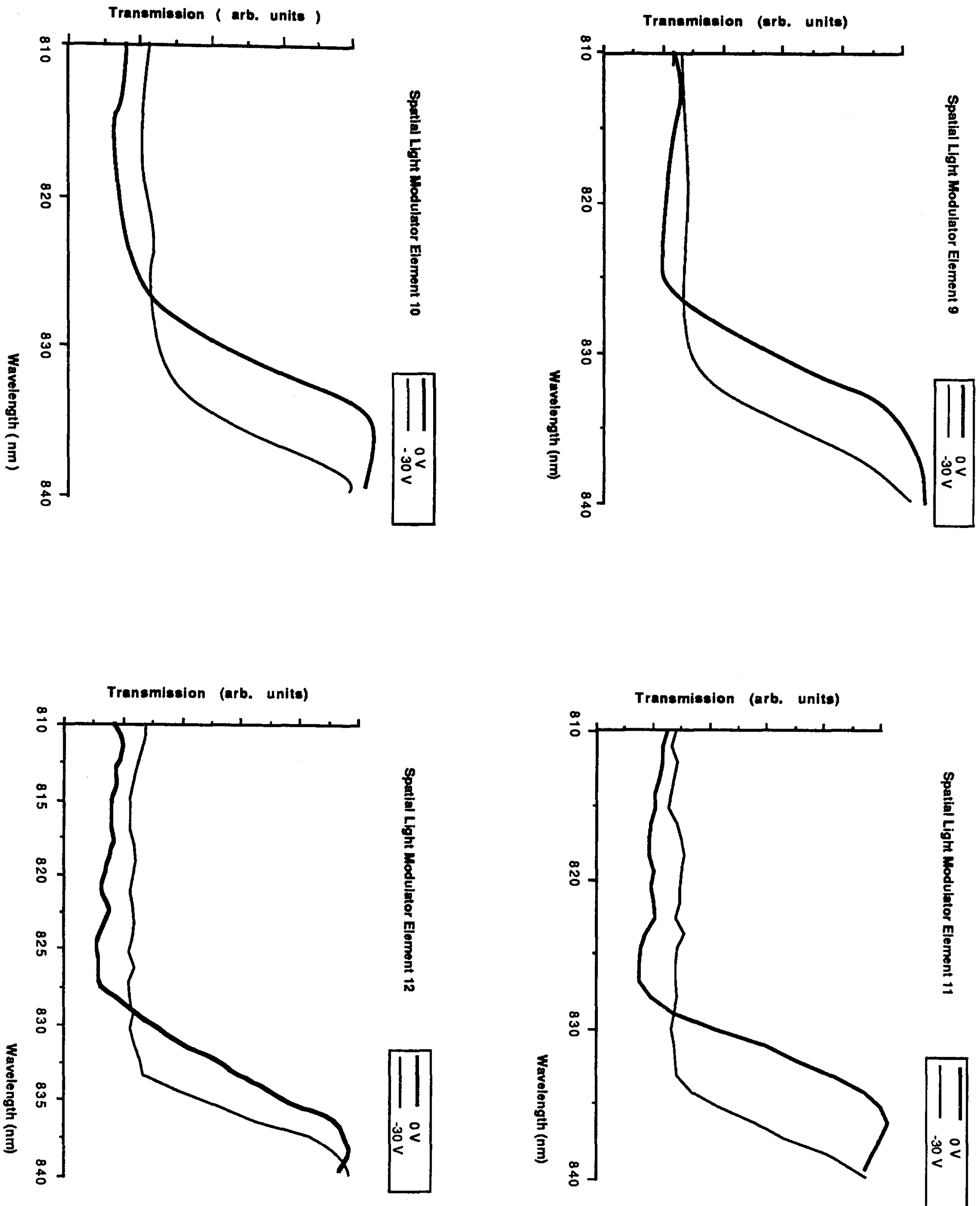

Figure 4.7.3.c Transmission spectra of elements 9, 10, 11 and 12

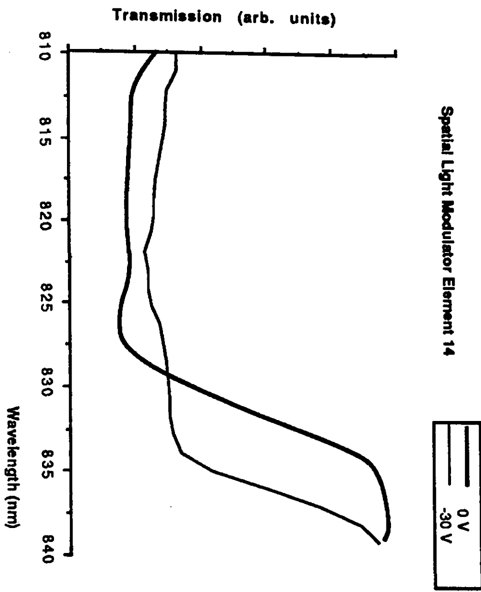

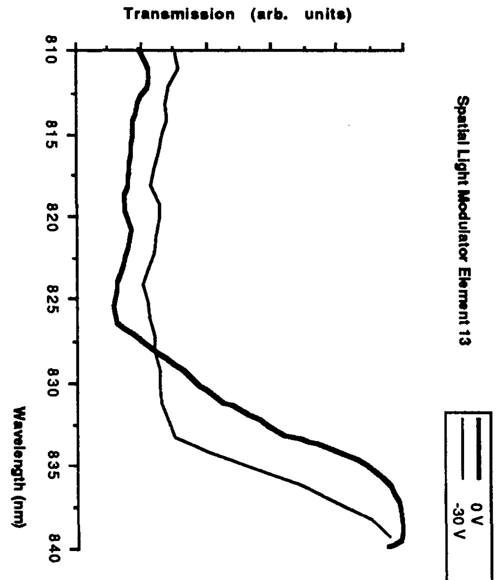

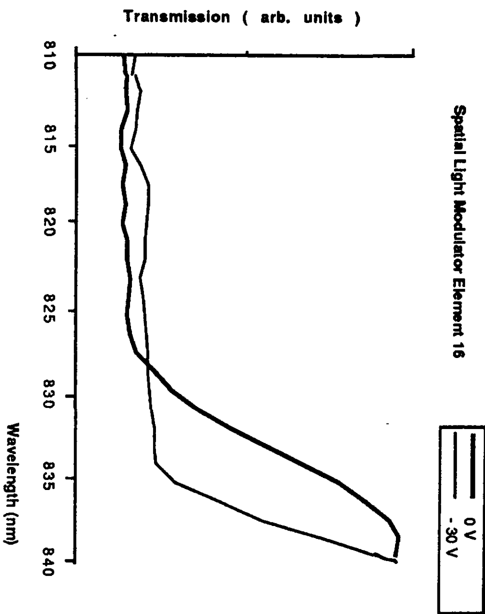

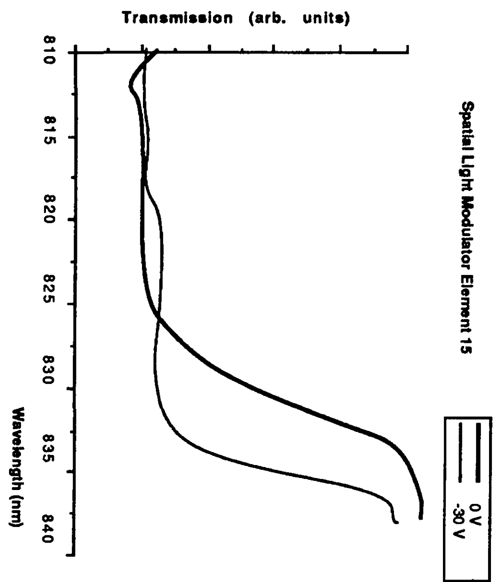

Figure 4.7.3 d Transmission spectra of elements 13,14,15 and 16

4.7.4 Device operation : Optimised condition

The optimum operating conditions of the device can be determined by using both the data obtained for the single modulator structure, which defines the quality of the material, and the wavelength variation over each element in the array for the zero biased condition.

Two conditions of bias are considered. The first is -25 V, the applied voltage which achieved the highest contrast ratio, and the second a lower drive voltage of -20 V. Since, as explained in section 4.4, some non-selected elements are also biased by half the drive voltage, it is necessary to consider the spectra of -12 V and -10 V respectively. In this array system the optical contrast ratio which becomes significant is the ratio between the drive voltage and half the drive voltage.

The contrast ratios found between -25 V and 0 V and between -12 V and 0 V are shown in Figure 4.7.4. To assess the crosstalk between these two conditions of bias, the contrast ratio was calculated. The last factor taken into consideration is the spread in wavelength of 2 nm over the elements, which is defined by the vertical lines. The device can be optimised to work in the region of the 2 nm spread in wavelength which provides the highest crosstalk, that is with the largest ratio between selected and non-selected elements. This wavelength is determined as 838.2 nm for this particular device, giving an optical contrast ratio of 4.8:1 (6.8 dB) between selected and non-selected elements. For this case the maximum contrast ratio obtained in the selected element is 7:1 (8.45 dB) with 1.4:1 (1.46:1) in the non-selected element. If the spectra are examined at the extremes of the wavelength variation, that is ± 1 nm, i.e. at 837.2 nm and 839.2 nm the crosstalk is 4:1 (6 dB). Thus the variation of the zero bias spectra due to the growth non-uniformity can be tolerated for this device.

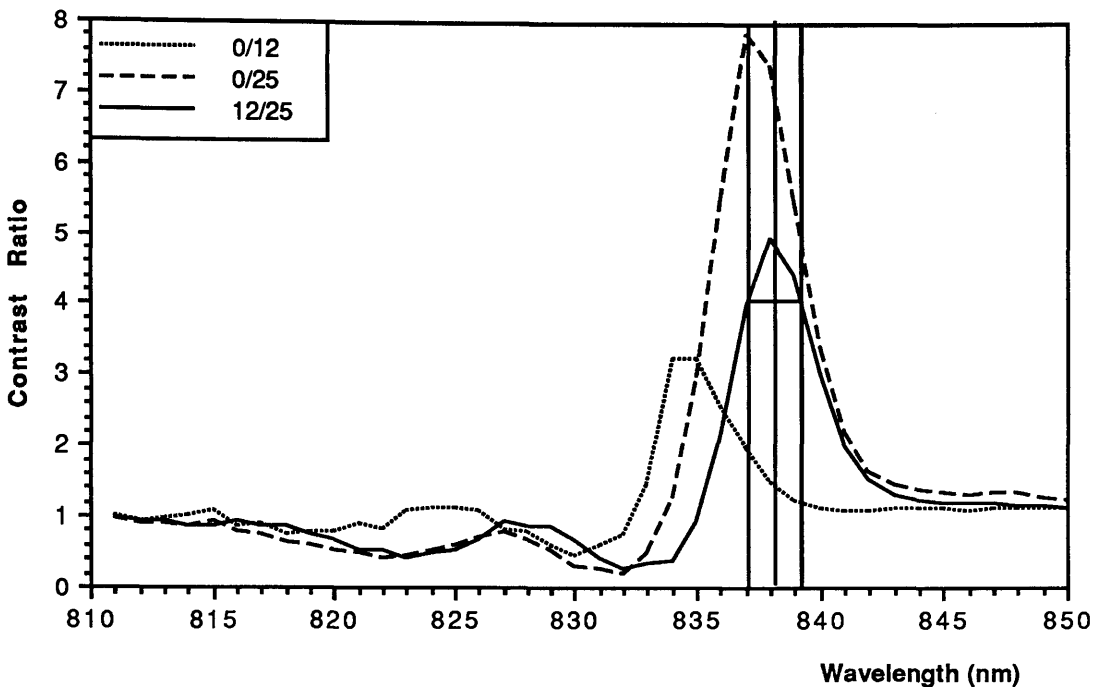

Figure 4.7.4 Optimised operating wavelength for a drive voltage of -25 V

Equally competitive values of crosstalk can be obtained by using a lower drive voltage. It can be seen that because the exciton feature remains well resolved, particularly for low applied fields, that the contrast ratio between the lower biased spectra and the zero condition is low resulting in high values of crosstalk rejection. Consider the spectra of 0,-10 and 20 V as shown in Figure 4.7.5. Again the vertical lines represent the variation in wavelengths over the devices. This time the maximum value of crosstalk, 4.3:1 (6.33 dB), is obtained at a wavelength of 837.1 nm, with the maximum contrast ratio for a selected element being 6.6:1 (8.2 dB) and the non-selected element contrast ratio being 1.6:1 (2 dB). This value of crosstalk drops to 3.5:1 at wavelengths of 838.1 nm and 836.1 nm. Therefore, although the maximum value of crosstalk is not as high as that obtained for the higher drive voltage of -25 V, it is possible to operate the device in systems which demand the use of lower drive voltages. In both cases, i.e. -25 and -20 V bias, the optimum wavelength is slightly shifted from that calculated for the single device.

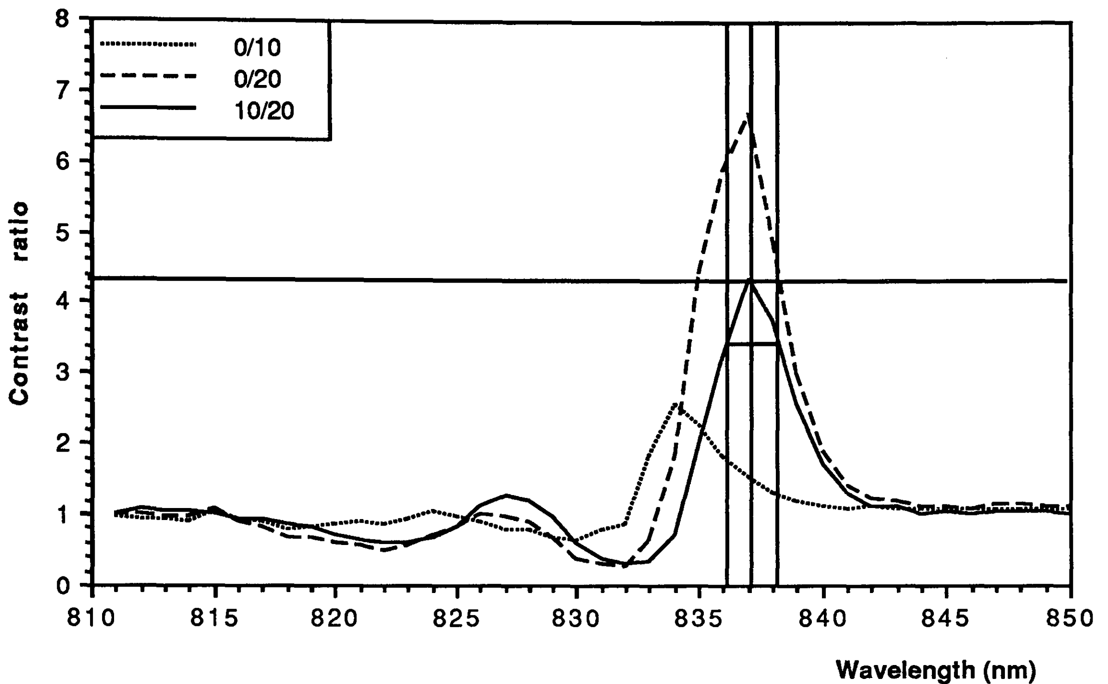

Figure 4.7.5 Optimum wavelength of operation for a drive voltage of -20 V

4.7.5 Discussion

It can be seen from the results presented in this chapter that this design of spatial light modulator is useful for the routing of optical signals.

Each of the elements in the array was capable of modulating light, as demonstrated. There were problems associated in both the fabrication of the device and the recording of the transmission spectra. The fabrication problems were in the main overcome by use of a combination of dry and wet-etching techniques and photosensitive polyimide. It was however more difficult to alleviate the assessment complications. Steps, such as employing both vertical and horizontal slits to aperture the optical beam were taken, and these reduced the problems.

The undesirable biasing of non-selected elements is shown to be tolerable and useful modulation can be obtained (6 dB at worst for -25 V bias) with acceptable levels of crosstalk. The design of the device can also be altered to suit applications other than

optical signal routing, as explained in section 4.5.5, and much larger arrays are possible using this configuration.

Chapter Four : References

D.B. CARLIN, B. GOLDSTEIN, J.P. BEDNARZ, M.G. HARVEY and N.A. DINKEL
'A ten-element array of individually addressable channeled-substrate-planar AlGaAs diode lasers'
IEEE Journal of Quantum Electronics Volume QE-23 Number 5
Page 476-477
5 May 1987

G.J. DUNNING, E. MARCOM, Y. OWECHKO, B.H. SOFFER
'Optical Holographic Associative Memory using a Phase Conjugate Resonator'
Proceedings of SPIE-International Society for Optical Engineering
Volume 625
Page 205-213
1986

Dror G Feitelson
Optical Computing : A survey for computer scientists
MIT Press
1988

W.D. GOODHUE, B.E. BURKE, K.B. NICHOLS, G.M. METZE and G.D. JOHNSON
'Quantum well charged coupled devices for charge coupled device addressed multiple quantum well spatial light modulators'
Journal of Vacuum Science and Technolgy B Volume 4 Number 3
Page 769- 772
May/June 1986

R.H. KINGSTON, F.J. LEONBERER
'Fourier transformation using an electroabsorptive CCD spatial light modulator'
IEEE Journal of Quantum Electronics Volume QE-19 Number 9
Page 1443- 1451
9 September 1983

R.H. KINGSTON, B.E. BURKE, K.B. NICHOLS and F.J. LEONGBERGER
'An electroabsorptive CCD spatial light modulator'
Proceedings of SPIE-International Society for Optical Engineering Volume 465
Page 9-11
1984

R.H. KINGSTON, B.E. BURKE, K.B. NICHOLS and F.J. LEONGBERGER
'Spatial light modulator using electroabsorption in a GaAs charge coupled device'

Applied Physics Letters Volume 41 Number 5
Page 413- 415
1 September 1982

R.H. KINGSTON, F.J. LEONBERGER
'Fourier Transformation using an electroabsorptive CCD spatial light modulator'
IEEE Journal of Quantum Electronics Volume QE- 19 Number 9
Page 1443- 1451
9 September 1983

S.H LEE, S.C. ESNER, M.A. TITLE and T.J. DRABIK
'2-D silicon/PLZT spatial light modulators : system application potential'
Proceedings of SPIE-International Society for Optical Engineering
Volume 625
Page 62- 71
1986

F. MOK, J. DIEP, H-K LIU, D.PSALTIS
'Real-time computer-generated hologram by means of liquid-crystal television spatial light modulator'
Optics Letters Volume 11 Number 11
Page 748- 750
November 1986

K.B NICHOLS, B.E. BURKE, B.F. AULL, W.D. GOODHUE, B.F. GRAMSTORFF, C.D. HOYT and A.VERA
'Spatial light modulators using charge coupled device addressing and electroabsorption effects in GaAs/AlGaAs multiple quantum wells'
Applied Physics Letters Volume 52 Number 14
Page 1116- 1118
4 April 1988

M.A.Z. REJMAN-GREENE, E.G. SCOTT, E. Mc GOLDRICK
'Planar 3x3 Array of GaInAs/InP multiple quantum well surface optical modulators grown by gas-source MBE'
Electronic Letters Volume 24 Number 25
Page 1583- 1584
8 December 1988

J. SINGH, S. HONG, P.K. BHATTACHARYA, R. SAHAI, C. LATUFKA, and H.R. SOBEL
'System requirements and feasibility studies for optical modulators based on GaAs/AlGaAs multiple quantum well structures for optical processing'
Journal of Lightwave Technology Volume 6 Number 6

Page 818- 831
6 June 1988

T.H. WOOD, E.C. CARR, C.A. BURRUS, J.E. HENRY, A.C. GOSSARD and J.H. ENGLISH
'High-speed 2x2 electrically driven spatial light modulator made with GaAs/AlGaAs multiple quantum wells'
Electronic Letters Volume 23 Number 17
Page 916- 917
13 August 1987

CHAPTER FIVE
COUPLED QUANTUM WELL MODULATORS

Introduction

Although the electroabsorption modulator described in Chapter 3 exhibited a relatively high contrast ratio for such a device, other designs of modulator which also have the advantage of low drive voltages are of interest. To achieve both of these objectives the modulator could either be operated in reflection mode [Whitehead 1989] or the natural reflection properties of the interfaces, to optimize the device, could be used. [Whitehead 1989] Another approach to improve the modulator operation, and the one which is the topic of this chapter, is to vary size of the wells and the barriers.

The layers of the intrinsic region of the previously fabricated electroabsorption modulator, CB 2, were altered to allow coupling between the individual wells. Results for two designs of coupled well devices are presented. The first consisted of a superlattice of 200 wells which was modified to contain pairs of coupled wells, in an attempt to enhance the results.

5.1 Variations in the design of the absorption layer

The intrinsic region of the previous isolated quantum well MOCVD grown layers, CB 2, was modified to form a region of coupled quantum wells. In this geometry, the theoretical shift of the absorption edge as a function of applied field is much larger than that achievable with isolated wells [Bleuse 1988]. An effective blue shift of the absorption edge takes place rather than the red shift observed in Chapter 3.

In order to study the effect of coupling the wells two separate geometries were considered. The first of these was a superlattice, where all the wells were coupled by thin barriers (< 40 Å). In the second geometry coupling between the wells was again exploited but in this case pairs of coupled wells were isolated by thick barriers (> 40Å). These pairs of wells exhibited different behaviour to that of the superlattice device.

5.2 Superlattice theory

Superlattice structures consist of wells no longer isolated from each other, but coupled through thin barriers i.e. the width of the barrier between consecutive wells is reduced to allow electrons and holes to tunnel through the barrier. This results in the wells being coupled at zero field by the resonant tunneling effect and, therefore, in the formation of electronic minibands of width ΔE_1 and ΔH_1 rather than discrete electronic energy levels (see Figure 5.2.1). The resulting effect is that, under zero field conditions, the bandgap of the superlattice is reduced from that of the isolated well structures by an amount $\frac{1}{2}(\Delta E_1 + \Delta H_1)$.

On the application of an electric field this resonant effect is turned off as the levels become displaced from each other. In contrast to isolated well devices where on the application of an electric field the bandgap is effectively reduced, the bandgap of the superlattice should become larger. Due to the electric field the energy levels in adjacent wells are misaligned by an amount eFd and the resonance condition is turned off if $eFd > \Delta E_1$. The initial effect of this is to regain the discrete energy levels associated with the isolated wells. Thus transitions can only take place at energies higher than those in the zero bias condition, resulting in a blue shift of the absorption edge. In theory this shift should be much larger than the associated red

shift of isolated quantum wells. [Bleuse 1988]

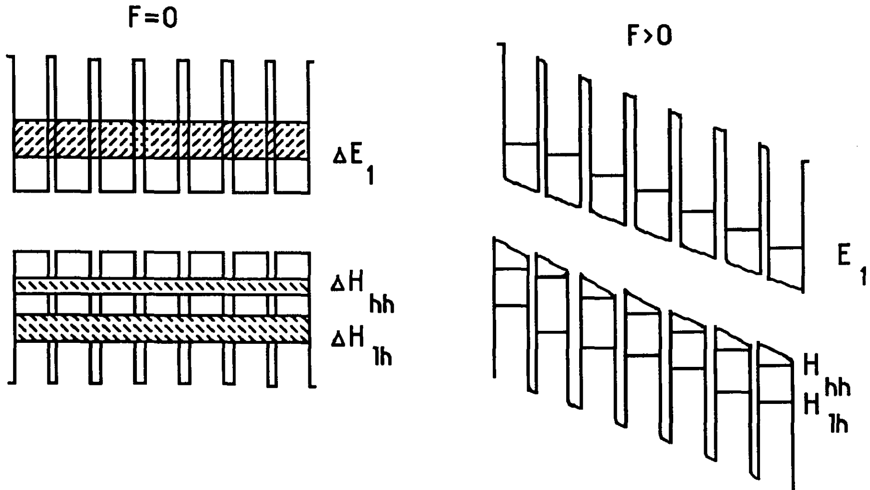

Figure 5.2.1 Formation of minibands in a superlattice, and the effect of the electric field on the energy levels

In coupled well structures in the presence of an electric field the wavefunction becomes localized over a few wells near the centre of the superlattice (Figure 5.2.2).[Bleuse 1988] This leads to the formation of a 'Wannier Stark Ladder' where, rather than a sharp excitonic effect appearing in the absorption spectrum, a series of steps is obtained, due to the energy levels in adjacent wells being misaligned by an amount eFd and the fact that the wavefunctions are not confined to a single well.

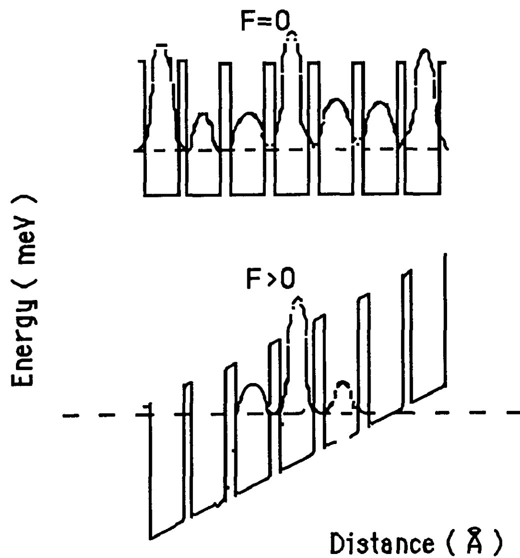

Figure 5.2.2 Wavefunction in a superlattice conduction band, effect of electric field on the wavefunction

At higher fields the effect which caused the 'red shift' in the isolated wells - i.e the QCSE shift in the energy levels due to the applied electric field - becomes significant once more. The absorption edge therefore appears to shift to lower energies once again.

5.2.1 Kronig-Penney Model

The formation of sub-bands and their widths can be calculated using the Kronig-Penney model. Consider the potential distribution in the direction of growth of the semiconductor layers (z direction) for a superlattice as shown in Figure 5.2.1. The periodic potential due to the difference in bandgap between the layers and is superposed on the intrinsic periodic potential in the crystal. The band structure of the complete structure depends on the magnitude of the electron mean free path, l, in relation to the period d. For $l<<d$, the periodic potential seen by the electrons is that of the crystal with the individual layers and the band structure of interest is that of the compound forming a particular layer. On the other hand, when $l>>d$, an electron may be considered to belong to the complete structure. The energy level diagram for the direction transverse to the z direction remains unaffected but that in the z direction is modified by the superlattice potential.

The modified band diagram may be worked out by solving the Schrödinger equation in the extra periodic potential of the superlattice using the effective masses of the electron and holes in the material forming the superlattice. This is similar to the Kronig-Penney model described in Chapter 2. The model required to calculate the energy levels and the miniband widths of a superlattice structure is outlined in Appendix A.

5.3 Literature review : Superlattice structures

The emphasis on coupled well structures has been mainly theoretical as described above, but recently the predicted behaviour of the absorption spectrum has been supported by experimental studies. [Bleuse 1988, Bhattacharya 1989]

The theoretical studies [see for example Bleuse 1988, Ferreira 1988, and Bastard 1987] have modelled the coupled structures using a tight-binding analysis of the envelope wavefunctions as described in Appendix B. Bastard [1985] calculated the

electronic energy levels in both semiconductor quantum wells and superlattices. These values were then used to predict the absorption spectrum of superlattice structures and the effect of an electric field on the spectrum. [Bastard 1989] It was found than when an electric field of equivalent magnitude to the sub-band width is applied to a superlattice structure then the resonant tunneling previously possible between the coupled wells is inhibited. The minibands are replaced by a Wannier Stark Ladder in the absorption spectrum, as previously discussed. This work was verified experimentally by Bleuse [1988] using the $Al_{0.24}Ga_{0.24}In_{0.52}As$-$Ga_{0.47}In_{0.53}As$ superlattice system. Two structures were investigated, firstly a 50 period superlattice with 50 Å wells and 55 Å barriers and secondly a 50 period superlattice with 40 Å wells and 45 Å barriers. In the first structure, with an applied voltage of 1.25 V, the absorption edge had an effective blue shift of 5 meV. The second structure behaved similarly to the first with a maximum shift of the heavy hole exciton of 12 meV being observed.

Bhattacharya performed similar experiments in the GaAs / $Al_{0.3}Ga_{0.7}As$ system and also found excellent agreement with theoretical predictions. Yan [1989] investigated a symmetric 41 period superlattice with a superperiod of 40 Å. For an applied voltage of -3 V a blue shift of the absorption edge was observed. Recently therefore blue shifts of the absorption edge have been both theoretically predicted and experimentally observed.

5.4 Design of superlattice modulator layers- CB 102

One of the aims in the design of the superlattice layers was to maintain the maximum level of absorption obtained by using a large total thickness of GaAs in the intrinsic region of the previous device. Thus a total of 200, 50 Å GaAs wells was again used (see Figure 5.4.1). These wells were coupled through 30 Å $Al_{0.3}Ga_{0.7}As$ tunnelling barriers. The design of the other layers of the modulator, already successfully tested in the isolated modulator device, remained the same as shown in Figure 5.4.2. As with layer CB 2, this structure was grown by MOVPE at the University of Sheffield. One of the problems with this type of design is that it is difficult to maintain a uniform electric field in the intrinsic region due to the level of doping. This leads to discontinuities between the theoretical and experimental results presented later in this chapter.

CQW : CB 102

GaAs	50 Å	x 200
AlGaAs 30%	30 Å	

Figure 5.4.1 Superlattice layer CB 102

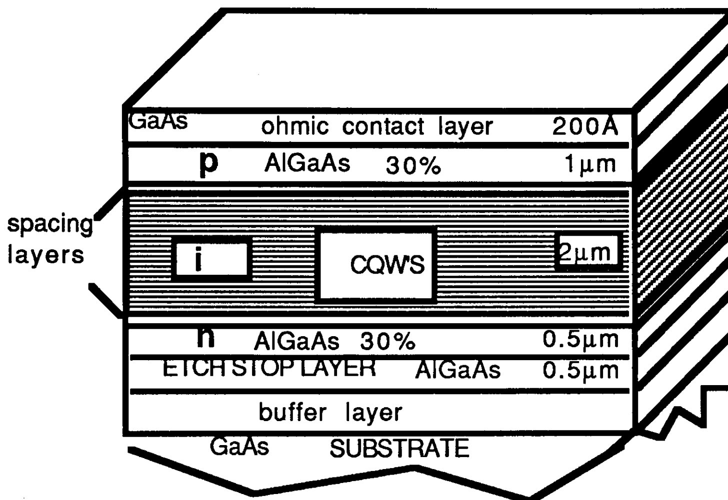

Figure 5.4.2 Overall design of modulator layers

5.5 Theoretical modelling of absorption spectra of superlattice structure

The modelling of the absorption spectrum for the superlattice structure was based on the theory of Bleuse [1988]. To use this model it was necessary to first calculate the zero field energy band structure of the superlattice structure, CB 102.

The energy levels and miniband widths of CB 102 were calculated using the adapted version of the Kronig-Penney model outlined in Appendix A. The equations in Appendix A were solved using a computer program with the required material parameters being summarised in Table 5.5.1.

Well Width Å	Barrier Width Å	Effective Mass Electron $*m_o$	Heavy hole $*m_o$	Light hole $*m_o$	Concentration of aluminium %
50	30	0.067	0.08	0.45	30

Temperature 300 K Band misalignment 60/40

Table 5.5.1 Parameters necessary for use in the Kronig-Penney model

Figure 5.5.2 is a plot of the results obtained using the Kronig-Penney model. From this plot the miniband widths and energy levels, and thus energy transitions between the valence band and conduction band, can be determined as summarised in Table 5.5.3. Bastard [1985 Figure 5] has previously calculated the width of the conduction band miniband as a function of both well and barrier width and aluminium concentration using a tight-binding analysis. Estimated from his results, for an aluminium concentration of 20 %, the miniband width is 35 meV. Allowing for the difference in the aluminium concentration, the equivalent value calculated here using the Kronig-Penney model, of 24.4 meV is in reasonable agreement.

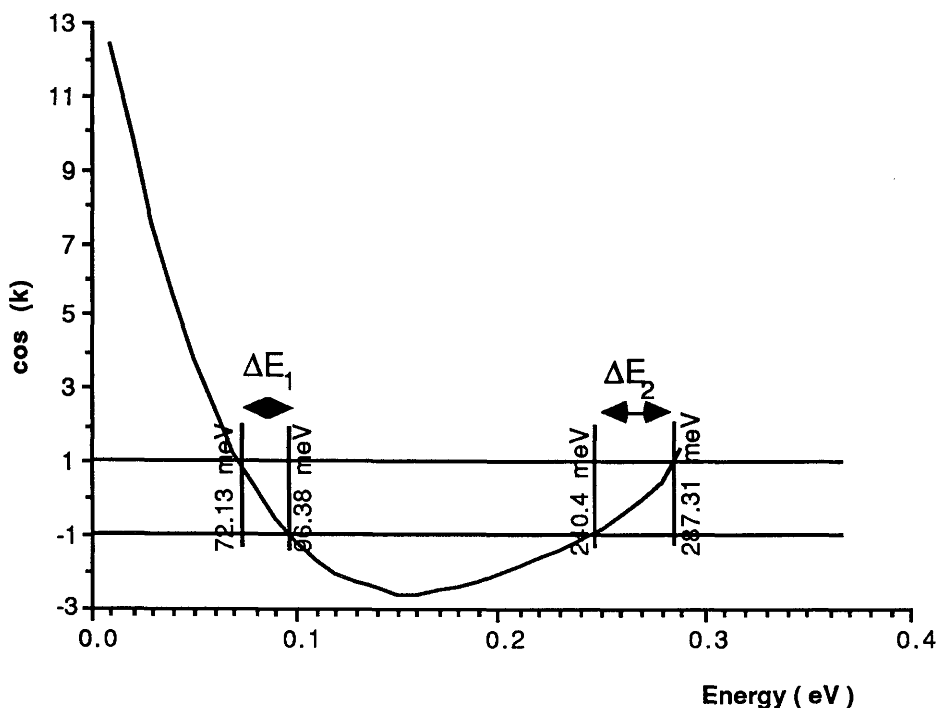

Figure 5.5.2 cos (k) as a function of energy obtained from the Kronig-Penney model for a superlattice with 50 Å wells and 30 Å barriers

E_1	ΔE_1	H_1	ΔH_1	L_1	ΔL_1 (meV)
72.13	24.247	12.03	3.39	16.28	26.09

Temperature 300 K Band misalignment 60/40

Table 5.5.3 Miniband edges and widths determined from Figure 5.5.2 for a superlattice with period 80 Å

Using this data in the computer program described in Appendix B the absorption spectra of the superlattice structure were calculated for various values of electric field. The spectra were normalised to give the same value of absorption in the short wavelength region of the spectrum.

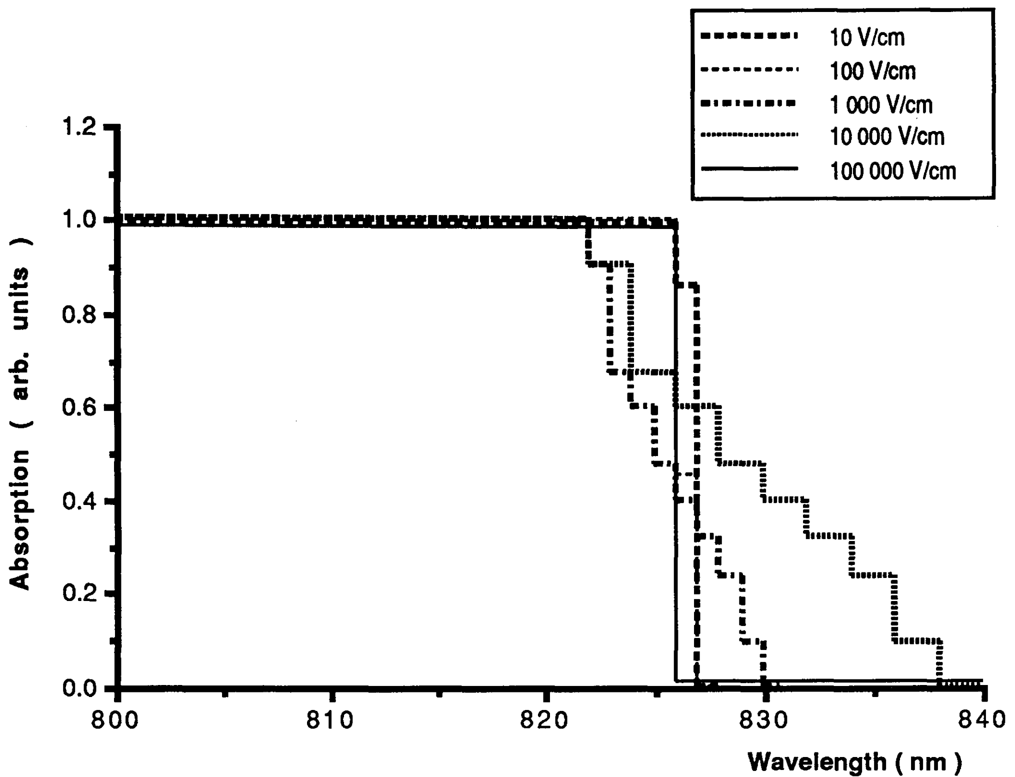

Figure 5.5.4 Theoretically calculated absorption spectra of superlattice CB 102

The change in the normalised absoprtion spectrum with increasing electric field is shown in Figure 5.5.4. Spectra are shown for electric fields between 10 V/cm and 10^5 V/cm.

The spectrum for the lowest electric field, which can be equated with the zero bias condition, is dominated by a transition at 827 nm (1.499 eV). Increasing the field slightly to 10^2 V/cm has little effect on the spectrum except for a reduction in the magnitude of the main transition on the high energy side of the zero bias absorption edge. When the field is further increased to 10^3 V/cm many more new transitions are observed. On the lower energy side of the zero bias spectrum these result in larger absorption, while a reduction in absorption takes place on the high energy side. This can be compared to the Franz-Keldysh effect : in bulk semiconductors minibands are also formed, of the order of a few eV's and, on the application of an electric field, there is increased absorption at lower energies coupled with decreased absorption at higher energies. The latter effect is due to the

reduction in overlap of the electronic wavefunctions and a similar process is taking place in the superlattice. The wavefunctions are not prevented from tunneling through the barriers and so there is a reduction in the amount of overlap between conduction band and valence band states. Further increases in the field accentuate this behaviour, see for example 10^4 V/cm. At the highest electric fields considered, 10^5 V/cm and above, the effect saturates and is once again dominated by a single absoprtion edge at 826 nm. Direct comparisons are drawn between the experimental observations and these theoretical calculations in section 5.7, after the experimental results have been discussed.

5.6 Superlattice CB 102-Experimental results

The transmission spectra of the superlattice structure were recorded as outlined in Section 3.4.

The zero applied field spectrum is shown in Figure 5.6.1 together with the spectrum for an applied voltage of -1 V. If the diode is considered to have a built-in potential in the region of 1.2 to 1.4 V then these spectra correspond approximately to fields of 8.75×10^3 V/cm and 1.5×10^4 V/cm, respectively. From these graphs it appears that the 'Wannier Stark Ladder' referred to by Bleuse [1988] is present. Unlike those recorded for the isolated well devices, shown in chapter 3.5, these spectra are not smooth and many transitions are present as expected. The Franz-Keldysh like behaviour of the superlattice is also prominent in these results with an increase in absorption at energies below the zero bias absorption edge and a decrease in absorption at higher energies. The movement of the different transitions results in crossover points between the two sets of data. Thus, depending on where the spectra are examined, it may be argued that a 'blue shift' of the absorption edge is taking place.

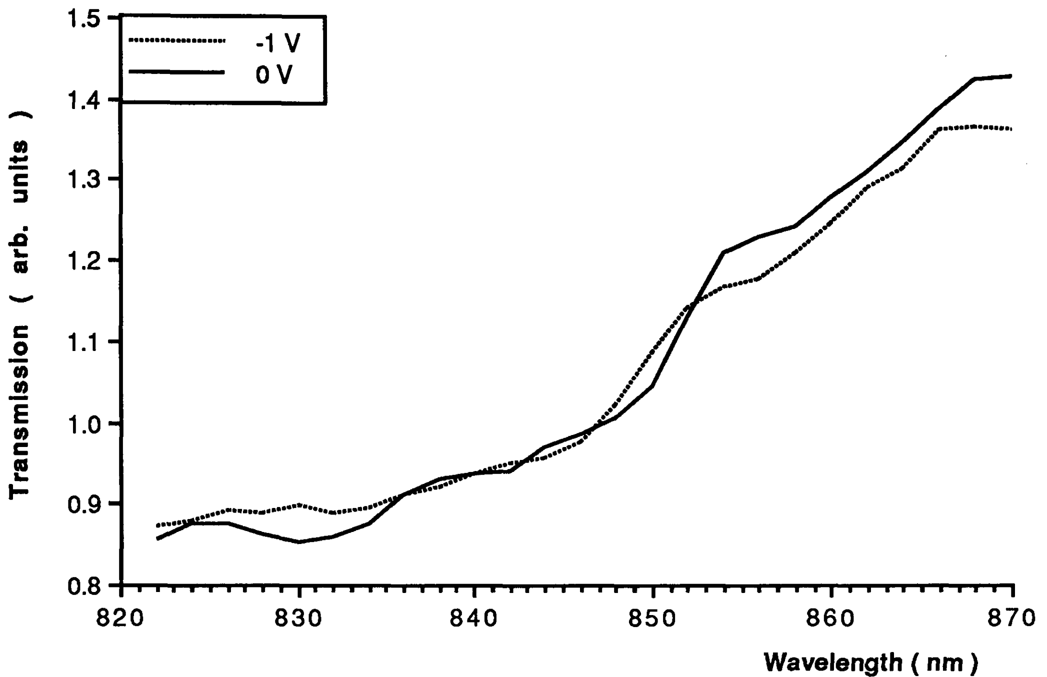

Figure 5.6.1 Transmission spectra of CB 102 for applied voltages of 0 V and -1 V

By further increasing the voltage, a further increase in absorption at longer wavelength can be seen, with a decrease at short wavelengths. Figure 5.6.2 shows spectra for a range of applied voltages : 0 V, -10 V, -20 V and -30 V. The dominant transition at 852 nm (1.4554 eV), present in the zero applied bias condition, becomes much less sharp as the field is increased. At wavelengths below this value a decrease in the absorption is observed until the highest applied field examined, –30 V (2×10^5 V/cm), where the absorption starts to decrease. Coupled with these changes is an apparent saturation of the absorption at energies just lower than the bandgap, that is 870 nm (1.425 eV). These spectra can now be compared to the theoretical calculations.

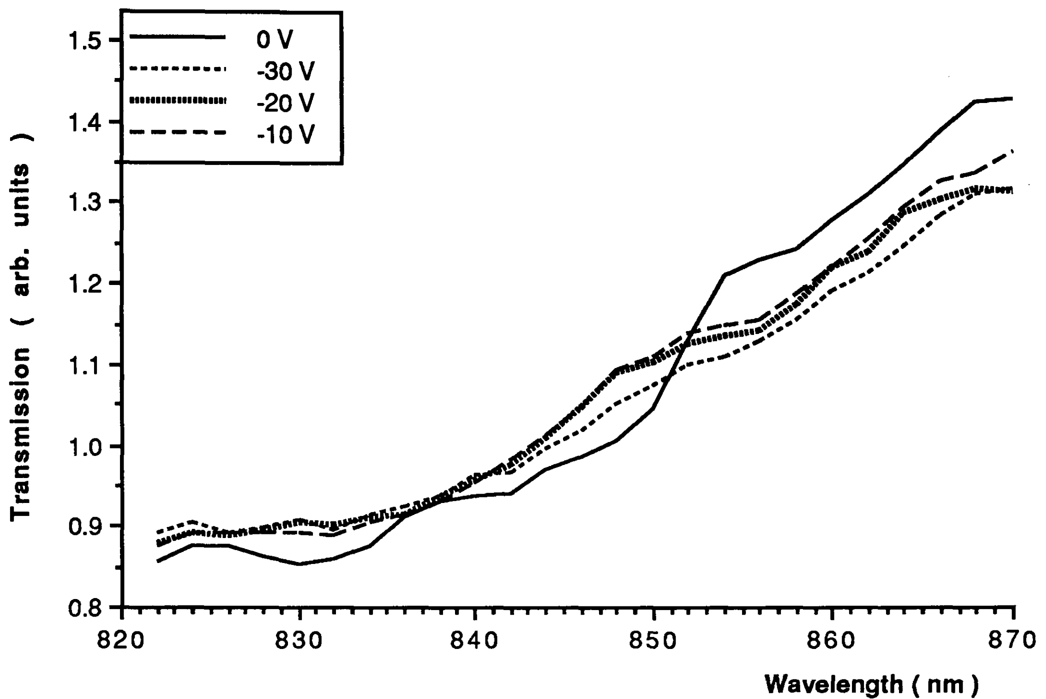

Figure 5.6.2 Transmission spectra of CB 102 at applied voltages of 0 V, -10 V, -20 V and -30 V

5.7 Comparison between theoretical and experimental results- CB 102

The results for the superlattice device, both theoretical and experimental, are shown in Figure 5.7.1 for the zero applied bias condition and -1 V. The first obvious difference is the wavelength at which the transitions take place. In the experimental case the dominant transition occurs at 850 nm, but theoretically no transitions are observed at wavelengths longer than 840 nm. This discrepancy may have arisen for a number of reasons, the most likely being that the well and barrier widths in layer CB 102 may not actually correspond to the design. This was the case in the isolated well structure where the wells were actually 62 Å wide, although the design was for 50 Å wells. Comparisons can still be made between the spectra by considering the effect of applied electric fields.

Both spectra under the conditions of 8.75 x 10^3 V/cm (zero applied bias) exhibit

many transitions although it is more difficult to determine the position of these transitions from the experimental data. When the electric field is increased slightly to 1.5×10^4 V/cm the transitions shift in position. Depending at which wavelength the spectra are examined, then these shifts can appear as a blue or red shifts of the absorption edge. The overall effect in the experimental spectra is similar to the Franz-Keldysh effect, that is the edge appears to bend leading to a reduction of the absorption at energies just below the bandgap. As higher fields are induced in the device this effect continues, see Figure 5.7.2, eventually saturating, as discussed in the previous section. The theoretical data also exhibit similar saturation at fields greater than 200 000 V/cm. The theoretical data shows a reduction in the number of transitions at such fields but this effect is not so easy to see in the experimental data.

The main conclusions which can be drawn between the two sets of data are that, as a result of the coupling together of wells, a 'Wannier Stark Ladder' is formed the effect of which can be seen in both the theoretical and experimental absorption spectra. Although saturation occurs at similar fields in both the experimental and theoretical spectra (200 000 V/cm), a detailed correlation of features in the two spectra is difficult to make.

The largest absorption changes due to the application of the electric field are, however, much smaller than desired with a maximum value of 1074 cm^{-1} at 832 nm. To increase the absorption changes another well geometry was investigated both experimentally and theoretically. The problem with the superlattice is that the electronic wavefunctions are free to tunnel throughout the whole structure, leading to little overlap between those in the conduction band and those in the valence band. Thus a new design, while still exploiting the coupling between wells, should include a means of restricting this coupling to fewers wells as discussed in the next section.

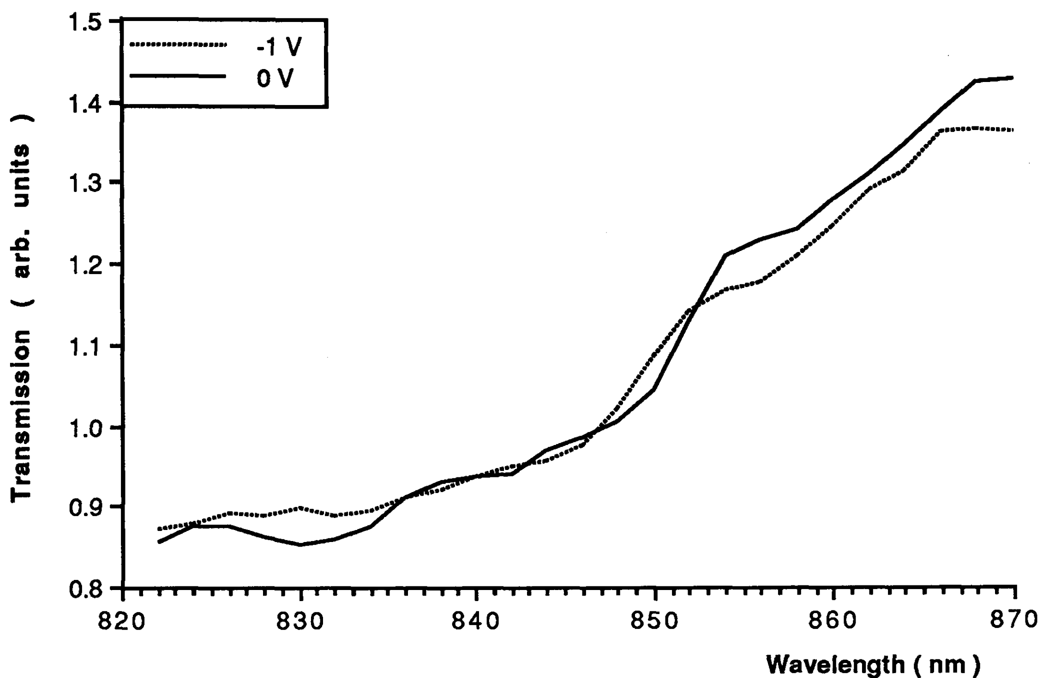

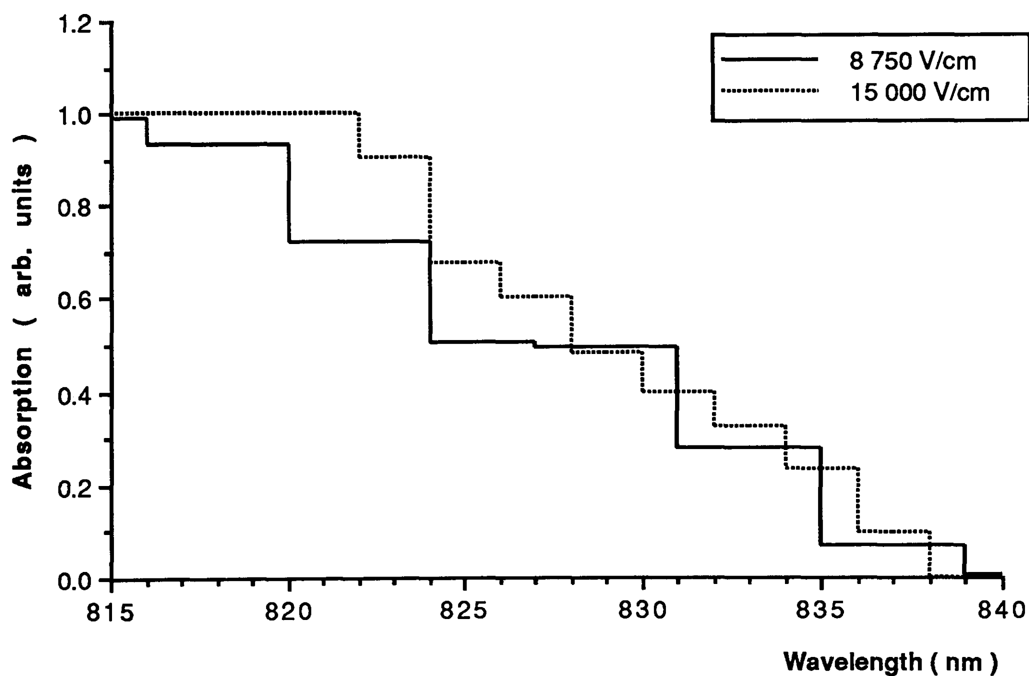

Figure 5.7.1 Comparison between theoretical and experimental electroabsorption results for low applied electric fields

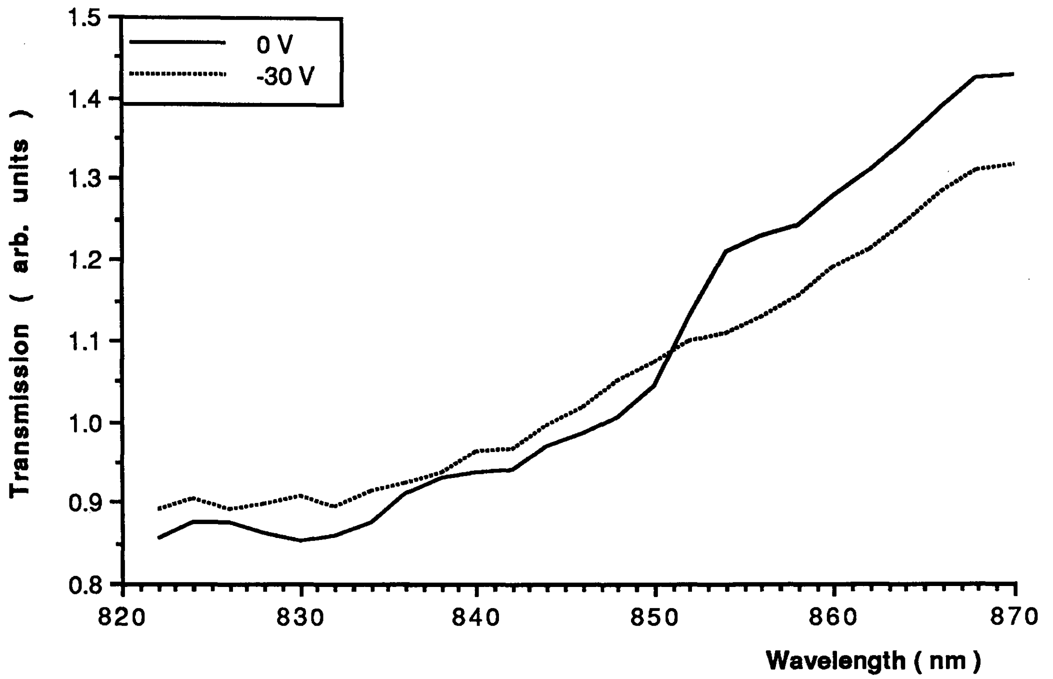

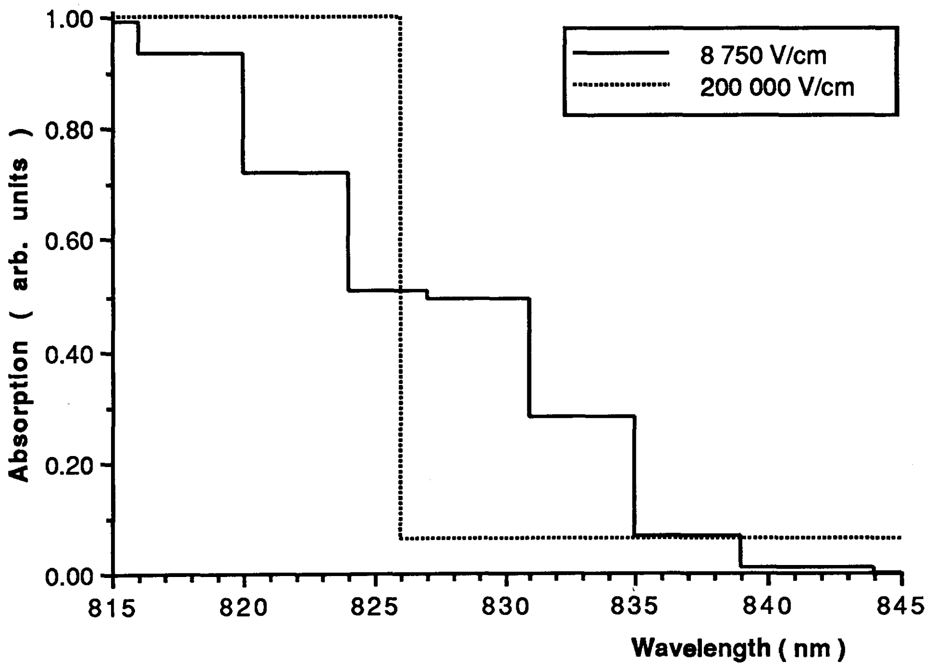

Figure 5.7.2 Comparison between theoretical and experimental electroabsorption results for high applied electric fields

5.8 Theory of coupled quantum wells - Pairs of wells

A second coupled well structure was designed in which only adjacent pairs of wells were coupled. In this case the two wells can couple through a thin barrier (<40 Å) but are isolated from neighbouring pairs of wells by thick barriers (>40 Å). Again sub-bands are formed as the two wells are coupled together but this time the excitonic effects are enhanced by the isolation of these pairs. This localizing of the tunneling wavefunctions serves to enhance the 'blue shift'. The energy levels split into those corresponding to symmetric and antisymmetric wavefunctions as described below.

In an isolated quantum well structure the effect of applying an electric field is to reduce the conduction and valence band energies and the 2D exciton binding energies. In a pair of coupled quantum wells, however, the split levels of the coupled electronic states move in opposite directions as a function of applied field, leading to several exciton transitions which shift rapidly to lower or higher energies as the field is increased. [Chen 1987]

The behaviour of the electronic levels in a pair of coupled wells is shown in Figure 5.8.1, both with and without an electric field. In the absence of an electric field only transitions between electron and hole states of the same symmetry (S) are allowed, i.e. 1,3,6,8. On the application of an electric field, the wavefunction symmetries are distorted, and all transitions become allowed, thus 2,4,5,7 are now allowed. These transitions (2,4,5,7) experience the regular QCSE and are only weakly affected by the coupling, while the energies of 1 and 3 decrease much more rapidly with electric field and 6 and 8 increase much more rapidly.

Although the effect is described as a 'blue shift', the absorption edge, synonymous with the lowest transition (e_1-hh_1), actually moves to lower energies thus 'red shifting'. This is a rapid shift, with respect to the applied field, and there is also an associated large decrease in oscillator strength of this transition, due to the reduction in overlap of the wavefunctions. Therefore even at low applied voltages the transition is quenched and is not clearly observed in the absorption spectrum. Thus the next lowest transition, e_1-hh_2 (antisymmetric), which exhibits an increase in absorption with applied field is responsible for the apparent blue shift of the

absorption edge. Therefore it is the effect of the electric field on the higher allowed transitions which dominates the absorption spectrum.

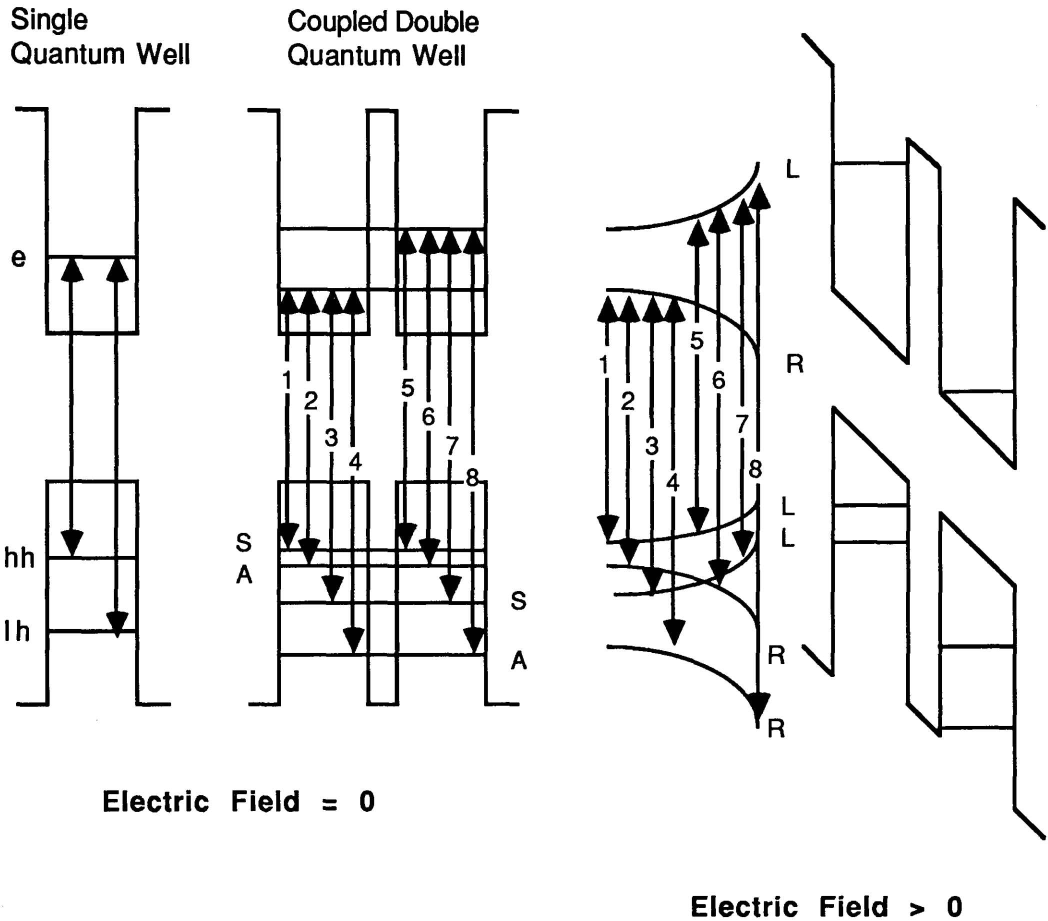

Figure 5.8.1 The effect of an electric field on the energy levels in a pair of coupled quantum wells (after Chen 1987)

In the coupled wells the wavefunctions become shared between both wells and then mix in a bonding or anti-bonding mode, see Figure 5.8.2. The energy band structure of the wells can be adjusted by applying an electric field to tilt the bands. On the application of an electric field in the symmetric case the hole and electron are forced in opposite directions and there is a reduction in the overlap of the wavefunctions. CQW's can be designed to obtain a large absorption change by varying the overlap between the electron and hole wavefunctions using the electric field. In principle the reduction in the overlap with this kind of structure may be larger than that of a comparable rectangular well, as a function of applied electric field.

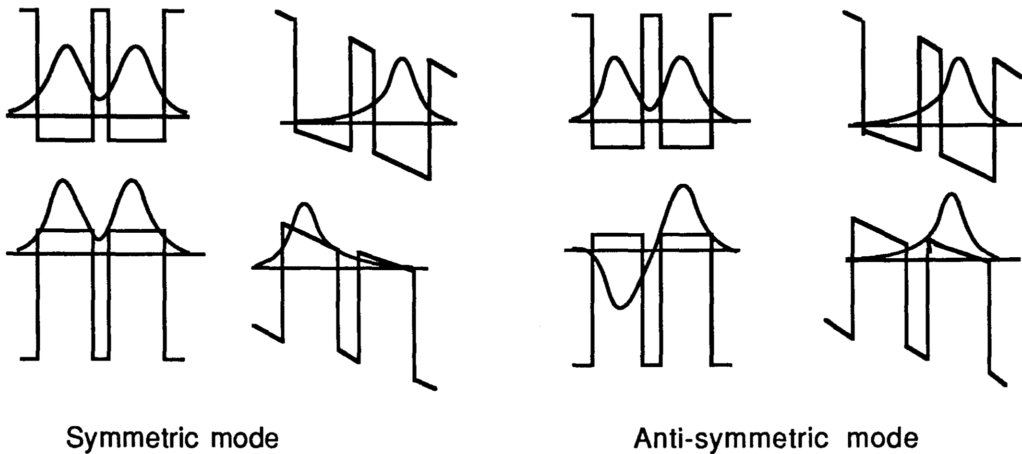

Symmetric mode Anti-symmetric mode

Figure 5.8.2 Coupling of the electronic wavefunction in a pair of coupled wells

5.8.1 Energy levels in pairs of coupled wells

Although the Kronig-Penney model can applied in the superlattice case where there is a finite but large number of wells it does not apply to this case with only two wells coupled. The method to calculate the energy levels for pairs of wells was proposed and carried out by James Whiteaway of STC Technology (private communication). This involved amending a finite difference program previously used to calculate waveguide parameters. The results of this calculation are presented later in the chapter.

5.9 Literature review : Coupled quantum wells

A limited amount of theoretical and experimental work has been carried out on pairs of coupled wells. Early work was carried out in waveguide structures : Islam et al [1987] demonstrated an electroabsorption waveguide modulator with a modulation depth of 14:1, which consisted of two 46 Å wells coupled through a 11.5 Å barrier. This performance was achieved by switching the applied voltage between 1.1 V and -2.4 V .

Coupled double quantum wells (CDQW) were also investigated by Chen [1988] Both intrawell and interwell exciton transitions were observed, as predicted by the theory outlined in Section 5.8. Photoluminescence (PL) and PL excitation techniques were employed to investigate a single pair of 75 Å GaAs wells coupled through an 18 Å $Al_{0.27}Ga_{0.73}As$ barrier. An external field was applied to counteract the built-in field of the diode. The transitions described in Section 5.8 could be observed for

this zero bias condition. On the application of an electric field, the previously forbidden transitions were observed in the absorption spectra. It was found that coupling the electronic levels in the structure led to an enhancement of the quantum-confined Stark effect , producing energy shifts as much as 5 times greater that of the single quantum well case for the same applied field.

Coupled well structures have also very recently been investigated by Atkinson [1990]. A GaAs/AlGaAs structure containing 5 pairs of 50 Å wells coupled through 15 Å barriers was investigated theoretically and experimentally. A low electric field (40 kV/cm) quenched the ground state transition and the e_1-hh_2 transition increased in magnitude.

5.10 Pairs of quantum wells layer design-CB 184

To improve upon the performance of CB 102, the intrinsic region of the superlattice was modified. This involved localizing the wavefunctions by confining them to only two wells anticipating that a more prominent 'blue shift' of the absorption edge would become visible. The layers were therefore modified to contain pairs of isolated wells as shown in Figure 5.10.1.

CQW region : CB 184		
AlGaAs 30%	50Å	x 100
GaAs	50Å	
AlGaAs 30%	30Å	
GaAs	50Å	

Figure 5.10.1 Pairs of coupled wells layer CB 184

5.11 Theoretical modelling of the absorption spectra of CB 184

The modelling of absorption spectra for pairs of coupled wells is essentially the same as that for the superlattice structure. The zero field energy levels were obtained by a different method as previously discussed in Section 5.8.1, and the

results are presented in Table 5.11.1. These values were then used in the computer program based on work by Bleuse, described in Appendix B, which was adapted to model the behaviour of only 2 wells. It is assumed that this model is valid for this structure as each pair of wells is considered to be isolated by thick enough barriers to prevent coupling between neighbouring pairs. The only difference between modelling one pair of wells, and the experimental structure which contained 100 pairs of wells will then be the magnitude of the absorption coefficient.

Well	Barrier	Effective Mass			Exciton Transition			
Width	Width	Electron	Heavy hole	Light hole	Heavy		Light	
Å	Å	$*m_0$	$*m_0$	$*m_0$	eV	nm	eV	nm
50	30	0.067	0.08	0.45	1.514	819.0	1.546	802.2

Temperature 300 K   Band misalignment 60/40

Table 5.11.1 Calculations of energy levels in the pairs of coupled wells (after Whiteaway)

The modelled absorption spectra for a range of electric fields are shown in Figure 5.11.2. For a low electric field of 10 V/cm there is only one transition in the wavelength region (780 nm - 850 nm), corresponding to the e_1-hh_1 transition at 821 nm and increasing the electric field by a factor of 10 has no effect on the spectrum. A further increase to 1 000 V/cm results in a new transition at a wavelength just below 821 nm, with the original transition red shifting slightly. The existence of these new transitions is explained in Section 5.8. When the field is as high as 10 000 V/cm many transitions can be observed in the spectrum and, as with the superlattice, depending on where the spectra are examined blue shifts or red shifts of the absorption spectra are observed. It is also possible to see the reduction in the oscillator strength of the original e_1-hh_1 transition, which is the lowest energy transition of this spectrum. The effect then saturates between 20 000 V/cm and 40 000 V/cm with the main transition occurring once more at 821 nm.

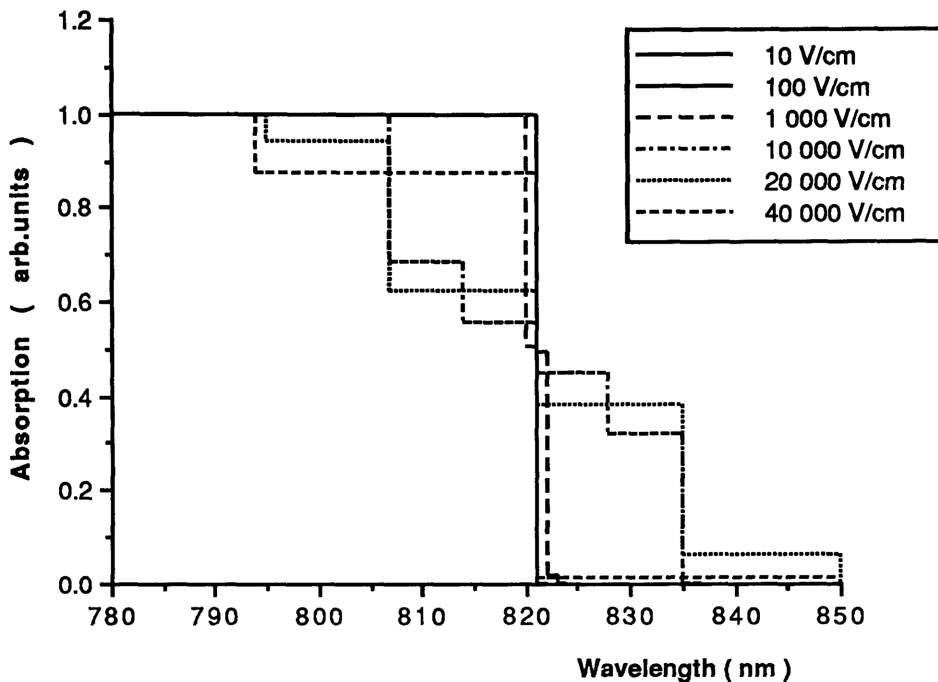

Figure 5.11.2 Theoretical modelling of absorption spectra of layer CB 184

5.12 Pairs of wells CB 184-Experimental results

Photocurrent spectra of sample CB 184 were acquired rather than transmission spectra. Transmission measurements could not be made as, on the removal of the substrate by chemical wet-etching cleaves appeared in the remaining epitaxial layers, as shown in Pictures 5.1 and 5.2, and it was impossible to make electrical contacts to them. No such problem occured before the substrate was removed and so photocurrent spectra were recorded. This photocurrent data was subsequently normalised by multiplying by the photon energy and then converting into transmission spectra, by estimating a maximum value of absorption, to allow a realistic estimate of the contrast ratio to be made.

A forward bias was placed on the device in attempt to counteract the built-in voltage of the diode, thus achieving a true zero biased condition, however the photocurrent spectrum was distorted to such an extent by this process that no sensible data could be recorded. Spectra were also recorded from zero applied bias down to an applied voltage of -1 V but the zero bias curve did not change until the latter voltage was

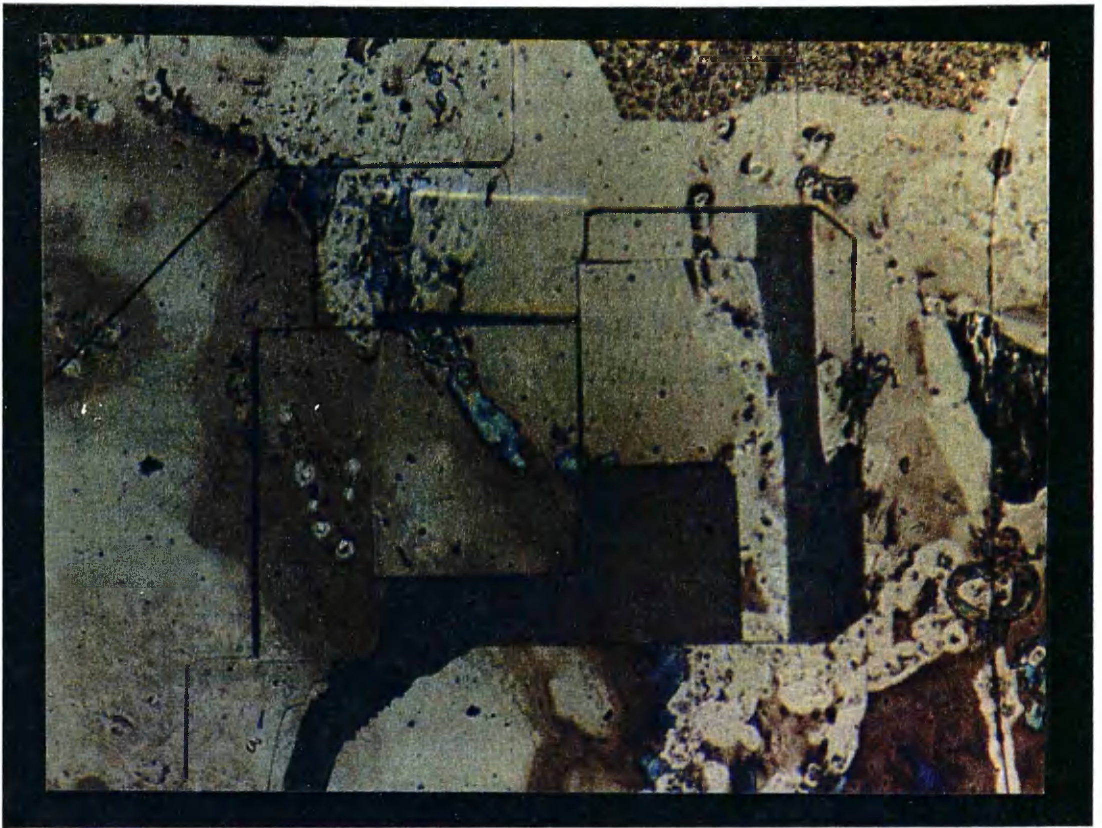

Photograph 5.1 The epitaxial layers of CB 184 after the removal of the substrate Area shown is at the edge of the crystal

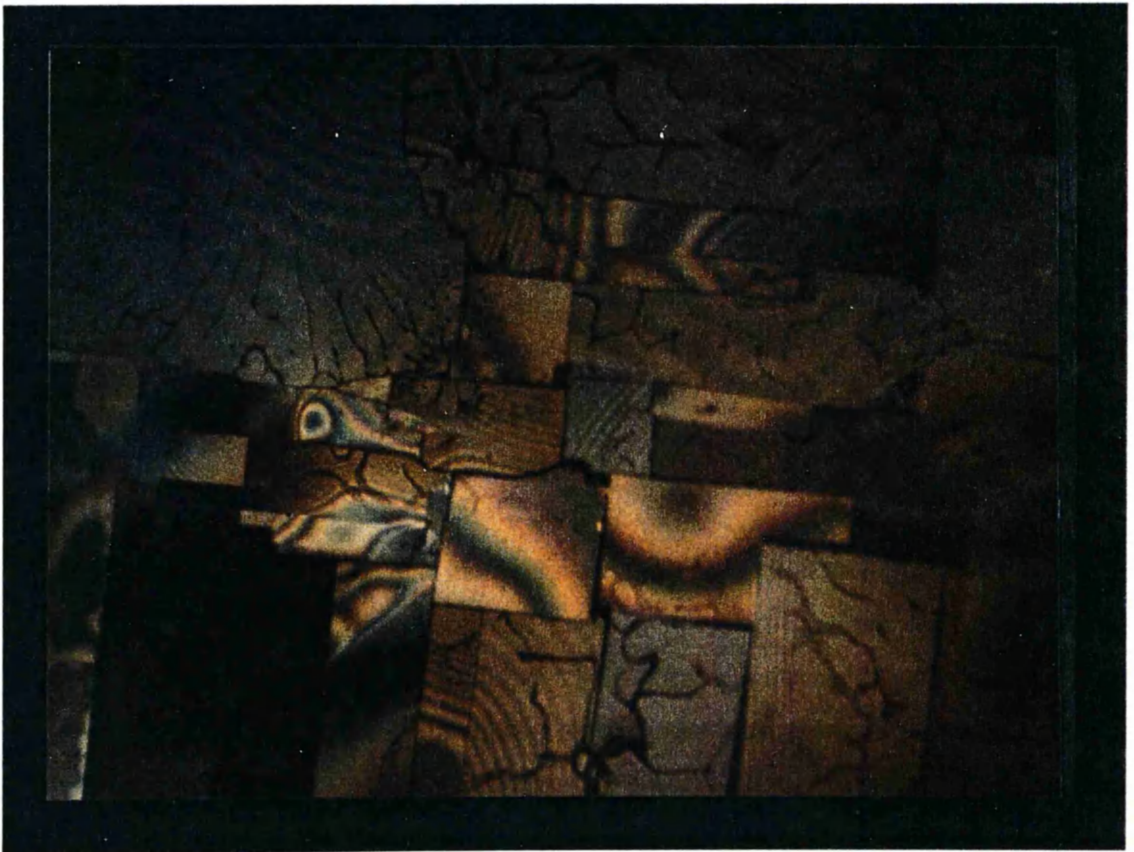

Photograph 5.2 The epitaxial layers of CB 184 after the removal of the substrate Area shown is at the centre of the crystal

reached.

The calculated low voltage transmission spectra are shown in Figure 5.12.1. The main transition, corresponding to the e_1-hh_1 transition in the zero applied voltage curve, occurs at 814 nm. On the application of a voltage of -1 V to the device an effective 'blue shift' of the absorption edge takes place. The main transition now occurs at 806 nm.

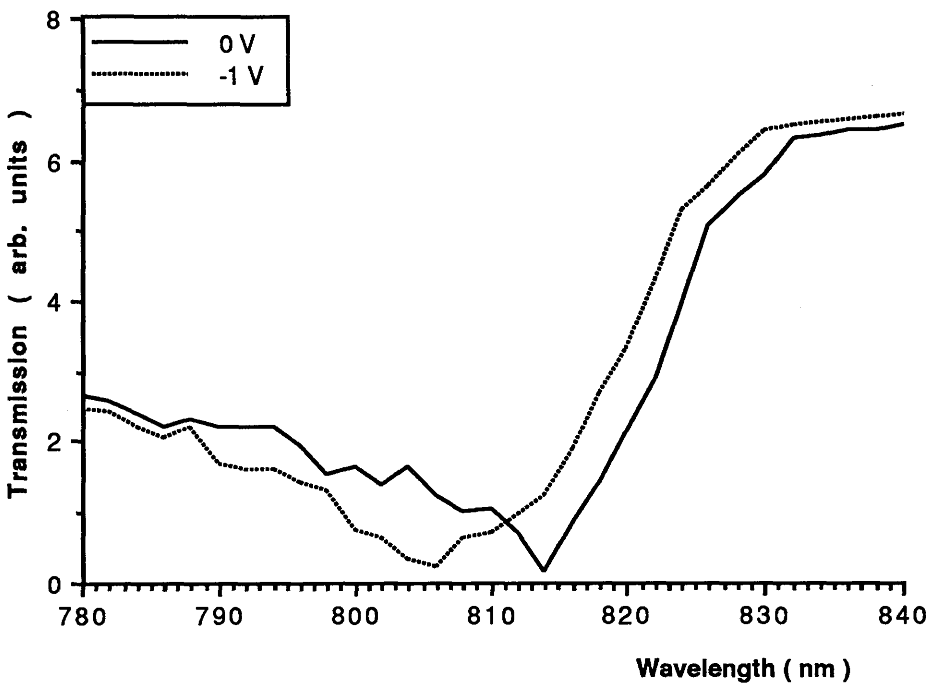

Figure 5.12.1 Transmission spectra of CB 184 obtained from photocurrent results for 0 V and -1 V

The applied voltage was then increased to -2 V, as shown in Figure 5.12.2. It can now be observed that the absorption edge is no longer clearly shifted to higher energies but is starting to shift in the low energy direction. Two reasons can be offered for this: the first is that many more transitions are now allowed and the measuring apparatus is not sensitive enough to discriminate between these, and the second is that the band bending effect described by the Franz-Keldysh effect is once more taking place. The highest absorption now occurs at a wavelength of 809 nm red

shifted by 3 nm from that of the the -1 V spectrum.

Further increasing the reverse voltage to -3 V results in removal of the 'blue shift'. From Figure 5.12.3 it can be seen that the absorption edge in the -3 V spectrum and in the zero applied bias occur at approximately the same wavelength with the main transition now occurring on the low energy side of the zero bias condition at 811 nm. There is also a reduction in the strength of the main absorption peak for a bias of -3 V.

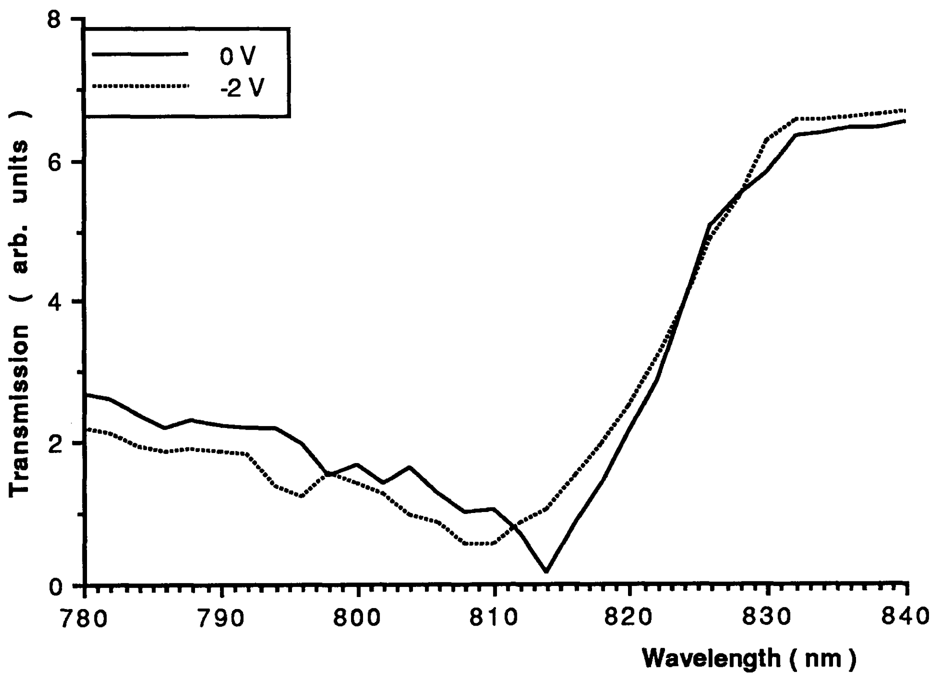

Figure 5.12.2 Transmission spectra of CB 184 at 0 V and -2 V

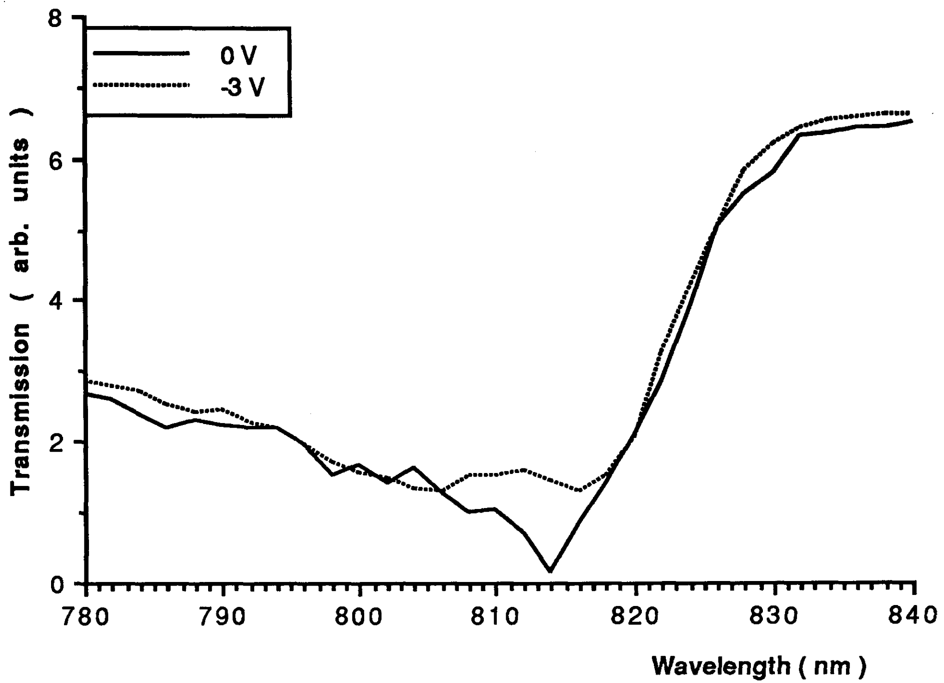

Figure 5.12.3 Transmission spectra of CB 184 at 0 V and -3 V

The red shift of the main absorption transition continues as the reverse voltage is further increased (see Figure 5.12.4), although as in the previous spectra it is difficult to positively identify the various transitions from these curves. The peak strength of the absorption is also continuing to weaken.

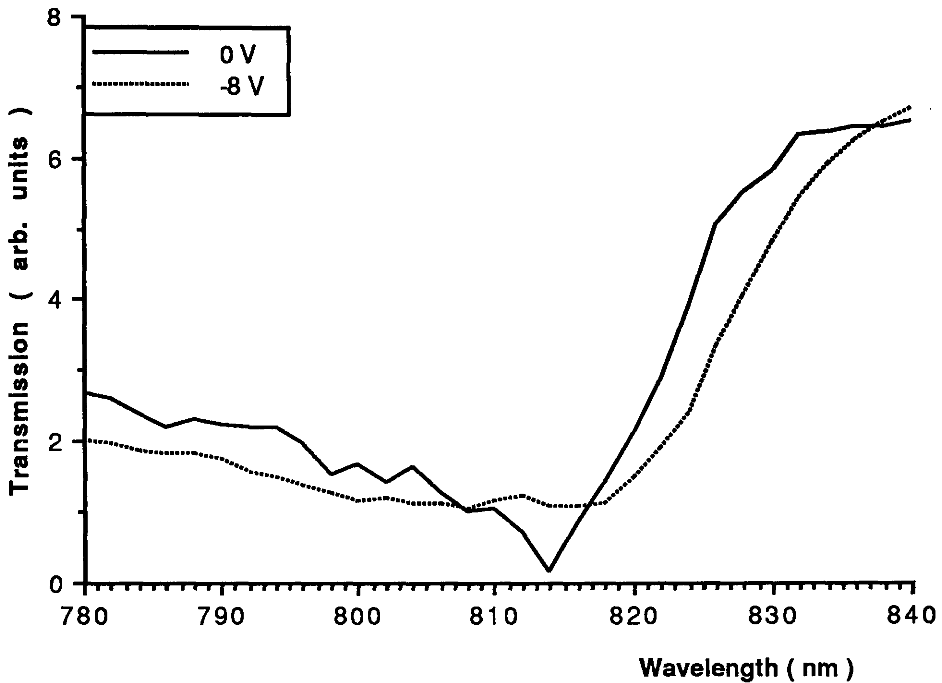

Figure 5.12.4 Transmission spectra of CB 184 for 0 V and -8 V

5.13 Comparison between experimental and theoretical results-CB 184

As with the superlattice results, in order to compare the experimental results with the computer model it is necessary to calculate the actual electric field in the diode including the built-in voltage. The built-in voltage was once more assumed to be 1.4 V, corresponding to an electric field of 7 800 V/cm in the diode at zero applied electric field.

In Figure 5.13.1 the theoretical spectra corresponding to applied voltages of -1 V and 0 V are shown. These can be directly compared to the results presented in Figure 5.12.1. One interesting feature of the theoretical curve is that many more transitions exist for the higher electric field condition than the lower. The wavelengths at which transitions occur in both the theoretical and experimental results agree more closely than in the case of the superlattice results. For example, consider the 0 V condition for both sets of data. Theoretically transitions occur at 810, 821 and 834 nm. In the experimental results transitions occur at 808, 814 (both clear transitions), 822 and 826 nm (neither of which are very well defined).

There is therefore some agreement between the two sets of data. A clearer comparison can be made by considering the crossover points between the spectra for 0 V and -1 V. In both the experimental and theoretical spectra there is a crossover point at 811 nm where the higher electric field curve experiences less absorption than the lower. In addition however the theoretical curve contains many more crossover points than the experimental one. Finally if the size of the blue shift is observed for the theoretical results then there is a 'blue shift' from 810 nm to 807 nm and also 821 nm to 814 nm. Experimentally there is a 'blue shift' from 814 nm to 806 nm and also from 822 nm to 814 nm. It can therefore be concluded that there is reasonable agreement between theory and experiment.

The highest electric field experimentally investigated for this structure was 5.2 x 10^4 V/cm (8 V) and the device behaviour is now dominated by a 'red shift' of the absorption edge which is not predicted theoretically. Theoretically transitions exist only at two wavelengths, namely 858 nm and 821 nm but experimentally there is a transition at 815 nm and possibly also at 824 nm. In the experimental data a possible 'blue shift' exists from 817 nm to 808 nm but the spectrum is dominated by a red shift between 824 nm and 827 nm. In the theoretical data there are 'blue shifts' from 834 nm to 821 nm and 810 nm to a non determined wavelength. Two red shifts are also present, from 810 nm to 821 nm and 834 nm to 858 nm. Thus is little agreement between the predicted theoretical results and those obtained experimentally for this electric field.

The theoretical model shows saturation at electric fields lower than the maximum field applied to this device (> 25 000 V/cm). Above this field however the QCSE still operates which the model does not account for. From the experimental results it would appear that it is the QCSE which is occurring at the higher electric field values.

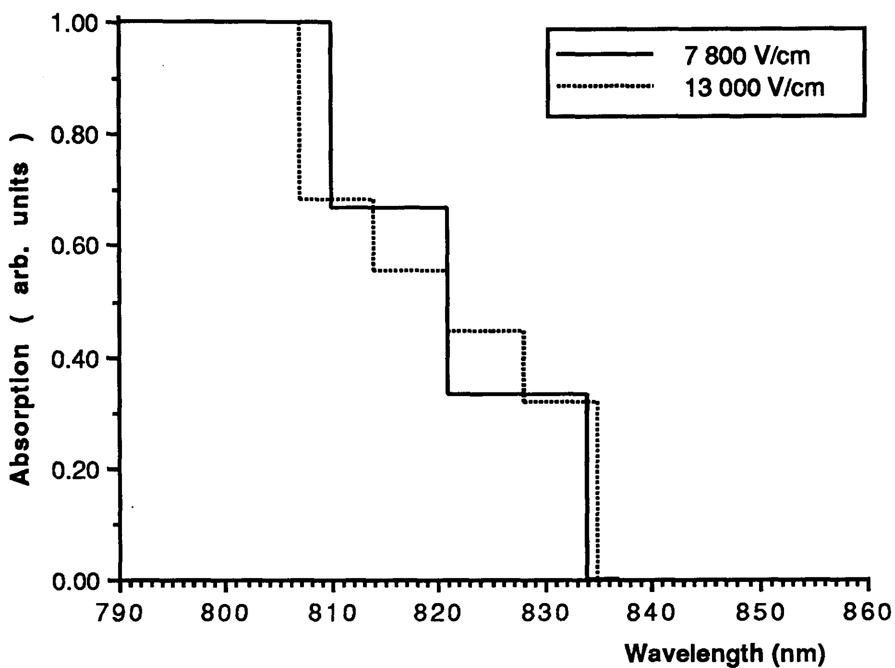

Figure 5.13.1 Theoretical absorption spectra of CB 184 corresponding to 0 V and -1 V

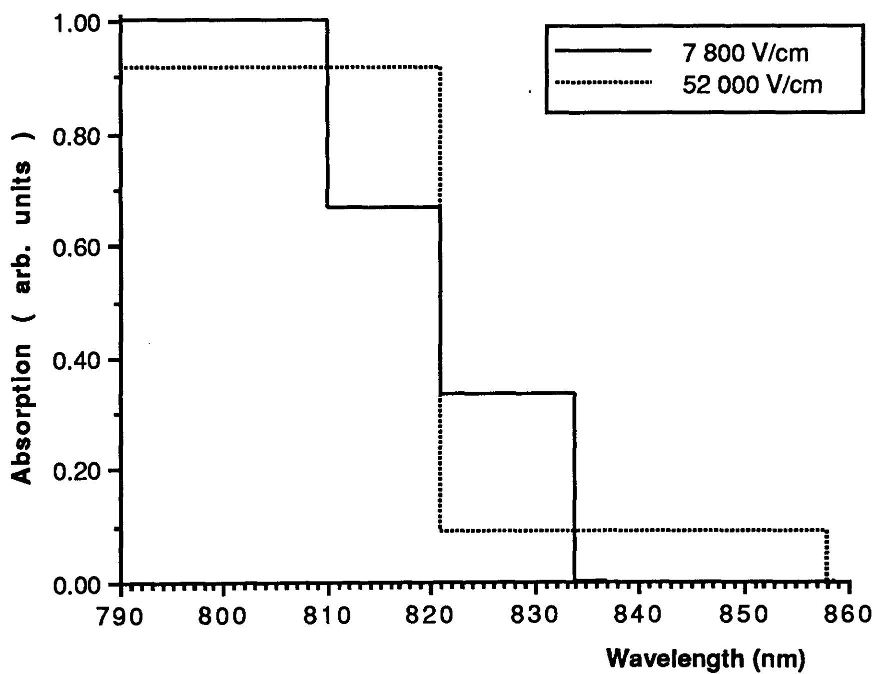

Figure 5.13.2 Theoretical absorption spectra of CB 184 corresponding to 0 V and -8 V

Experimentally the blue shift of the absorption edge saturates for an applied voltage of -3 V (24 000 V/cm), as shown in Figure 5.13.4. A similar effect is predicted by the theoretical model at this field, as shown in Figure 5.13.3. The theoretical zero bias spectrum (7 800 V/cm) is very similar to that of 24 000 V/cm spectrum. The same number of transitions are present, which does not occur for fields above or below 24 000 V/cm, and these transitions take place at wavelengths close to those exhibited by the zero bias condition. It is there reasonable to assume that the behaviour of the experimental results are accurately predicted by the theoretical model at this value of electric field.

The simple model used adequately predicts the behaviour of the coupled well structure, particularly at fields <24 000 V/cm. Even at higher fields there are similarities between the theoretical and experimental results. The red shift due to normal Stark shift at the highest field investigated 5.5 x 10^4 V/cm, could not be properly accounted for.

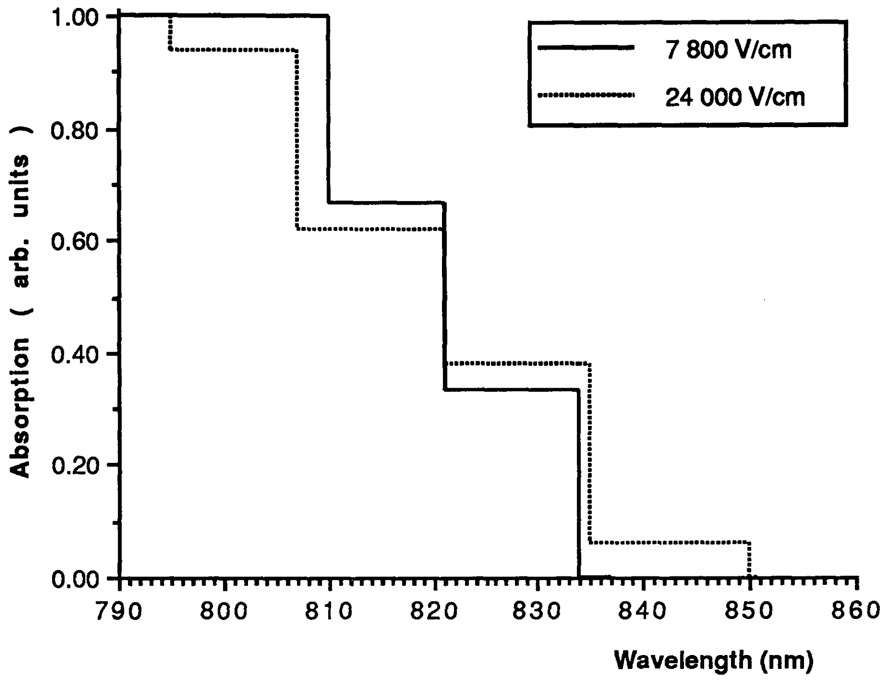

Figure 5.13.3 Theoretical absorption of of CB 184 at 24 000 V/cm

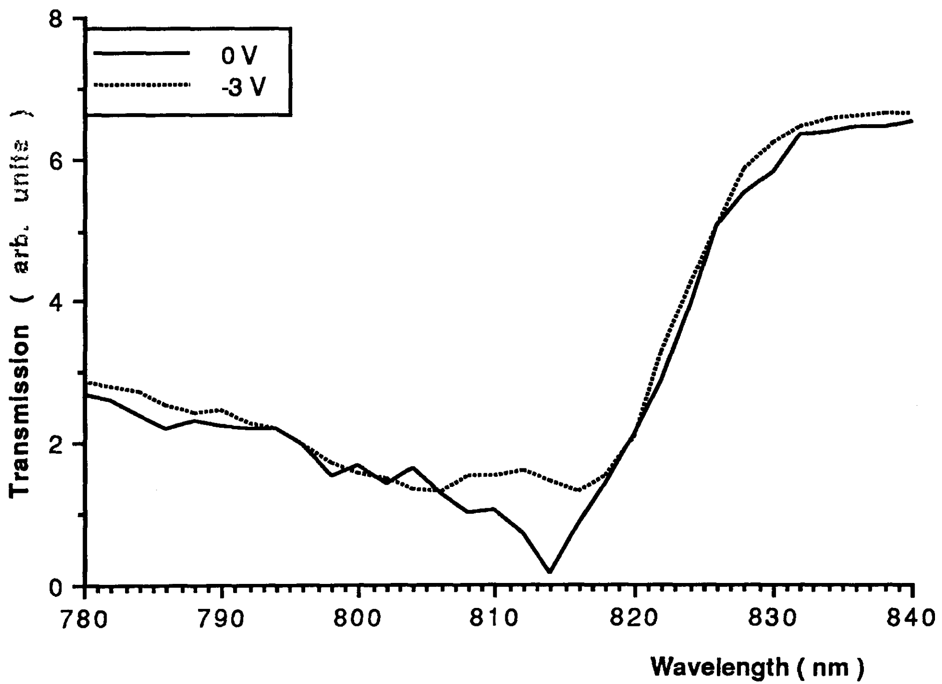

Figure 5.13.4 Experimental saturation of the 'blue shift' in CB 184

5.14 Contrast ratio of CB 184

The experimental spectra of Section 5.13 were used to estimate the contrast ratio which would be obtained from an electroabsorption modulator fabricated from a structure containing 100 pairs of coupled wells. As previously described the photocurrent spectra were transformed into transmission spectra and the latter used to estimate the optical contrast ratio for various values of electric field. A few examples of this are presented in this section. The aim of the coupled well structures was to obtain a high contrast ratio device using a low drive voltage. Figure 5.14.1 is a plot of the contrast ratio obtained between 0 V and -1 V for CB 184. It is possible to see that the aim of the experiment has been fulfilled with a maximum contrast ratio of 7.5:1 (8.7 dB) being obtained for this voltage at a wavelength of 814 nm. This value of optical contrast is very sensitive to the maximum value of absorption chosen to convert the photocurrent spectra and may, in fact, be an underestimate. Maximum contrast occurs at the position of the absorption peak for the zero bias spectrum and therefore a device switched between 0 and –1 V would operate in normally off mode.

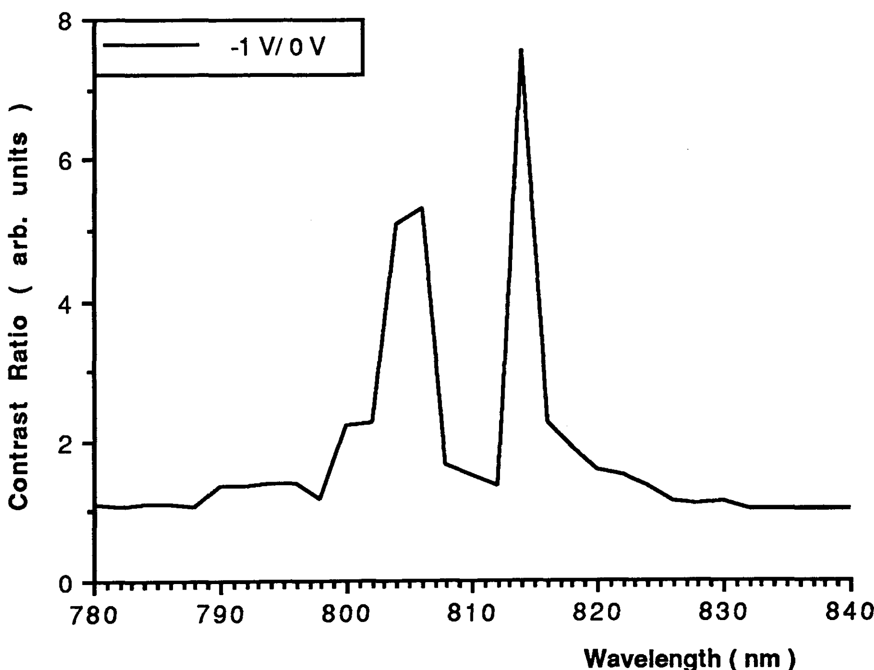

Figure 5.14.1 Contrast ratio between 0 V and -1 V spectra for CB 184

Increasing the voltage to -2 V results in a slightly reduced contrast ratio of 6.5:1 at the same wavelength, 814 nm, as shown in Figure 5.14.2.

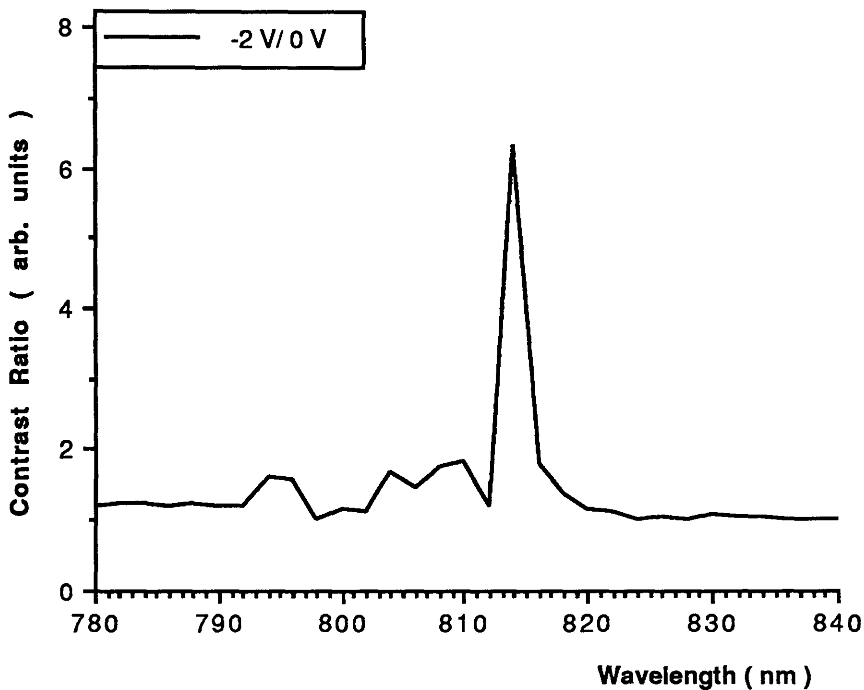

Figure 5.14.2 Contrast ratio between 0 V and -2 V spectra for CB 184

At higher applied voltages, after the blue effect has saturated, there is maximum contrast of 5:1 at an applied reverse voltage of -8 V (Figure 5.14.3). This time however the wavelength providing this contrast is 805 nm. The contrast of 2.4:1 occurring at 820 nm is not as sensitive to the values used in the calculation and a device operated at this wavelength would works in a normally on mode. This device has the potential to operate at much lower voltages than the isolated well structure while still providing competitive contrast ratios.

The insertion loss for the device operating at –1 V in transmission can also be estimated from the calculated values. This varies from 7.3 dB at the zero bias exciton peak to 14 dB at lower wavelengths. This figure is improved upon by operating at an applied voltage of –8 V, where the contrast of 4 dB is accompanied by a low insertion loss of 3 dB, with an accompanying value of 7.7 dB at shorter wavelengths where the optical contrast is 7 dB.

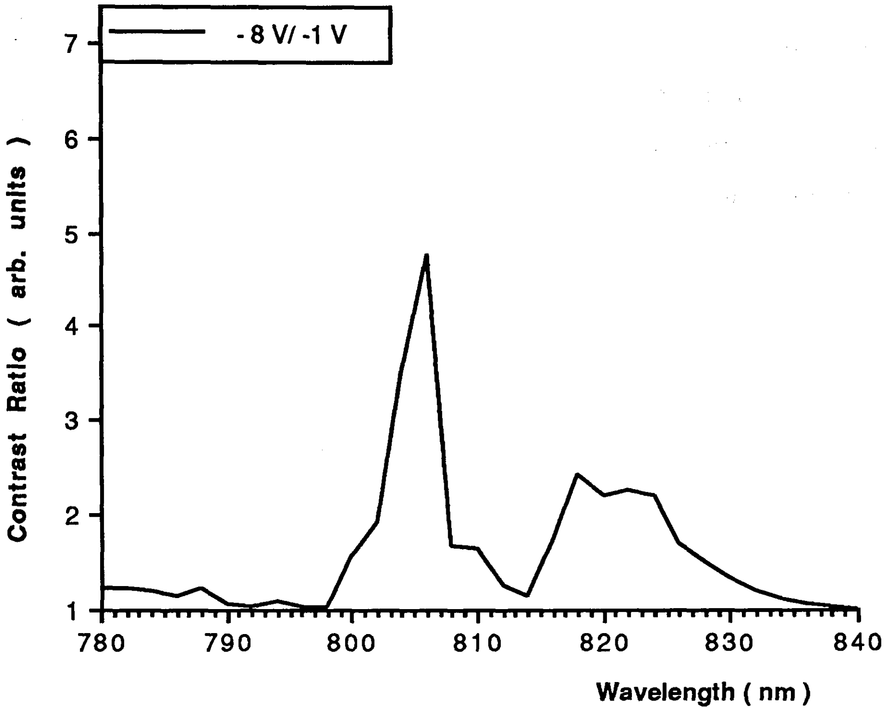

Figure 5.14.3 Contrast ratio between -1 V and -8 V spectra for CB 184

5.15 Discussion and conclusion

The design and fabrication of two coupled well structures has been undertaken. In the first structure 200 wells were coupled together to form a superlattice. As with the previous isolated well device an electroabsorption transmission modulator was fabricated. On assessing this device however it was found that rather than any clear 'blue shift' of the absorption edge taking place on the application of a reverse voltage, the effect observed is similar to the Franz-Keldysh effect. This is not surprising considering that the electronic wavefunctions are not inhibited from tunneling through the thin barriers, leading to a large reduction in overlap between them.

The spectra were compared with theory and it was possible to draw a few comparisons between the two sets of data. Both sets of data showed many transitions for the condition of zero applied bias, although it was more difficult to determine the position of these transitions in the experimental data. When the electric field was increased the number of transitions decreased in both the theoretical and experimental results. The most interesting feature of the comparison is that there

were many crossover points between the zero applied condition and that of an applied reverse voltage. It is at these positions that 'blue shifts' of the absorption edge appear to take place. The wavelengths of the crossover points between theoretical and experimental results are often similar but uncertainties in the well width of the experimental structure and effects of unintentional doping and non uniform electric field mean that the modelled and experimental results are not in perfect agreement.

On the basis of the experimental results obtained for the superlattice structure CB 102, a new active layer was designed. The previous results had shown that it was not possible to see a clear shift of the absorption edge in either direction. It was decided that the probable reason for this was that the wavefunction could tunnel throughout the structure unhindered by the thin barriers. In the case of isolated wells the Franz-Keldysh effect was enhanced over bulk materials by confining the wavefunction to potential wells, and the logical step from the superlattice structure to an enhanced modulator was also to confine the wavefunction, but without completely destroying the effect due to coupling. This was achieved by forming pairs of coupled wells, where thick barriers 50 Å were used to isolate pairs of 50 Å wells coupled by 30 Å barriers.

Unfortunately in this case it was impossible to fabricate a transmission electroabsorption modulator as the epitaxial layers fractured on removal of the substrate. It was however possible to assess the structure using photocurrent spectroscopy. The photocurrent results showed a clear 'blue shift' of the absorption edge for an applied voltage of -1 V. This effect saturated at -3 V and then the absorption edge appeared to red shift to lower energies.

There was reasonable agreement between the experimental and theoretical behaviour of this structure up to fields of 30 kV/cm, with transitions occurring at similar wavelengths and similarities in the magnitude of the shifts. Most significantly, in both sets of results the effect saturated at the same value of electric field, -3 V (24 000 V/cm). Discrepancies between theory and experimental results are probably due to uncertainty in the well and barrier width. At higher fields the model broke down but the experimental data showed a red shift.

From these results it was possible to deduce that it is possible to fabricate a low drive voltage (-1 V) normally off modulator capable of a maximum contrast ratio 7.5:1 (8.75 dB) at 814 nm using pairs of coupled wells. Other low electric fields also provide equally competitive contrast ratios for this layer design e.g. –8 V giving an optical contrast of 5:1 (7 dB). Future work in this area would be to test a new layer of this design capable of operating as a reflection modulator. Optimised devices could also be designed on the basis of the theoretical model which closely predicted the behaviour of the coupled wells.

The coupled pairs of wells coupled also be used to fabricate a SLM. Due to the nature of the shifts, both blue and red, achieved with this design it would be possible to make a very low drive voltage device capable of high contrast ratios at a number of wavelengths.

Chapter Five : References

D. ATKINSON, G. PARRY and E.J. AUSTIN
'Modelling of electroabsorption in coupled quantum wells with applications to low-voltage optical modulation'
Semiconductor Science Technology 5
Page 516-524
1990

G. BASTARD, J. BLEUSE, R. FERREIRA and P.VOISIN
'Wannier-Stark Quantization in Semiconductor Superlattices'
Superlattices and Microstructures Volume 6 Number 1
Page 77-81
1989

J. BLEUSE, G. BASTARD and P.VOISIN
'Electric-Field Induced Localization and Oscillatory Electro-optical Properties of Semiconductor Superlattices'
Physics Review Letters Volume 60 Number 3
Page 220-223
18 January 1988

J. BLEUSE and P.VOISIN
'Blue shift of the absorption edge in AlGaInAs-GaInAs superlattices: Proposal for an original electro-optical modulator'
Applied Physics Letters Volume 53 Number 26
Page 2632- 2634
26 December 1988

Y.J. CHEN, E.S. KOTELES, B.S. ELMAN and C.A. ARMIENTO
'Effect of electric fields excitons in a coupled double-quantum-well structure'
Physical Review B Volume 36 Number 8
Page 4562- 4565
15 September 1987

N. DEBBAR, S. HONG, J. SINGH, and P. BHATTACHARYA
Coupled GaAs/ AlGaAs quantum well electroabsorption modulators for low electric field optical modulation'
Journal of Applied Physics Volume 65 Number 1
Page 383-385
1 January 1989

L. FRIEDMAN, W.L. BLOSS and G. COOPERMAN
'Enhanced optical nonlinearities of superlattices within the Kronig-Penney model incorporating inherent bulk nonlinearities'
Superlattices and Microstructures Volume 1 Number 3
Page 193- 196
1985

M.N ISLAM, R.L. HILLMAN, D.A.B. MILLER, and D.S. CHEMLA
A.C. GOSSARD and J.H. ENGLISH
'Electroabsorption in GaAs/AlGaAs coupled quantum well waveguides'
Applied Physics Letters Volume 50 Number 16
Page1098- 1520
20 April 1987

H.Q. LE, J.J. ZAYHOWSKI and W.D. GOODHUE
'Stark effect in modulator AlGaAs/GaAs coupled quantum wells'
Applied Physics Letters Volume 50 Number 21
Page 1518- 1520
25 May 1987

H.Q LE, J.V. HRYNIEWICZ, W.D. GOODHUE and V.A.MIMS
'Optical nonlinearities in AlGaAs/GaAs asymmetric coupled quantum wells'
Optics Letters Volume 13 Number 10
Page 859-861
October 1988

D.A.B. MILLER
'Optical bistability in self-electro-optic effect devices with asymmetric quantum wells'
Applied Physics Letters Volume 54 Number 3
Page 202-204
16 January 1989

H. ONOSE, H. YOSHIMURA and H. SAKAKI
'Field-induced decoupling of quantized levels and blue shift of absorption edge in a potential inserted quantum well'
Applied Physics Letters Volume 54 Number 22
Page 2221- 2223
29 May 1989

M.A. REED and J.W. LEE
'Resonant tunneling in a GaAs/AlGaAs barrier/InGaAs quantum well heterostructure'
Applied Physics Letters Volume 50 Number 13

Page 845- 847
30 March 1987

R.P VASQUEZ
'Use of the R-matrix propagation technique to calculate the electronic energy levels of aperiodic structures: Application to an AlAs/GaAs quasiperiodic superlattices'
Journal of Applied Physics Volume 62 Number 8
Page 3237- 3240
15 October 1987

P. VOISIN and J. BLEUSE
C.BOUCHE, S GALLIARD and C. ALIBERT
'Observation of the Wannier-Stark Quantization in a semiconductor superlattice'
Physics Review Letters Volume 61 Number 14
Page 1639- 1642
1988

CHAPTER SIX
CONCLUSIONS

6 Conclusion

The investigation of multiple quantum well modulators has been undertaken : three transmission electroabsorption modulator were studied, an isolated well device, a coupled well superlattice device and a device in which pairs of coupled wells were isolated from each other by barriers. The isolated device was subsequently fabricated into a 4 x 4 array for use a spatial light modulator.

Each of the modulators were designed to incorporate equal amounts of GaAs in their intrinsic regions, thus with the same amount of absorbing material in the devices direct comparison of the absorption coefficient is possible. This was found to vary slightly between the three structures. For the isolated well device where the amount of GaAs in the intrinsic region was 1.24 μm, the maximum value of the absorption coefficient was 39000 cm^{-1}. For the pairs of coupled wells device this was reduced to 36000 cm^{-1} with the amount of GaAs in the intrinsic region designed to be 1 μm. A lower maximum absorption coefficient of 29000 cm^{-1} was obtained for the superlattice device which was also designed to have 1 μm of GaAs in the intrinsic region. The discrepancy between these values arises because the actual width of the wells in the intrinsic region were not determined for layers CB 102 and CB 184. This could have been performed using TEM but access to such equipment was not available.

For the isolated well structure, layer CB 2, the maximum $\Delta\alpha$ was calculated to be 16000 cm^{-1} at 837 nm for a drive voltage of -25 V, as shown in Figure 6.1. A much reduced value of 1100 cm^{-1} was found for the coupled well superlattice, which was attributed to the inability of this structure to prevent the wavefunction from tunneling through the thin barriers (Figure 6.2).

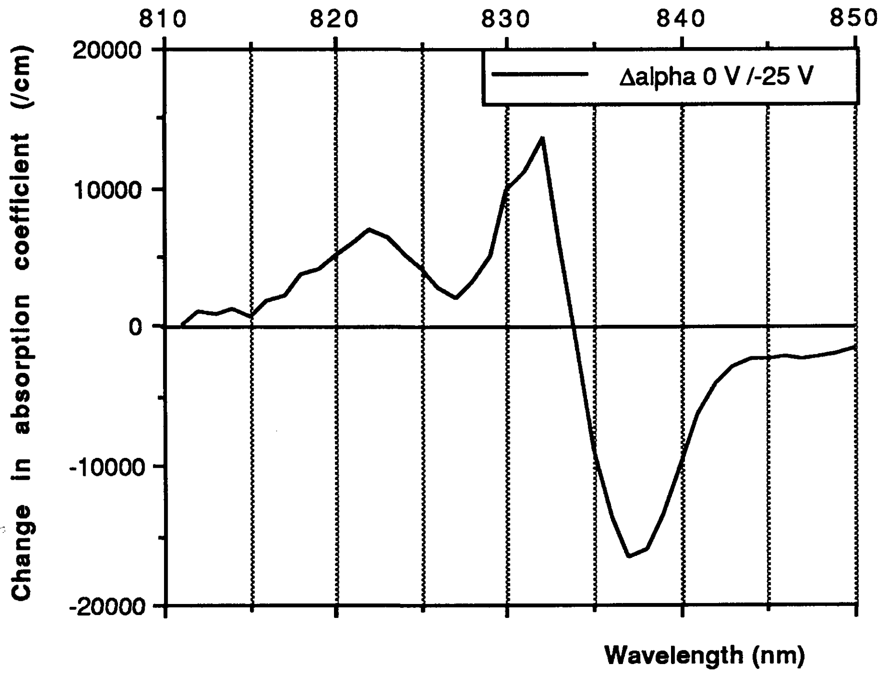

Figure 6.1 Maximum change in the absorption coefficient obtained for CB 2

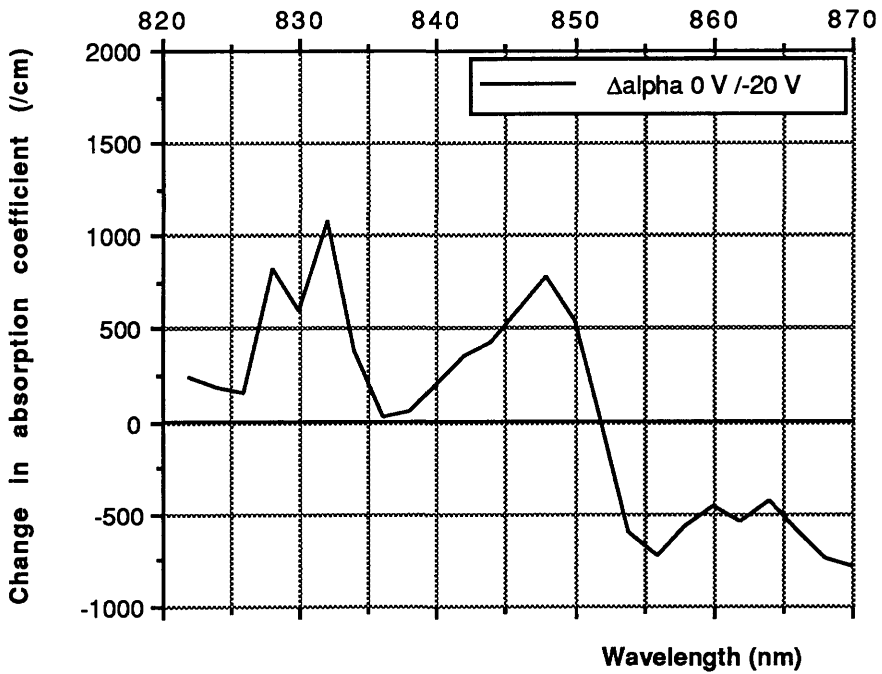

Figure 6.2 Maximum change in the absorption coefficient obtained for CB 102

In the coupled pairs of well device, where coupling of the wavefunction was still exploited but confined to two wells, a much larger $\Delta\alpha$ was obtained. For a drive voltage of -1 V $\Delta\alpha$ was found to be 20000 cm^{-1} at a wavelength of 814 nm, as shown in Figure 6.3. This device exhibited interesting behaviour and up to fields of 24 000 V/cm closely followed the theoretically expected behaviour. The results however were obtained using photocurrent spectroscopy and so there is some uncertainty about the actual performance that would be obtained from a transmission modulator.

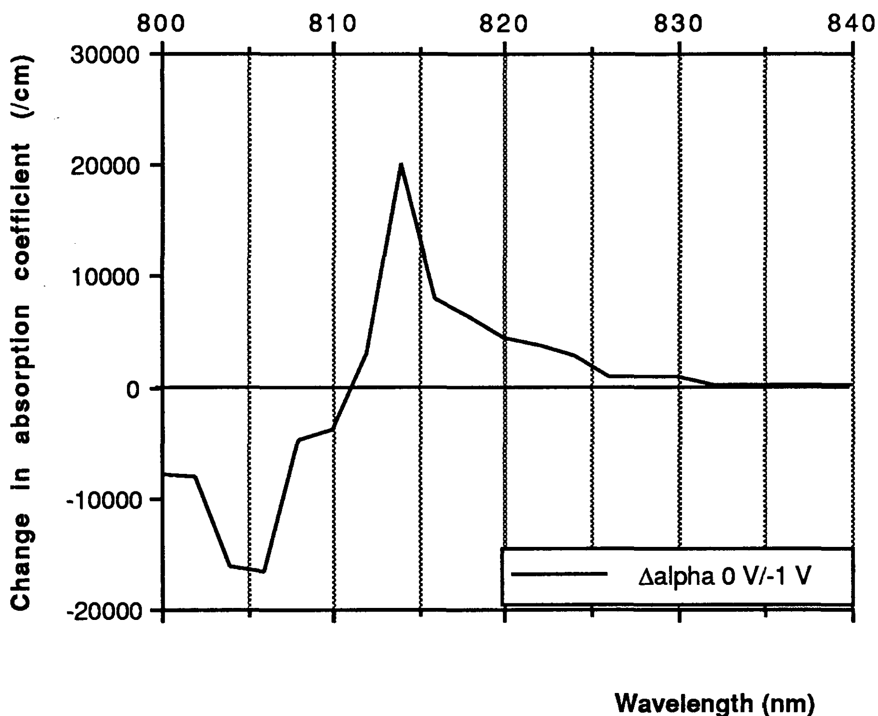

Figure 6.3 Maximum change in absorption obtained for CB 184

The isolated well device exhibited a high contrast ratio 8.95 dB for a drive voltage of –25 V at a wavelength of 837 nm. The insertion loss at this wavelength was 4.9 dB which, by the use of anti-reflection coatings, could be reduced to 1.9 dB. At lower drive voltages (–20 V) a useful optical contrast is also obtained (8.26 dB).

The isolated well modulator was used to form the elements of a 4 x 4 array of an SLM. Using a more complicated fabrication process than required for the single devices, it was possible to make an SLM capable of being both optically and electrically addressed. The operation of the device was not significantly affected by

the line addressing system employed which resulted in a voltage half the drive voltage being applied to non-selected elements. However the crosstalk involved due to this determined that the device should be operated at 838.1 nm and the optical contrast would be reduced to 6.1 dB. The advantage of using such an addressing system is that it can be easily utilised in larger arrays.

The superlattice device investigated did not exhibit high contrast ratios but rather the behaviour was similar to that observed for bulk devices. There were some similarities between the experimental and theoretical behaviour of the layer design, but uncertainties in the well widths and the non uniform electric field meant that complete agreement could not be obtained. The second of the two coupled well structures CB 184, which incorporated pairs of wells isolated by thick barriers, exhibit the highest change in the absorption coefficient of the three devices. This was 20000 cm^{-1} at a wavelength of 814 nm for an applied bias of –1 V. The behaviour of this device was also adequately predicted by theory at electric fields <24 000 V/cm. Above this field the device exhibited the red shift normally observed in isolated well structures.

In future work the incorporation of the coupled pairs of well design in the SLM could lead to an array device capable of high optical contrast over a large wavelength range, with very low voltages required to drive it. The structure described as part of this work layer CB 184 could be optimised further by using the theoretical model described in Chapter 5. Finally, if the pairs of coupled wells were incorporated in a reflection modulator such as those mentioned in Chapter 1 then very large optical contrast ratios should be possible at low electric fields and thus low drive voltages. The use of reflection mode enhances the contrast ratio by ~ 14 dB [G. Parry private communication].

Appendix A

Theoretical model to calculate the energy levels and the miniband widths of a superlattice

The Kronig-Penney model was outlined in Chapter 2. This model can be used to determine information about the energy bands of a superlattice structure where the barriers between the wells is thin enough to allow coupling between them.

This model is adapted to account for the effective mass difference. The equations derived for this method, are summarised below and the help and work on this by Clivia Sotomayor Torres of this Department is gratefully acknowledged.

Consider a superlattice with well width a, barrier thickness b and barrier height V as shown in Figure A.1

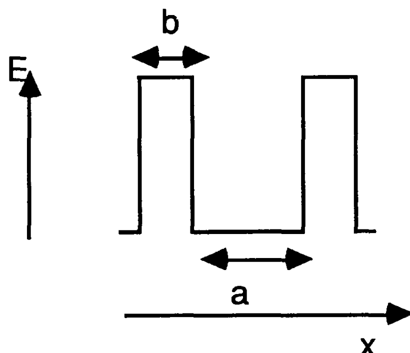

Figure A.1 Superlattice Structure

Let the mass in the well be m_w, that is the GaAs mass, and the mass in the barrier be m_b, that is the AlGaAs mass. The miniband dispersion relation E(k) is given by:

E < V

$$\frac{\frac{v}{r} - \varepsilon r}{2\sqrt{v\varepsilon}} \sinh(\sqrt{v}\, f) \sin(\sqrt{\varepsilon}(1-f)) + \cosh(\sqrt{v}\, f) \cos(\sqrt{\varepsilon}(1-f)) = \cos(k)$$

E > V

$$\frac{-\frac{v}{r-\varepsilon r}}{2\sqrt{v\varepsilon}} \sin(\sqrt{v}\,f)\sin(\sqrt{\varepsilon}(1-f)) + \cos(\sqrt{v}\,f)\cos(\sqrt{\varepsilon}(1-f)) = \cos(k)$$

E = V

$$\frac{-\sqrt{\varepsilon}\,r\,f}{2} \sin(\sqrt{\varepsilon}(1-f)) + \cos(\sqrt{\varepsilon}(1-f)) = \cos(k)$$

where the dimensionless parameters are:

$$\varepsilon = 2(a+b)^2 m_w \frac{E}{\hbar^2}$$

$$v = 2(a+b)^2 m_b \frac{|V-E|}{\hbar^2}$$

$$k = (a+b)\,k$$

$$f = \frac{b}{(a+b)}$$

$$r = \frac{m_b}{m_w}$$

The solutions of these give the minibands. By plotting E against k the miniband edges can be obtained. These occur when $k=n\pi$, that is the roots of 1, 2, and 3 when cos(k)= -1 or 1.

A computer program called Kronig-Penney was written to provide these solutions and using the relevant parameters results for the superlattice structure CB 102 were obtained.

Appendix B

Theoretical modelling of the absorption spectrum for a superlattice structure

The modelling in this thesis of the absorption spectra was based directly on that demonstrated by Bleuse [1988].

The electroabsorption of a superlattice is studied here within the framework of a tight binding analysis of the envelope wavefunctions, where several approximations have been used. A (2N+1) period superlattice terminated by infinite potential barriers is considered. A constant electric field F is applied along the growth axis z, and the associated electrostatic potential eFz vanishes at the centre of the structure. Let $\phi(z)$ be the envelope eigenfunction of the ground state of an isolated quantum well centered at the origin. In the simple nearest neighbour tight binding analysis, only one level per quantum well is retained, and the superlattice eigenstates are expanded as

$$\chi_q(z) = \sum_{-N}^{N} c_{nq}\, \phi(z - nd) \qquad \text{B.1}$$

At zero electric field, this method leads to the well known quasicontinuous spectrum of the conduction miniband:

$$\varepsilon_q = E_1 - 2\lambda_c \cos(qd) \qquad \text{B.2}$$

with

$$qd = \frac{i\pi}{2(N+1)} \quad (1 \le i \le 2N+1) \qquad \text{B.3}$$

The corresponding eigenfunctions are extended through the entire structure, as

$$c_{nq} = \left[\frac{1}{(N+1)}\right]^{\frac{1}{2}} \begin{cases} \sin(nqd), \text{ with } qd = \dfrac{j\pi}{(N+1)} & (1 \le j \le N) \\ \cos(nqd), \text{ with } qd = \dfrac{\left(j' + \frac{1}{2}\right)\pi}{(N+1)} & (0 \le j' \le N) \end{cases} \qquad \text{B.4}$$

With the same assumptions, in the presence of an electric field F strong enough so that the total potential drop is larger than the miniband width ($2\lambda_c \ll NeFd$), the same tight-binding analysis predicts that the miniband spectrum is replaced by an evenly spaced spectrum hereafter called a Wannier-Stark ladder,

$$\varepsilon_v = E_1 + veFd, \qquad -N \leq v \leq +N \tag{B.5}$$

and the corresponding eigenfunctions are given by equation 1, with

$$c_{nv} = J_{n-v}\left(\frac{2\lambda_c}{eFd}\right) \tag{B.6}$$

where J_m is the Bessel function of integer index m. The asymptotic expansion of J_{n-v} for small arguments yields

$$c_{nv} = \left[\frac{1}{(|n-v|)!}\right]\left(\frac{\lambda_c}{eFd}\right)^{|n-v|} \tag{B.7}$$

which corresponds, at large electric fields, to a faster than exponential localization of the wave function of state v in the vicinity of the quantum well of the same index.[Kazarinov 1972 and Luban 1987]

It can be shown that the difference between the exact spectrum and the regular spaced ladder is an edge effect, which becomes negligible for most of the states v<N, as soon as N becomes large. It is thus relevant to calculate the absorption spectrum using the spectrum given be equation B.5 and the associated wave functions, equation B.6. In the limit of thick superlattices, the absorption is found to be equal to

$$\alpha(\hbar\omega) = (2N+1)\alpha_o \sum_{m=-N}^{+N} J2_m\left(\frac{-2}{f}\right) Y\left(\hbar\omega - \left(E_g + E_1 + H_1 + meFd\right)\right) \tag{B.8}$$

E_g	bandgap of the well material
Y	the unit step function
f	$= \dfrac{eFd}{\lambda_c + \lambda_v}$
λ_c	the modulus of the transfer integral between nearest neighbours

	in the conduction band
λ_v	the modulus of the transfer integral between nearest neighbours in the valence band
α_o	$= \frac{2\pi e^2 P^2 M}{ncm_o^2 \hbar^2 \omega} = 0.006$
M	in-plane reduced mass of the electron-hole pair
P	is the Kane matrix element
n	optical index
$J_m\ (x)$	Bessel function of order x and index m
h	Planks constant = 6.626 x 10^{-34} J-s

A computer program was written to solve this equation, B.8, and thus the absorption spectra of the superlattice layer CB 102 and also the pairs of coupled wells structure, CB 184, under an applied field were modelled. These results are presented in chapter 5. A more detailed account of the theory of this model can be found in Bleuse 1988.